Theoretical and experimental studies of energy transfer dynamics in collisions of atomic and molecular species with model organic surfaces

William Andrew Alexander

Dissertation submitted to the faculty of the
Virginia Polytechnic Institute and State University
in partial fulfillment of the requirements for the degree of

DOCTOR OF PHILOSOPHY
in
Chemistry

Diego Troya, Chair
John R. Morris
T. Daniel Crawford
James M. Tanko
Edward F. Valeev

1 April 2009
Blacksburg, Virginia

Keywords: potential-energy surface derivation, classical-trajectory simulations, molecular-beam scattering, self-assembled monolayers, rotational and vibrational energy transfer, stereodynamics

Copyright 2009, William A. Alexander

Theoretical and experimental studies of energy transfer dynamics in collisions of atomic and molecular species with model organic surfaces

William Andrew Alexander

(ABSTRACT)

A full understanding of chemical reaction dynamics at the gas/organic-surface interface requires knowledge of energy-transfer processes that happen during the initial gas/surface collision. We have examined the influence of mass and rovibrational motion on the energy-transfer dynamics of gas-phase species scattering from model organic surfaces using theory and experiment. Molecular-beam scattering techniques were used to investigate the rare gases, Ne, Ar, Kr, and Xe, and the diatomics, N_2 and CO, in collisions with CH_3- and CF_3-terminated self-assembled monolayer (SAM) surfaces. Complementary molecular-dynamics simulations were employed to gain an atomistic view of the collisions and elucidate mechanistic details not observable with our current experimental apparatus. We developed a systematic approach for obtaining highly accurate analytic intermolecular potential-energy surfaces, derived from high-quality ab initio data, for use in our classical-trajectory simulations. Results of rare gas scattering experiments and simulations indicate mass to be the determining factor in the energy-transfer dynamics, while other aspects of the potential-energy surface play only a minor role. Additionally, electronic-structure calculations were used to correlate features of the potential-energy surface with the energy-transfer behavior of atoms and small molecules scattering from polar and non-polar SAM surfaces. Collisions of diatomic molecules with SAMs are seen to be vibrationally adiabatic, however translational energy transfer to and from rotational modes of the gas species, while relatively weak, is readily apparent. Examination of the alignment and orientation of the final rotational angular momentum of the gas species reveals that the collisions induce a stereodynamic preference for the expected "cartwheel" motion, as well as a surprising propensity for "corkscrew" or "propeller" motion. The calculated stereodynamic trends suggest that the CH_3-SAM is effectively more corrugated than the CF_3-SAM. Finally, the feasibility for collisional-energy promoted, direct gas/organic-surface reactions was interrogated using the 1,3-dipolar azide-alkyne cycloaddition reaction. We found that geometrical constraints prevented the reaction from proceeding at the probed conditions.

Acknowledgments

Special thanks go to my advisor, Dr. Diego Troya, for recognizing my potential and accepting nothing less. Diego's enthusiasm, drive, and joie de vivre are infectious and inspiring. Thank you for teaching me so much.

Special thanks also go to Dr. John Morris. John has made me a better experimentalist and communicator. He has been an amazing role model for me.

Thanks go out to the rest of my committee, Dr. Daniel Crawford, Dr. James Tanko, and Dr. Edward Valeev. I couldn't have asked for a better group of people to guide my graduate studies.

I would like to acknowledge all the members of the Morris group past and present, including Scott Day, Larry Fiegland, Wes Gordon, Allyn Milojevich, Josh Uzarski, Dimitar Panayotov, Megan Bennett, Wes Sanders, Leslie Adamczyk, Erin Davis, Jessica Lu, Alec Wagner, and Amanda Bolger. You guys made lugging steel chambers, scraping up solidified pump oil, rewiring fried circuits, and risking the occasional minor explosion all worth it!

A special word of thanks goes to my original "Beam Team" cohorts, Megan and Jessica.

Paula Weiss, Josh Layfield, Uros Tasic, and Andrew Sweeney, as well as Ryan Fortenberry and Kyle Wilmsmeyer for making the "Troya Lifestyle Center" into more of a second home than a computational lab.

Mike Perfetti and Aaron Commons, for many a stimulating and intoxicating discussion.

Paul Deck, Shelli Fowler, Jeshua Pacifici, and Karen DePauw for their influence and insight into the world of academia.

Daniel and Lindsay Johnson, Matt Hill, and Andy Green for being true, life-long friends.

I thank my parents for teaching me how to walk a noble path through life, and letting me blaze my own trail. My mother's creativity and father's scientific mind have no doubt positively shaped me into the practitioner I am today.

I am constantly in awe of my wife, April. Without her ever-present support and encouragement, as well as her infinite patience and understanding during my graduate studies, we certainly would have failed. For my daughter Kennedy, you bring joy and meaning to my life everyday. Thanks for waiting for me so many late nights; I love you to the stars.

W.A.A., April 2009, *Christiansburg, VA*

Attribution

Several colleagues and collaborators aided the author in research and manuscript preparation throughout various chapters within this dissertation. A brief description of their contributions are included here.

Prof. Diego Troya (Department of Chemistry, Virginia Tech) is the primary Advisor and Committee Chair. Prof. Troya provided guidance for the computational aspects of the research contained herein. He collaborated with the author in preparing the previously-published manuscripts included within this dissertation.

Prof. John R. Morris (Department of Chemistry, Virginia Tech) is also an Advisor and Committee Member. Prof. Morris provided guidance for the experimental aspects of the research contained herein. He collaborated with the author in preparing many of the previously-published manuscripts included within this dissertation.

Prof. B. Scott Day (Department of Chemistry, Marshall University), formerly a member of the Morris research group, provided initial mentorship of the author with regards to the experimental research described in Chapter 5. He collaborated with the author in preparation of the manuscript in Chapter 5.

Prof. T. Randall Lee (Department of Chemistry, University of Houston) provided access to molecules synthesized in his research group which the author used throughout the research presented herein. Prof. Lee collaborated with the author in preparation of the manuscript included in Chapter 5.

Megan E. Bennett (Department of Chemistry, Virginia Tech), currently in the Department of Radiochemistry at UNLV, was a member of the Morris research group and collaborated with the author in performing the experiments described in Chapter 6. She also collaborated in preparation of the manuscript included in Chapter 6.

Jessica W. Lu (Department of Chemistry, Virginia Tech) is a member of the Morris research group and collaborated with the author in performing the experiments described in Chapter 6.

H. Justin Moore (Department of Chemistry, University of Houston) synthesized molecules in the lab of Prof. Lee, which were subsequently used in the author's experimental research.

Table of Contents

List of Figures

List of Tables

Chapter 1

Introduction

Thesis statement

The objective of the research presented herein is to further our understanding of energy transfer dynamics at the gas/organic-surface interface.

1.1. MOTIVATING FACTORS

The study of thin-film organic materials is relevant to many disciplines including electrochemistry, wetting, lithography, microcontact printing, adhesion, and microelectronic circuit fabrication,[1–3] among others. Collisions of gas-phase species with organic films are involved in many important processes, especially in biological interfaces and membranes, corrosion protection, and atmospheric chemistry.[4–6] Reactions taking place on the surface of aerosol particles have been found to play a major role in the ozone balance in the stratosphere.[7] The chemistry of aerosols is complicated by the finding that these particles are often coated with long chain amphiphilic molecules. Samples of both marine and continental aerosols have been shown to contain fatty acids with alkyl chains 14 to 30 carbons long, forming a boundary layer that gas-phase species must transverse before reacting with the aerosol core.[8,9] High energy gas/surface collisions degrade satellite and spacecraft coatings in the low earth orbit environment.[10,11] An example of an important gas/surface interaction in biology is mammalian respiration, which requires the permeation of air through surfactant coatings in the lungs.[5]

When a gas-phase species impinges upon an organic surface it collides first with the outermost region of the interface. The result of the gas/surface collision is highly dependent on energy exchange between the gas-phase species and the surface. The first few encounters the gas atom/molecule experiences with the surface serve to determine whether the impinging species is directed back into the gas phase, or the surface absorbs the gas' kinetic energy, allowing it to stick and thermally equilibrate. Determining the factors responsible for the flow of energy between organic surfaces and gas-phase particles is of fundamental importance for a full understanding of gas/surface collisions. The likelihood that a gas species will trap

on the surface depends on such factors as the gas' incident collision energy, approach angle, internal rovibrational states and impact point on the surface. The gas/surface attractive forces, temperature, physical and chemical nature of the surface, and relative masses of the gas and surface also play a role in determining the scattering dynamics. Use of inert gaseous species as projectiles eliminates reactions, allowing one to probe the dynamics of the initial impact. Systematic studies varying the impinging

particles and properties of the surface will add to our understanding of gas/surface interfacial chemistry.

1.2. GAS/ORGANIC SURFACE SCATTERING

The energy-transfer dynamics of gas/surface interfaces has been studied extensively for over fifty years. Since the 1960s, much attention has be given to a host of atomic and molecular projectiles impinging upon various solid (usually metal) surfaces.[12–18] Gas/metal systems were amenable to experimental study via collisions of molecular beams in high vacuum because of the relative ease of preparing a clean, well characterized metal surface. In addition, interpretation of results is eased by the simple structure and interactions with the metal surface.

A lineage of classical scattering models has spawned from efforts to build predictive models for experimental studies. The first, simplest, and probably most well-known of these models was developed by Logan and Stickney and is commonly referred to as the *Hard-Cube model*.[19,20] In this model, the gas-phase species of mass m_{gas} interacts with a cube having an effective surface mass, $m_{surface}$. Energy transfer is allowed only in the direction normal to the cube's surface such that $\frac{\Delta E}{E_\perp} = \frac{4\mu}{(\mu+1)^2}$, where $\mu = \frac{m_{gas}}{m_{surface}}$, and ΔE is the change in the energy component along the surface normal, $E_\perp$. This model of scattering behavior is simplistic in that it neglects, among others, corrugation of the surface, surface vibrations, electrostatic and dispersive attraction between the gas and the surface, and energy transfer in non-normal directions.[21] It does, however, do a fine job of predicting trends for gases scattering from smooth, hard surfaces, and it is still used, giving highly quantitative agreement with experiment for systems in which its use is optimal.[22]

There have been developed many more sophisticated models for gas/surface scattering that attempt to account for some of the interactions neglected in the Hard-Cube model,

each with varying degrees of complexity and success. The *Soft-Cube model* incorporates a repulsive exponential potential effective at short gas/surface distances, and an attractive step potential.[23] These simple additions to the model yield significantly better agreement with experiment when applied to systems of rare-gas scattering from various precious metals.[15,20]

The *Washboard model* extends theory further by adding an adjustable parameter to describe surface corrugation.[24] For liquid or polymeric surfaces, another correction to the model was needed to incorporate the flexibility of these surfaces. The *Washboard with Moment of Inertia model* (WBMI) developed by Yan et al.[25] includes parameters to describe the moment of inertia of the effective surface object involved in the collision. The model introduces dependencies of the energy transfer efficiency on both the position and direction of impact with the surface, a feature that was shown in molecular dynamics simulations to be critical.[25] The WBMI model has been directly applied to collisions of Ne and Ar with an alkanethiolate self-assembled monolayer, and is able to reproduce qualitatively many of the major dynamical results (i.e., a bimodal final energy distribution with a low-energy component well-fit to a Boltzmann distribution) when compared to experiment[26,27] and classical trajectory simulations.[25,28,29] The WBMI model is designed to work well for surfaces with periodic corrugation, and as such is not expected to do well in describing rougher, more amorphous surfaces. Quite recently, Tully and co-workers developed a more general model based on the washboard model that is suitable to describe surfaces of arbitrary roughness.[30] This "rough washboard" model reproduces results of the WBMI model, and can be applied to rough, but uncorrugated surfaces. Although these models are successful in reproducing important aspects of the dynamics of gas/surface scattering, truly quantitative studies require use of atomistic molecular dynamics simulations.

As a result of collision with a surface, an impinging gas-phase species may display a wide range of product dynamics. In the absence of reaction, the colliding particles may simply interact impulsively with the surface and rebound after only one or a few brief encounters during which minimal energy is transferred; these direct scattering processes are a limiting case referred to commonly as impulsive scattering (IS). During collision, IS trajectories sample mostly the repulsive wall of the potential energy surface and do not lose enough energy to become trapped by the attractive gas/surface potential well. The products tend to recoil at near specular angles and retain a large portion of their initial energy. The other limiting mechanistic channel in these collisions consists of trapping (on or below the

surface interface) followed by subsequent desorption back into the gas phase. In trapping-desorption (TD) events, the impinging particle does lose enough of its energy to sample the attractive potential well. TD collisions are characterized by multiple encounters, complete thermalization with the surface, and relatively long residence times. Gas-phase particles interacting through a TD mechanism desorb with a Maxwell-Boltzmann distribution (at the surface temperature) of energies, and a cosine angular distribution. Penetration into the surface may occur in both IS (ballistic penetration) and TD (penetrating trapping desorption) events, although it is generally minimal except for the heaviest and most energetic of gas projectiles. If the impinging atom has sufficient energy, any of these processes may occur.

The first reported study of molecular beam scattering from ordered organic monolayers was in 1987 by Cohen et al.[31] They scattered He, Ar, O_2, and NO from SAMs of n-octadecyltrichlorosilane (OTS), and perfluorinated acid ester (PFAE) on glass. This early work addresses many of the questions that molecular beam/SAM scattering experiments seek to answer and the general observations of this study will serve well as an introduction to the other experiments. For the rare gases and O_2, energy transfer to the OTS SAM was greatly enhanced relative to the more massive PFAE surface. In addition, at the low collision energies examined, He was more fully thermalized on both SAMs (28% and 43% kinetic energy loss to the PFAE and OTS SAMs, respectively) relative to Ar (4% and 29% loss, same surfaces). The low energy component of the TOF distributions was able to be fit with a Maxwell-Boltzmann distribution at the surface temperature of 300K. The authors posit that the energy loss from these low-energy beams is, "probably dominated by partial migration into and tortuous exit from the chains."[31] However, the authors promote the idea that, in addition to penetration of the surface, low-frequency surface modes could sequester the translational energy, an idea that has received much recent theoretical study.[32–34] They also advance the fact that, at least for the case of PFAE, the most exterior CF_3 group dominates the interaction. Use of the Hard-Cube model revealed that, for He scattering, the effective surface mass for PFAE was large enough that the He atom would have to interact with a full CF_3 group as opposed to a single fluorine atom. Finally, the authors comment on the lack of information about energy disposal for the diatomic molecules, resulting in difficulty in interpreting the data for these molecules. The need for probes of internal energy changes (translational $\rightarrow$ vibrational, rotational energy) was pointed out. This difficulty of

probing the internal states of polyatomic molecules in scattering events is one motivation for our theoretical investigations into rovibrational energy transfer in diatomic molecular projectiles presented in Chapters 8, 9, and 10.

Bosio and Hase published the first attempts to model collisions of gas-phase species with SAMs.[35] They studied energy transfer in systems of Ne colliding with an n-hexylthiolate SAM using classical molecular dynamics simulations. Incident energies ranging from 1.2 to 40 kcal·mol^{-1}, and incident angles ranging from 10 to 80 degrees from the surface normal were simulated. Trapping-desorption was shown to be the dominant mechanism for trajectories with low incident energies; Ne with E_{coll}=1.2 kcal·mol^{-1} yields 100% TD, while 20 kcal·mol^{-1} yields 31.25% TD and 40 kcal·mol^{-1} yields 24.5% TD. The IS channel also becomes more dominant at glancing incident angles (θ_i $\sim$90°) (i.e. with E_{coll}=20 kcal·mol^{-1} and θ_i=80° only 1.8% TD is predicted, while θ_i=10° gives 37% TD). Final angular distributions all peak at near specular angles. These data were found to be in good agreement with experimental studies by Nathanson and co-workers of Ne scattering from liquid squalane surfaces.[36]

After pioneering efforts by Bosio and Hase, the Hase and Sibener groups published a number of studies designed to elucidate the origin of the bimodal final translational-energy distribution,[28] and the mechanisms of gas-translational to surface-vibrational energy partitioning in Ne collisions with SAMs.[29,33,34] Their investigations focused on study of what modes accept the rare gas' translational energy. The first investigations into the origins of the Boltzmann component (what we have thus far referred to as TD) of the translational-energy distributions of Ne scattered from n-alkane SAMs revealed that a Ne-SAM intermediate (i.e. trapped Ne) is not necessarily responsible for the Boltzmann-like behavior, since the vast majority of trajectories are single-encounter collisions. Instead, a combination of effects from penetration into the SAM and impulsive collision processes must contribute to the Boltzmann component (BC). (The authors prefer the term BC to TD for this low energy scattering channel as a result of the observation that trapping plays a minor role in this channel; we use these terms interchangeably, while the scattering community at large seems to prefer TD.) As penetration is minimal at small E_{coll} and large θ_i, both the IS and BC components of systems at these energies and angles must arise from direct impulsive-type collisions. These results prompted further study of energy partitioning into surface modes. Yan et al. studied mode-specific energy transfer and intramolecular vibrational energy redistribution (IVR) within the SAM to try to shed light on the mechanisms whereby both IS

and BC components could result from impulsive scattering collisions. Simulations using a normal-mode coordinate system revealed that collision energy is preferentially transferred to low-frequency, large-amplitude surface modes, and as E_{coll} increases, higher frequency modes begin to become excited.[34] Comparing both a normal mode and anharmonic mode model of the SAM, it was found that the energy transfer increased with the anharmonic model, suggesting that efficient energy transfer to highly anharmonic modes of the monolayer surface resulted in the Boltzmann component of the translational-energy distribution.[34]

Yan et al. further investigated the influence of intramolecular vibrational redistribution within the SAM surface.[33] It was found that the surface modes excited depend on the surface site at which the impinging atom collides. For inefficient energy transfer sites, intramolecular motions of single chains (such as CCC bending modes) are preferentially excited, while collision sites which promote efficient energy transfer preferentially excite torsions and chain wagging motions. Comparison of the autocorrelation functions of the CCC bending modes and torsional modes revealed that relaxation of the bending modes is slow and longer than 2.0 ps, while relaxation of the torsional modes is fast and less than 0.5 ps. If IVR from the initially excited modes happens on a time scale faster or similar to the residence time of the colliding atom, energy transfer may be very efficient, even in a single encounter. As the collision time of Ne on the SAM surface was shown to be between ∼0.2-0.5 ps, initial excitation of CCC bending modes will sequester energy until well after the collision event. However, IVR from torsional modes will compete with Ne's residence time on the surface. This coupling of the Ne translation to a "bath of modes" could have the effect of "thermalizing" the impinging atom and result in a Boltzmann-like component in the final translational-energy distribution.[33]

1.3. SAM STRUCTURAL EFFECTS

The properties of self-assembled monolayers allow us, via organic synthetic techniques, to build a variety of organic surfaces with similar structure but different chain lengths, terminal functional groups, and surface densities. This offers opportunities to investigate how the chemical and physical properties of the exposed groups influence the interfacial characteristics of the organic surface. The effect of chain length has been studied by many groups. Rosenbaum et al. studied how chain length effects low-energy surface vibrations of

the striped phase of n-alkanethiol SAMs using both inelastic helium scattering and molecular dynamics simulations.[37,38] While for $2 < n < 6$ (where n is the number of carbon units in the chain), some chain-length dependency was observed, they found that for $n > 6$, the alkanethiols have essentially the same vibrational energies, which agrees with earlier studies of alkanes on Cu(111) by Wöll and co-workers.[39–41] Day and Morris have investigated the dynamics of 80 kJ·mol^{-1} Ar colliding with the dense $\sqrt{3} \times \sqrt{3}$ R30° phase of n-alkanethiol SAMs of varying chain length. They found that for short chain lengths ($2 < n < 6$), the fractional energy transfer and extent of thermalization of the Ar atoms during collision is directly proportional to chain length, while longer chains ($n > 6$) showed no such dependence on chain length.[42] In addition, with the long chains they observed an oscillating odd-even effect in the intensity of the IS channel due to the differential orientation of the terminal methyl groups.[42] Ferguson et al. furthered understanding of this chain length dependency by studying SAMs with buried hydrogen bonding groups.[43] They synthesized SAMs with a carbamate functionality in the middle of the alkyl chain, and varied the number of carbons in the alkyl chain exterior to this functionality. The carbamate groups form a rigid hydrogen-bonding network, which constrains the interior portions of the chains. A chain-length effect is again observed for $n < 6$ carbons above the carbamate group.[43] These results suggest that long-range molecular motions involving up to six carbon atoms are involved in the energy-transfer process.

Day et al. have also studied the influence of surface density on the dynamics of Ar + SAM collisions using both molecular-beam experiments[32] and molecular dynamics simulations.[44] Experimentally, they scattered Ar from various alkanethiol SAMs formed on both Au(111) and Ag(111). The 4.98 Å nearest-neighbor distance of the sulfur atoms absorbed on gold is decreased to 4.67 Å on silver. This tighter packing forces the alkanethiol chain tilt angle to decrease from ∼30° for SAMs on gold to ∼13° for SAMs grown on silver. Collisional energy transfer to the surface was shown to be independent of chain length for $n > 10$ carbon units for the silver substrate SAMs, as opposed to six carbons for the SAMs on gold; the odd-even effect is not as pronounced for the silver SAM systems. As a result of the tighter packing on Ag, atoms interacting via the IS channel transfer about 7% less energy in collision with the SAM/Ag surfaces than with SAMs formed on Au. With 80 kJ·mol^{-1} incident Ar, the TD fraction when scattering from the SAMs on Ag is 25% smaller than those formed on Au. Molecular dynamics studies using a hybrid united-atom/explicit-atom approach developed

by Troya and co-workers[45] investigated dodecanethiolate SAMs with lattice spacings of 4.30, 4.67, 4.98, 5.20, and 5.40 Å.[44] They found that decreasing the density of SAMs promotes energy transfer due to three main reasons: 1) the probability of multiple encounters with the surface increases for sparse SAMs, 2) the increase in lattice spacing promotes surface penetration, and 3) the vibrational frequencies of low-frequency, large-amplitude modes decrease for less dense SAMs. Troya et al. also noted that the final angular distributions in penetrating events does not follow a cosine shape, but instead displays a preference to desorb along the chain-tilt direction.[44]

Studies of Wysocki and co-workers of low-energy ion scattering from Langmuir-Blodgett and SAM films have shown that the identity of the terminal group is the single most important factor in determining the extent of energy transfer from the impinging atoms to the surface.[46,47] The Morris group has studied rare gas scattering from SAMs with a variety of functional groups including methyl groups,[42] vinyl groups,[48] and a number of hydrogen-bonding groups (-OH, -COOH, -NH_2).[48–50] Generally, hydrogen-bonding functional groups seem to form hydrogen-bonding networks at the gas/surface interface, making the surfaces effectively more rigid, and hence decreasing energy transfer from impinging gas species to the surface. Seemingly unaffected by the difference in mass between the two terminal groups, transfer of energy from 80 kJ·mol^{-1} Ar was found to be nearly identical for the OH- and COOH-terminated SAMs. However, it was found that energy transfer in the IS channel when scattering from the hydrogen bonding SAMs was around 5% less than when scattering from the methyl- and vinyl-terminated SAMs. The TD fraction for the hydrogen-bonding SAMs was 43% compared to 61% for the methyl- and vinyl-terminated SAMs. Amine-terminated monolayers were also shown to behave similarly to OH- and COOH-terminated SAMs.[49] The effect of hydrogen bonding at the surface was further examined by scattering from mixed monolayers of CH_3- and OH- terminated alkanethiols.[49] It was found that energy transfer was independent of OH concentration up to about 33% OH. After this point, energy transfer decreases with increasing OH concentration. This observation gives further evidence that the extent of hydrogen bonding serves to dampen the low-energy, high-amplitude motions of the chains that have been shown to be largely responsible for efficient energy transfer. We further note these observations are in line with the investigations of various gases scattering from squalane and glycerol of Nathanson and co-workers.[36]

The studies outlined above indicate that the exposed group of the SAM plays a crucial

role in the dynamics of gas/surface energy transfer. Their exist many possible origins of the different energy transfer behavior of the gas-phase species scattering from SAMs with different functionality at the terminus, including changes in mass, different interactions within the SAM, and different interactions with the gas species. In an attempt to separate these contributions, fluorinated SAMs, as suggested in the work of Cohen et al., may provide a route to investigate the unique effect of mass on the scattering dynamics.

Although not specifically involved with scattering studies, Lee and co-workers have done extensive characterization of selectively fluorinated alkanethiolate SAMs.[47,51–53] They have been able to synthesize a family of semifluorinated alkanethiol molecules, and thereby can readily tune the SAM terminus.[54] While it has been shown via atomic force microscopy,[55] polarization modulation infrared reflection adsorption spectroscopy,[56] and other techniques[53] that ω,ω,ω-trifluoroalkanethiol SAMs (CF_3-SAMs) and n-alkanethiol SAMs (CH_3-SAMs) have similar structures, their interfacial properties are quite different due to the difference in the exposed terminal groups. Extensive work by Lee and co-workers[51,52,57] indicates that CF_3-SAMs interact more strongly with water than CH_3-SAMs. This behavior has been rationalized as due to the presence of a dipole at the CF_3-SAM terminus emerging from the charge separation in the terminal CH_2-CF_3 moiety.[58]

1.4. HIGH-ENERGY EFFECTS

Thus far, we have described systems of rare gases impinging on self-assembled monolayers with collision energies ranging from near-thermal to what is sometimes referred to as the superthermal regime (up to $\sim$ 1 eV). We review in this section a few interesting studies of hyperthermal (>1 eV) rare gas collisions with SAMs. The Sibener group has recently scattered 2.1 eV Ar and 1.54 and 3.6 eV Xe from a decanethiol SAM and the resulting time-of-flight distributions exhibit the expected IS and TD channels.[59] In addition, however, their experiments show evidence for a third scattering mechanism. At incident angles near surface-normal, they observe a third mode peaked at energies intermediate to the TD and IS channels, which they attribute to a new channel they term "directed ejection." The directed ejection process involves deep penetration of the rare gas into the channels between the aligned chains of the SAM, locally deforming the surface. After disposal of the collision energy into the various sink modes of the monolayer, the gas molecule is forced back into the

vacuum as the chains rebound to their equilibrium positions. As a result, the expelled gas leaves the surface with energy substantially higher than the thermal distribution expected for TD processes, and with a final polar angle distribution peaked close to the chain-tilt direction. While not as easily seen with Ar or with the lower energy Xe, this effect is readily apparent as a trimodal final energy distribution for the Xe system at 3.6 eV with θ_i=20°. This effect, while convincingly presented by Sibener, had also been theorized and observed in simulations and experiments of other systems prior to this work.[28,32,44]

Fogarty and Kandel have also studied Ar and Xe collisions with SAMs at energies approaching the hyperthermal regime.[60,61] They have scattered 0.6 eV Ar and 1.3 eV Xe from an *n*-octanethiol SAM and monitored the influence these collisions have on structural changes in the monolayer via in situ scanning tunneling microscopy. Their results indicate that bombardment by energetic atoms leaves the well-ordered, close packed domains of the SAM largely unchanged, while the collisions do induce changes in the monolayer at domain boundaries and vacancy sites, as well as inducing phase changes.

1.5. SUMMARY AND RESEARCH OBJECTIVES

The research presented herein aims to further the understanding of gas/organic-surface processes by studying the energy-transfer dynamics of the collisions. We have examined the effect of mass on the collision dynamics by scattering rare gases from CH_3- and CF_3-SAM surfaces. Complementary classical-trajectory simulations reveal a wealth of information about the atomic-level details of the energy-transfer dynamics. These simulations required the development of high-accuracy potential-energy surfaces, which were derived from high-quality ab initio data. Electronic-structure calculations were further used to correlate features of the potential-energy surface with the energy-transfer behavior of small molecules scattering from polar and non-polar SAM surfaces.

The influence of rotational and vibrational degrees of freedom on energy-transfer dynamics was investigated via molecular-beam scattering and classical-trajectory simulations of N_2 and CO collisions with CH_3- and CF_3-SAM surfaces. Molecular-dynamics simulations were used to determine the extent of collisional energy transfer to/from the gas-phase molecule's rotational and vibrational modes, while molecular beam experiments provided final translational-energy distributions, which are additionally used to validate our com-

putational model. In our simulations, analysis of the alignment and orientation of the rotational angular momentum vector of the diatomic gas species allows us to additionally glean information about stereodynamic aspects of the collisions.

Finally, we probed the feasibility of a collisional-energy promoted, direct gas/organic-surface reaction. The 1,3-dipolar azide-alkyne cycloaddition reaction was interrogated via use of alkynic molecular beams impinging on azide-terminated SAM surfaces. These studies add to the ever-growing body of knowledge of gas/organic-surface chemical reaction dynamics.

REFERENCES

[1] L. H. Dubois and R. G. Nuzzo, Annu. Rev. Phys. Chem. **43**, 437 (1992).

[2] A. Ulman, *An introduction to ultrathin films: from Langmuir-Blodgett to self-assembly* (Academic Press, 1991).

[3] A. Ulman, *Self-assembled monolayers of thin films*, vol. 24 (Academic Press, San Diego, 1998).

[4] D. J. Donaldson and V. Vaida, Chem. Rev. **106**, 1445 (2006).

[5] G. M. Nathanson, P. Davidovits, D. R. Worsnop, and C. E. Kolb, J. Phys. Chem. **100**, 13007 (1996).

[6] S. L. Koontz, L. J. Leger, J. T. Visentine, D. E. Hutton, J. B. Cross, and C. L. Hakes, J. Spacecraft and Rockets **32**, 483 (1995).

[7] S. K. Friedlander, *Smoke, Dust, and Haze: fundamentals of aerosol dynamics* (Oxford University Press, New York, 2000), 2nd ed.

[8] R. E. Peterson and B. J. Tyler, Atmos. Environ. **36**, 6041 (2002).

[9] J. Tervahatta, J. Juhanoha, and K. Kuipiainen, J. Geophys. Res. (Atmos.) **107**, 4319 (2002).

[10] D. Troya and G. C. Schatz, Int. Rev. Phys. Chem. **23**, 341 (2004).

[11] T. K. Minton, M. Tagawa, and G. M. Nathanson, J. Spacecr. Rockets **117**, 6239 (2002).

[12] R. Sau and R. P. Merrill, Surface Science **34**, 268 (1973).

[13] F. O. Goodman and H. Y. Wachman, *Dynamics of Gas-Surface Scattering* (Academic Press, New York, 1976).

[14] G. A. Somorjai, *Principles of Surface Chemistry* (Prentice-Hall, Inc., Englewood Cliffs, New Jersey, 1972).

[15] H. Saltsburg and J. N. Smith, Jr., J. Chem. Phys. **45**, 2175 (1966).

[16] S. T. Ceyer and G. A. Somorjai, Annu. Rev. Phys. Chem. **28**, 477 (1977).

[17] J. N. Smith, Jr., Surface Science **34**, 613 (1973).

[18] P. S. Weiss, A. Amirav, P. L. Trevor, and M. J. Cardillo, J. Vac. Sci. Technol. A **6**, 889 (1988).

[19] R. M. Logan and R. E. Stickney, J. Chem. Phys. **44**, 195 (1966).

[20] R. M. Logan, J. C. Keck, and R. E. Stickney, Rarefied Gas Dynamics **1**, 49 (1967).

[21] R. B. Subbarao and D. R. Miller, J. Chem. Phys. **58**, 5247 (1973).

[22] Y. Watanabe, H. Yamaguchi, M. Hashinokuchi, K. Sawabe, S. Maruyame, Y. Matsumoto, and K. Shobatake, Eur. Phys. J. D **38**, 103 (2006).

[23] R. M. Logan and J. C. Keck, J. Chem. Phys. **49**, 860 (1968).

[24] J. C. Tully, J. Chem. Phys. **92**, 680 (1990).

[25] T.-Y. Yan, W. L. Hase, and J. C. Tully, J. Chem. Phys. **120**, 1031 (2004).

[26] K. D. Gibson, N. Isa, and S. J. Sibener, J. Chem. Phys. **119**, 13083 (2003).

[27] N. Isa, K. D. Gibson, and S. J. Sibener, J. Chem. Phys. **120**, 2417 (2004).

[28] T.-Y. Yan and W. L. Hase, Phys. Chem. Chem. Phys. **2**, 901 (2000).

[29] T.-Y. Yan and W. L. Hase, J. Phys. Chem. B **106**, 8029 (2002).

[30] N. Mateljevic, J. Kerwin, S. Roy, J. R. Schmidt, and J. C. Tully, J. Phys. Chem. C **113**, 2360 (2009).

[31] S. R. Cohen, R. Naaman, and J. Sagiv, Phys. Rev. Lett. **58**, 1208 (1987).

[32] B. S. Day and J. R. Morris, J. Chem. Phys. **122**, 234714 (2005).

[33] T.-Y. Yan, N. Isa, K. D. Gibson, S. J. Sibener, and W. L. Hase, J. Phys. Chem. A **107**, 10600 (2003).

[34] T.-Y. Yan and W. L. Hase, J. Phys. Chem. A **105**, 2617 (2001).

[35] S. B. M. Bosio and W. L. Hase, J. Chem. Phys. **107**, 9677 (1997).

[36] M. E. Saecker and G. M. Nathanson, J. Chem. Phys. **99**, 7056 (1993).

[37] A. W. Rosenbaum, M. A. Freedman, S. B. Darling, I. Popova, and S. J. Sibener, J. Chem. Phys. **120**, 3880 (2004).

[38] S. B. Darling, A. W. Rosenbaum, and S. J. Sibener, Surface Science **478**, L313 (2001).

[39] G. Witte, D. Fuhrmann, and C. Woll, Chem. Phys. Lett. **265**, 347 (1997).

[40] D. Fuhrmann and C. Woll, New J. Phys. **1**, 1.1 (1998).

[41] G. Witte and C. Woll, J. Chem. Phys. **103**, 5860 (1995).

[42] B. S. Day and J. R. Morris, J. Phys. Chem. B **107**, 7120 (2003).

[43] M. K. Ferguson, J. R. Lohr, B. S. Day, and J. R. Morris, Phys. Rev. Lett. **92**, 073201 (2004).

[44] B. S. Day, J. R. Morris, W. A. Alexander, and D. Troya, J. Phys. Chem. A **110**, 1319 (2006).

[45] B. S. Day, J. R. Morris, and D. Troya, J. Chem. Phys. **122**, 214712 (2005).

[46] C. Gu, V. H. Wysocki, A. Harada, H. Takaya, and I. Kumadaki, J. Am. Chem. Soc. **121**, 10554 (1999).

[47] D. L. Smith, V. H. Wysocki, R. Colorado, Jr., O. E. Shmakova, M. Graupe, and T. R. Lee, Langmuir **10**, 3895 (2002).

[48] B. S. Day, G. M. Davis, and J. R. Morris, Anal. Chim. Acta **496**, 249 (2003).

[49] B. S. Day, S. F. Shuler, A. Ducre, and J. R. Morris, J. Chem. Phys. **119**, 8084 (2003).

[50] S. F. Shuler, G. M. Davis, and J. R. Morris, J. Chem. Phys. **116**, 9147 (2002).

[51] R. Colorado, Jr. and T. R. Lee, J. Phys. Org. Chem. **13**, 796 (2000).

[52] H. Fukushima, S. Seki, T. Nishikawa, H. Takiguchi, K. Tamada, K. Abe, R. Colorado, Jr., M. Graupe, O. E. Shmakova, and T. R. Lee, J. Phys. Chem. B **104**, 7417 (2000).

[53] L. Houssiau, M. Graupe, R. Colorado, Jr., H. I. Kim, T. R. Lee, S. S. Perry, and J. W. Rabalais, J. Chem. Phys. **109**, 9134 (1998).

[54] M. Graupe, T. Koini, V. Y. Wang, G. M. Nassif, R. Colorado, Jr., R. J. Villazana, H. Dong, Y. F. Miura, O. E. Shmakova, and T. R. Lee, Journal of Fluorine Chemistry **93**, 107 (1999).

[55] H. I. Kim, T. Koini, T. R. Lee, and S. S. Perry, Langmuir **13**, 7192 (1997).

[56] H. I. Kim, M. Graupe, O. Oloba, T. Koini, S. Imaduddin, T. R. Lee, and S. S. Perry, Langmuir **15**, 3179 (1999).

[57] D. M. Alloway, M. Hofmann, D. L. Smith, N. E. Gruhn, A. L. Graham, R. Colorado, Jr., V. H. Wysocki, T. R. Lee, P. A. Lee, and N. R. Armstrong, J. Phys. Chem. B **107**, 11690 (2003).

[58] E. G. Shafrin and W. A. Zisman, J. Phys. Chem. **61**, 1046 (1957).

[59] K. D. Gibson, N. Isa, and S. J. Sibener, J. Phys. Chem. A **110**, 1469 (2006).

[60] D. P. Fogarty and S. A. Kandel, J. Chem. Phys. **124**, 111101 (2006).

[61] D. P. Fogarty and S. A. Kandel, J. Chem. Phys. **125**, 174710 (2006).

Chapter 2

Experimental methodology

2.1. OVERVIEW OF THE APPROACH

Our experiment is designed to examine how the translational energy of an impinging gas is gained/lost upon collision with model organic surfaces. We utilize three main technologies to achieve this: 1) self-assembled monolayers, 2) atomic or molecular beams, and 3) ultra-high vacuum. First, we use self-assembled monolayers (SAMs) as models of organic surfaces. SAMs can be formed by spontaneous absorption of alkylthiols on metal (Au, Ag, Cu) surfaces and result in well-ordered surfaces whose interfacial properties can be tuned via organic synthesis techniques. SAMs also have the property of being stable in an ultra-high vaccuum (UHV) environment, unlike many common organics. (Ultra-high vaccuum is the third necessary technology for our experiments, described below.) SAMs represent one of the two collision partners in our gas/surface scattering experiment; well-collimated, nearly monoenergetic beams of atoms or molecules represent the second. Atomic and molecular beams formed by supersonic expansion techniques allow us to carefully tune the impinging gas' translational energy over a wide range. We direct the atomic/molecular beams onto the SAM surfaces in an UHV environment. Ultra-high vaccuum is required to ensure that the surface remains free of contamination from ambient gas-phase species throughout the scattering experiment. Additionally, UHV conditions ($<1\times10^{-8}$ torr) eliminate virtually all possibility for atoms and molecules in the beam to collide with ambient species before or after collision with the surfaces. Therefore, any change in the beam's translational energy profile can be attributed solely to energy transfer as a result of collision with the surface. Each of these three experimental techniques is described separately and in detail below. We then describe the scattering experiment and data analysis.

2.2. SELF-ASSEMBLED MONOLAYERS

2.2.1. Background

For reliable experimental gas/surface scattering studies, the surfaces studied must be well-ordered and clean throughout the experiment. The classic methods employed to obtain well-ordered metal or inorganic surfaces (i.e. cleavage, cutting, or polishing, followed by flame annealing, or ion bombardment in UHV for cleaning) can not be applied to most polymers or other organic materials due to their highly amorphous character, thermal instability, and propensity to sublime in UHV.[1] The amorphous character of most polymers and other organic surfaces (both solid and liquid) presents a challenge when trying to probe interactions with specific functional groups.[2] Characterization of such surfaces is difficult with traditional surface characterization techniques because they are prone to radiation damage as a result of electron or ion bombardment.[1] (This is also true of the SAM surfaces used in this study, and makes alternative characterization techniques neccesary.)

Only in the past twenty years have there been techniques developed to circumvent these difficulties and produce highly-ordered, well-characterized organic surfaces for study.[3] It is well known that small volatile organic molecules can form stable overlayers on clean metal substrates.[4] For example, the reaction of ethylene gas with the Pt(111) surface forms a surface of ordered ethylidyne groups.[5,6] However, preparation of surfaces via vapor deposition presents many limitations, including the fact that only small volatile organics can be used, caution must be used in selecting the functional groups of the organics, and sparse coverage of the metal surface.

Another way to obtain an ordered organic monolayer is with the Langmuir-Blodgett technique.[7] Langmuir-Blodgett (LB) films are formed by forcing surfactant molecules to order on a liquid surface by squeezing the molecules into a smaller and smaller surface area by means of a trough with a movable wall. These molecules must usually be long chain amphiphiles to ensure proper ordering during film synthesis. The film is then transferred to a solid surface, usually via careful mechanical dipping.[7] If carefully formed, these surfaces can have a high level of order, but the complicated process involved in the surface preparation (especially the highly empirical dipping process) makes LB films difficult to work with. In addition, the monolayer-substrate bond is weak, usually being either simple van der Waals or

hydrogen-bonded interactions, giving the films limited thermal stability.[1] Functional groups amenable to study are also limited by the requirement of the molecules to possess both a polar and non-polar end.

Self-assembled monolayers (SAMs) of functionalized alkanethiols absorbed on gold (also on silver and copper) have several advantages over vapor-deposited volatile organics and LB films. The alkanethiol molecules bind covalently with the gold substrate giving them enhanced thermal stability over LB films. At the same time, SAMs can be formed with long chain molecules, whose chain-chain interactions ensure tight packing. As gold has a higher binding affinity for sulfur-containing functional groups (thiols, disulfides, thioacetates, etc.) than most other functional groups,[1,8] the terminal groups of the SAMs can be varied through simple organic synthetic techiques.[9] SAM sythesis is very simple: a clean gold slide is placed in a dilute solution of the thiol; the alkylthiol chains spontaneously self-assemble into well-ordered, stable films on the metal surface. When ready to use, the gold slides are simply removed from solution and rinsed.

Surface characterization can be achieved via a variety of methods including, but not limited to, reflection absorbance infrared spectroscopy (RAIRS), temperature-programmed desorption (TPD), X-ray photoelectron spectroscopy (XPS), atomic force microscopy (AFM), and scanning-tunneling microscopy (STM).[1,10] Electron and ion bombardment techniques commonly used in characterization of metallic and inorganic surfaces are not generally employed because of the potential harm these methods can inflict upon the surfaces. A detailed discussion of our surface characterization approaches is described later in this chapter.

The work of Whitesides and co-workers[11–20] and Nuzzo and co-workers[18–25] has been especially important in the study of SAMs. The first SAM made by immersion of a clean gold surface in a dilute solution of dialkyldisulfide was reported in 1983.[22] It was quickly found that higher quality films could be made by the analogous alkylthiols.[11,14,20,25] Alkanethiol self-assembled monolayers on Au(111) are found to form strong bonds ($\sim$50 kcal$\cdot$mol^{-1}) between the sulfur head groups and the gold substrate. Due to van der Waals interactions between the alkyl chains and the metal surface, the alkyl chains arrange themselves first in an ordered lying-down striped phase.[10] As the surface coverage is increased, the chains transition to a standing-up phase with a chain tilt angle of $\sim$30° from the surface normal. Ordering is driven by the 1-2 kcal$\cdot$mol^{-1} of energy per methylene unit due to dispersion forces between the hydrocarbon chains.[23] The strong Au-S interaction influences the sulfur

head groups to absorb on specific sites on the gold substrate which creates a stable $\sqrt{3} \times \sqrt{3}$ $R30°$ lattice within its related c(4×2) superlattice.[10] The question of which specific sites (atop, hollow, bridging, etc.) in the underlying gold lattice are involved in the absorption is still an open debate.[26–29]

The hexagonally packed chains in normal alkanethiolate SAMs have a nearest-neighbor spacing of 4.98±0.02 Å, resulting in a chain density in a fully covered monolayer of about 21.7 $Å^2 \cdot molecule^{-1}$, which is similar to polymethylene chains in bulk, crystalline *n*-alkanes.[1] While gold is the preferred substrate, SAMs can be formed on other metals (Ag, Cu, Pt, Ni, Fe) and semiconductors (GaAs), altering the overall structure (especially as related to packing density) of the monolayer.[10,20,30,31] We use Au substrates exclusively in the research described within this dissertation because it is inert to most chemical species and therefore stays clean until a SAM is formed.

2.2.2. SAM synthesis

Our SAM surfaces are made in the conventional way of spontaneous absorption of alkanethiolate on clean gold surfaces during submersion in an ∼1 mM ethanolic solution of the corresponding alkanethiol species. The gold substrates were created by evaporation onto Cr-coated glass slides (EMF Corp). Previous work using SAMs prepared on both gold-coated glass (polycrystalline Au) and gold-coated mica (near single-crystal Au) slides found the scattering results to have an insignificant dependence on the underlying substrate used for the monolayer, despite the differences in the polycrystalline structure of the two gold surfaces.[33,34] Before introduction of the slides into the SAM solutions, the gold-coated slides were prepared by cleaning in pirahna solution (70/30 (v/v) mixture of concentrated H_2SO_4 / 30% H_2O_2) for a minimum of 45 min. prior to use. After soaking in pirahna solution, the slides were rinsed with copius amounts of deionized water, followed by rinsing in absolute ethanol before being placed in the corresponding ethanolic solution.

Three main types of SAMs have been used in our studies: normal (CH_3-terminated), ω-fluorinated (CF_3-terminated), and ω-azido (N_3-terminated) SAMs. These were formed from the corresponding alkanethiols, most of which are commercially available. The *n*-alkanethiols ($HS(CH_2)_{n-1}CH_3$, where n=15 or 16) where obtained from Aldrich and used as received. 11-azido-undecanethiol ($HS(CH_2)_{11}N_3$) was purchased from Prochimia Surfaces (Poland) and

used as received. The terminally-fluorinated alkylthiols ($HS(CH_2)_{n-1}CF_3$ where n=15, 16) are not currently available for commercial purchase and were synthesized by collaborators in the T. Randall Lee group by their own published methods.[32]

We also discuss, in Chapter 6, molecular beam scattering from hydroxyl (OH-terminated) and amine (NH_2-terminated) SAMs carried out in our lab and reported in the thesis work of Megan Bennett.[35] Those surfaces were constructed from n-hydroxylalkanethiols ($HS(CH_2)_nOH$, where n=11 or 16) (Aldrich) and 11-amino-undecanethiol ($HS(CH_2)_{11}NH_2$) (Dojindo as the stable hydrochloride, $HS(CH_2)_{11}NH_3^+Cl^-$).

The SAM solutions were made by dissolving these alkanethiols in absolute ethanol to an ~1 millimolar concentration. The freshly prepared gold slides are submerged in the SAM solutions for a minimum of 12 hours (overnight) and generally for 24-48 hours before use. Previous work in our lab has shown indistinguishable characteristics when scattering rare gases from SAMs kept in solution for various times (ranging from 1 to 24 hours).[33] The SAMs were removed from solution just before needed, rinsed with copious amounts of absolute ethanol to remove unbound thiols and physisorbed multilayers, dried under a stream of ultra-high purity (UHP) N_2, installed on our sample mount, and immediately introduced into our UHV chamber through a load-lock system (described below). [After drying, the amino-terminated SAMs were additionally rinsed with triethanolamine (TEA) to deprotonate the SAM and remove the chlorine, rinsed again with ethanol, and dried in the stream of UHP N_2. XPS measurements confirmed that the TEA rinse was effective at removing the chlorine from the surface.][35]

2.2.3. Confirming monolayer quality

To confirm our ability to reproducibly make well-ordered surfaces, we regularly characterize our surfaces using 2% Ar/H_2 scattering, reflection absorption infrared spectroscopy (RAIRS), and X-ray photoelectron spectroscopy (XPS). As our chamber has only recently been interfaced to our infrared spectrometer, and currently does not have in situ XPS capabilities, the majority of the RAIR and XPS spectra done for surface characterization have been performed on another UHV chamber in our lab designed by Larry Fiegland.[36] RAIR spectra collected on that instrument were performed with a Bruker IFS 66v spectrometer source and an MCT detector. Recently, we have been able to use the Bruker 80v spec-

trometer for ex situ characterization of samples in the internal sample compartment, or in situ characterization within the UHV chamber (see Fig. 2.4) The general rubric for judging quality of the SAM surfaces is by position and shape of the symmetric and asymmetric CH_2 stretching modes, which occur at or below ∼2853 and ∼2918 cm^{-1}.[1] Broad peakshapes at higher wavenumbers are taken as indicators of poor monolayer crystallinity. The surface-selection rule for RAIRS is such that only vibrational modes that have a transition dipole moment component in the surface-normal direction are detectable. As such, information about the orientation about the alkyl chains can be attained by examination of relative intensities of the methylene units in comparison with functional groups at the ω-terminus of the SAM. For instance, the N_3-SAM shows a very intense asymmetric azide stretch signal at ∼2104 cm^{-1} and weak CH_2 peaks, corresponding to behavior expected for alkyl chains with near surface-normal chain tilt angles. For a methyl SAM, CH_2 modes are much more intense, and comparison of these modes with the symmetric and asymmetric CH_3 stretching modes corresponds to integrated ratios near that expected for a chain-tilt angle of ∼30°. XPS spectra were collected using a Physical Electronics spectrometer using Mg(Kα) radiation (1235.6 eV). XPS provides information on atomic concentrations at the interface, and was used as a way to confirm addition or loss of atomic species from the monolayer (especially for the work presented in Chapter 11).

While RAIRS and XPS measurements were regularly used for confirmation of monolayer quality, for the majority of our studies these spectra had to be obtained outside of our UHV chamber. However, we do have a good in situ way to monitor our ability to reproducibily synthesize quality monolayers. We performed scattering experiments of a standard 2% Ar/H_2 gas mixture routinely from our SAM surfaces as a way to probe their character. Rare-gas scattering is fairly sensitive to surface changes, as has been documented in surface-temperature dependent studies. As such, any change from day-to-day or surface-to-surface in the final time-of-flight distributions was taken as an indication of changes in the SAM structure. Incomplete monolayer formation, poor gold substrates, contamination of the SAM solutions, and degradation due to reaction with ambient species are all reasons that a non-ideal SAM surface would be attained. Scattering the same exact gas mixture, 2% Ar/H_2, from the surfaces confirmed that the SAM structural makeup was equivalent from experiment to experiment. Shown in Figure 2.1 are examples of time-of-flight spectra for 2% Ar/H_2 scattering from SAM surfaces that were recorded weeks or months apart from

one another. Panel (a) shows the high level of reproducibility we can obtain in the scattered Ar signal for the CH_3-SAM surface. The two plotted distributions were recorded 26 *months* apart from each other and show remarkable agreement, which is a testament to the stability of our experimental apparatus and reproducibility of our data. Panel (b) shows three time-of-flight distributions recorded for our standardized Ar beam scattering from a perfluorinated SAM. Good agreement is seen between the red and black circle curves, which were recorded 3 months apart from one another. The blue diamond curve shows poor agreement with the other curves, and was recorded about halfway between the other two curves. The blue curve's distribution is shifted to longer flight times, meaning that a larger fraction of molecules accomodate with the surface. This sort of increased TD behavior can be indicative of a poorly made surface (many defects in the otherwise quite rigid PF-SAM leads to increased TD), or of some problem with the experimental setup (such as poor angular alignment - which would direct the specular IS component away from the detector or a partially clogged nozzle - which would lead to a less energetic incident beam; both situations would subsequently lead to more relative TD signal). In the case presented, this deviation was found to be due to the experimental setup. This example brings up the secondary purpose of using the standardized 2% Ar/H_2 beam: not only is standardized Ar scattering a good technique for characterization of the surfaces, it also facilitates testing the performance of the entire experimental setup. It should be mentioned that our ability to use standard Ar scattering as a characterization tool leverages the extensive body of knowledge gained through Ar scattering studies performed by Scott Day in our group.[33] For the benefit of Morris group members, characteristic time-of-flight spectra scattering from a range of SAM surfaces can be found in Figure 2.2.

2.3. ULTRA-HIGH VACUUM

2.3.1. The requirement of ultra-high vacuum

Once a surface has been synthesized and characterized, it must stay that way throughout the experiment to glean any sort of reliable information. For this purpose, ultrahigh vacuum conditions ($<10^{-8}$ torr) must be achieved in the main scattering chamber.[37] UHV conditions are necessary to ensure that the freshly prepared surface remains clean of ambient gas-phase

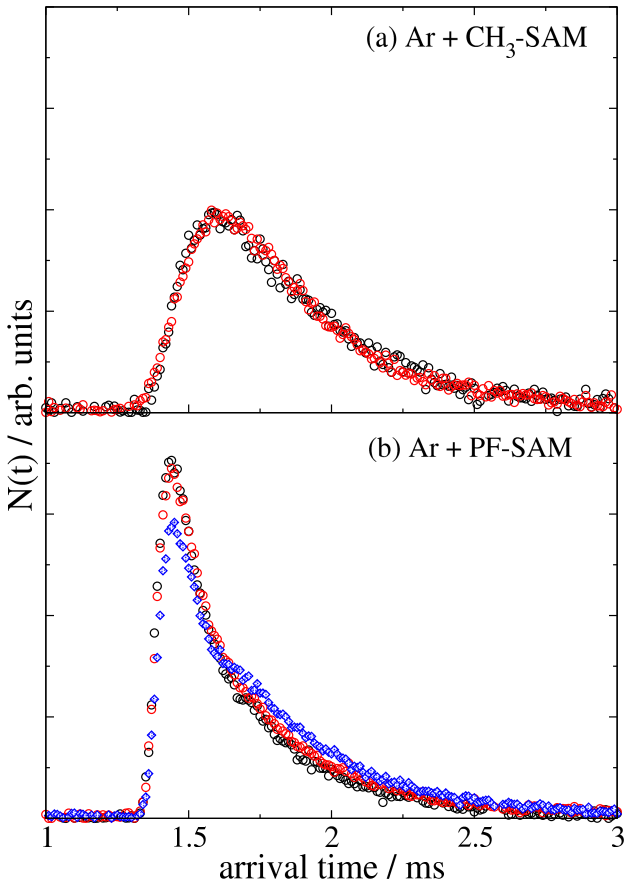

FIG. 2.1: Example TOF distributions displaying the reproducibility of 2% Ar/H_2 scattering from (a) CH_3- and (b) perfluorinated-SAMs. The blue diamonds in panel (b) show deviation from the expected distribution characteristic of what happens when we have a problem with the experimental setup or when scattering from a poor-quality PF-SAM.

contaminants. The reason for this is readily apparent when one considers that at a pressure of 10^{-6} torr — already 9 orders of magnitude less than atmospheric pressure, around 10^{15} ambient molecules strike an exposed surface area of 1 cm^2 every second. Given normal surface atom densities of between 10^{14}-10^{15} molecules·cm^{-2} for a typical surface, in one second each atom on the surface has on average been struck by at least one gas molecule. If a reasonable fraction of those impinging gas-phase species stick to the surface, the entire surface will be contaminated in a matter of a few seconds.[2] If this pressure is reduced to 10^{-10} torr or below, the surface will stay clean for at least 2.5-3 hours, which is enough time to run an experiment.[37]

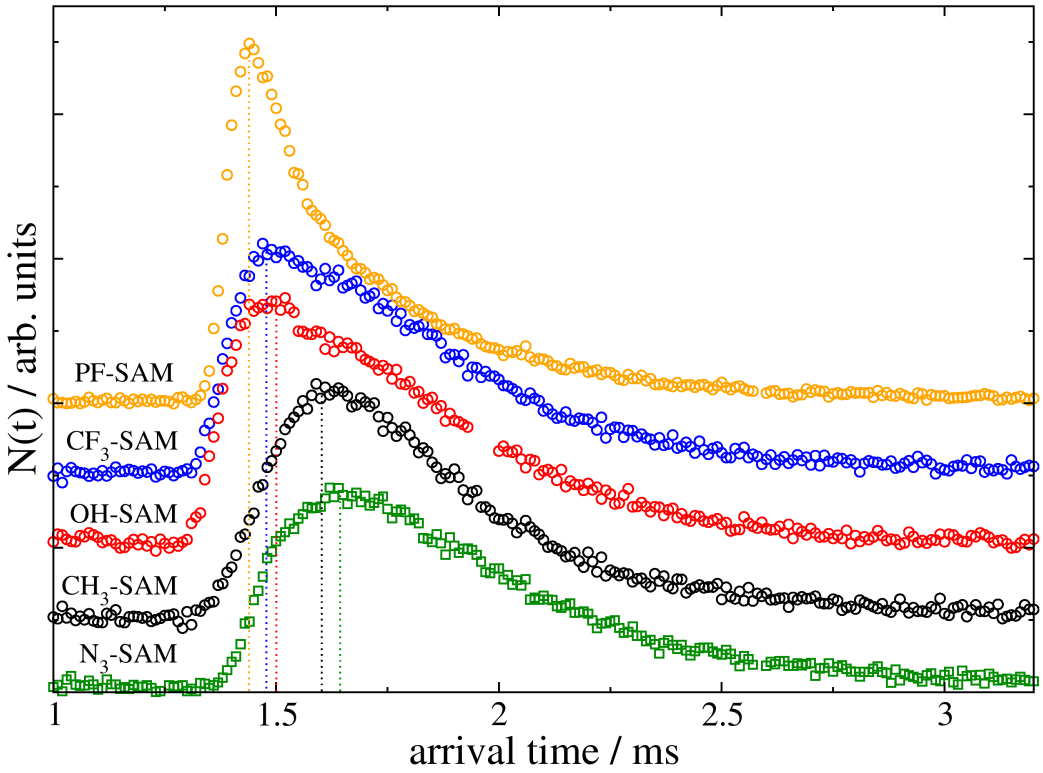

FIG. 2.2: Characteristic time-of-flight distributions for 2% Ar/H_2 scattering from the SAM surfaces indicated in the figure.

Additionally, under UHV conditions, collisions with molecules in the atomic and molecular beam with ambient background gases in the chamber are virtually non-existent. In the absense of interaction with background gases, any change in the characteristics of the initial molecular beam distribution seen in the final translational-energy distribution can be inferred to have manifested solely as a result of collision with the SAM surface.

2.3.2. UHV chamber setup

To write "ultra-high vacuum is a requirement for our studies" is simple enough, but in practice, achieving and maintaining an UHV environment is anything but trivial. Specially designed UHV chambers and pumping systems are needed. We briefly describe in this section the experimental apparatus used for our scattering studies. A schematic of the "Beam Machine" is shown in Figure 2.3 and will be referenced throughout this discussion. The main UHV chamber is maintained at or below 5×10^{-10} torr by simultaneous pumping by a turbomolecular pump (Pfieffer, 1500 $L\cdot s^{-1}$) and a cryogenic pump (Austin Scientific,

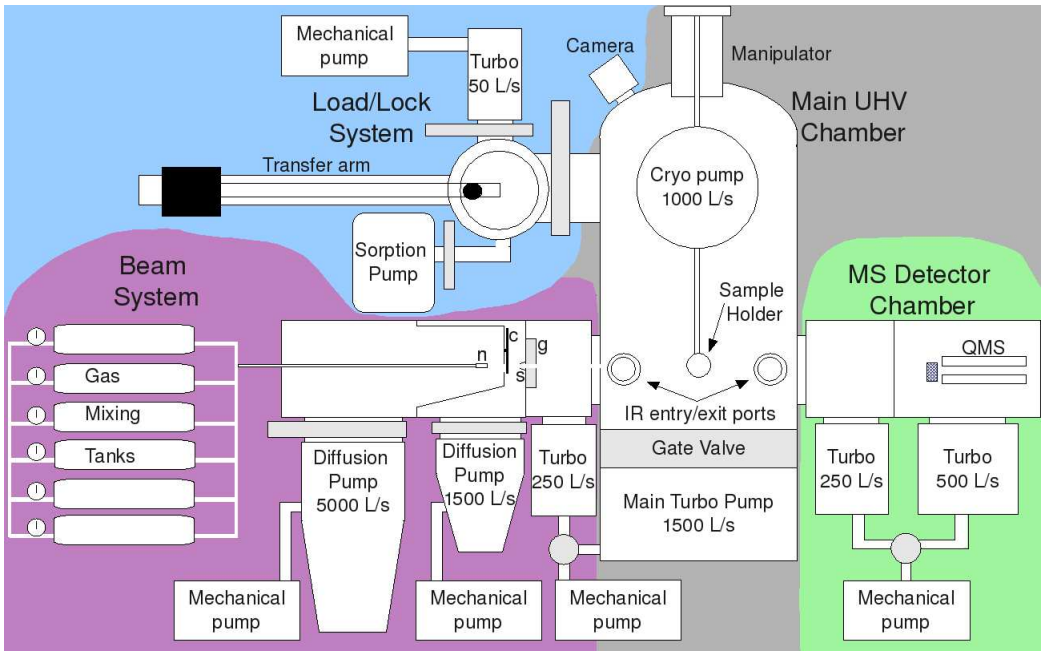

FIG. 2.3: Schematic of the experimental beam scattering chamber.

1000 L·s^{-1}). The chamber operates with a dual tier design in which the top section is used for rapid sample transfer through our load/lock system. The bottom half of the chamber is setup for the scattering experiment. The sample is translated between these two tiers using a mainpulator system (McCallister MA2012), which allows for sample motion in five degrees-of-freedom (x, y, z, rotation, and tilt) for sample alignment. The pressure in the main chamber is monitored with a cold-cathode pressure gauge, and is interfaced through a desktop computer running a LabVIEW program. In case of an unexpected rise in pressure, the LabVIEW-controlled interlock box shuts the gate valves (gray in the figure) to the pumps to protect from backstreaming of pump oil, and the chamber is backfilled with UHP N_2.

Installation of new samples is achieved through the load/lock chamber (MDC Vacuum). The small chamber is separated from the main chamber by a large manual gate valve that allows one to vent the load/lock, install a new sample, and pump back down without compromising the pressure in the main. With the gate valves to the main, load/lock turbo, and sorption pump closed, the load/lock chamber is vented by backfilling with UHP N_2 and a freshly prepared SAM surface is installed on the transfer arm. The load/lock chamber is roughed out to $\sim 10^{-4}$ torr by the sorption pump, which we generally allow about 20 min. Then the valve is closed to the sorption and opened to the turbo pump (Pfeiffer, 50 L·s^{-1}) to

allow the chamber to fully pump down to $\sim 10^{-7}$ torr, for which we generally allow another 20 min. Upon achieving pressures of $\sim 10^{-7}$ torr, the gate valve to the main chamber is opened and the sample installed on the manipulator via use of the transfer arm. While this whole process can be done in a shorter time span (by introduction of the sample into the main chamber when the load/lock displays pressures around 10^{-6} torr), if the load/lock is allowed to pump down to the low 10^{-7} torr, the base pressure in the main chamber is regained immediately once the transfer has been completed and the gate valve to the load/lock is closed. A video camera is mounted on a windowed flange on top of the chamber and the image displayed on monitors to aid our ability to transfer the sample from the transfer arm onto the manipulator.

After the sample is installed, it is lowered into the lower tier of the chamber via the manipulator. Currently, there are five flange ports used at this scattering level. Two ports are used for entry and exit of the laser beam for reflection absorption infrared spectroscopy; two ports are used for mass spectrometry — one for characterization of the incident beam and one for characterization of the scattered beam; and one port for interfacing our atomic/molecular beam source.

2.4. ATOMIC AND MOLECULAR BEAMS

It is experimentally difficult to observe the interaction of a gaseous species with an organic surface at the position and time of impact directly. Our experimental approach is to infer the dynamics of a gas/surface collision by observing properties of the gaseous species before and after collision. Molecular beams used in an ultrahigh vacuum environment are well suited for this purpose. Molecular beams consist of collimated beams of molecules with well-characterized average velocities. There exist two regimes for these types of beams. Effusive beams are formed when a rather low pressure of gaseous molecules pass through orifices whose diameter is smaller than the mean free path of the molecule. As such, the properties of these beams are described by the kinetic theory of gases. The directional character of effusive beams manifests from the fact that only molecules with the proper component of their velocity vector directed through the aperture will compose the beam. These beams have a thermal distribution of velocities, which corresponds to the impinging molecules having incident collision energies that follow a Maxwell-Boltzmann distribution.

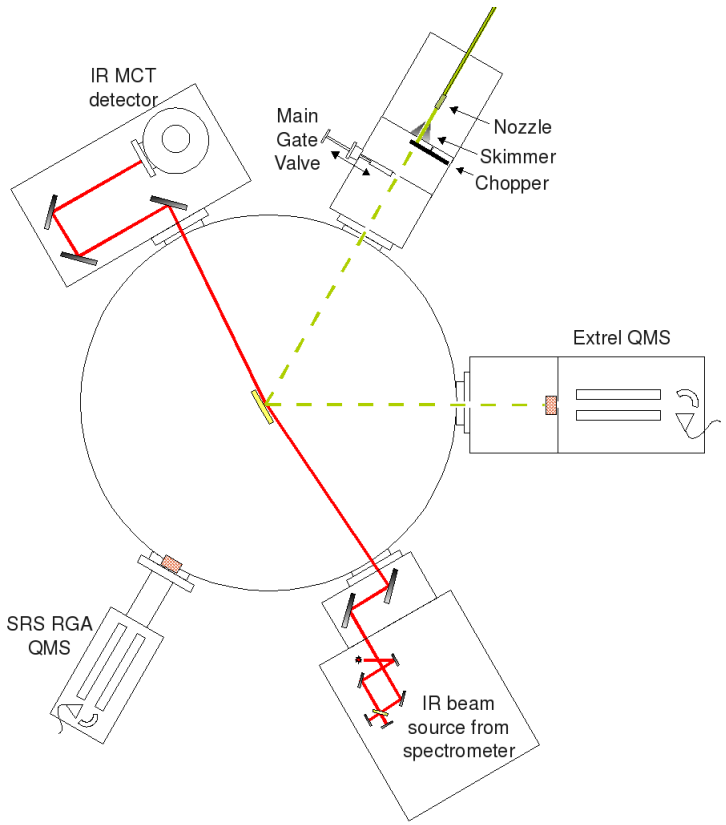

FIG. 2.4: Experimental scattering arrangement.

The theoretical Maxwell-Boltzmann distribution of arrival times that would be achieved in our experimental geometry is plotted as a dashed line in Figure 2.5 for acetylene.

For the experiments in this study, we have used exclusively nozzle-source, also called supersonic, atomic/molecular beams. In nozzle source beams, the backing pressure on the non-vacuum side of the aperture is increased such that the mean free path of the molecules is smaller than the size of the aperature. Under these higher pressure conditions, the gas is forced through the aperture in a hydrodynamic flow. As the gas expands into the vacuum chamber, the molecules accelerate due to the local pressure differential. When the pressures on either side of the hole differ by a large ratio (around 2 for all gases),[38] the expanded gases can reach the local speed of sound at the exit of the nozzle. After exiting the nozzle, the gas is still underexpanded in relation to the overall vacuum chamber and a further, supersonic expansion occurs.[38] At a sufficient distance from the nozzle, since they have spread far apart, the gases reach a nearly constant velocity and intermolecular collisions are very few. At this point in the expansion, another aperture can be placed at the centerline of the beam to

extract a nearly monoenergetic, collimated beam of molecules.

In our experimental setup, we achieve supersonically expanded beams via use of a triply-differentially pumped beam source (see Figure 2.4). We make supersonic atomic/molecular beams by expanding gases at 700 torr through a 0.05 mm diameter nozzle (General Valve) into the first differential chamber, which is pumped by a 5000 $L{\cdot}s^{-1}$ diffusion pump (Varian VHS10). The beam is separated into $\sim$50 μs pulses by use of a slotted chopper wheel located directly after the nozzle. A 0.40 mm diameter conical skimmer 6 mm from the nozzle allows only the central region of the supersonic expansion to enter the second differential chamber (pumped by a 1500 $L{\cdot}s^{-1}$ diffusion pump (BOC Edwards Diffstak MK2)). The beam traverses the second differential chamber and passes through a 1.5 mm collimating aperature into the third differential stage (pumped by a 250 $L{\cdot}s^{-1}$ turbomolecular pump (Pfeiffer)), where it passes through a second 2.2 mm collimating aperature before entering the main chamber. The pressures of the first, second, and third differential stages are $\sim 10^{-4}$, 10^{-6}, and 10^{-8} torr when the beam is running. After entering the main chamber, the beam produces an $\sim$1 cm^2 spot on the sample. The main chamber pressure rises to $\sim 1 \times 10^{-9}$ torr during a typical scattering experiment.

The incident beam profile is characterized by an in-line mass spectrometer (SRS RGA) located directly across the chamber from the source. The sample is raised out of the beam path, and the time-of-flight profiles are recorded. Supersonic beams achieve higher average collision energies than effusive beams. By way of example, we plot in Figure 2.5 the theoretical time-of-flight distribution for an effusive beam (black dashed curve) with our experimental geometry, compared to the incident TOF profile we measured for a pure, supersonic acetylene beam (blue curve). The Maxwell-Boltzmann distribution peaks at 2.5 $kJ{\cdot}mol^{-1}$, while the pure nozzle-source beam's incident distribution is peaked at 9.3 $kJ{\cdot}mol^{-1}$ As is evidenced from the figure, supersonic beams also yield much narrower distributions of incident collsion energies than in effusive beams. These narrow distributions allow us to ascribe any dynamical effects to a specific range of collisional energies, while the broad distribution seen in effusive beams makes assignment of behavior to certain energy regimes difficult.

The peak energy of the molecular beams can be tuned by mixing the probe gas in another, inert carrier gas of a different mass. In general, for atomic probe gases, the velocity of the

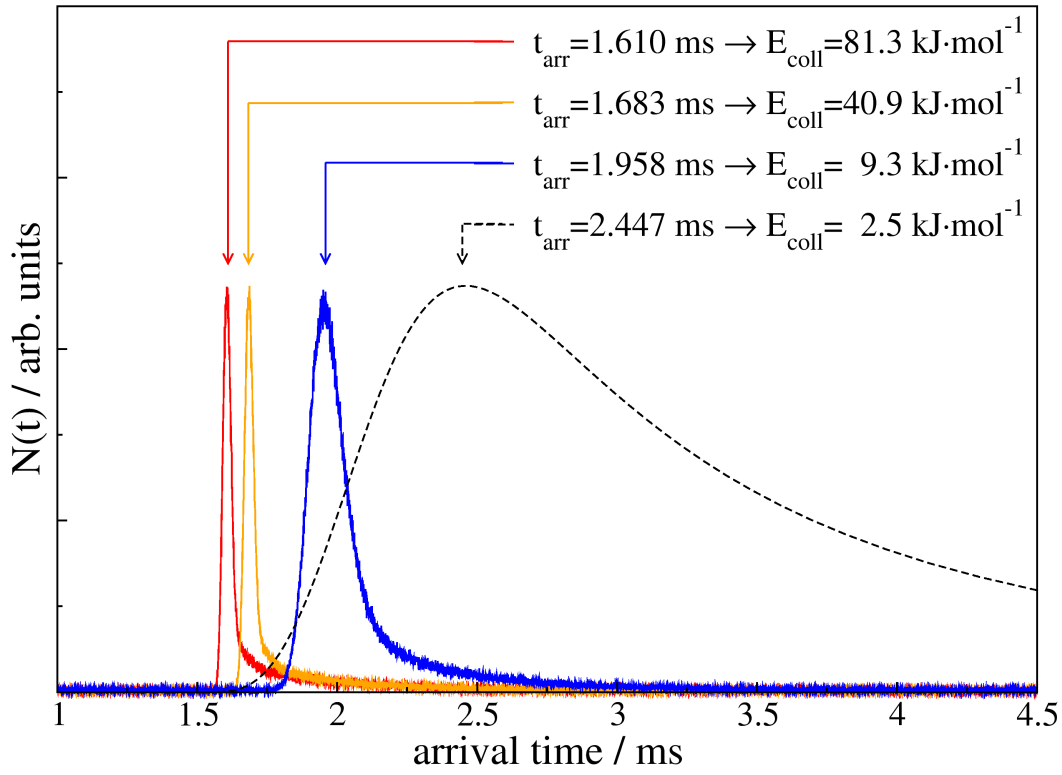

FIG. 2.5: Acetylene incident molecular beam profiles (solid lines) compared to a Maxwell-Boltzmann distribution (dashed line) at 300 K. The incident profiles are scaled to equal peak heights.

mixed gas expansion is related inversely to the average mass of the mixture:

$$\mathbf{v} = \sqrt{\frac{5RT}{\mathbf{M}}} \tag{2.1}$$

where $\mathbf{v}$ is the probe gas' velocity after expansion, $\mathbf{M}$ is the average mass of the gas mixture, R is the gas constant, and T is the temperature of the nozzle. By varying the mixing ratio of a heavier or lighter gas with the probe gas, a wide range of collision energies can be obtained. During the expansion process hundreds of binary collisions are experienced by each molecule.[38] If a heavy probe gas is seeded in a lighter carrier, the heavier gas will be accelerated to the velocity of the lighter gas as the molecules are kicked and dragged. The orange curve in Figure 2.5 corresponds to ~5% C_2H_2 diluted in ultrahigh purity H_2, yielding a beam peaked at 40.9 kJ·mol^{-1} with full width at half maximum of ~12 kJ~mol^{-1}. By carefully controlling the mixing ratio we are able to tune the peak energy to within about 1 kJ·mol^{-1}. Slower beams may also be made by mixing the probe gas in a heavier gas, such as argon. Figure 2.6 displays a series of incident $^{15}N_2$ beams that we recorded during dilution of

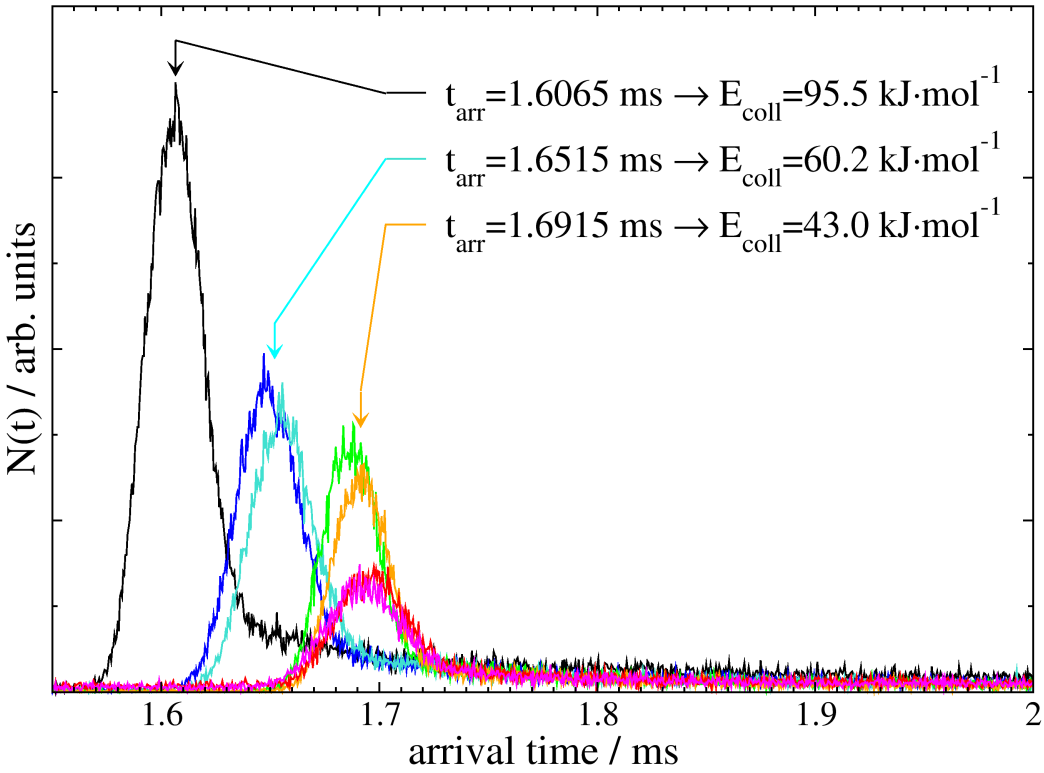

FIG. 2.6: Various incident $^{15}N_2$ molecular beam profiles displaying the effect of dilution with 5% Ar/H_2. Characteristic peak arrival times are labelled with the corresponding peak translational energy.

an initially ∼2% N_2/H_2 beam mixture by addition of a 5% Ar/H_2 mixture. As the beam is diluted, the intensity must obviously decrease. This puts a practical limitation on the range of values that can be obtained with seeding techniques. In Figure 2.7 we display a series of ^{13}CO incident beams as a function of subsequent dilutions in H_2 to give a sense of the control we can exert over the translational energy. Molecular beam seeding techniques allow us to dial in a specific translational energy with relatively narrow distributions of collisional energy, thereby giving us a method to study energy transfer dynamics as a function of translational energy.

2.5. SCATTERING

Once we have a well characterized SAM surface and a well defined molecular beam, we can perform scattering experiments. The SAM surfaces are laser-aligned such that a HeNe laser directed through the center of a small window at the back of the mass spec detector

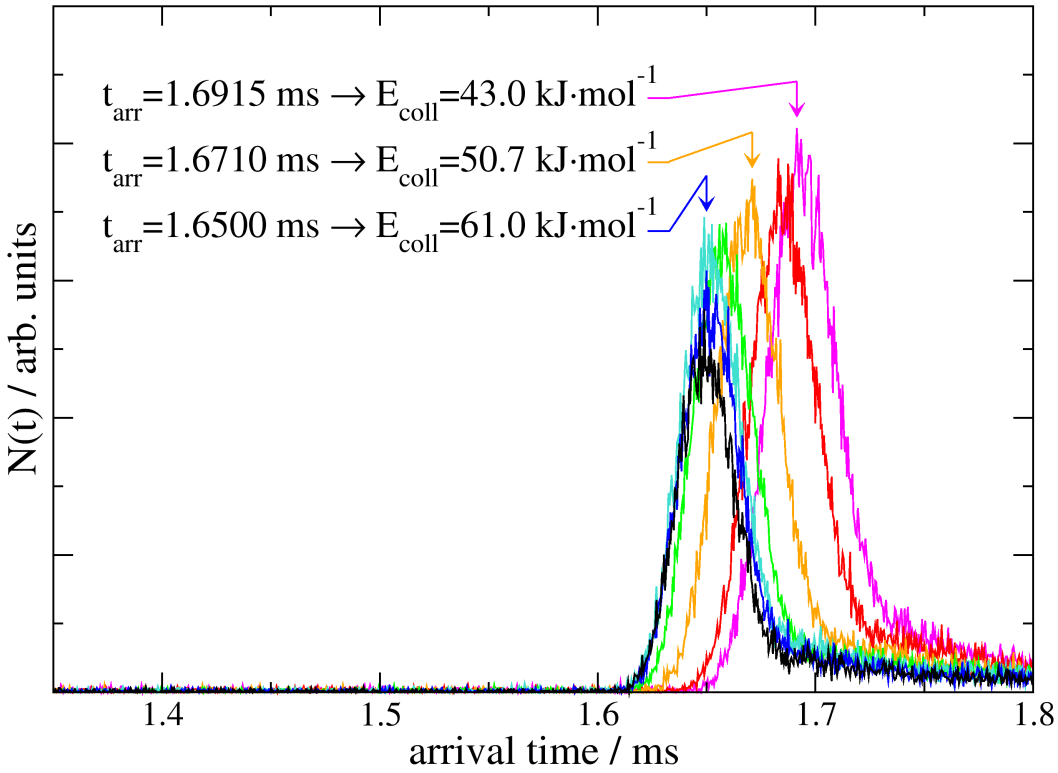

FIG. 2.7: Various incident ^{13}CO molecular beam profiles displaying the effect of dilution with H_2. Characteristic peak arrival times are labelled with the corresponding peak translational energy.

chamber hits the center of the sample surface and is reflected to be colinear with the path of the molecular beam (by adjusting the manipulator to direct the reflected HeNe into the final source collimating aperture). Once the sample has been aligned in this scattering position, the atomic or molecular beam is introduced into the chamber by opening the main gate valve separating the second and third differential chambers. A fraction of the gas-phase species that scatter from the surface are intercepted by a doubly differentially pumped Extrel mass spectrometer located 60° from the incident beam such that θ_i=θ_f=30°. The detector chamber containing an ABB Extrel quadrupole mass spectrometer is separated from the main chamber by a 4.3 mm aperture, and the first and second differential stages are separated by a 4.7 mm aperture. The first and second differential stages are pumped by 250 and 500 L·s^{-1} turbomolecular pumps, respectively, with the quadrupole mass spectrometer (QMS) being housed completely within the second differential stage.

The TOF distributions of the scattered species are recorded by monitoring the mass spectrometer signal as a function of time. Each TOF scan is started when the chopper wheel

slit passes through an LED photogate arrangement which sends a 5V pulse to trigger a multi-channel scalar (Ortec). The multi-channel scalar allows us to integrate the spectrometer signal in 10 μs intervals.

Because we know the distances that the atoms/molecules must traverse to arrive and be counted in the mass spectrometer, TOF distributions give us a direct way to probe the post-collision velocity (and subsquently kinetic energy) distributions of the gas-phase species. Analysis of these TOF data is described below. Additionally, we have recently interfaced our chamber with a Bruker 80v infrared spectrometer. When the sample is well aligned in the scattering position, the spectrometer laser impinges on the surface at about 84°, reflects forward at the specular angle through a windowed flange across the chamber and is focused onto a MCT IR detector. This allows us to interrogate the *surface* in real time while scattering and collecting information on the gas-phase products with our mass spectrometer. We can also use the IR spectra to characterize the SAM surface in situ before and after an experiment, or from day-to-day to monitor monolayer quality.

2.6. DATA ANALYSIS

The shape of the raw time-of-flight data obtained from our mass spectrometer is dependent on our specific experimental geometry. As such, it is common practice to transform our raw spectra into the energy domain to allow comparison across instruments. We can calculate the final energy probability distribution if we know the final velocity. The raw TOF data must first be corrected for certain experimental timing offsets, which include the electronic lag in the photodiode assembly, a lag time associated with the difference in the rotational arrangement of the diode and the source aperture (time it takes for the chopper slit to move from the LED trigger to the source aperture), the flight time of the gas from the chopper to the SAM surface, and the ion flight time in the spectrometer:

$$t_{surf-ion} = t_{arrival} - (t_{elec} + t_{LED-ap} + t_{chop-surf} + t_{ms}) \tag{2.2}$$

where $t_{arrival}$ is the raw arrival time recorded by the spectrometer, t_{elec} is the electronic offset, t_{LED-ap} is the lag time associated with the chopper moving from the LED trigger to the source aperture, $t_{chop-surf}$ is the gas flight time from the chopper to the surface, and t_{ms} is the time spent in the mas spectrometer. For our experiments, t_{elec} is 8 μs. $t_{chop-surf}$ is

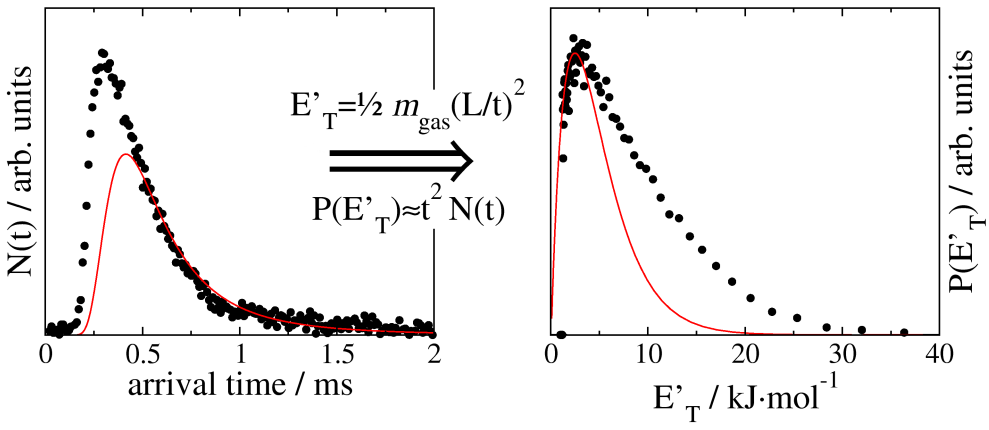

FIG. 2.8: Experimental TOF distribution corrected for timing offsets (left panel) and the transformed final translational-energy distribution (right panel) for 60 kJ·mol^{-1} Ne scattering from a CH_3-SAM surface. The red traces are a 300K Maxwell-Boltzmann fit to the low-energy portion of the data.

determined by calculating the time it takes for the gas species to travel from the chopper to the surface (L=31 cm) if the gas had a translational energy corresponding to the peak of the incident energy profile; for a 60 kJ·mol^{-1} Ne beam, this takes 126 μs. t_{LED-ap} varies depending on the chopper wheel speed; with the chopper spinning counter-clockwise (CCW) at 250 Hz, the timing offset is 933 μs. t_{ms} is dependent on the mass of the gas and the specifics of the mass spectrometer:

$$t_{ms} = \alpha\sqrt{m/z} \tag{2.3}$$

where m/z is the mass-to-charge ratio and α we will refer to as the mass spec parameter. The mass spec parameter can be determined by recording the TOF distributions for a projectile that fragments into multiple ionic species, or a series of multiply ionized atoms. The peak arrival times of these distributions are plotted as a function of $\sqrt{m/z}$, and the mass spec parameter, α, is the slope of the best linear fit to the data. α has most recently been determined to have a value for our mass spectrometer of 6.5.[33,35] This leaves $t_{surf-ion}$, which is the time for the gas to travel from the surface to the ionizer. From $t_{surf-ion}$, and with the knowledge of the surface to ionizer distance, we can obtain the scattered gas' final velocity distribution or final energy distribution P(E'$_T$). We exclusively transform our TOF data to energy distributions.

The raw signal from the spectrometer is porportional to the number density, N(t), and is

used to determine the probability, P(E'$_T$), of a gas leaving the surface with a particular final translational energy. Translational-energy distributions are calculated using the relations

$$E'_T = \frac{1}{2} m_{gas} (\frac{L}{t})^2 \tag{2.4}$$

and

$$P(E'_T) \approx t^2 N(t) \tag{2.5}$$

where m_{gas} is the mass of the impinging gas species, t is the time for the gas to travel from the surface to the ionizer ($t_{surf-ion}$), and L is the distance from the surface to the ionizer (31 cm). The faster-moving species (early arrival times, higher final energies) correspond to those atoms/molecules which undergo little energy transfer during their interaction with the surface and make up the impulsive scattering component of the distribution. The slow-moving portion of the distribution (longer arrival times, thermal final energies) is attributable to atoms/molecules whose interaction with the surface has allowed thermalization of its translational energy. We deconvolute these two limiting channels using the energy distributions. The TD component is assigned by fitting the low-energy part of the P(E'$_T$) distribution to a Maxwell-Boltzmann distribution:

$$P_{TD}(E'_T) = E'_T (RT_{surf})^{-2} e^{\frac{-E'_T}{RT_{surf}}} \tag{2.6}$$

where R is the gas constant and T_{surf} is the surface temperature (set at 300 K for all data herein). The IS component is assigned to the difference between P(E'$_T$) and P$_{TD}$(E'$_T$), with the constraint such that P$_{IS}$(E'$_T$)=0 for E'$_T \leq RT_{surf}$. Shown in Figure 2.8 are TOF and P(E'$_T$) distributions for 60 kJ·mol^{-1} Ne scattering from a CH_3-SAM. The red curves in Figure 2.8 are the Boltzmann component fit to the low energy region of the P(E'$_T$) distribution.

To unravel the influence of varying gas and surface properties on the collision dynamics, throughout the subsequent chapters, we can analyze the total average final translational energy, <E'$_T$>, the fractional energy transfer, $\frac{E_{coll} - \langle E'_T \rangle}{E_{coll}}$, and the fraction of atoms/molecules that scatter with a Boltzmann distribution of velocities (TD fraction). Comparison of these quantities across gases and surfaces can give us insight into the surface rigidity, gas-surface

interactions, and surface accomodation, among others.

REFERENCES

[1] L. H. Dubois and R. G. Nuzzo, Annu. Rev. Phys. Chem. **43**, 437 (1992).

[2] S. R. Holmes-Farley, R. H. Reamey, R. G. Nuzzo, T. J. McCarthy, and G. M. Whitesides, Langmuir **3**, 799 (1987).

[3] S. L. Bernasek, *Heterogeneous Reaction Dynamics* (VCH Publishers, Inc., 1995).

[4] G. A. Somorjai, *Principles of Surface Chemistry* (Prentice Hall, Inc., 1972).

[5] L. L. Kesmodel, L. H. Dubois, and G. A. Somorjai, Chem. Phys. Lett. **56**, 267 (1978).

[6] L. L. Kesmodel, L. H. Dubois, and G. A. Somorjai, J. Chem. Phys. **70**, 2180 (1979).

[7] A. Ulman, *An introduction to ultrathin films: from Langmuir-Blodgett to self-assembly* (Academic Press, 1991).

[8] M. I. Bethencourt, L. O. Srisombat, P. Chinwangso, and T. R. Lee, Langmuir **25**, 1265 (2009).

[9] A. Ulman, Chem. Rev. **96**, 1533 (1996).

[10] C. Vericat, M. E. Vela, and R. C. Salarezza, Phys. Chem. Chem. Phys. **7**, 3258 (2005).

[11] C. D. Bain, E. B. Troughton, Y. T. Tao, J. Evall, G. M. Whitesides, and R. G. Nuzzo, J. Am. Chem. Soc. **111**, 321 (1989).

[12] G. M. Whitesides and P. E. Laibinis, Langmuir **6**, 87 (1990).

[13] G. M. Whitesides and G. S. Ferguson, Chemtracts: Organic Chemistry **1**, 171 (1988).

[14] C. D. Bain, H. A. Biebuyck, and G. M. Whitesides, Langmuir **5**, 723 (1989).

[15] C. D. Bain, J. Evall, and G. M. Whitesides, J. Am. Chem. Soc. **111**, 7155 (1989).

[16] C. D. Bain and G. M. Whitesides, Science **240**, 62 (1988).

[17] C. D. Bain and G. M. Whitesides, Angewandte Chemie **101**, 522 (1989).

[18] P. E. Laibinis, C. D. Bain, and R. G. Nuzzo, J. Phys. Chem **99**, 7663 (1995).

[19] E. B. Troughton, C. D. Bain, G. M. Whitesides, R. G. Nuzzo, D. L. Allara, and M. D. Porter, Langmuir **4**, 365 (1988).

[20] P. E. Laibinis, G. M. Whitesides, D. L. Allara, Y. T. Yao, A. N. Parikh, and R. G. Nuzzo, J. Am. Chem. Soc. **113**, 7152 (1991).

[21] A. R. Bishop and R. G. Nuzzo, Current Opinion in Colloid & Interface Science **1**, 127 (1996).

[22] R. G. Nuzzo and D. L. Allara, J. Am. Chem. Soc. **105**, 4481 (1983).

[23] L. H. Dubois, B. R. Zegarski, and R. G. Nuzzo, J. Chem. Phys. **98**, 678 (1993).

[24] R. G. Nuzzo, B. R. Zegarski, K. M. Korenic, and L. H. Dubois, J. Chem. Phys. **96**, 1355 (1990).

[25] R. G. Nuzzo, L. H. Dubois, and D. L. Allara, J. Am. Chem. Soc. **112**, 558 (1990).

[26] P. Maksymovych, D. C. Sorescu, and J. T. Yates, Jr., J. Phys. Chem. B **110**, 21161 (2006).

[27] M. C. Vargas, P. Giannozzi, A. Selloni, and G. Scoles, J. Phys. Chem. B **105**, 9509 (2001).

[28] Y. Yourdshahyan and A. M. Rappe, J. Chem. Phys. **117**, 825 (2002).

[29] J.-G. Zhou and F. Hagelberg, Phys. Rev. Lett. **97**, 045505 (2006).

[30] B. S. Day and J. R. Morris, J. Chem. Phys. **122**, 234714 (2005).

[31] C. W. Sheen, J.-X. Shi, J. Martensson, A. N. Parikh, and D. L. Allara, J. Am. Chem. Soc. **114**, 1514 (1992).

[32] M. Graupe, T. Koini, V. Y. Wang, G. M. Nassif, R. Colorado, R. J. Villazana, H. Dong, Y. F. Miura, O. E. Shmakova, and T. R. Lee, J. Flourine Chem. **93**, 107 (1999).

[33] B. S. Day, Ph.D. thesis, Virginia Polytechnic Institute and State University (2005).

[34] B. S. Day and J. R. Morris, J. Phys. Chem. B **107**, 7120 (2003).

[35] M. E. Bennett, Master's thesis, Virginia Polytechnic Institute and State University (2007).

[36] L. R. Fiegland, Ph.D. thesis, Virginia Polytechnic Institute and State University (2008).

[37] C. T. Ceyer, D. J. Gladstone, M. McGonigal, and M. T. Schulberg, *Molecular Beams: Probes of the Dynamics of Reactions on Surfaces*, Physical Methods of Chemistry (Wiley, New York, 1988), 2nd ed.

[38] D. J. Auerbach, G. Comsa, B. Poelsema, M. Asscher, and G. Somorjai, *Atomic and molecular beam methods* (Oxford University Press, New York, 1992).

Chapter 3

Classical trajectory method

3.1. INTRODUCTION

In its broadest definition, the field of molecular dynamics is concerned with understanding the motion and interactions of atomic and molecular species at an atomistic level of detail. Within this chapter, we describe our application of the classical trajectory approach for simulation of the dynamics of gas/organic-surface scattering. While all systems are ultimately governed under the rules of quantum mechanics, a classical treatment of nuclear motion is adequate for a qualitative, and sometimes quantitative, description of the relevant properties for many systems.

A classical description of our gas/surface system is contingent upon the Born-Oppenheimer approximation,[1] which depends on the differences in timescales between nuclear and electronic motions. Due to their relatively small mass, electrons move at speeds many orders of magnitude greater than their associated nuclei. Nuclear motion can therefore be described by the assumption that nuclei move within the force field generated by the electrons. The dynamics of the system then are governed by the forces acting on the nuclei during the gas/surface collision. Under the Newtonian description of mechanics, this concept is given in Newton's Second Law of Motion, $F = ma$, or:

$$F_i = m_i \frac{d^2 q_i}{dt^2} \tag{3.1}$$

where F_i is the force acting on each nuclei, m_i and q_i are the mass and coordinates of the nuclei, respectively, and t is time. This relation implies that if the position and forces acting on the system are known at some initial time, the position, $q_0 + \Delta q$, can be determined for some time, $t_0 + \Delta t$. In a macroscopic classical case, such as a ball firing from a cannon, the major force acting on the ball, gravity, is constant and known at all times, leaving the problem of solving for projectile motion a trivial one. However, in the atomic realm, the forces vary as a function of atomic position. Intramolecular stretches, bends, and torsions, in addition to non-bonded coulombic, dipolar, and dispersion forces may all contribute to the time-dependent potential energy. This potential energy subsequently changes the forces

acting on the system due to:

$$F_i = -\frac{dU(\boldsymbol{q})}{dq_i} \tag{3.2}$$

where $U(\boldsymbol{q})$ is the potential energy as a function of all atomic coordinates of the system. Combining equations 3.1 and 3.2 reveals that if one is able to obtain the potential energy of the system as a function of the molecular position, time-dependent nuclear dynamical behavior can be predicted:

$$-\frac{dU(\boldsymbol{q})}{dq_i} = \frac{d^2q_i}{dt^2} \tag{3.3}$$

The potential-energy surface (PES) is a conceptual motif that describes the potential energy of a system as a function of the atomic positions. Commonly, the PES is formed as a combination of the individual interactions within the system. For our gas/organic-surface systems, the PES is formed as a sum of stretches, bends, and torsions within the organic surface as well as non-bonded interactions between surface species and between the gas-phase projectile and the surface. We describe in detail these interactions below. Since the information included within the PES directly influences the equations of motion, the outcome of a classical molecular dynamics trajectory is highly dependent on the accuracy of the PES.[1] A common way to obtain high-accuracy PESs is through fitting quality ab initio data to multiparametric analytical potential-energy functions.[2] Using ab initio calculations to derive analytical PESs has the advantage that the quality of the PES is reflective of the quality of the electronic structure calculations. In fact, if the fitting errors are negligible, and high-quality ab initio calculations are affordable for the system of interest, predictive PESs can be derived. A paradigmatic example of the improvement in the predictive character of analytic PESs with an improvement in the ab initio data included in the PES fit can be seen in the work of Mielke and co-workers on the H + H_2 reaction.[3] In their study, PESs were built using different levels of electronic structure theory, with the most accurate PES providing quantitative agreement with experiment.

Once a potential-energy surface has been derived for the system, and initial conditions are generated, molecular dynamics simulations can be performed by integration of the equations of motion. As Equation 3.3 is a single differential in position on the left hand side and a double differential in time on the right hand side, an analytical solution does not exist, forcing the use of numerical solution techniques, which we will describe in more detail below.

During the trajectory, data are collected about the instantaneous atomic positions and

momenta. Initial and final properties of interest are also recorded. We use these data to obtain observables such as final translational-energy distributions, angular distributions, and accomodation fractions of the scattered species. Comparison of these observables to experiment confirms legitimacy of our model and allows us confidence to examine properties of the system not currently attainable in our experiment. This information includes microscopic mechanistic details of the gas/surface collisions, rovibrational distributions, and stereodynamic characteristics of the scattered gas species.

Within this chapter, we detail the aspects of our computational approach. We first introduce the PES used for our SAM model. We then we discuss derivation of our gas/SAM intermolecular potential including methods employed to obtain high-quality ab initio data and analytical potential fitting procedures. Generation of initial conditions, propagation of the equations of motion, and data analysis conclude the chapter.

3.2. POTENTIAL ENERGY SURFACES

3.2.1. The SAM model

Simulation of gas/SAM collisions first requires a model that accurately represents the true behavior of the organic surface. The first model of SAM surfaces is the Hautmann-Klein united-atom (HKUA) model.[4] Within this model, the alkanethiol chains are treated with a united atom approach; each methyl and methylene unit is treated as a single pseudoatom where the individual influence of the carbon and hydrogen atoms are averaged into the overall potential. Intramolecular potentials were taken from the united atom version of the optimized potentials for liquid simulations (OPLSUA) force field developed by the Jorgensen group.[5,6] Use of the united-atom approach greatly decreases the number of potential terms that need to be computed at each timestep, which decreases the computational expenditure. The HKUA model gave an average tilt angle of 28.0° for the hexadecanethiol chains, and a film thickness of 20.1 Å, which can be compared to values of ∼30° and 20±2 Å as reported in the literature.[7,8]

Bosio and Hase published the first attempts at modeling collisions of gas-phase species with SAMs.[9] They studied energy transfer in Ne collisions with an united-atom *n*-hexylthiolate SAM model which incorporated SAM potential parameters from the Universal

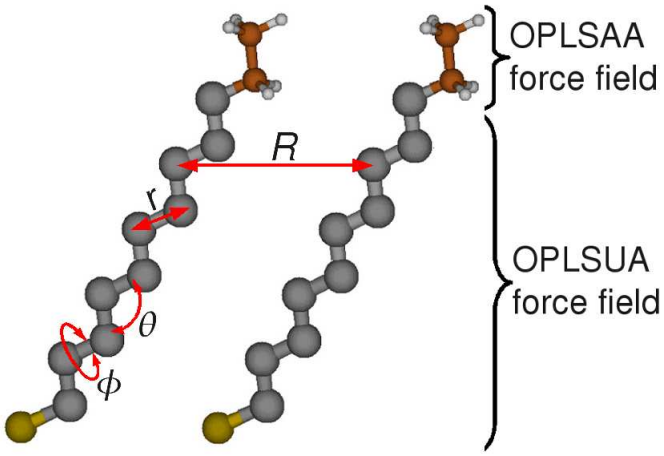

FIG. 3.1: Schematic of the SAM intramolecular potential terms.

Force Field (UFF),[10] and the HKUA model.[4] Their treatment of the intermolecular potential resulted in an average chain tilt angle of ∼28°, which was found to be in good agreement in comparison to experimental values for the tilt of near 30°.[9]

Mar and Klein's all-atom (MKAA) model improved upon the HKUA model by including an explicit description of hydrogens and a more accurate description of the sulfur-gold interaction.[11] The all-atom OPLS force field (OPLSAA) is used for the intramolecular potentials.[12] While HKUA gave alkyl chains tilted toward the nearest neighbor direction, MKAA showed the chains tilting the in next-nearest neighbor direction, which was found to be more consistent with experimental data, especially that of He diffraction and synchrotron X-ray scattering studies.[13–15] An alkyl chain tilt angle of ∼30° was observed, also in good agreement with experiment. Subsequent comparative studies in the Hase group of gas/SAM scattering from united- and all-atom descriptions of the SAM surface showed that better agreement with experiment was achieved when the hydrogen atoms were explicitly considered.[16]

We have taken a hybrid approach that aims to incorporate the accuracy of an all-atom description of the gas/SAM intermolecular interactions, while retaining much of the computational efficiency of united-atom models. As such, we split the SAM surface into two regions, the outer-most ethyl termini of the SAM chains, and the remaining, interior region. The interior region is given a united-atom treatment where each methylene moeity is treated as a single pseudoatom. Additionally, the interior region of the SAM includes the sulfur head groups. The intramolecular potential for this interior region is described by the OPLSUA

force field. All atoms in the ethyl termini are treated explicitly and their intramolecular potentials are described by OPLSAA. This hybrid OPLSUA/OPLSAA approach is shown schematically in Figure 3.1. Within OPLS, two-atom bond stretching and three-atom angle bending are treated as harmonic potentials, four-atom dihedral torsions are treated as a summation of a series of cosine terms, and non-bonded interactions are described by a traditional 6-12 Lennard Jones potential. In such formulation, the total intramolecular SAM potential takes the form:

$$\begin{aligned} U(r,\theta,\phi,R) \;=\; & \sum_{stretches} \frac{1}{2}k_r(r-r_0)^2 + \sum_{bends} \frac{1}{2}k_\theta(\theta-\theta_0)^2 + \sum_{dihedrals} \sum_{n=1}^{3} \frac{1}{2}k_n[1+cos(n\phi-\phi_n)] \\ & + \sum_{Coulombic} \frac{q_i q_j}{4\pi\epsilon_0 R} + \sum_{Lennard-Jones} 4\epsilon[(\frac{\sigma}{R})^{12} - (\frac{\sigma}{R})^{6}] \end{aligned} \tag{3.4}$$

where r is the distance between two bonded atoms, θ is the angle formed by three bonded atoms, ϕ is the dihedral angle defined by four subsequently bound atoms, and R is the through-space distance between any two atoms separated by more than three bonds. The r_0 and θ_0 parameters describe equilibrium bond lengths and bond angles, and k_r and k_θ are the harmonic stretching and bending force constants. The torsional potential consists of a summation of terms with force constants k_n multiplied by cosine functions expanded about the angles of ϕ_n. While up to three cosine functions can be combined in the OPLS torsional potential, in practice, the symmetrical nature of the straight-chain alkanes yields torsional potential parameters that consist of only one simple cosine function. If charged species are present (generally not the case for the work presented in this dissertation, except for in Chapter 11), each pair of atomic subsitituents via a Coulombic potential which consists of an inverse R term, where q_i and q_j are the atomic partial charges of the two interacting species, and ϵ_0 is the vacuum permittivity. Pairs of atoms on different chains, as well as atoms separated by more than three bonds on the same chains interact through-space via a Lennard-Jones potential, which consists of the sum of a repulsive inverse R^{12} term and an attractive inverse R^6 term. The Lennard-Jones parameters, ϵ and σ, describe the depth of the potential well, and the distance at which $U(R)$=0, respectively. ϵ is therefore a measure of the attraction between the interacting species, and σ is a measure of their size. Unlike the model used by Bosio and Hase,[9] which considered non-bonding interactions between only those atoms within two positions of each other on neighboring chains, we calculate all interactions of non-bonded atoms within a cutoff distance of 12 Å (provided the interacting

TABLE 3.1: Parameters to describe the intramolecular potential in the SAM model for the CH_3- and CF_3-SAMs.

interaction	parameters
bond stretches	
C-H	k_r=340.0 ($\times 10^3$)K·Å^{-2}, r_0=1.090 Å
C-F	k_r=367.0 ($\times 10^3$)K·Å^{-2}, r_0=1.332 Å
C-C [EA-EA]	k_r=268.0 ($\times 10^3$)K·Å^{-2}, r_0=1.529 Å
C-C [EA-UA]; C-C [UA-UA]	k_r=260.0 ($\times 10^3$)K·Å^{-2}, r_0=1.526 Å
S-C [UA-UA]	k_r=222.0 ($\times 10^3$)K·Å^{-2}, r_0=1.810 Å
angle bends	
H-C-H	k_θ=33.0 ($\times 10^3$)K·rad^{-2}, θ_0=107.8°
F-C-F	k_θ=77.0 ($\times 10^3$)K·rad^{-2}, θ_0=109.1°
C-C-H [EA-EA-EA]	k_θ=37.5 ($\times 10^3$)K·rad^{-2}, θ_0=110.7°
C-C-F [EA-EA-EA]	k_θ=50.0 ($\times 10^3$)K·rad^{-2}, θ_0=109.5°
C-C-H, C-C-F, C-C-C [UA-EA-EA]; C-C-C [UA-UA-UA]	k_θ=63.0 ($\times 10^3$)K·rad^{-2}, θ_0=112.4°
S-C-C	k_θ =50.0 ($\times 10^3$)K·rad^{-2}, θ_0=112.4°
dihedral torsions[a]	
H-C-C-H, H-C-C-F, C-C-C-H, C-C-C-F	k_3=0.3 kcal·mol^{-1}, ϕ_3=0.0°
C-C-C-C, S-C-C-C	k_3=2.0 kcal·mol^{-1}, ϕ_3=0.0°
Lennard-Jones	
H	σ=2.50 Å, ϵ=0.030 kcal·mol^{-1}
F	σ=2.95 Å, ϵ=0.053 kcal·mol^{-1}
C(H,F) (EA)	σ=3.50 Å, ϵ=0.066 kcal·mol^{-1}
C,S (UA)	σ=3.905 Å, ϵ=0.118 kcal·mol^{-1}

[a] k_1 and k_2 are both equal to 0.0, making the torsional terms simple, single cosine functions.

atoms are not within three bonds of the same chain). The parameters used in our description of the SAMs are collected in Table 3.1.

Our model considers alkanethiol (or ω-trifluoroalkanethiol) chains consisting of 12 carbon units for all simulations herein. We take 36 chains and arrange the sulfur head groups to mimic the experimentally determined $\sqrt{3} \times \sqrt{3}$ R30° lattice, with a 4.98 Å nearest-neighbor

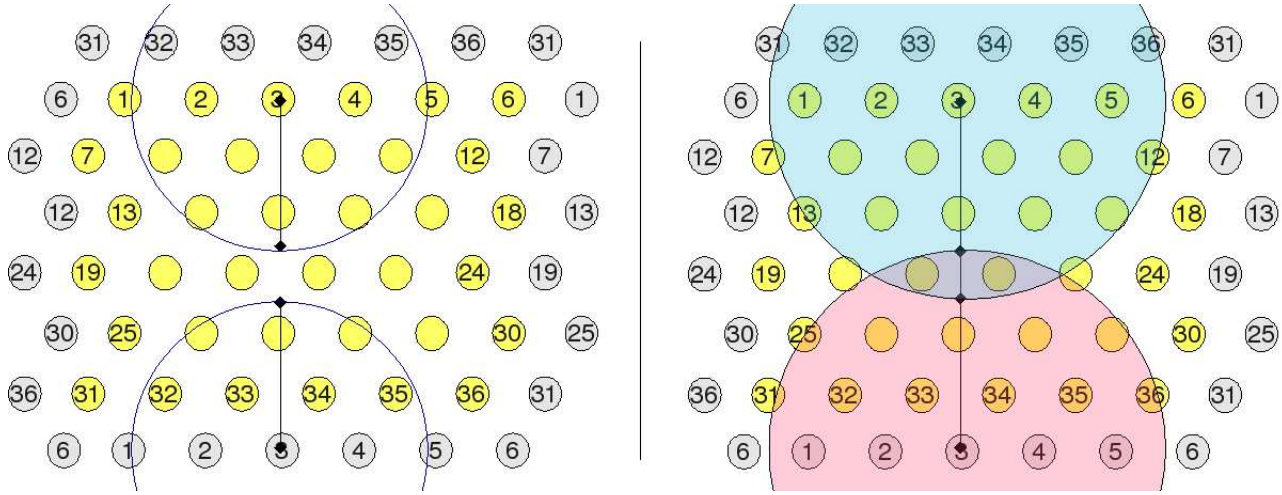

FIG. 3.2: Schematic of the periodic boundary conditions technique. Yellow circles represent the real molecules in the slab, while gray circles represent image molecules.

spacing. While some previous studies explicitly consider the gold substrate, we do not. Instead, we fix the locations of the sulfur atoms in the aforementioned lattice and do not allow them to move during simulation. This approximation has been shown to have no effect on the scattering dynamics, and eliminates the computational expenditure that would be needed for explicit treatment of the gold slab. Additionally, previous experiments in the Morris lab have found that no distiguishable changes are seen in the scattering dynamics of SAMs with various chain lengths for chains over 6 carbons long; lending validity to this approach.[17,18] The 36 chain slab is replicated in two directions using the periodic boundary conditions (PBC) algorithm as implemented in the TINKER suite of programs.[19] The use of PBC allows one to represent the SAM as an infinite 2-d surface by allowing the chains on opposite sides of the slab to interact with one another. Figure 3.2 shows a schematic of the implementation of periodic boundary conditions. PBC is implemented by letting chains on one side of the slab interact with "image" chains translated accross the slab unit cell. When using periodic boundary conditions, the shortest dimension of the replicated slab must be at least double the cutoff distance for non-bonding interactions (Fig. 3.2, left panel); if the cutoff distance is greater than half of the shortest cell dimension, cyclical interactions can arise from chains interacting with a second chain and the second chain's translated image (right panel). A 6×6 SAM slab has the dimensions of 24.77×29.88 Å which is sufficiently larger than the 12 Å non-bonding cutoff distance.

3.2.2. The gas/SAM interaction

Within this section we describe our derivation of analytical gas/SAM potential energy functions. Our method involves obtaining highly accurate ab initio data using counterpoise-corrected energies and a combination of the focal-point approach and complete basis set extrapolation techniques. This data is subsequently fit to analytic potential-energy functions.

3.2.2.1. Ab initio intermolecular potential energy data

Methods and basis sets. The simplest ab initio method for approximating the solution of the electronic Schrödinger equation is the Hartree-Fock (HF) self-consistent field method. Computational requirements for HF calculations scale as N^4, where N is the number of functions used to describe the electronic basis set of the system. For the sytems of interest for our calculations (atom or diatom + methane or perfluoromethane), HF calculations are quite fast. However, the properties we are interested in studying are intermolecular dispersion interactions, which inherently require electron-electron correlation, something entirely neglected in the HF method. Second-order Möller-Plesset perturbation theory (MP2) incorporates electron correlation via perturbation of the HF wavefunction. MP2 represents the simplest ab initio method that can describe non-bonded van der Waals type interactions, but it scales as N^5 in the number of functions. Ab initio information at the coupled-cluster level of theory is the "gold standard" for the types of calculations we are interested in. Specifically coupled-cluster theory with single, double, and perturbative treatment of triple excitations (CCSD(T)) is used in our studies. CCSD (without treating the triple excitations) scales as N^6 in the number of basis functions, and addition of the perturbative triples brings CCSD(T) to scale as N^7.

Generally, these methods make use of a linear combination of gaussian-type basis functions to describe the electronic wavefunction. As the number of basis functions increases, the calculation becomes more accurate; an infinite basis set would return the exact solution to the Schrödinger equation for the method - the HF limit, for instance. However, as the methods with electronic correlation - needed for the description of dispersion interactions - scale from fifth to seventh order of the number of basis functions, simply loading the calculation

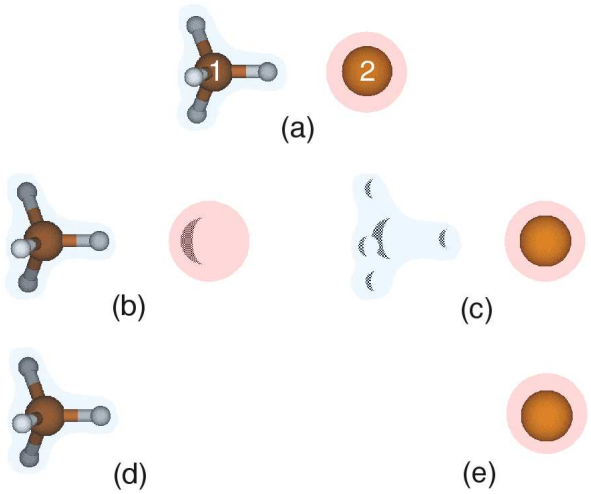

FIG. 3.3: Schematic of the counterpoise method used to correct for basis-set superposition error. The blue and pink shaded areas represent the basis functions of species 1 and 2, respectively.

with more and more basis functions to achieve higher levels of accuracy is prohibitive even for the relatively small systems we would like to describe (6-7 atoms; ∼20-60 electrons). As such, it would be desirable to have families of basis sets that display systematic convergence as the basis set size increases. This systematic convergence behavior would make extrapolation techniques to the complete basis set limit amenable. The cc-pVNZ (where N is D, T, Q, 5,...) family of basis sets developed by Dunning and co-workers has been optimized to give systematically convergent behavior of the electron correlation energy.[20–22] Augmentation of the cc-pVNZ basis sets with diffuse functions (aug-cc-pVNZ) improves the accuracy of calculating dispersion interactions, and as such we have employed the augmented basis sets in our calculations.

Correcting the basis set superposition error. It was discovered in the 1970's that, in absence of a complete basis set, application of a variational procedure to solve the electronic Schrödinger equation can lead to molecular fragments "stealing" basis functions from neighboring species.[23] The superposition of basis functions results in an artificial lowering of the calculated energy. This problem is especially problematic when trying to determine energetics of non-bonding interactions, such as are responsible for the stabilization of van der Waals clusters. A number of methods have been developed to deal with the so-called basis set superposition error (BSSE), with differing levels of rigor and complexity. We have employed the simple, yet proven and effective, counterpoise method of Boys and Bernardi to correct

for BSSE in all of our calculated intermolecular potential energy profiles.[23] The counterpoise method consists of doing five separate calculations for each intermolecular geometry. The approach is depicted schematically in Figure 3.3. First, the complex is calculated in the conventional way with all of the basis functions and the presence of all atoms (a). This gives the non-BSSE-corrected energy for the complex. Then, the energy of each individual monomer species (Ar or CH_4 in the example) is calculated with the basis functions of both species, but the atoms of the other species are replaced with ghost atoms (i.e. the basis functions exist in the absense of the nuclear attraction and repulsion and the electrons of the other species), (b) and (c). Finally, the energy of each individual monomer is calculated in the absence of the other with only its own basis functions (d) and (e). This gives the energy of each monomer species in the absence of the influence of the other. The energetic difference in (b) and (d) then gives the added stabilization energy of species 1 due to the addition of the basis functions of species 2. The BSSE correction is given by the energy of (b)+(c)-(d)-(e). This is then added back to the energy obtained in (a) to give the BSSE-corrected energy.

Application of the focal-point approach. As was mentioned above, while ab initio data obtained via coupled-cluster methods are superior to MP2 theory, these calculations quickly get prohibitively computationally expensive. It would, therefore, be advantageous to find a systematic way to estimate coupled-cluster energies from less-expensive, lower-accuracy methods. In the work of Allen and co-workers, it was found that the difference in CCSD(T) and MP2 energies was essentially constant when increasing the basis set size for high-quality basis sets.[24,25] Therefore, if the differences between MP2 and CCSD(T) energies are calculated with an affordable basis set (aug-cc-pVDZ for instance) over a range of geometries, those differences can be used to estimate CCSD(T) energies (fp-CCSD(T) data) with larger basis sets (e.g. aug-cc-pVTZ and aug-cc-pVQZ) from less expensive MP2 calculations. A detailed examination of the legitimacy of the focal-point approach is given in Chapter 4 in our study of the ab initio intermolecular potential energy surfaces of rare-gases interacting with hydrocarbons and fluorocarbons. The focal-point approach affords us an opportunity to obtain high quality data with reduced computational expense. For instance, one point in the Ar-CF_4 system requires $\sim$60$\times$ more CPU time for a full CCSD(T)/aug-cc-pVQZ calculation than the cumulative time necessary for the three calculations (MP2/aug-cc-pVDZ, MP2/aug-cc-pVQZ, and CCSD(T)/aug-cc-pVDZ) to obtain fp-CCSD(T)/aug-cc-pVQZ data.[26]

Extrapolation to the complete basis set limit. Ab initio calculations can be further improved by use of extrapolation techniques to estimate the energy at the complete basis set (CBS) limit. Two common procedures used to obtain CBS estimates are those by Peterson et al.[27] and Halkier et al.[28] For the systems we are interested in, we have determined both methods give comparable accuracy, so we have chosen to use the simpler, two-point procedure for our calculations. The two-point extrapolation procedure is of the following form:

$$E_{CBS} = \frac{4^3 E_{QZ} - 3^3 E_{TZ}}{4^3 - 3^3} \tag{3.5}$$

where E_{QZ} and E_{TZ} refer to the MP2 or fp-CCSD(T) energies calculated using the aug-cc-pVQZ and aug-cc-pVTZ basis sets, respectively. This procedure gives us a way to obtain MP2/CBS or fp-CCSD(T)/CBS estimates from our data.

3.2.2.2. Analytical potential energy functions

For the description of non-bonded intermolecular interactions, the Lennard-Jones potential[29] found popularity in early molecular dynamics calculations because of its computational efficiency. As described above in the description of the SAM intramolecular potential, the Lennard-Jones potential is of the 6-12 form:

$$U_{Lennard-Jones} = 4\epsilon[(\frac{\sigma}{r_{ij}})^{12} - (\frac{\sigma}{r_{ij}})^{6}] \tag{3.6}$$

where r_{ij} is the particle separation, ϵ is the depth of the potential well, and σ is the distance at which the intermolecular potential is zero. This formulation is computationally simple in that only elementary operations are necessary for evaluation. The attractive inverse r^6 term has widely been accepted as the correct form to describe the dispersion interactions which give rise to the van der Waals well.[30] However, the functional form needed to desribe the repulsive wall is not well understood. The inverse r^{12} term, although computationally advantageous, is sometimes too steep, and use of an exponential function to describe the repulsive wall generally gives better results. Buckingham's formulation[31] for the intermolecular potential is of the 6-exp form:

$$U_{Buckingham} = Ae^{-Br_{ij}} - Cr_{ij}^{-6} \tag{3.7}$$

where A, B, and C are fitting parameters specific to the atom pair involved. While evaluation of the exponential function is computationally more taxing, with contemporary computing

technology the increased accuracy overweighs this expense. The Buckingham function can be generalized by letting the inverse r^6 term vary its exponent as a fourth fitting parameter, n. While we have tried to constrain our functional forms within this work, this additional parameter proved necessary for our decription of the CO/SAM intermolecular potential (see Chapter 7).

In practice, once we obtain ab initio fp-CCSD(T)/CBS intermolecular interaction energies for the system in a variety of approaches, we use a non-linear least squares procedure to fit the parameters in Equation 3.7 over all approaches simultaneously. For this purpose, we have used a modified Levenberg-Marquardt algorithm as implemented in the MINPACK libraries.[32] Previous work by Day and co-workers has shown that ab initio based analytical potential-energy surfaces are necessary for quantitative prediction of experimental scattering behavior.[33] That work compared the accuracy of a united atom intermolecular potential based on gas-phase experimental data (GPBUA), with that of OPLSUA and an analytical potential fit to high-level ab initio data, and showed that only the ab initio-based gas/surface potential reproduces experiment.

3.3. INITIAL CONDITIONS

3.3.1. SAM initial conditions

Thermal simulation of our SAM model at 300 K under the canonical ensemble [using a molecular Beeman integration method with a Berendson thermostat] as implemented in the TINKER[19] package of programs reveals the hybrid united-atom/all-atom potential to adequately predict the experimentally determined ∼30° tilt of the alkyl chains.[7] Specifically, we find the chain tilt angle to be 29.9° by time and ensemble averaging over a 1.0 ns MD simulation of the thermally equilibrated SAM. The average thickness of the monolayer (defined as z-axis distance from sulfur atom to terminal carbon atom) is found to be 13.2 Å, which is consistent with film thickness measurements of a dodecanethiolate SAM of 14.8 Å (the value of 14.8 Å is obtained by substracting the Au–S distance [1.2±0.4 Å, via ellipsometry methods[34]] from the overall thickness value of 16.1±0.2 Å from ellipsometry[35] [∼16 Å determined via STM[36]]). Figure 3.4 shows the calculated chain tilt and film thickness during a 1.5 ns canonical simulation at 300 K. The standard deviation in the tilt

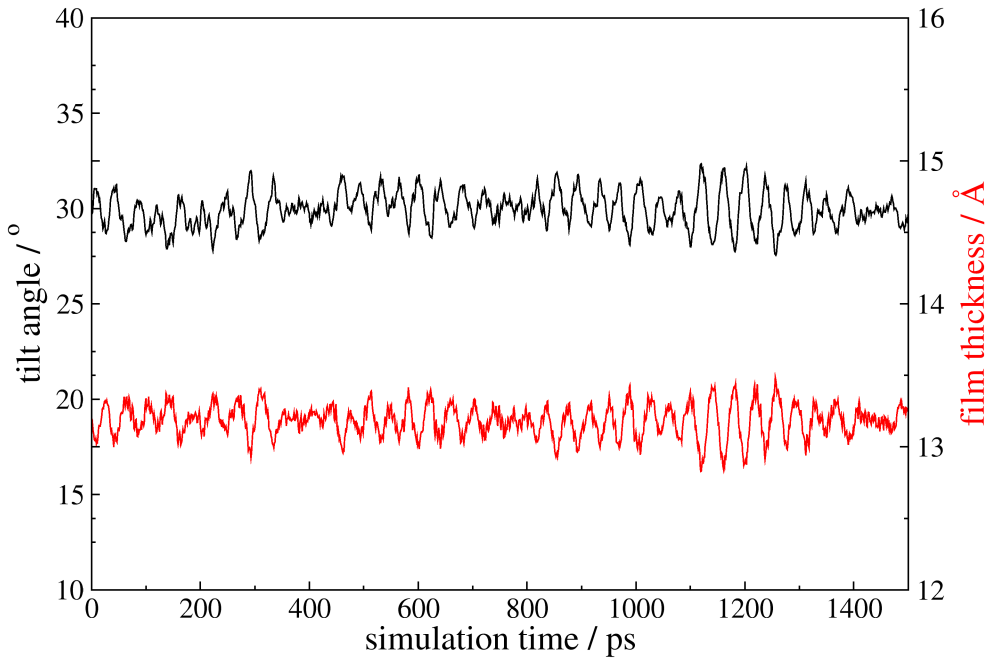

FIG. 3.4: Average chain tilt and film thickness of a dodecanethiolate SAM as function of simulation time.

and height values over the 1.5 ns simulation are 2.2° and 0.1 Å . It is observed from the plot that these values oscillate over time; animation of trajectories shows these oscillations to be correlated, long-range waving motions of the chains, which conjure the image of a field of grain blowing in a gentle breeze.

To build initial conditions (atomic positions and momenta) for use in our gas/surface trajectory calculations, we first run a long (typically on the order of 0.5 ns with a 1.0 fs timestep) canonical simulation of only the SAM at the desired surface temperature (300 K). After this initial equilibration run, we continue the thermal simulation, taking snapshots at regular intervals (usually every 0.5 ps). The coordinates and momenta of the SAM atoms at each of these snapshots is recorded for later use as input in the gas/surface molecular dynamics simulations.

3.3.2. Gas initial conditions

Just as we have described production of initial surface conditions, we here describe how we obtain initial conditions for the impinging gas-phase species. For rare gases, the selection of initial conditions is rather simple, concerning only geometrical considerations. With the

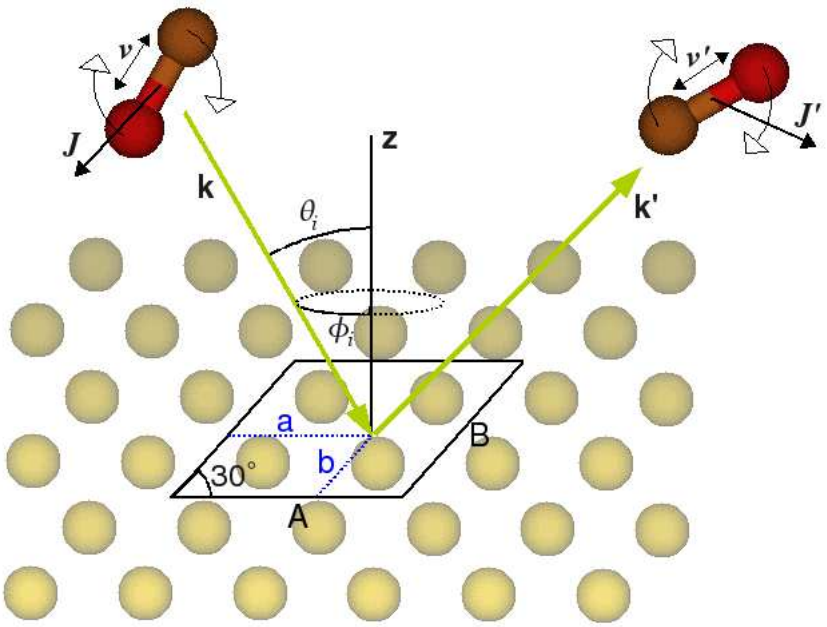

FIG. 3.5: Schematic of relevant initial and final vector and angle terms. The yellow spheres represent the methyl termini of a SAM.

diatomic projectiles, rotational and vibrational states also have to be determined, as well as the initial spatial orientation of the molecule.

3.3.2.1. Aiming point sampling

To make connection with experiment, the angle of incidence, θ_i, of the impinging gas' initial velocity vector, **k**, with respect to the surface normal, is usually set at 30°, but can be varied. The initial angle (azimuthal angle, ϕ_i) formed between **k** and the alkanethiol chain tilt direction is randomly sampled from a uniform distribution. In the experiment, the SAM surface deviates from our pristine model in that with a real SAM surface, there are many domains rotated with respect to one another, which essentially corresponds to a random sampling of the initial azimuthal angle, ϕ_i, as the molecular beam covers an area of $\sim$1 cm^2. These angles are defined schematically in Fig. 3.5. The aiming point at which **k** vector impacts on the surface is randomly selected within a region of the SAM twice the size of the unit cell defined by the rhombus formed by four adjacent sulfur atoms in the central region of the slab, depicted by "A" and "B" in Fig. 3.5. The x,y coordinates of the aiming point within this sampling region are determined by generation of two fresh random

numbers in the range 0.0→1.0, which give fractional positions, 'a' and 'b', along the 2×2 unit cell dimensions 'A' and 'B' in Fig. 3.5. The initial position for the impinging gas is then determined by translating it from the surface impact point along the reverse **k** vector until it has a z coordinate with at least 10 Å separation from the closest atom of the surface.

3.3.2.2. Assigning molecular rotation, vibration, and orientation

For atomic species, assignment of impact point, initial separation, and initial momenta is all that is neccesary to define initial conditions for trajectory propogation. However, with molecular species, a host of additional degrees-of-freedom need to be dealt with and controlled. We make use of the sampling capabilities of the VENUS96[37] program to select initial rotational and vibrational states of diatomic species, and initial molecular orientation. Although we do not currently have a method of analyzing the incident rovibrational populations in our experiment, our supersonic beam expansion should give rotational and vibrational temperatures that are cooled to around ∼10 and 270 K, respectively (perhaps lower for vibration), based on comparison with similar experimental setups which can measure these temperatures.[38] However, for diatomic species, thermal sampling is not available within the VENUS program, so we chose to specifically select initial rotational and vibrational states. The v=0,j=0 state was used for comparison with experiments, as less than 1 in 10^4 molecules exist in v=1 or above state at 270 K, and less than 5% of molecules exist in the j=3 or above state at 10 K (values based on Boltzmann distribution at indicated temperatures for CO). Other rotational and vibrational states were selected for studies investigating the influence of rovibrational excitation on scattering dynamics (see Chapter 9). By default, VENUS assigns the molecule a random spatial orientation based on random rotation through Euler's angles. While this random starting geometry was appropriate for a majority of our studies (especially when comparison with experiment was desired), our study of collision stereodynamics (see Chapter 10) required the impinging gas species to be oriented/aligned in specific starting collision geometries. For this purpose, the ROTATE and INITEBK subroutines of the VENUS code were altered to specifically confine the assignment of rotational angular momentum to a specific cartesian plane (for instance, the rotational motion was confined to the x,y plane to produce helicopter motion),[39] and the random rotation about Euler's angles was suppressed to give molecules initially aligned along the x or

z-axes.[40] The collision geometry was subsequently assigned during selection of impact point by rotating the molecule to be parallel or perpendicular with the projection of **k** on the x,y-plane, depending on what was desired.

3.4. PROPAGATION

Once an appropriate potential energy surface is constructed, and initial conditions are assigned, the only remaining component needed for propagation of trajectories is an appropriate scheme to integrate the equations of motion. Since the Newtonian equation of motion, Eq. 3.3, is a single differential in position on the left hand side and a double differential in time on the right, no analytical solution exists, and it is necessary to employ numerical integration techniques. There exist many algorithms to accomplish this; some of the simpler ones are the Verlet,[41] velocity-Verlet,[42] Beeman,[43] and leapfrog[44] algorithms. Each of these algorithms are based on manipulation of a Taylor series expansion of t, truncated at various orders of Δt, and provide a method to update the atomic positions and momenta after each timestep of a molecular dynamics simulation. The typical Taylor series expansion of the coordinate variable $q(t)$ is of the form:

$$q(t+\Delta t) = q(t) + \Delta t q'(t) + (\frac{\Delta t^2}{2})q''(t) + ...(\frac{\Delta t^n}{n!})q^{(n)}(t) \tag{3.8}$$

where $q'(t)$, $q''(t)$, and $q^{(n)}(t)$ are the 1^{st}, 2^{nd}, and nth derivatives of the position at the current time, $q(t)$. Truncation at different orders of the expansion, followed by subsequent algebraic manipulation yield the various integration methods. It is instructive to explicitly illustrate the derivation for one of these methods. Since the Beeman algorithm is implemented in the TINKER dynamics program used for determination of the initial conditions of the SAM surface, we will derive this method. Following Equation 3.8, substituting in the velocity, $v(t)$, and acceleration, $a(t)$, and truncation after the Δt^3 term gives:

$$q(t+\Delta t) = q(t) + v(t)\Delta t + (\frac{1}{2})a(t)\Delta t^2 + (\frac{1}{6})b(t)\Delta t^3 + O(\Delta t^4) \tag{3.9}$$

where $b(t)$ is the third derivative of $q(t)$ and $O(\Delta t^4)$ indicates that the truncation error is of the fourth order magnitude of Δt. The $b(t)$ term can be replaced after manipulation of the Taylor expansion of the acceleration of the previous timestep, $a(t-\Delta t)$, truncated after the

Δt term (this corresponds to truncation after Δt^3 in the position expansion):

$$\begin{aligned} a(t-\Delta t) &= a(t) - b(t)\Delta t + O(\Delta t^2) \\ b(t)\Delta t &= a(t) - a(t-\Delta t) + O(\Delta t^2) \\ b(t)\Delta t^3 &= a(t)\Delta t^2 - a(t-\Delta t)\Delta t^2 + O(\Delta t^2) \\ \frac{1}{6}b(t)\Delta t^3 &= \frac{1}{6}a(t)\Delta t^2 - \frac{1}{6}a(t-\Delta t)\Delta t^2 + O(\Delta t^2) \end{aligned} \tag{3.10}$$

Substitution of Eq. 3.10 into 3.9 gives the Beeman algorithm for updating the molecular positions:

$$q(t+\Delta t) = q(t) + v(t)\Delta t + \frac{2}{3}a(t)\Delta t^2 - \frac{1}{6}a(t-\Delta t)\Delta t^2 + O(\Delta t^4) \tag{3.11}$$

The velocity relationship is derived similarly and takes the form:

$$v(t+\Delta t) = v(t) + \frac{1}{3}a(t+\Delta t)\Delta t + \frac{5}{6}a(t)\Delta t - \frac{1}{6}a(t-\Delta t)\Delta t + O(\Delta t^3) \tag{3.12}$$

where t is the current time, Δt is the timestep, and $q(t)$, $v(t)$, and $a(t)$ are the position, velocity, and acceleration at time t. The Beeman method gives errors in the position on the order of Δt^4 and in the velocites (hence momenta) on the order of Δt^3.

For our classical trajectory simulations, we use our own in-house molecular dynamics code, "MDTINKER," which was initially developed by Prof. Diego Troya during postdoctoral work in the lab of Dr. George Schatz. For integration of the equations of motion, our scheme employs a Gear fifth-order predictor, sixth-order corrector algorithm.[45] The Predictor-Corrector (P-C) algorithms are of higher accuracy than the other integrators we have mentioned above, but at the expense of increased complexity and computational time. Whereas the Beeman algorithm needs only information about the positions and velocities at t and $t-\Delta t$ to generate q and p at $t+\Delta t$, the "multivalue" P-C needs much more data. The general scheme of the P-C algorithm is as follows. In the prediction step, an extrapolation based on derivatives calculated at earlier times is used to forecast the positions at $t+\Delta t$. The general form for this prediction step to fifth order is:

$$P: q(t+\Delta t) = q(t) + \Delta t(\beta_1 v(t) + \beta_2 v(t-\Delta t) + \beta_3 v(t-2\Delta t) + \beta_4 v(t-3\Delta t) + \beta_5 v(t-4\Delta t)) + O(\Delta t^6) \tag{3.13}$$

where the β_i terms are coefficients dependent on the integration method and P-C order. Our implementation is based on the Adams-Moulton method[46] and uses coefficients described

by Gear.[45] It is plainly seen that for this fourth-order prediction equation, information on the derivatives calculated at the current and three previous steps are necessary to predict the next point, $P : q(t + \Delta t)$. At this point, the potentials are evaluated at $P : q(t + \Delta t)$ to get a predicted $v(t + \Delta t)$ at the next point. The predicted $v(t + \Delta t)$ is then used to get the corrected positions, $C : q(t + \Delta t)$, according to the sixth order prediction step:

$$C : q(t + \Delta t) = q(t) + \Delta t(\ \beta_0 v(t + \Delta t) + \beta_1 v(t) + \beta_2 v(t - \Delta t) + \beta_3 v(t - 2\Delta t) + \beta_4 v(t - 3\Delta t) + \beta_5 v(t - 4\Delta t) \ ) + O(\Delta t^6) \qquad (3.14)$$

The P-C process is finalized by evaluation of the potentials at $C : q(t + \Delta t)$ to get the corrected derivatives, and subsequent updating of the "previous derivatives" array for use in the next P-C step. This approach is sometimes referred to as PECE (for prediction-evaluation-correction-evaluation).

While propagation of the equations of motion is accomplished via our own implementation of the Gear P-C algorithm, our MD driver leverages the extensive force field capablities of TINKER to evaluate the forces. A flow chart of the entire trajectory process from generation of initial conditions to data analysis is presented in Figure 3.6. After both the predictor and corrector steps of the molecular dynamics code, MDTINKER passes the instantaneous coordinates and momenta of all the atoms in the system to the TINKER subroutines responsible for calculation of the potential energy using the previously defined force fields (in our case the modified hybrid OPLSUA/OPLSAA force field) in combination with our externally determined gas/SAM intermolecular Buckingham potential. After the forces have been calculated, they are passed back to the MDTINKER driver and the subsequent integration step is performed.

The selection of timestep length (time between updating the forces) in the solution of the equations of motion is important; with large timesteps there is a tendency for poor conservation of total energy as the simulation progresses. Obviously, shorter timesteps will result in more accurate trajectory propagation, and choosing the shortest timestep is ideal. This is balanced, however, by the fact that a costly new set of forces must be calculated more often as the timestep is decreased. One would like to choose the longest timestep possible, so long that it is short enough to conserve well the total system energy. This is dictated by the specifics of the system and is often limited by the nature of the fastest molecular motion inherent to the system. For our gas/SAM systems, this limiting motion corresponds

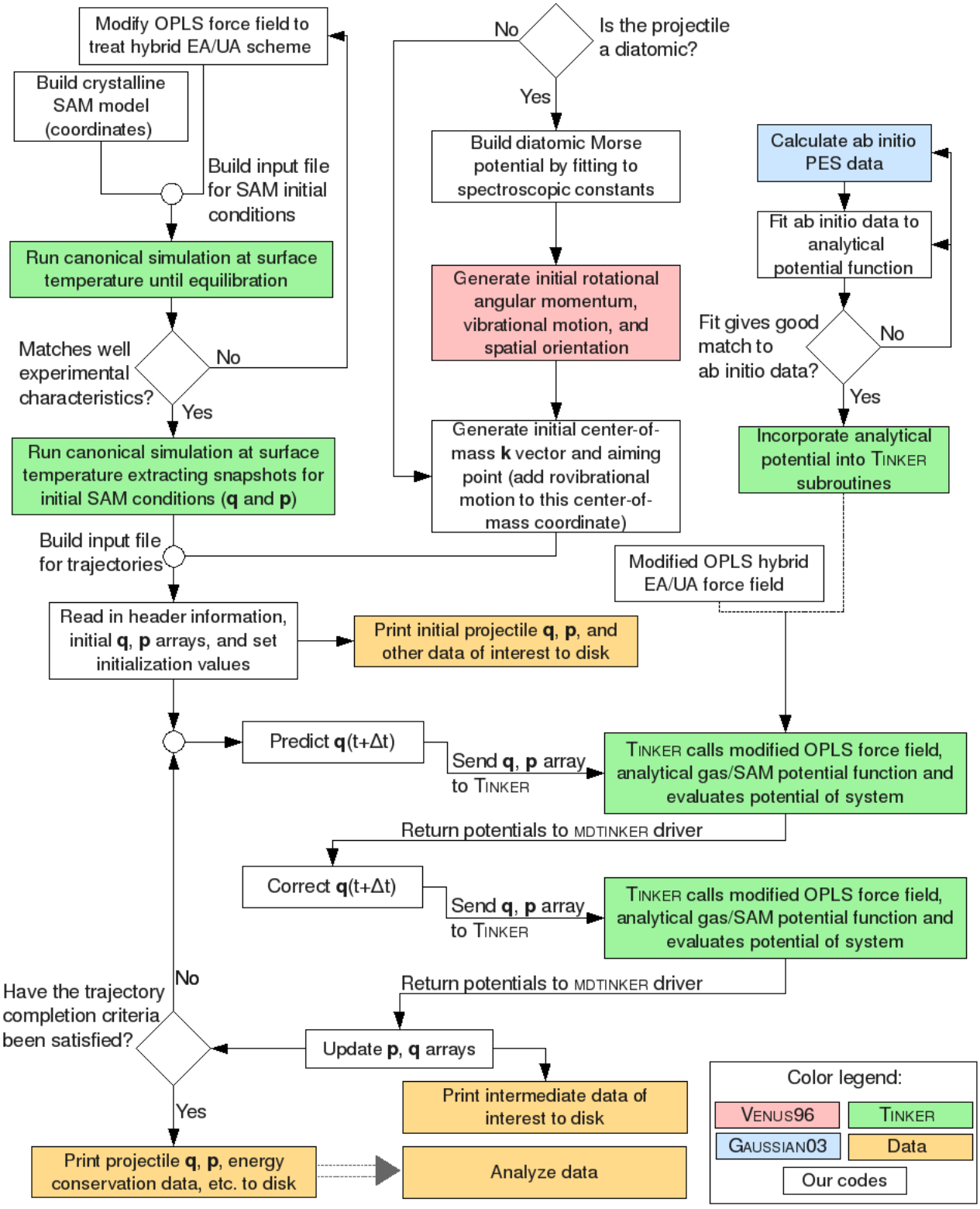

FIG. 3.6: Schematic of the classical trajectory calculation process.

to that of the explicitly defined hydrogen atoms at the ethyl SAM terminus. We found that while a 25 a.u. timestep is satisfactory, superior energy conservation was achieved with a 10 a.u. timestep. As such, we have used a 10 a.u. (0.24 fs) timestep for all of the trajectories described herein.

3.5. DATA ANALYSIS

During the trajectories, information about the overall kinetic, potential, and total energy of the system is recorded at intermediate timesteps to ensure our trajectories conserve energy. Typical energy loss is on the order of 2 parts in 10^5 of the total energy. At these intermediate timesteps we also record the coordinates and momenta of the gas-phase species for analysis. We record the initial and final positions and momenta of the gas species and use these data to calculate the final translational energy, E'$_T$, scattering angle, θ_f, and azimuthal angle, ϕ_f, (and rotational state, j', and vibrational state, v', for diatomic species) for each trajectory. E'$_T$ is determined by the magnitude of the **k'** vector, as defined in Fig 3.5. θ_f and ϕ_f are analogous to the initial angles defined in Fig. 3.5. For diatomic projectiles, in addition to calculating the classical final rotational and vibrational states, stereodynamic information may be obtained by examination of the direction of the **J'** vector with respect to a set coordinate axis system (further details on determination of stereodynamics characteristics are given in Chapter 10).

From the data recorded at intermediate timesteps throughout the trajectory, we can obtain information about the molecule during the trajectory, including whether the gas penetrates into the SAM surface, the number of encounters it has with the surface (determined by turning points in value of the gas' center-of-mass z-coordinate), and the minimum height (in the surface normal z-coordinate) it attains.

REFERENCES

[1] D. M. Hirst, *Potential energy surfaces: Molecular structure and reaction dynamics* (Taylor and Francis, 1985).

[2] J. N. Murrell, S. Carter, S. Frantos, P. Huxley, and A. J. C. Varandas, *Molecular potential energy functions* (John Wiley & Sons, 1984).

[3] S. L. Mielke, K. A. Peterson, D. W. Schwenke, B. C. Garrett, D. G. Truhlar, J. V. Michael, M.-C. Su, and J. W. Sutherland, Phys. Rev. Lett. **91**, 063201 (2003).

[4] J. Hautmann and M. L. Klein, J. Chem. Phys. **91**, 4994 (1989).

[5] W. L. Jorgensen, J. D. Madura, and C. J. Swenson, J. Am. Chem. Soc. **106**, 6638 (1984).

[6] W. L. Jorgensen and J. Tirado-Rives, J. Am. Chem. Soc. **110**, 1657 (1988).

[7] F. Schreiber, Progress in Surface Science **65**, 151 (2000).

[8] C. D. Bain, H. A. Biebuyck, and G. M. Whitesides, Langmuir **5**, 723 (1988).

[9] S. B. M. Bosio and W. L. Hase, J. Chem. Phys. **107**, 9677 (1997).

[10] A. K. Rappe, C. J. Casewit, K. S. Colwell, W. A. Goddard, III, and W. M. Skiff, J. Am. Chem. Soc. **114**, 10024 (1992).

[11] W. Mar and M. L. Klein, Langmuir **10**, 118 (1994).

[12] W. L. Jorgensen, D. S. Maxwell, and J. Tirado-Rives, J. Am. Chem. Soc. **118**, 11225 (1996).

[13] N. Camillone, III, C. E. D. Chidsey, G.-Y. Liu, and G. Scoles, J. Chem. Phys. **98**, 3503 (1993).

[14] P. Fenter, P. Eisenberger, and K. S. Liang, Phys. Rev. Lett. **70**, 2447 (1993).

[15] N. Camillone, III, C. E. D. Chidsey, P. Eisenberger, P. Fenter, J. Li, K. S. Liang, G.-Y. Liu, and G. Scoles, J. Chem. Phys. **99**, 744 (1993).

[16] T.-Y. Yan and W. L. Hase, J. Phys. Chem. B **106**, 8029 (2002).

[17] B. S. Day and J. R. Morris, J. Phys. Chem. B **107**, 7120 (2003).

[18] M. K. Ferguson, J. R. Lohr, B. S. Day, and J. R. Morris, Phys. Rev. Lett. **128**, 073201 (2004).

[19] J. W. Ponder and F. M. Richards, J. Comput. Chem. **8**, 1016 (1987).

[20] T. H. Dunning, Jr., J. Chem. Phys. **90**, 1007 (1989).

[21] D. E. Woon and T. H. Dunning, Jr., J. Chem. Phys. **98**, 1358 (1993).

[22] A. K. Wilson, D. E. Woon, K. A. Peterson, and T. H. Dunning, Jr., J. Chem. Phys. **110**, 7667 (1999).

[23] S. F. Boys and F. Bernardi, Mol. Phys. **19**, 553 (1970).

[24] A. G. Csaszar, W. D. Allen, and H. F. Schaefer, III, J. Chem. Phys. **108**, 9751 (1998).

[25] A. L. L. East and W. D. Allen, J. Chem. Phys. **99**, 4638 (1993).

[26] W. A. Alexander and D. Troya, J. Phys. Chem. A **110**, 10843 (2006).

[27] K. A. Peterson, D. E. Woon, and T. H. Dunning, Jr., J. Chem. Phys. **100**, 7410 (1994).

[28] A. Halkier, T. Helgaker, P. Jorgensen, W. Klopper, H. Koch, J. Olsen, and A. K. Wilson, Phys. Lett. **286**, 243 (1998).

[29] J. E. Lennard-Jones, Proc. Phys. Soc. **43**, 461 (1931).

[30] F. London, Z. Phys. **63**, 245 (1930).

[31] R. A. Buckingham, Proc. Royal Soc. London **168**, 264 (1938).

[32] *www.netlib.org/minpack*.

[33] B. S. Day, J. R. Morris, and D. Troya, J. Chem. Phys. **122**, 214712 (2005).

[34] J. Shi, B. Hong, A. N. Parikh, R. W. Collins, and D. L. Allara, Chem. Phys. Lett. **246**, 90 (1995).

[35] C. D. Bain, E. B. Troughton, Y.-T. Tao, J. Evall, G. M. Whitesides, and R. G. Nuzzo, J. Am. Chem. Soc. **111**, 321 (1989).

[36] L. A. Bumm, J. J. Arnold, L. F. Charles, T. D. Dunbar, D. L. Allara, and P. S. Weiss, J. Am. Chem. Soc. **121**, 8017 (1999).

[37] W. L. Hase, R. J. Duchovic, X. Hu, A. Komornicki, K. F. Lim, D. h. Lu, G. H. Peslherbe, K. N. Swamya, S. R. V. Linde, A. Varandas, et al., Quantum Chemistry Program Exchange Bulletin **16**, 671 (1996).

[38] B. G. Perkins, Jr., T. Haber, and D. J. Nesbitt, J. Phys. Chem. B **109**, 16396 (2005).

[39] The total angular momentum is stored within the INITEBK subroutine within the variable AL; preferential confinement of this rotation to specific plane was achieved by selectively setting the component angular momentum variables AM(1), AM(2), and AM(3) either to zero or AL — AM(1)=AM(2)=0, AM(3)=AL corresponds to helicopter motion.

[40] Supression of the Euler rotation is achieved by selectively setting tthe PHI, and CHI variables to 0° or 90° and by setting the CSTHTA variable to -1, 0, or 1 within the ROTATE subroutine — PHI=CHI=90, CSTHTA=-1 aligns a diatomic molecule on the x-axis.

[41] L. Verlet, Phys. Rev. **159**, 98 (1967).

[42] W. C. Swope, H. C. Anderson, P. H. Berens, and K. R. Wilson, J. Chem. Phys. **76**, 637 (1982).

[43] D. Beeman, J. Comp. Phys. **20**, 130 (1976).

[44] M. P. Allen and D. J. Tildesley, *Computer simulation of liquids* (Oxford Press, 1989).

[45] C. W. Gear, *Numerical initial value problems in ordinary differential equations* (Prentice-Hall, 1971).

[46] F. R. Moulton, *New methods in exterior ballistics* (University of Chicago Press, 1926).

Preface: Rare gas scattering

A full understanding of chemical reaction dynamics at the gas/surface interface requires knowledge of energy transfer processes that happen as a result of a gas-phase species colliding with the surface. The extent of energy transfer between the various degrees of freedom of the surface and the impinging species determines the propensity for gas accomodation and subsquent chemical reaction. Energy transfer in the initial impact can also reveal information regarding the likelihood for reaction through direct processes. Rare gases scattering from surfaces represents an ideal situation to study the characteristics of energy transfer in the absence of gas-phase degrees of freedom. In Chapters 4 and 5, we describe our efforts in using rare-gas scattering from model organic surfaces to determine the effect of gas and surface mass on energy transfer dynamics. We have chosen to use CH_3- and CF_3-terminated self-assembled monolayers to vary the effective surface mass, and have used Ne, Ar, Kr, and Xe to vary the gas mass.

In Chapter 4, we present a theoretical study of the intermolecular potentials for the Ne, Ar, Kr, and Xe–CH_4, CF_4 systems, with the goal of obtaining analytic potentials for use in scattering simulations of rare-gas–SAM systems. The potential-energy surfaces of these systems have been calculated utilizing second-order Möller-Plesset perturbation theory and coupled-cluster theory in combination with correlation-consistent basis sets (aug-cc-pVNZ; N=D,T,Q). The calculations show that the stabilizing interactions between the rare gases and the molecules are slightly larger for CF_4 than for CH_4. Moreover, the rare-gas–CX_4 (X=H,F) potentials are more attractive for Xe than for Kr, Ar, and Ne. Our highest quality ab initio data (focal-point-CCSD(T) extrapolated to the complete basis set limit) have been used to develop pair-wise analytical potentials for rare-gas/hydrocarbon (and fluorocarbon) systems. We use these potentials in classical-trajectory studies of rare gases interacting with hydrocarbon and fluorocarbon surfaces in our subsequent studies.

In addition to the practical goal of building analytic potentials for use in scattering studies, we have evaluated the focal-point approach which allowed us to obtain CCSD(T)-quality data from substantially less expensive MP2 calculations. We also investigated the influence of the presence of a dipole in the hydrocarbon backbone on the rare-gas–hydrocarbon intermolecular potential-energy surface. This study resulted in an article published in the Journal of Physical Chemistry A.[1]

In Chapter 5, the effect of mass on gas/organic-surface energy transfer is explored via investigation of the scattering dynamics of rare gases (Ne, Ar, and Kr) from regular (CH_3-terminated) and ω-fluorinated (CF_3-terminated) alkanethiol self-assembled monolayers (SAMs). Molecular-beam scattering experiments carried out in ultrahigh vacuum and molecular-dynamics simulations based on high-accuracy potentials are used to obtain the rare-gases' translational-energy distributions after collision with the SAMs. Simulations indicate that mass is the most important factor in determining the changes in the energy exchange dynamics for Ne, Ar, and Kr collisions on CH_3- and CF_3-terminated SAMs. Other factors, such as changes in the gas/surface potential and intra-surface interactions, play only a minor role in determining the differential dynamics behavior for the systems studied. This study was published in the Journal of Chemical Physics.[2] With this study, we were able to directly and specifically probe the influence of mass on gas/organic-surface energy transfer, something that had not been done in prior studies. Unlike the hydrogenated and fluorinated organic liquids used in prior studies, CH_3- and CF_3-SAM surfaces present identical structures below the terminal groups and therefore the differences in interfacial behavior was attributable to the exposed groups.

[1]W. A. Alexander and D. Troya, *J. Phys. Chem. A* **110**, 10834 (2006).

[2]W. A. Alexander, B. S. Day, H. J. Moore, T. R. Lee, J. R. Morris, and D. Troya, *J. Chem. Phys.* **128**, 014713 (2008).

Chapter 4

Theoretical study of the Ne–, Ar–, Kr–, and Xe–CH_4, –CF_4 intermolecular potential-energy surfaces

Reproduced in part with permission from W. A. Alexander and D. Troya, *J. Phys. Chem. A* **110**, 10834 (2006). Copyright 2006 American Chemical Society.

4.1. INTRODUCTION

The result of a chemical dynamics simulation depends strongly on the characteristics of the potential-energy surface employed in the integration of the equations of motion.[1] Commonly, potential-energy surfaces used in chemical dynamics simulations consist of multiparametric analytic functions that are fitted to ab initio calculations.[2] An advantage of using ab initio calculations in the derivation of analytic potential-energy surfaces is that, ideally, the quality of the analytic surface is reflective of the quality of the electronic-structure calculations. Therefore, if high-quality ab initio calculations are affordable for the molecular system under study, and the errors introduced in the fitting process are negligible, predictive analytic potential-energy surfaces (PESs) can be derived. A paradigmatic example of the improvement in the predictive character of analytical PESs with an improvement in the ab initio calculations involved in the PES fit is given by the hierarchical PES for the H+H_2 reaction of Mielke et al.[3] In that study, PESs built using different levels of electronic-structure theory provide different levels of agreement with experiment, with the most-accurate PES providing quantitative agreement with experiment.

In this work, we aim at deriving accurate analytic potential-energy surfaces for chemical dynamics simulations of collisions of rare gases with hydrocarbon and fluorocarbon surfaces. Study of the scattering dynamics of rare gases from organic surfaces is important because it provides a convenient starting point for a detailed characterization of the interfacial chemistry of these important surfaces at a molecular level. Many experiments have provided a wealth of information about several aspects of the dynamics of collisions of rare gases with both liquid[4–7] and solid[8–16] organic surfaces. Of particular relevance to the work presented herein are the recent molecular-beam experiments of Day et al. on scattering of

Ar, Kr, and Xe from various alkanethiol self-assembled monolayers (SAMs) absorbed on a gold surface.[17] These experiments indicate that the scattering dynamics of the rare gases depends on the nature of the exposed terminus of the SAM. For instance, the amount of energy transferred from the impinging rare gas to a CF_3-terminated SAM is smaller than to a fully hydrogenated (CH_3-terminated) SAM. This enhanced rigidity of a SAM surface upon fluorination of the exposed group concurs with earlier experiments.[18] To adequately simulate those molecular-beam scattering experiments at the atomic level and elucidate the origin of the different energy transfer from rare gases to different SAMs, accurate rare-gas/hydrocarbon(fluorocarbon) potentials are needed. In this work, we present high-quality ab initio calculations of the potential-energy surface of the Ne, Ar, Kr, and Xe–CH_4 and CF_4 systems. The ab initio calculations are used to derive pair-wise analytic potential-energy surfaces that can be used in dynamics simulations of collisions of Ne, Ar, Kr, and Xe with regular and fluorinated alkanethiol SAMs.

Additional goals that we aim to adress within this chapter include the evaluation of the focal-point approach[19,20] to estimate CCSD(T) energies from MP2 calculations for the systems under consideration, and the investigation of the effect of a dipole in the hydrocarbon backbone on the rare-gas–hydrocarbon intermolecular potential-energy surface.

4.2. ELECTRONIC STRUCTURE CALCULATIONS

4.2.1. Computational details

We have calculated intermolecular potential-energy curves for the Ne, Ar, Kr, and Xe–CH_4, CF_4 systems by scanning the rare-gas–molecule center-of-mass coordinate from the asymptote to repulsive energies of about 20 kcal·mol^{-1}. Typically, the separation between the points of the scan is 0.1 Å, but the determination of the potential well is accurate to 0.05 Å. The equilibrium tetrahedral geometry of the CH_4 and CF_4 molecules has been held fixed throughout the scans (r(C-H)=1.089 Å, r(C-F)=1.330 Å). In this work, we have investigated two different approaches of the Ne, Ar, Kr, and Xe rare gases to CH_4 and CF_4: perpendicular to one of the faces of the CH_4 and CF_4 tetrahedra (referred to as "facial approach" hereafter), and along the vertex of the tetrahedra and collinear to a C–X (X=H,F) bond ("vertex approach"). Note that both approaches are C_{3v}-symmetric.

The electronic Schrödinger equation has been solved at each step of the scans using second-order Möller-Plesset perturbation theory in combination with the double, triple, and quadruple-zeta family of correlation-consistent basis sets of Dunning,[21–23] augmented with diffuse functions (aug-cc-pVDZ, aug-cc-pVTZ, aug-cc-pVQZ, respectively). In the case of Xe, we have also used correlation-consistent basis sets, but relativistic effects are introduced in the basis set through small-core pseudopotentials as implemented in the aug-cc-pVNZ-PP (N=D,T,Q) basis sets of Peterson et al.[24,25] Coupled cluster calculations with explicit single and double excitations, and perturbative treatment of triple excitations (CCSD(T)) have also been carried out with the aug-cc-pVDZ basis set. The focal-point approach of Allen and co-workers[19,20] has been used to estimate CCSD(T) energies with the aug-cc-pVTZ and aug-cc-pVQZ basis sets. (Hereafter, we refer to the focal-point CCSD(T) energies as fp-CCSD(T).) The focal-point approach is based on the observation that the difference between MP2 and CCSD(T) energies is essentially independent of the basis set for high-quality basis sets. Therefore, if the differences between MP2 and CCSD(T) energies are calculated with an affordable basis set (e.g., aug-cc-pVDZ) for a variety of intermolecular geometries, those differences can be used to estimate CCSD(T) energies with larger basis sets (e.g., aug-cc-pVTZ, aug-cc-pVQZ) from MP2 calculations (fp-CCSD(T) data). The legitimacy of this approach is examined in detail later in Section 4.2.4.

Complete basis set (CBS) estimates are obtained for both MP2 and fp-CCSD(T) calculations using the two-point extrapolation procedure of Halkier et al.[26] The equation employed for this extrapolation is:

$$E_{CBS} = \frac{4^3 E_{QZ} - 3^3 E_{TZ}}{4^3 - 3^3} \tag{4.1}$$

where E_{QZ} and E_{TZ} refer to the MP2 or fp-CCSD(T) calculated energies using the aug-cc-pVQZ and aug-cc-pVTZ basis sets, respectively. We have removed the basis-set superposition error using the standard counterpoise method[27] in all of the points of the calculated potential-energy surfaces. The electronic structure calculations have been carried out with the Gaussian03[28] and PSI3[29] suites of programs.

4.2.2. Ab initio intermolecular potentials for Ne, Ar, Kr, Xe–CH_4

Figure 4.1 shows the intermolecular energy of the Ne–CH_4 system as a function of the rare-gas–hydrocarbon separation as predicted by various ab initio methods. Included in

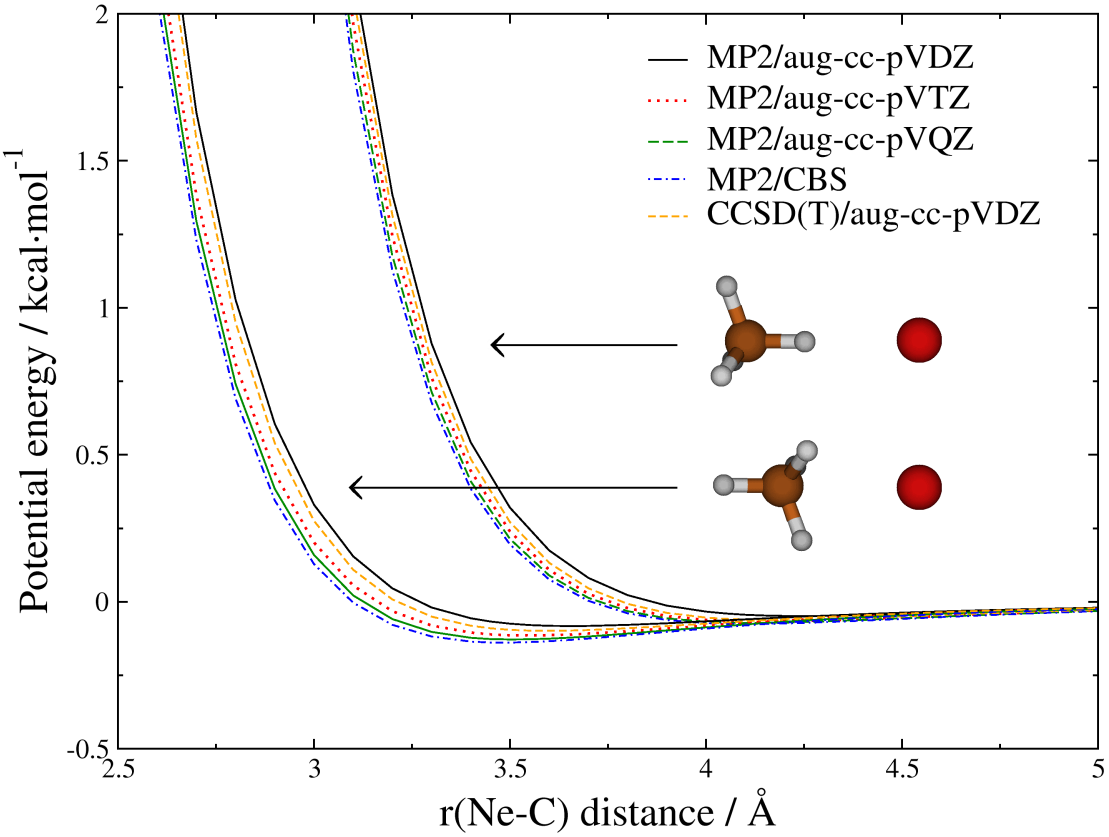

FIG. 4.1: Calculated intermolecular potential energy for the Ne–CH_4 system as a function of the Ne–C distance. MP2/CBS corresponds to the complete basis-set limit estimate based on MP2 energies.

the figure are both the facial and vertex approaches. The intermolecular potential-energy curves show the prototypical features of the interaction between two non-polar closed-shell species: a steep wall at short distances due to the repulsive overlap of electronic clouds, and a shallow well at longer separations due to weak, stabilizing dispersion interactions. The figure clearly shows that the locations of the repulsive walls for both approaches are different. As expected, the direct overlap of the electronic densities of Ne and a hydrogen atom that occurs in the vertex approach pushes the repulsive wall to Ne–C distances ∼0.4 Å longer than in the case of the facial approach. With respect to the van der Waals wells occurring at larger separations, Figure 4.1 shows that the well along the facial approach is notably deeper than along the vertex approach. This result seems independent of the calculation method.

A close examination of the dependence of the Ne–CH_4 intermolecular potential on the

basis set reveals that, for MP2 calculations, increases in the size of the basis set result in lower intermolecular energies (see Figure 4.1). In addition, the location of the well occurs at shorter Ne–C distances with larger basis sets. The MP2 energy curves with different basis sets do not cross, which enables use of extrapolation procedures to obtain a complete basis-set estimate. As expected from the polynomial convergence of MP2 energies with the size of the basis set, the difference between the aug-cc-pVDZ and aug-cc-pVTZ energies is larger than between aug-cc-pVTZ and aug-cc-pVQZ data. In terms of root-mean-square deviations (RMSD), while the RMSD between MP2/aug-cc-pVDZ and aug-cc-pVTZ energies is 0.24 kcal·mol^{-1} for the overall 50 points calculated along the facial and vertex approaches, the RMSD between aug-cc-pVTZ and aug-cc-pVQZ data diminishes to 0.10 kcal·mol^{-1}.

As mentioned above, we have also calculated the intermolecular potential-energy curves for the six rare-gas–hydrocarbon systems considered in this work using the CCSD(T) method with the aug-cc-pVDZ basis set. These calculations are helpful in learning the effect of the electronic-correlation treatment considered in the electronic-structure calculations on the characteristics of the calculated potential-energy surfaces. Remarkably, the differences between MP2 and CCSD(T) data in the Ne–CH_4 calculations are minor throughout the range of energies explored in this work. These small differences can be quantified by the RMSD between the MP2/aug-cc-pVDZ and CCSD(T)/aug-cc-pVDZ sets of energies, which is 0.05 kcal·mol^{-1}. The CCSD(T) and MP2 intermolecular potential-energy curves do not cross in the energy range studied, and at a given Ne–C separation, the CCSD(T) value is always below the MP2 estimate. Further examination of the MP2 and CCSD(T) curves indicates that the differences between these two methods are particularly small in the region of the the minima. For instance, MP2 predicts that the well depth along the facial approach is only 0.02 kcal·mol^{-1} deeper than the CCSD(T) estimate. A summary of the location and depths of the minima along the facial and vertex approaches as predicted by various methods is shown in Tables 4.1 and 4.2, respectively. Our best estimate of the depth and location of the Ne–CH_4 absolute minimum (0.161 kcal·mol^{-1}, r(Ne-C)=3.45 Å at the fp-CCSD(T)/CBS level, where CBS stands for complete basis-set limit) is in excellent agreement with earlier calculations of Gao et al.,[30] which used fourth order Möller-Plesset (MP4) perturbation theory (0.169 kcal·mol^{-1}, r(Ne-C)=3.5 Å). Previous molecular-beam experiments on the Ne–CH_4 system estimated that the well depth and location of the van der Waals well are 0.13 kcal·mol^{-1} and r(Ne-C)=3.78 Å, respectively.[31] In these experiments, the approach

TABLE 4.1: Energy and geometry of the van der Waals minimum along the facial approach in rare-gas–CH_4, CF_4 systems.[a]

	MP2/ADZ	MP2/ATZ	MP2/AQZ	MP2/CBS	CCSD(T)/ADZ	fp-CCSD(T)/ATZ	fp-CCSD(T)/AQZ	fp-CCSD(T)/CBS
Ne-CH_4	0.082(3.65)	0.114(3.55)	0.128(3.50)	0.139(3.50)	0.099(3.60)	0.135(3.50)	0.150(3.45)	0.161(3.45)
Ar-CH_4	0.282(3.85)	0.361(3.70)	0.397(3.70)	0.425(3.65)	0.265(3.85)	0.340(3.75)	0.375(3.70)	0.401(3.70)
Kr-CH_4	0.332(3.95)	0.437(3.85)	0.489(3.80)	0.529(3.80)	0.302(4.00)	0.400(3.90)	0.449(3.85)	0.488(3.80)
Xe-CH_4	0.378(4.25)	0.518(4.10)	0.587(4.05)	0.642(4.00)	0.339(4.25)	0.468(4.10)	0.533(4.05)	0.584(4.05)
Ne-CF_4	0.135(3.65)	0.189(3.50)	0.210(3.50)	0.226(3.45)	0.164(3.60)	0.225(3.45)	0.248(3.45)	0.265(3.45)
Ar-CF_4	0.338(3.95)	0.462(3.80)	0.519(3.75)	0.564(3.75)	0.331(3.95)	0.451(3.80)	0.508(3.80)	0.552(3.75)
Kr-CF_4	0.370(4.15)	0.524(4.00)	0.605(3.95)	0.669(3.90)	0.353(4.15)	0.501(4.00)	0.578(3.95)	0.639(3.90)
Xe-CF_4	0.390(4.40)	0.582(4.20)	0.682(4.15)	0.763(4.10)	0.366(4.40)	0.547(4.25)	0.643(4.15)	0.719(4.10)

TABLE 4.2: Energy and geometry of the van der Waals minimum along the vertex approach in rare-gas–CH_4, CF_4 systems.[a]

	MP2/ADZ	MP2/ATZ	MP2/AQZ	MP2/CBS	CCSD(T)/ADZ	fp-CCSD(T)/ATZ	fp-CCSD(T)/AQZ	fp-CCSD(T)/CBS
Ne-CH_4	0.048(4.25)	0.067(4.15)	0.072(4.10)	0.075(4.10)	0.061(4.15)	0.083(4.05)	0.089(4.05)	0.093(4.05)
Ar-CH_4	0.172(4.40)	0.219(4.30)	0.240(4.25)	0.256(4.20)	0.172(4.40)	0.219(4.30)	0.240(4.25)	0.256(4.25)
Kr-CH_4	0.205(4.55)	0.273(4.40)	0.303(4.35)	0.326(4.35)	0.199(4.55)	0.265(4.40)	0.294(4.35)	0.317(4.35)
Xe-CH_4	0.239(4.75)	0.335(4.55)	0.374(4.50)	0.405(4.50)	0.227(4.75)	0.319(4.60)	0.358(4.55)	0.387(4.50)
Ne-CF_4	0.070(4.60)	0.102(4.45)	0.112(4.45)	0.120(4.40)	0.085(4.55)	0.120(4.40)	0.131(4.40)	0.139(4.40)
Ar-CF_4	0.188(4.85)	0.250(4.75)	0.274(4.70)	0.293(4.70)	0.185(4.85)	0.246(4.75)	0.269(4.70)	0.288(4.70)
Kr-CF_4	0.209(5.00)	0.287(4.90)	0.323(4.85)	0.350(4.85)	0.202(5.05)	0.277(4.90)	0.311(4.85)	0.335(4.85)
Xe-CF_4	0.228(5.25)	0.324(5.10)	0.371(5.05)	0.408(5.00)	0.217(5.30)	0.308(5.10)	0.355(5.05)	0.391(5.05)

[a] Energies below the asymptote in kcal·mol^{-1}. Values between parentheses correspond to the rare-gas–C distance in Å. ANZ (N=D,T,Q) refers to the aug-cc-pVNZ (N=D,T,Q) basis sets. CBS stands for complete basis-set limit.

of Ne to CH_4 is not controlled. The reported depth and location of the well is therefore expected to be an average of the minima in all of the possible approaches of Ne to CH_4. A tentative comparison between theory and experiment should thus consider an average of theoretical values. Averaging the fp-CCSD(T)/CBS values of the minima along the facial and vertex approaches, we obtain a well depth of 0.127 kcal·mol^{-1} at r(Ne-C)=3.75 Å, which give remarkable reproduction of experimental values.

In Figure 4.2(b), we show the interaction potential in the minima region for the Ar–CH_4 system calculated by various levels of theory. For the Ar–CH_4 system, we have also included in Figure 4.2(a) a wide view to better display the repulsive region of the potential energy curves. As seen with Ne, the direct overlap of the electronic densities of Ar and hydrogen in the vertex approach pushes the repulsive wall to Ar–C distances ∼0.4 Å longer than in the facial approach. Both the Ar–CH_4 and –CF_4 repulsive walls occur at larger distances than seen with Ne, due to the larger van der Waals radius of Ar compared to Ne. This in turn affects the location of the minimum wells. The van der Waals wells occur at larger separations than with Ne, and Figure 4.2(b) shows that for Ar, just as for Ne, the well along the facial approach is notably deeper than along the vertex approach.

We see similar dependencies of the potential with the calculation method as described with Ne: larger basis sets give deeper van der Waals wells at shorter separation distances. The RMSD between MP2/aug-cc-pVDZ and aug-cc-pVTZ energies is 0.77 kcal·mol^{-1} overall along the facial and vertex approaches, with the RMSD between aug-cc-pVTZ and aug-cc-pVQZ data diminishing to 0.21 kcal·mol^{-1}. As with Ne, the differences between MP2 and CCSD(T) data in the Ar–CH_4 calculations are minor, with an RMSD value between the MP2/aug-cc-pVDZ and CCSD(T)/aug-cc-pVDZ energies of 0.19 kcal·mol^{-1}. Again, the CCSD(T) and MP2 intermolecular potential-energy curves do not cross in the energy range studied. Interestingly, however unlike the Ne–CH_4 system, the CCSD(T) values are always above the MP2 values throughout the energy range. The differences between these two methods are particularly small in the region of the the minima. where MP2 predicts that the well depth along the facial approach is only 0.02 kcal·mol^{-1} deeper than the CCSD(T) estimate.

A summary of the location and depths of the minima along the facial and vertex approaches as predicted by various methods is shown in Tables 4.1 and 4.2, respectively. Our best estimate of the depth and location of the Ar–CH_4 absolute minimum (0.402

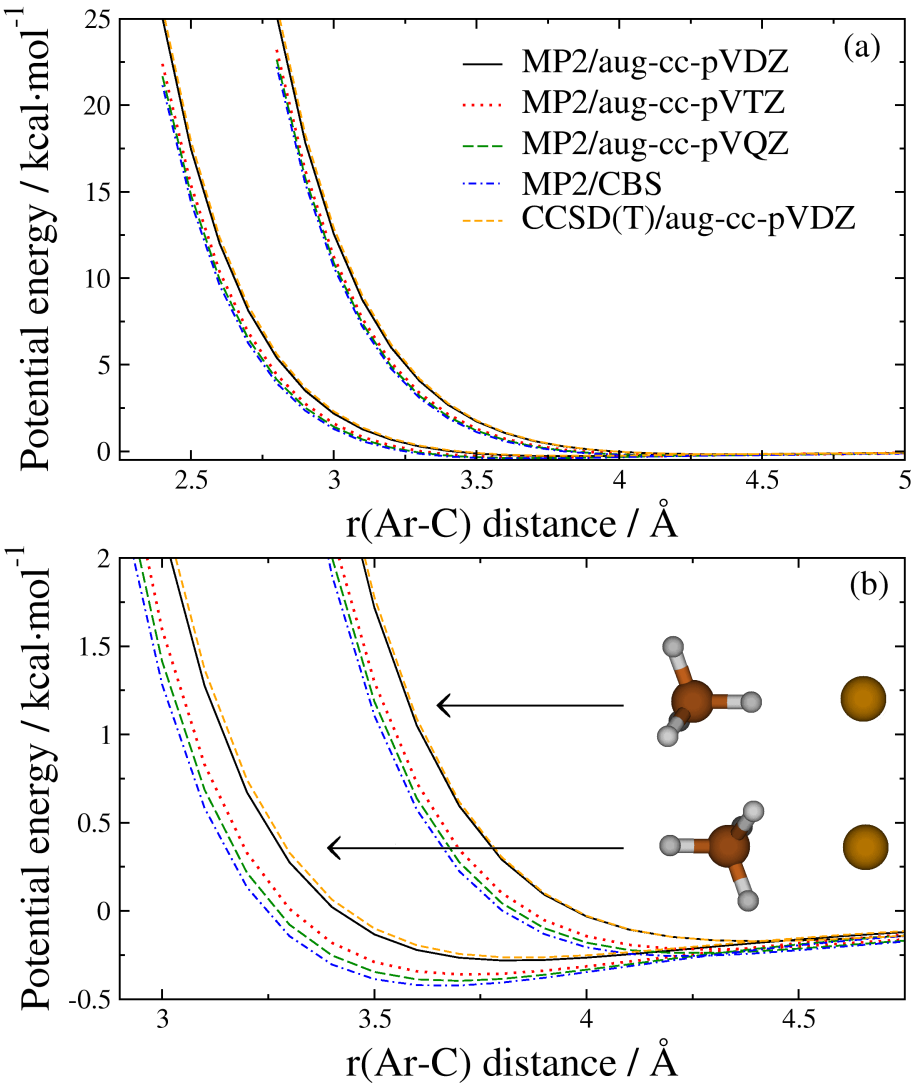

FIG. 4.2: Calculated intermolecular potential energy for the Ar–CH_4 system as a function of the Ar–C distance. (a) Full-energy range; (b) minimum region. MP2/CBS corresponds to the complete basis-set limit estimate based on MP2 energies.

kcal·mol^{-1}, r(Ar-C)=3.70 Å at the fp-CCSD(T)/CBS level, where CBS stands for complete basis-set limit) is in excellent agreement with earlier calculations by Heijmen et al.,[32] which used symmetry-adapted perturbation theory (0.41 kcal·mol^{-1}, r(Ar-C)=3.7 Å). Previous molecular-beam experiments estimated that the well depth and location of the van der Waals well are 0.32 kcal·mol^{-1} and r(Ar-C)=3.88 Å, respectively.[31] As was done when comparing the Ne–CH_4 potentials to experiment, we compare the experimental data to an average of our theoretical values, since the approach of Ar to CH_4 is not controlled in the experiment. Averaging the fp-CCSD(T)/CBS values of the minima along the facial and vertex

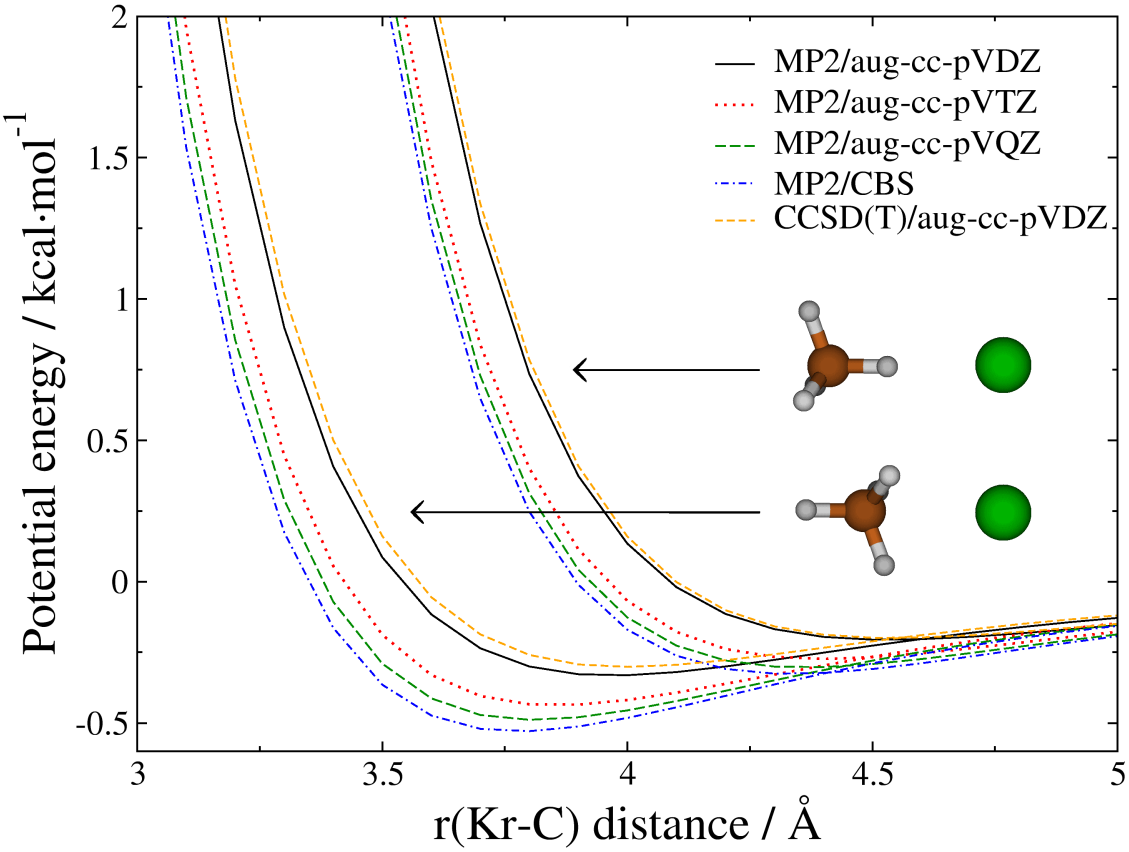

FIG. 4.3: Calculated intermolecular potential energy for the Kr–CH_4 system as a function of the Kr–C distance. MP2/CBS corresponds to the complete basis-set limit estimate based on MP2 energies.

approaches yields a well depth of 0.33 kcal·mol^{-1} at r(Ar-C)=3.98 Å, which satisfactorily reproduce experiments.

Figure 4.3 shows the interaction potential in the minima region for the Kr–CH_4 system calculated at different levels of theory. The trends in the dependence of the potential with the calculation method are analogous to those described before for Ar–CH_4: larger basis sets result in deeper wells with shorter rare-gas–CH_4 distances. The RMSD between MP2/aug-cc-pVDZ and aug-cc-pVTZ results is 0.77 kcal·mol^{-1}, decreasing to 0.22 kcal·mol^{-1} between the MP2/aug-cc-pVTZ and aug-cc-pVQZ data sets. The figure also shows the comparison between MP2 and CCSD(T) calculations with the aug-cc-pVDZ basis set. The differences between these methods are also minor (RMSD=0.19 kcal·mol^{-1}), with the CCSD(T) intermolecular potential energy curve being above the MP2 (as seen with Ar) one throughout the energy range explored (from the asymptote up to ∼20 kcal·mol^{-1}).

The depth and geometry of the minima along the facial and vertex approaches are listed in Table 4.1 and 4.2, respectively. The data in the tables indicate that the stabilizing interactions of CH_4 with Kr are slightly stronger than with Ar. Our best estimate (fp-CCSD(T)/CBS) yields wells that are 0.09 and 0.06 kcal·mol^{-1} deeper for Kr than for Ar along the facial and vertex approaches, respectively. Moreover, a comparison of the rare-gas–C distance at the energy minima along the facial and vertex approaches suggests that the van der Waals radius of Kr is about 0.1 Å larger than that of Ar. Our fp-CCSD(T)/aug-cc-pVTZ estimates of the depth and location of the well along the facial approach (0.449 kcal·mol^{-1} r(Kr-C)=3.85 Å) agree well with earlier full CCSD(T)/aug-cc-pVTZ calculations (0.451 kcal·mol^{-1}, r(Kr-C)=3.85 Å).[33] In addition, the averages of our best estimate for the depth and location of the van der Waals wells along the facial and vertex approaches (0.402 kcal·mol^{-1}, r(Kr-C)=4.08 Å) are in agreement with the values determined from previous molecular-beam experiments (0.39 kcal·mol^{-1}, r(Kr-C)=4.02 Å).[31]

Figure 4.4 shows the interaction potential in the region of the van der Waals wells for the Xe–CH_4 system calculated at different levels of theory. As one would expect, the dependency of the potential on the calculation method is just as that for Ar– and Kr–CH_4, with larger basis sets leading to deeper wells at shorter rare-gas–CH_4 distances. The RMSD between MP2/aug-cc-pVDZ-PP and aug-cc-pVTZ-PP results is 0.78 kcal·mol^{-1}, and, as for the other systems, the RMSD decreases substantially between MP2/aug-cc-pVTZ-PP and aug-cc-pVQZ-PP calculations (0.34 kcal·mol^{-1}). In addition to basis set comparison, the figure also illustrates the differences between the MP2 and CCSD(T) methods with the aug-cc-pVDZ-PP basis. As seen in the other rare gas potentials, these differences are small (RMSD=0.27 kcal·mol^{-1}), with the MP2 potential curve located below the CCSD(T) curve throughout the energy range of interest (up to ∼20 kcal·mol^{-1}).

Depth and location of the energy minima along the facial and vertex approaches are listed in Tables 4.1 and 4.2, respectively. The indication is that the Xe–CH_4 interaction is even more strongly stabilizing than that of Kr over Ar. Our best calculations yield wells that are 0.32, 0.18, and 0.09 kcal·mol^{-1} deeper than for Ne, Ar and Kr, respectively, with the facial approach, and 0.30, 0.13, and 0.07 kcal·mol^{-1} deeper in the vertex approach. Moreover, the Xe–C distance of the van der Waals well is 0.2 (0.3) [0.5] Å longer than that of Kr (Ar) [Ne]. We further note that our best estimates (fp-CCSD(T)/CBS) of the energy and location of the absolute minimum agree with very recent calculations at the CCSD(T) level using a

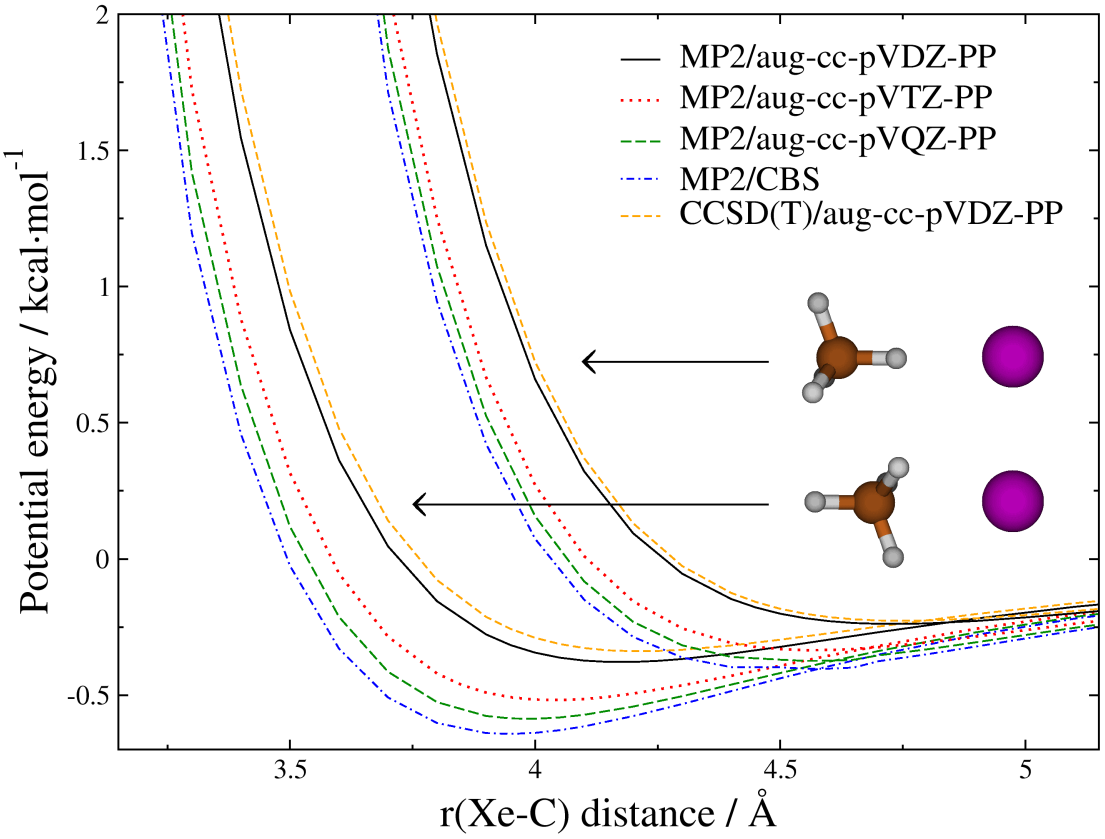

FIG. 4.4: Calculated intermolecular potential energy for the Xe–CH_4 system as a function of the Xe–C distance. MP2/CBS corresponds to the complete basis-set limit estimate based on MP2 energies.

basis set similar to those used here (0.53 kcal·mol^{-1}, r(Xe-C)=4.05 Å).[34] As with the Ar–CH_4 and Kr–CH_4 systems, the average of our best estimates of the energy and location of the absolute minimum (0.486 kcal·mol^{-1}, r(Xe-C)=4.28 Å) also agree with those obtained from molecular-beam scattering experiments (0.45 kcal·mol^{-1}, r(Xe-C)=4.24 Å).[31]

It should be noted that, although pseudopotentials are included within the basis sets utilized for xenon, these aug-cc-pnz-PP basis sets are expected to have similar accuracy to their aug-cc-pnz counterparts. We have tested this by calculating the same points for the intermolecular potential energy curve of Kr (for which both types of basis sets are available) approaching methane at the MP2 level utilizing both the aug-cc-pVTZ and aug-cc-pVTZ-PP basis sets along both the vertex and facial approaches. Geometries and depths of the van der Waals minima predicted by MP2/aug-cc-pVTZ (facial approach, 0.437 kcal·mol^{-1}, r(Kr-C)=3.85 Å; vertex approach, 0.273 kcal·mol^{-1}, r(Kr-C)=4.40 Å) are in excellent agreement

with those calculated via MP2/aug-cc-pVTZ-PP (facial, 0.443 kcal·mol^{-1}, r(Kr-C)=3.85 Å; vertex, 0.279 kcal·mol^{-1}, r(Kr-C)=4.40 Å). Only small differences exist between the MP2/aug-cc-pVTZ and aug-cc-pVTZ-PP curves. For the facial approach, the RMSD between the energies predicted by these two basis sets is 0.13 kcal·mol^{-1} for energies up to 20 kcal·mol^{-1}, and particularly good agreement is seen in the well region (RMSD=0.03 kcal·mol^{-1} for energies less than 2.0 kcal·mol^{-1}). Similar agreement is seen with the vertex approach (global RMSD=0.14 kcal·mol^{-1}, well RMSD=0.03 kcal·mol^{-1}). The differences between the aug-cc-pVTZ and aug-cc-pVTZ-PP basis sets are analogous for the Kr–CF_4 system, with a global RMSD of 0.10 (0.13) kcal·mol^{-1} for the facial (vertex) approach.

The small deviations in the potential energy surfaces between these basis sets confirms that the aug-cc-pVNZ and aug-cc-pVNZ-PP basis sets display similar levels of accuracy, lending validity to comparison between systems calculated with either basis. Figure 4.5(a) depicts a comparison of our best ab initio estimates (fp-CCSD(T)/CBS) of the intermolecular potential-energy curves for the X–CH_4 (X=Ne, Ar, Kr, Xe) pairs along the facial and vertex approaches. The figure shows that the well depths increase when going from Ne and Ar to Kr and Xe for both the facial and vertex approaches. In addition, the location of the wells and the repulsive walls occurs at longer rare-gas–C distances with increasing atomic number. This is the expected result of the larger van der Waals radius of Xe, with respect to Kr, Ar, and Ne.

4.2.3. Ab initio intermolecular potentials for Ne, Ar, Kr, Xe–CF_4

Recent experimental interest on scattering of rare gases from fluorinated organic surfaces[17] has motivated us to calculate the intermolecular potentials of the Ne, Ar, Kr, and Xe–CF_4 pairs with the goal of deriving analytical potential-energy functions for use in molecular dynamics simulations. For the sake of consistency, we have used the same level of theory in the ab initio calculations of these rare-gas–CF_4 systems as described above for the analogous rare-gas–CH_4 pairs. Nevertheless, it should be noted the larger number of valence electrons in the perfluorinated systems with respect to their hydrogenated counterparts entails a sharp increase in the computational expenditure required in the ab initio calculations. For instance, there is a roughly six-fold increase in the cpu time required for the calculation of one point of the Ar–CF_4 intermolecular potential-energy curve with respect to that for

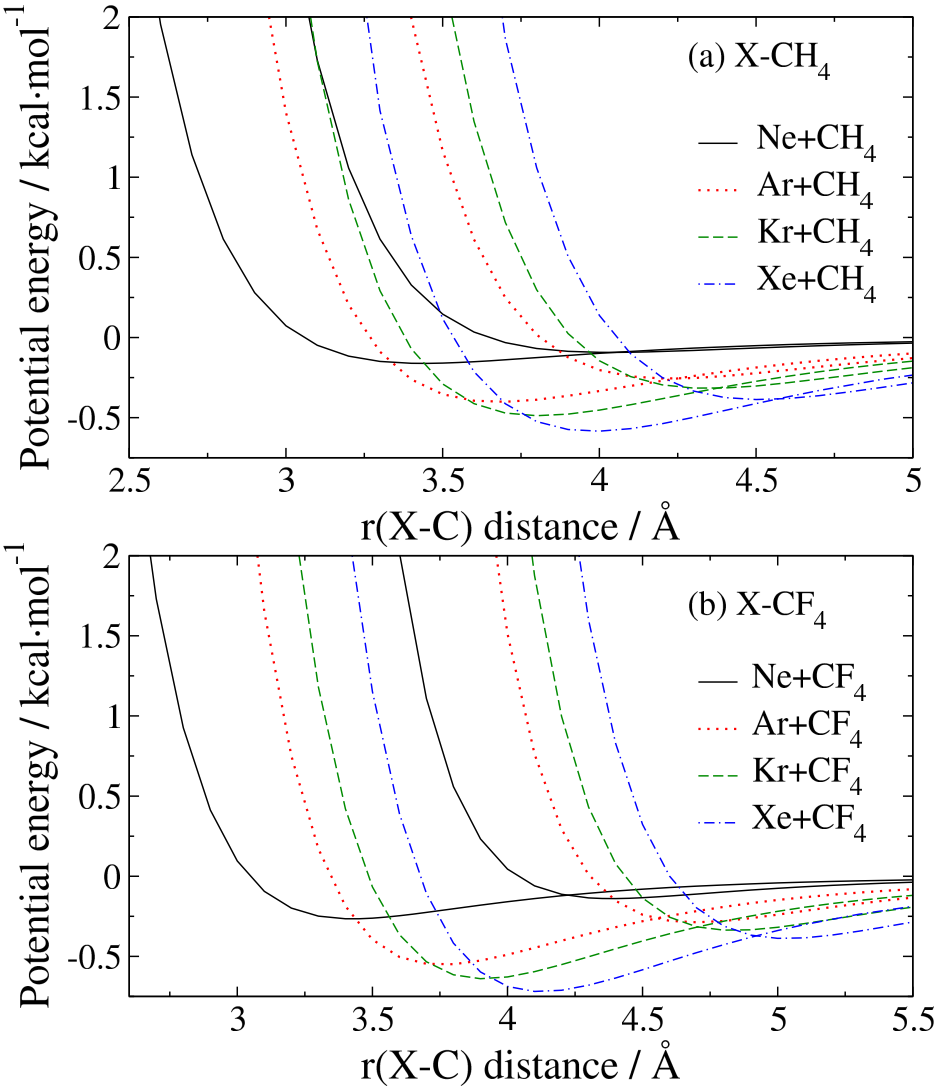

FIG. 4.5: Calculated fp-CCSD(T)/CBS intermolecular potentials for rare-gas–hydrocarbon (–fluorocarbon) pairs. (a) rare-gas–CH_4; (b) rare-gas–CF_4. In each graph, the curve whose repulsive wall occurs at longer rare-gas–C distances corresponds to the vertex approach of the rare gas to the hydrocarbon (fluorocarbon) and the other curve correponds to the facial approach.

Ar–CH_4 at the MP2 level with all three basis sets considered in this work.[35] The poorer scaling of the CCSD(T) method with the system size results in an ∼20-fold increase in the computation time when going from Ar–CH_4 to Ar–CF_4 and using the aug-cc-pVDZ basis set.

Figure 4.6 shows the intermolecular potential energy as a function of separation distance for the Ne–CF_4 system calculated at various levels of theory. The dependence of

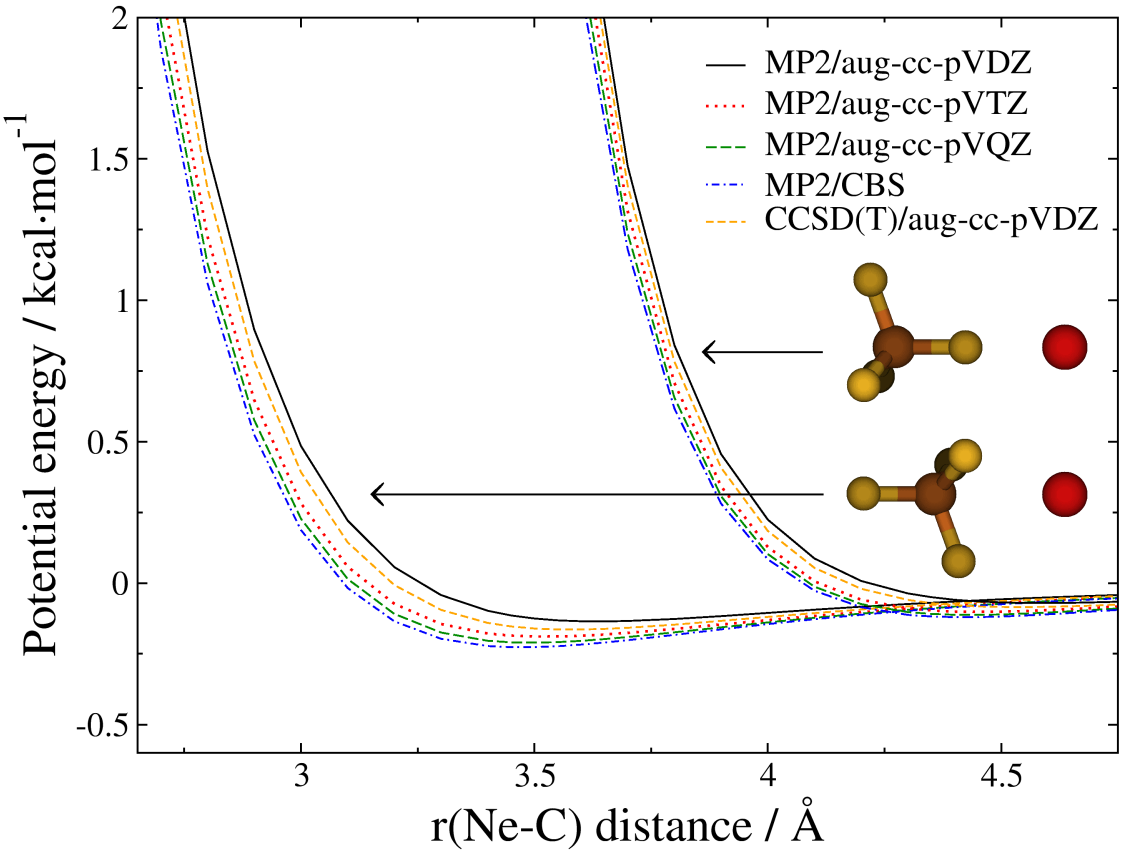

FIG. 4.6: Calculated intermolecular potential energy for the Ne–CF_4 system as a function of the Ne–C distance. (a) Full-energy range; (b) minimum region. MP2/CBS corresponds to the complete basis-set limit estimate based on MP2 energies.

the potential-energy curves on the method and basis set is just as for the Ne–CH_4 system. Larger basis sets give deeper van der Waals wells at shorter Ne–C distances. Increasing the basis set size seems to begin to quickly converge the MP2 energy. This is quantified by the RMSD values between various methods, as the 0.41 kcal·mol^{-1} deviation between the MP2/aug-cc-pVDZ and MP2/aug-cc-pVTZ levels decreases to 0.14 kcal·mol^{-1} between MP2/aug-cc-pVTZ and MP2/aug-cc-pVQZ. The differences between the CCSD(T) and MP2 methods with the aug-cc-pVDZ basis sets are minor, with a RMSD of 0.09 kcal·mol^{-1}. As was the case with Ne–CH_4, the MP2 energies do not cross and are always *above* the CCSD(T) estimates.

Figure 4.7 shows the dependence of the intermolecular potential energy on the separation distance for the Ar–CF_4 system along the facial and vertex approaches. As seen above with methane, the vertex approach is more repulsive than the facial approach. The

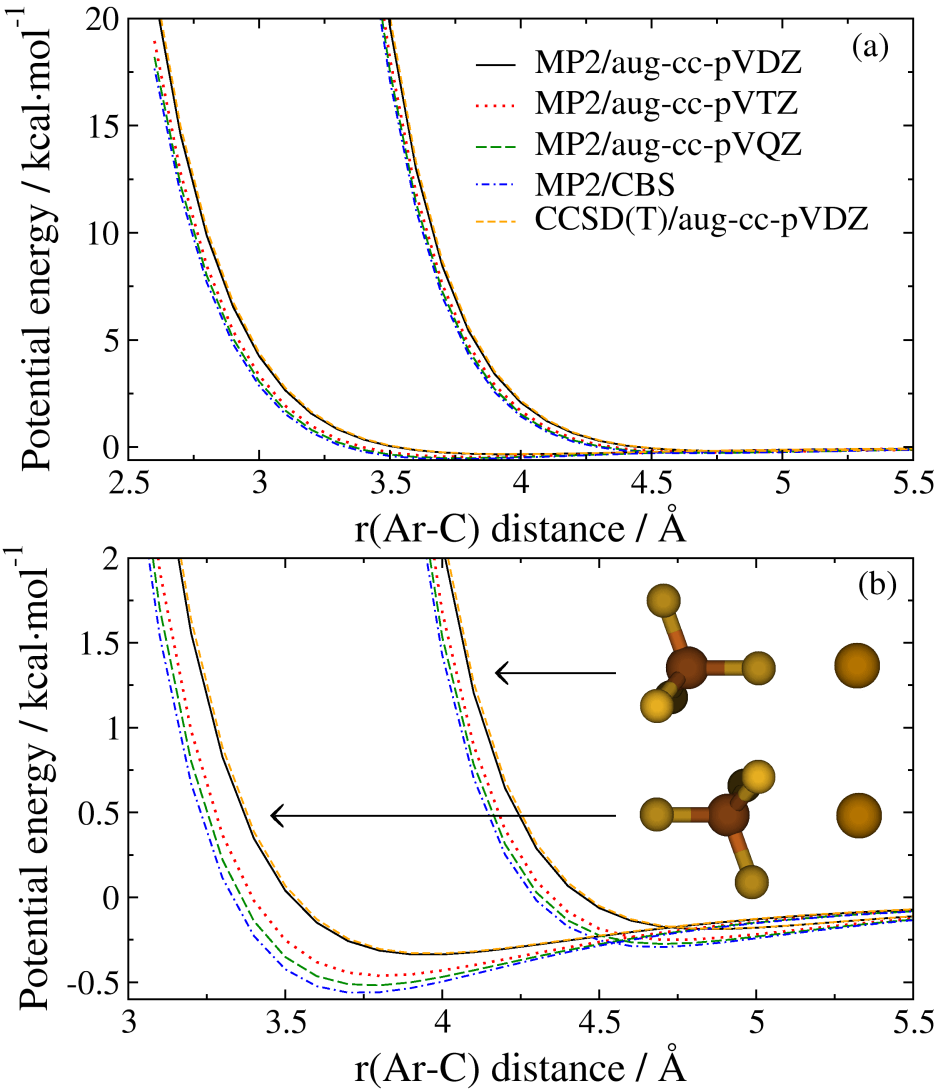

FIG. 4.7: Calculated intermolecular potential energy for the Ar–CF_4 system as a function of the Ar–C distance. (a) Full-energy range; (b) minimum region. MP2/CBS corresponds to the complete basis-set limit estimate based on MP2 energies.

dependence of the potential-energy curves on the basis set and ab initio method is also analogous to that seen for Ar–CH_4: use of larger basis sets results in deeper wells with shorter Ar–C distances for both the facial and vertex approaches. The RMSD deviation between MP2/aug-cc-pVDZ and aug-cc-pVTZ results (0.65 kcal·mol^{-1}) decreases by a factor of ∼3 (0.23 kcal·mol^{-1}) for the aug-cc-pVTZ/aug-cc-pVQZ sequence. Much as described above for the rare-gas–CH_4 pairs, a comparison between MP2 and CCSD(T) intermolecular energies with the aug-cc-pVDZ basis set reveals minor differences between both methods for

the Ar–CF_4 intermolecular potential-energy surfaces (RMSD=0.16 kcal·mol^{-1}). MP2 also overestimates the stabilization with respect to CCSD(T) predictions in the case of the fluorinated systems. All of these trends hold for the Kr–CF_4 and Xe–CF_4 systems, with the RMSD between MP2 and CCSD(T) calculations in Kr–CF_4 and Xe–CF_4 being 0.22 and 0.13 kcal·mol^{-1}, respectively. Further explicit description of the Kr– and Xe–CF_4 systems are not given here, but we display the analogous intermolecular potential energy curves in Figures 4.8 and 4.9.

Hase and coworkers have recently calculated the Ar–CF_4 intermolecular potential-energy surface with electronic-structure methods similar to those employed in this work.[36] In that paper, the minima along the vertex and facial approaches were calculated at the CCSD(T)/CBS level. Our calculations using the focal-point approach quantitatively reproduce the prior calculations. For the facial (vertex) approach, the CCSD(T)/CBS and fp-CCSD(T)/CBS well depths are 0.558 (0.295) kcal·mol^{-1} and 0.552 (0.288) kcal·mol^{-1}, respectively. The excellent agreement between CCSD(T) and fp-CCSD(T) results lends confidence to the legitimacy of the focal-point approach. A critical assessment of the quality of the focal-point approach for rare-gashydrocarbon potential-energy surfaces will be presented later.

Figure 4.5(b) shows our best estimates of the intermolecular potential-energy surfaces for the Ar, Kr, and Xe–CF_4 pairs along the facial and vertex approaches. The trends are identical to those discussed above for the rare-gas–CH_4 systems. A direct comparison between the well depths of the rare-gas–CH_4 and rare-gas–CF_4 systems can be seen in Figure 4.10 for both the facial and vertex approaches, as well as a third, "edge", approach (described in Section 4.3, below). The data displayed in the figure clearly show that the absolute minimum in the intermolecular potential is deeper by about 0.15 kcal·mol^{-1} for the rare-gas–CF_4 pairs than for rare-gas–CH_4 pairs. Interestingly, the calculations show a linear increase in well depth with the atomic number of the rare gas for both rare-gas–CH_4 and rare-gas–CF_4 systems. In addition, the rate of increase of the well depth with the rare-gas atomic number is analogous for the CH_4 and CF_4 pairs along the facial and edge approaches.

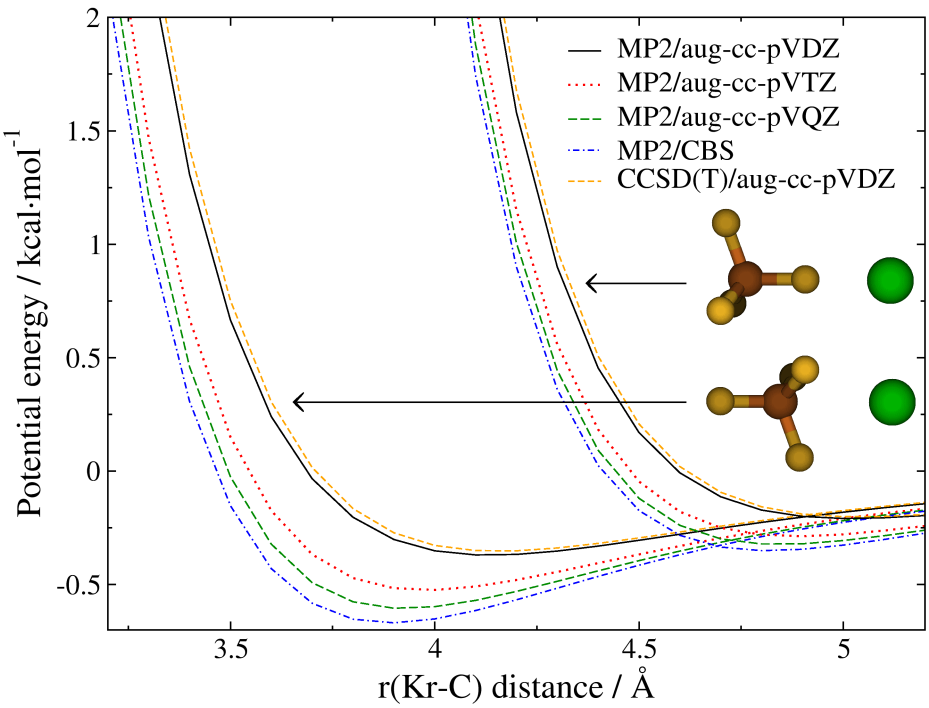

FIG. 4.8: Calculated intermolecular potential energy for the Kr–CF_4 system as a function of the Kr–C distance. MP2/CBS corresponds to the complete basis-set limit estimate based on MP2 energies.

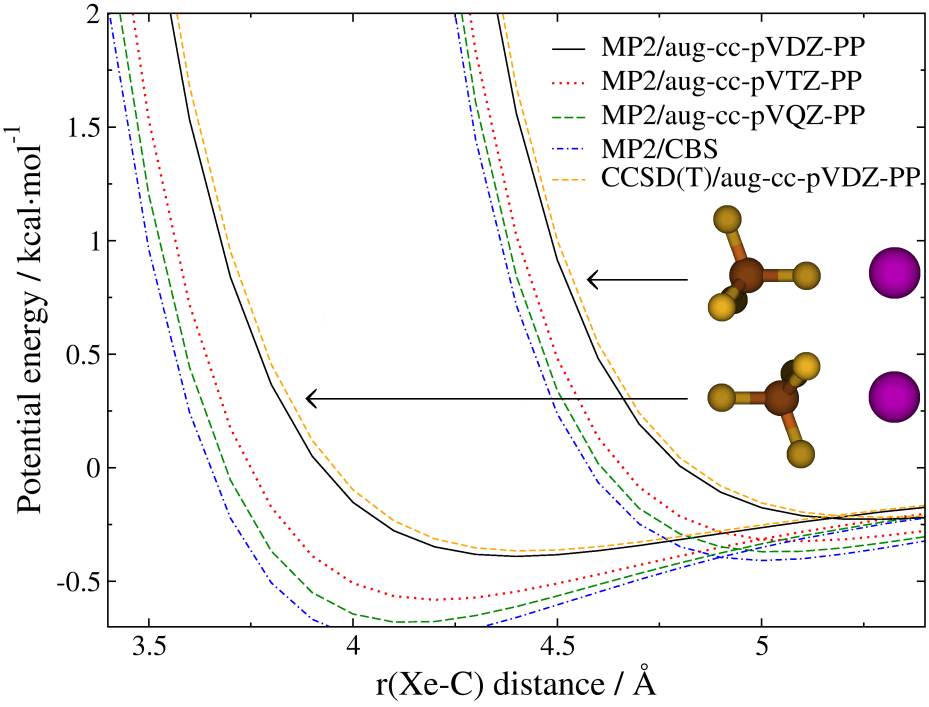

FIG. 4.9: Calculated intermolecular potential energy for the Xe–CF_4 system as a function of the Xe–C distance. MP2/CBS corresponds to the complete basis-set limit estimate based on MP2 energies.

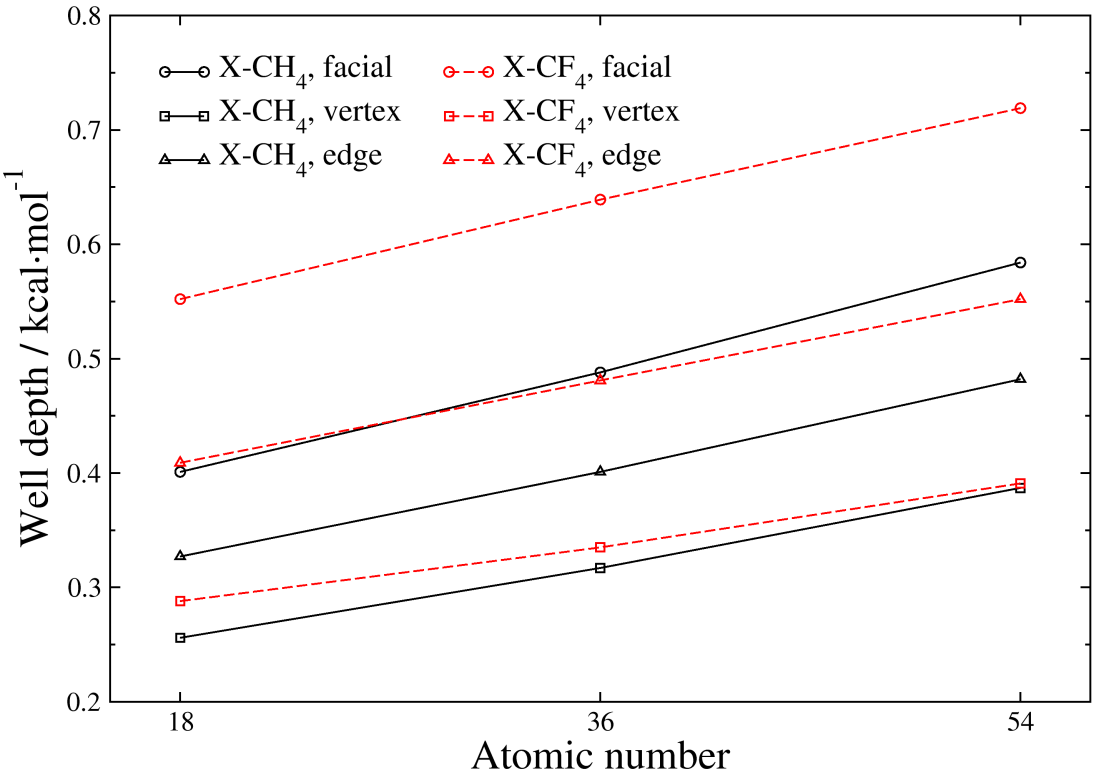

FIG. 4.10: van der Waals well depths in approaches of Ne, Ar, Kr, and Xe to CH_4 and CF_4 as a function of rare gas atomic number. The numerical values for the various approaches correspond to the fp-CCSD(T)/CBS estimates. The "edge" approach is described in Section 4.3, below.

4.2.4. The legitimacy of the focal-point approach

In this section, we examine the adequacy of the focal-point approach of Allen and co-workers[19,20] to estimate CCSD(T) energies from MP2 calculations for rare-gas–CX_4 (X=H,F) pairs.

We have verified the legitimacy of the focal-point approach by comparing the intermolecular potential-energy curves estimated at the fp-CCSD(T)/aug-cc-pVTZ level with full calculations at the CCSD(T)/aug-cc-pVTZ level for the Ar–CH_4 and Kr–CH_4 systems. In the case of Ar–CH_4, the RMSD between CCSD(T)/aug-cc-pVTZ and fp-CCSD(T)/aug-cc-pVTZ energies is 0.04 kcal·mol^{-1} for the overall 50 points calculated along the facial and vertex approaches. These points cover energies up to 20 kcal·mol^{-1}. For energies below 2.0 kcal·mol^{-1}, the deviation reduces to 0.01 kcal·mol^{-1} (37 ab initio points). Figure 4.11(a) displays a direct comparison between fp-CCSD(T) and CCSD(T) energies for Ar–CH_4. The

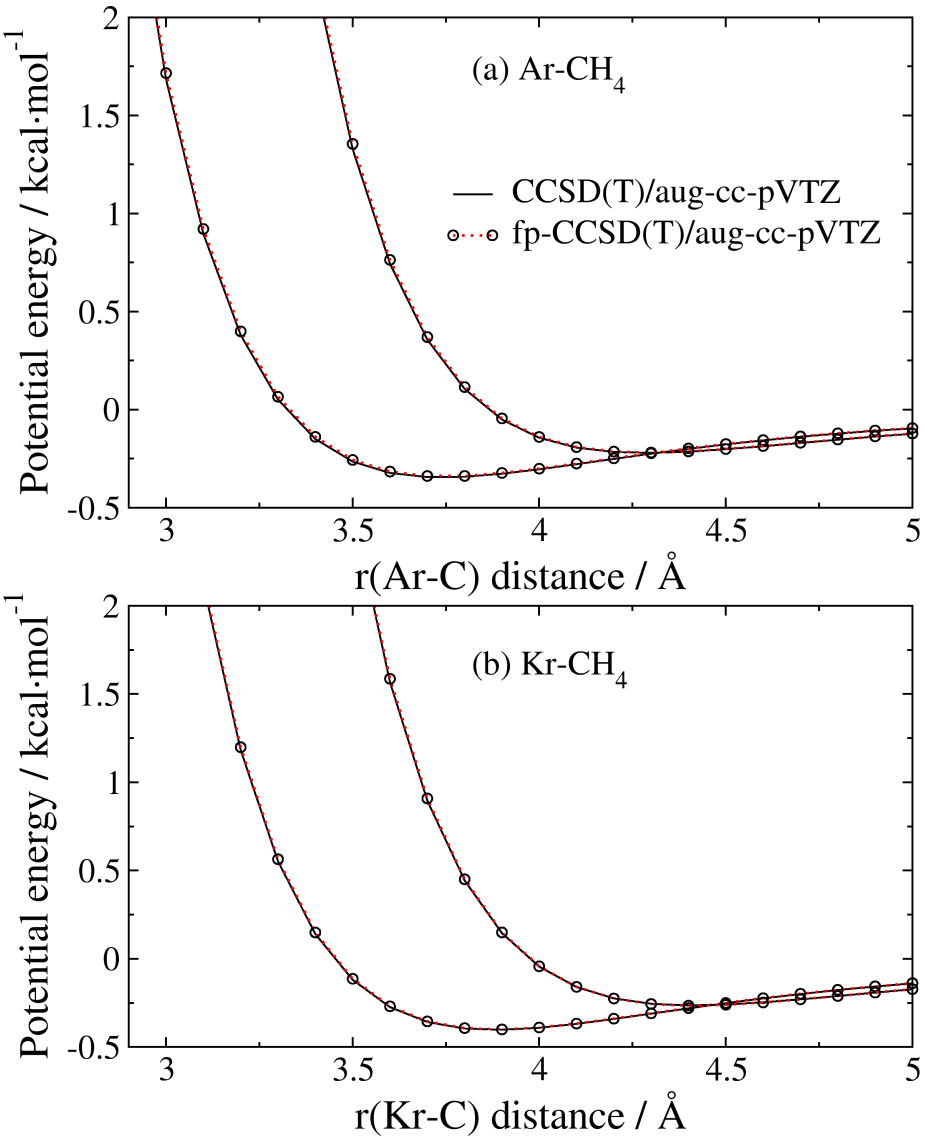

FIG. 4.11: Comparison of CCSD(T) and fp-CCSD(T) data for the facial and vertex approaches of (a) Ar and (b) Kr to CH_4. The calculations have been performed with the aug-cc-pVTZ basis set. In each figure, the curve whose repulsive wall occurs at longer rare-gas–C distances corresponds to the vertex approach of the rare gas to the hydrocarbon and the other curve corresponds to the facial approach.

figure clearly shows that for the minimum region, the error introduced by the focal-point approach is negligible.

For Kr–CH_4, the overall RMSD between fp-CCSD(T) and CCSD(T) energies with the aug-cc-pVTZ basis set is 0.03 kcal·mol^{-1} for the 48 ab initio points calculated for energies up to 20 kcal·mol^{-1}. As with Ar–CH_4, the RMSD reduces to 0.01 kcal·mol^{-1} for energies

below 2.0 kcal·mol^{-1}. This region of the intermolecular potential-energy surface is displayed in Figure 4.11(b).

The remarkably small differences between fp-CCSD(T) and CCSD(T) energies for a large number of configurations substantiate the legitimacy of the focal-point approach in this study. This is important because the focal-point approach results in tremendous savings in the computational time required to obtain accurate intermolecular energies. For instance, although three calculations are required in estimating the fp-CCSD(T)/aug-cc-pVTZ energies (MP2/aug-cc-pVDZ, CCSD(T)/aug-cc-pVDZ, and MP2/aug-cc-pVTZ), the combined time to obtain this fp-CCSD(T)/aug-cc-pVTZ estimate is ∼10 times smaller than a full CCSD(T)/aug-cc-pVTZ calculation for Ar–CH_4.[35] The computational savings increase for larger basis sets. Thus, the calculation of fp-CCSD(T)/aug-cc-pVQZ estimates requires ∼15 times less computer time than full CCSD(T)/aug-cc-pVQZ calculations for Ar–CH_4.

The focal-point approach is particularly advantageous for systems involving many heavy atoms, such as rare-gas–CF_4 systems. CCSD(T) calculations with the aug-cc-pVQZ basis set are so demanding for these systems that obtaining many points of the intermolecular potential-energy surface is prohibitive at this time. On the other hand, since the bottleneck in obtaining the fp-CCSD(T)/aug-cc-pVQZ estimate is in the MP2/aug-cc-pVQZ calculation, the focal-point approach enables mapping of the potential-energy surface in a timely manner. Quantitatively, for Ar–CF_4, the calculation of the fp-CCSD(T)/aug-cc-pVTZ estimate is ∼17 times faster than the full CCSD(T)/aug-cc-pVTZ calculation. In the case of a aug-cc-pVQZ basis set, a full CCSD(T) single-point energy calculation takes ∼65 times longer than the combined cpu time of the three calculations involved in obtaining the fp-CCSD(T) estimate.

4.2.5. The effect of a dipole: Ne, Ar, Kr, Xe + CH_3CH_3, CH_3CF_3, CF_3CH_3, CF_3CF_3 ab initio intermolecular potentials

One of the advantages of using self-assembled monolayers as models of organic surfaces is that one can vary the exposed terminus of the surface using organic synthesis techniques. The ability to build a variety of organic surfaces with similar structure but different chemical groups at the surface terminus offers great opportunities to investigate how the chemical and physical properties of the exposed groups influence the interfacial characteristics of

the organic surface. For instance, although ω,ω,ω-trifluoroalkanethiol SAMs (S-$(CH_2)_n$-CF_3) and fully hydrogenated alkanethiol SAMs have similar structures, their interfacial properties appear to be quite different due to the fact that the exposed groups are -CF_3 and -CH_3, respectively. Extensive work by Lee and co-workers[37–39] indicates that S-$(CH_2)_n$-CF_3 SAMs interact more strongly with water than S-$(CH_2)_n$-CH_3 SAMs. This behavior has been rationalized as due to the presence of a dipole at S-$(CH_2)_n$-CF_3 SAM terminus emerging from the charge separation in the CH_2-CF_3 moiety.[40] Recent molecular-beam experiments by Day et al. have studied the scattering dynamics of Ar, Kr, and Xe from S-$(CH_2)_n$-CH_3 and S-$(CH_2)_n$-CF_3 SAMs.[17] Unsurprisingly, the scattering properties are different for the two SAMs, but the origin of the distinct behavior of the S-$(CH_2)_n$-CH_3 and S-$(CH_2)_n$-CF_3 SAMs is still not fully understood. Three main factors might affect the scattering dynamics of rare gases from these surfaces. First, the collision kinematics are different, with the exposed CF_3 groups of the S-$(CH_2)_n$-CF_3 SAM being more massive than the exposed CH_3 groups of the regular SAM. Second, the interactions within the SAM at the terminus are different. Third, the rare-gas–SAM intermolecular potentials are different. Regarding the change in the intermolecular potentials, we have seen in previous sections that the van der Waals wells in rare-gas–CF_4 systems are $\sim$0.15 kcal·mol^{-1} deeper than in rare-gas–CH_4 systems. An added complication of S-$(CH_2)_n$-CF_3 SAMs is the presence of a dipole at the SAM terminus, which might alter significantly the intermolecular potential.

To shed light on the possibility that a dipole moment at the surface terminus might enhance the attraction between the approaching polarizable rare gas and the surface, we have investigated how rare gases interact with model organic molecules that possess an electric dipole along the carbon backbone. MP2 calculations with the aug-cc-pVDZ and aug-cc-pVTZ basis sets and CCSD(T) calculations with the aug-cc-pVDZ basis set have been used to map the intermolecular potential-energy curves for approaches of Ne, Ar, Kr, and Xe to ethane, perfluoroethane, and 1,1,1-trifluoroethane. Note that the 1,1,1-trifluoroethane molecule is a model of S-$(CH_2)_n$-CF_3 SAMs.

As in the methane and fluoromethane studies above, we have scanned the rare-gas–molecule coordinate from the asymptote to energies up to about 20 kcal·mol^{-1}. The typical separation between scan points is 0.1 Å, with a finer scan of 0.05 Å used for determination of the potential well. During the scan, the hydrocarbon (fluorocarbon) geometry was held fixed in the lowest-energy anti conformation, with equilibrium bond lengths as stated above,

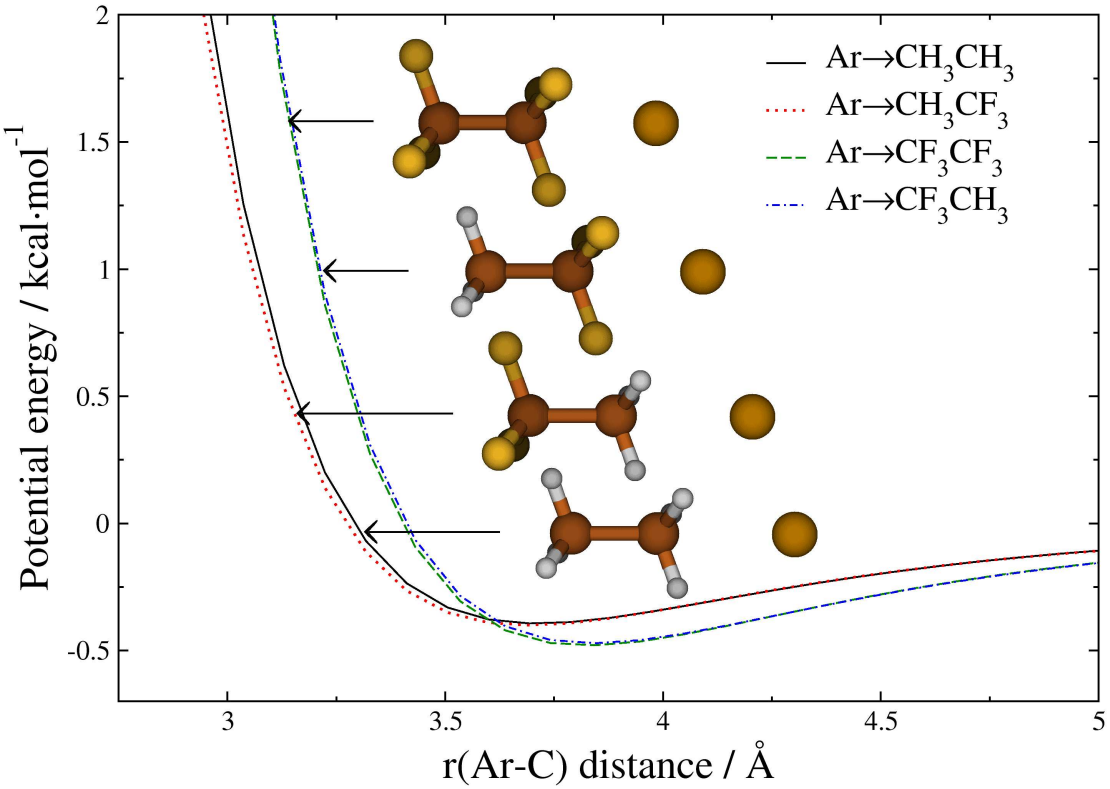

FIG. 4.12: Intermolecular potential-energy profiles for Ar in facial approaches to ethane, 1,1,1-trifluroethane, and perfluoroethane. Energies correspond to fp-CCSD(T)/aug-cc-pVTZ data.

and with the C-C bond set to 1.450 Å. The rare gas approaches collinearly to the C-C bond. Approaches to both the fluorine and hydrogen faces were scanned for the rare-gas–CH_3CF_3 pairs. All of the data presented here correspond to fp-CCSD(T)/aug-cc-pVTZ estimates.

The resulting fp-CCSD(T)/aug-cc-pVTZ potential-energy curves for the Ar systems are shown in Figure 4.12. The Ar–CH_3CF_3 curve shows an almost negligible deviation from the Ar–CH_3CH_3 curve. While the differences between the two intermolecular potential-energy curves are generally small (the RMSD for intermolecular energies up to ∼20 kcal·mol^{-1} is 0.14 kcal·mol^{-1}), the overlap between both systems is particularly remarkable in the well region (the RMSD for energies less than 2.0 kcal·mol^{-1} is 0.04 kcal·mol^{-1}). An analogous trend is found when comparing the Ar–CF_3CF_3 and Ar–CF_3CH_3 curves (global RMSD=0.03 kcal·mol^{-1}; RMSD=0.02 kcal·mol^{-1} for energies below 2.0 kcal·mol^{-1}). The locations and depths of the van der Waals minima for these and the analogous Ne, Kr and Xe systems are summarized in Table 4.3. The intermolecular potential-energy curves for the pairs involving Ne, Kr, and Xe (not shown) display similar behavior to that of the Ar systems.

TABLE 4.3: Effect of the presence of a dipole in the hydrocarbon backbone on energy and geometry of van der Waals minimum in rare-gas–CX_3CY_3 (Rg=Ne, Ar, Kr, Xe; X, Y=H, F) systems.[a]

	Ne	Ar	Kr	Xe
Rg-CH_3CH_3	0.15 (3.45)	0.39 (3.70)	0.47 (3.85)	0.55 (4.05)
Rg-CH_3CF_3	0.17 (3.45)	0.40 (3.70)	0.47 (3.85)	0.55 (4.05)
Rg-CF_3CF_3	0.23 (3.50)	0.48 (3.80)	0.54 (4.00)	0.59 (4.25)
Rg-CF_3CH_3	0.22 (3.50)	0.47 (3.85)	0.54 (4.00)	0.60 (4.20)

[a]Energies below the asymptote in kcal·mol^{-1}. Values between parentheses correspond to the rare-gas–nearest C atom distance in Å. The ab initio data correspond to fp-CCSD(T)/aug-cc-pVTZ values.

In addition to electronic structure calculations, the extent of the dipole effect can be estimated by calculating the magnitudes of the various attractive interactions between the rare gas and hydrocarbon species. For the systems under study here, the most important of these interactions are dipole-induced dipole interactions and dispersion interactions. Using the dipole-induced dipole energy expression as formulated by Debye,[41] the attraction of two interacting species, only one of which has a permanent dipole, is

$$V_{Debye} = -\frac{\sigma_i \mu_j^2}{(4\pi\epsilon_o)^2}\frac{1}{r_{ij}^6} \tag{4.2}$$

where μ_j is the dipole moment of the species with a permanent dipole, σ_i is the polarizability of the species lacking a dipole, r_{ij} is the distance separating the two, and ϵ_o is the permittivity in vacuum. The Debye interaction can be compared to the theoretical treatment for dispersion interactions developed by London in 1930.[42] Under such formulation, the attractive region of the intermolecular potential between two non-polar species can be described by:

$$V_{London} = -\frac{3}{2}\frac{I_i I_j}{(I_i + I_j)}\frac{\sigma_i \sigma_j}{(4\pi\epsilon_o)^2}\frac{i}{r_{ij}^6} \tag{4.3}$$

where I_i is the first ionization energy of species i, σ_i is the polarizability of species i, and r_{ij} is the separation between the interacting species. Both the London and the Debye formulations have inverse r_{ij}^6 terms, so for purposes of comparison, we have simply calculated the coefficients of these terms. Using the experimental ionization potentials,[43] polarizabilities,[44–46] and dipole moments[43] of the rare gases and the CH_3CF_3 molecule we have found these coefficients to be $-r_{ij}^6 \cdot V_{London}$=4891.4, 1743.8, 2509.1, and 3774.0 Å^6·kcal·mol^{-1} for the CH_3CF_3

interaction with Ne, Ar, Kr, and Xe, respectively, while $-r_{ij}^6 \cdot V_{Debye}$=29.53, 126.32, 192.19, and 310.76 Å^6·kcal·mol^{-1} for the same systems. These results indicate that the dispersion term heavily dominates the attractive region of the potential energy surface, as the size of the dipole-induced dipole contribution is more than an order of magnitude smaller that of the dispersion interaction.

As can be deduced from the data in Table 4.3 and Figure 4.12, as well as from comparisons of Debye and London theory, the presence of a dipole in the hydrocarbon backbone has no appreciable effect on the characteristics of the potential-energy surfaces of the examined systems. The difference in well depth for each pair of dipole/no-dipole systems (i.e., CH_3CF_3 vs. CH_3CH_3 and CF_3CH_3 vs.CF_3CF_3) is less than 0.01 kcal·mol^{-1} in all cases, and the well locations agree within the size of the scan step (0.05 Å). Even with Xe's almost three-fold increase in polarizablility over that of Ar, the hydrocarbon dipole has negligible influence on the PES. These results are important in the analysis of the experimental scattering dynamics of rare gases from S-$(CH_2)_n$-CH_3 and S-$(CH_2)_n$-CF_3 SAMs because they suggest that the presence of a dipole in the terminus of the S-$(CH_2)_n$-CF_3 SAMs will have only a minor effect on the intermolecular potential-energy surface. Therefore, the differences in the scattering dynamics of rare gases from S-$(CH_2)_n$-CH_3 and S-$(CH_2)_n$-CF_3 SAMs are likely dictated by the change in the intermolecular potential due to fluorination, the change in the interactions within the SAM, and kinematic factors.

4.3. ANALYTIC POTENTIAL-ENERGY SURFACES

A leading goal of this work is to obtain analytic potential-energy surfaces for rare-gas/hydrocarbon (fluorocarbon) systems that can be used in molecular dynamics simulations of rare-gas/organic-surface collisions. In this section, we describe the derivation of pair-wise analytic potentials for the Ne–CH_4, Ar–CH_4, Kr–CH_4, Xe–CH_4, Ne–CF_4, Ar–CF_4, Kr–CF_4, and Xe–CF_4 pairs using ab initio data at the fp-CCSD(T)/CBS level.

We note that although the discussion of the electronic structure calculations has focused solely on the facial and vertex approaches, additional points along a third approach ("edge approach") of the rare gas to the molecules have been included in the derivation of analytical potential-energy surfaces. In the C_{2v}-symmetric edge approach, the rare-gas exactly bisects an X-C-X (X=H,F) angle. Geometries of the CH_4 and CF_4 molecules are held fixed with

bond lengths as defined above, and the rare-gas–C distance is scanned in 0.1 Å steps, except at the minimum region, where we use a 0.05 Å scan step. Overall, general trends seen in the facial and vertex approach hold for the edge approach, which gives intermediate values between those of the facial and vertex approaches for location and depth of the van der Waals well minima for all systems. The repulsive wall is also between that of the facial and edge approaches. A full summary of the depth and geometry of the minima for the edge approach is listed in Table 4.4 for all six rare-gas–hydrocarbon (–flurocarbon) pairs studied in this work. These results reproduce earlier calculations by Sun et al. for Ar–CH_4[47]

The analytic potential-energy surfaces are constructed as a sum of two-body functions, where each two-body term is expressed as a Buckingham potential of the form:

$$V_{ij} = A_{ij}e^{-B_{ij}r_{ij}} + \frac{C_{ij}}{r_{ij}^6} \tag{4.4}$$

where A_{ij}, B_{ij}, and C_{ij} are adjustable parameters, and rij is the internuclear distance between the rare gas and the atoms of the hydrocarbon (fluorocarbon) molecule. We have used a non-linear least-squares procedure to obtain the values of the parameters A_{ij}, B_{ij}, and C_{ij} that minimize the differences between analytic energies obtained with the Buckingham potentials and the fp-CCSD(T)/CBS data.

The two-body Buckingham potentials provide good representation of the ab initio data in all cases. In terms of root-mean-square deviations, the total RMSD between the analytic and ab initio data are 0.33, 0.30, 0.43, 0.33, 0.40, 0.33, 0.30, and 0.26 kcal·mol^{-1} for the Ne–CH_4, Ar–CH_4, Kr–CH_4, Xe–CH_4, Ne–CF_4, Ar–CF_4, Kr–CF_4, and Xe–CF_4 systems, respectively. Each of the fits considers a total of about 75 points distributed roughly evenly between the facial, vertex, and edge approaches, and covering regions of the potential-energy surface from the asymptote to energies of up to ∼20 kcal·mol^{-1}. It should be noted that, in the fit, particular emphasis was given to the description of well region by giving points in the well region increased weight during the fit. All points with intermolecular energies below 2.0 kcal·mol^{-1} were weighted by factors of 15.0, 5.0, 7.0, 10.0, 15.0, 10.0, 5.0, and 10.0 for the Ne–CH_4, Ar–CH_4, Kr–CH_4, Xe–CH_4, Ne–CF_4, Ar–CF_4, Kr–CF_4, and Xe–CF_4 systems, respectively. These weights were selected to minimize the RMSD in the well region, while maintaining good agreement in the global fit and restricting fitted parameters to physically meaningful values. Therefore, the RMSD between analytic and ab initio energies for points corresponding to the region of the van der Waals wells is much smaller than the global

TABLE 4.4: Energy and geometry of the van der Waals minimum along the edge approach in rare-gas–CH_4, CF_4 systems.[a]

	MP2/ADZ	MP2/ATZ	MP2/AQZ	MP2/CBS	CCSD(T)/ADZ	fp-CCSD(T)/ATZ	fp-CCSD(T)/AQZ	fp-CCSD(T)/CBS
Ne-CH_4	0.062(3.90)	0.089(3.80)	0.100(3.75)	0.108(3.70)	0.076(3.85)	0.107(3.70)	0.119(3.70)	0.127(3.70)
Ar-CH_4	0.219(4.10)	0.287(3.95)	0.316(3.90)	0.339(3.85)	0.208(4.00)	0.277(3.95)	0.305(3.90)	0.327(3.90)
Kr-CH_4	0.259(4.20)	0.349(4.05)	0.392(4.00)	0.425(3.95)	0.240(4.20)	0.327(4.10)	0.368(4.05)	0.401(4.00)
Xe-CH_4	0.298(4.40)	0.418(4.25)	0.475(4.20)	0.520(4.15)	0.272(4.40)	0.386(4.30)	0.439(4.25)	0.482(4.20)
Ne-CF_4	0.093(4.00)	0.134(3.90)	0.152(3.90)	0.167(3.80)	0.113(4.00)	0.160(3.80)	0.181(3.80)	0.197(3.80)
Ar-CF_4	0.251(4.30)	0.344(4.15)	0.384(4.15)	0.416(4.10)	0.248(4.30)	0.339(4.15)	0.379(4.15)	0.409(4.10)
Kr-CF_4	0.278(4.50)	0.394(4.35)	0.453(4.25)	0.500(4.25)	0.267(4.50)	0.380(4.35)	0.436(4.30)	0.481(4.25)
Xe-CF_4	0.302(4.70)	0.444(4.55)	0.519(4.50)	0.581(4.45)	0.285(4.70)	0.421(4.55)	0.493(4.50)	0.552(4.45)

[a] Energies below the asymptote in kcal·mol^{-1}. Values between parentheses correspond to the rare-gas–C distance in Å. ANZ (N=D,T,Q) refers to the aug-cc-pVNZ (N=D,T,Q) basis sets. CBS stands for complete basis-set limit.

TABLE 4.5: Parameters of the analytic rare-gas/hydrocarbon (fluorocarbon) pair-wise Buckingham potentials.[a]

	Rare-gas/CH_3-SAM				Rare-gas/CF_3-SAM		
	A	B	C		A	B	C
Ne-H	5663.0	3.732	−77.664	Ne-F	93879.4	4.510	−128.869
Ne-C	147236.7	4.312	−158.838	Ne-C	3408.0	2.934	−297.301
Ar-H	11426.5	3.385	−374.119	Ar-F	118267.9	3.907	−579.357
Ar-C	96594.5	3.608	−356.575	Ar-C	31219.2	3.297	−230.926
Kr-H	13754.0	3.238	−621.784	Kr-F	124268.6	3.721	−872.830
Kr-C	112927.4	3.520	−268.460	Kr-C	44043.8	3.210	−304.523
Xe-H	18012.7	3.118	−1010.530	Xe-F	1000634.8	3.409	−1406.620
Xe-C	100460.4	3.285	−295.759	Xe-C	83822.2	3.268	−319.310

[a] Units are such that if internuclear distances are given in Å, then the potential energy is in kcal·mol^{-1}.

RMSD (the RMSD for intermolecular energies below 2.0 kcal·mol^{-1} is 0.06, 0.06, 0.07, 0.07, 0.07, 0.08, 0.07, and 0.06 kcal·mol^{-1} for the Ne–CH_4, Ar–CH_4, Kr–CH_4, Xe–CH_4, Ne–CH_4, Ar–CF_4, Kr–CF_4, Xe–CF_4 systems, respectively). The optimum parameters that minimize the differences between the analytic and ab initio energies for all of the systems investigated in this work are shown in Table 4.5.

A direct comparison between the analytic and ab initio data for all six rare-gas–hydrocarbon (–fluorocarbon) pairs studied in the work is displayed in Figure 4.13, and the location and depth of the van der Waals wells along the facial, vertex, and edge approaches are shown in Table 4.6.

The table shows that the rare-gas–hydrocarbon (fluorocarbon) separation at the minima furnished by the analytic potential-energy surfaces are in all cases within 0.1 Å of the fp-CCSD(T)/CBS estimates. The difference in energy between the analytic and ab initio wells is never larger than 0.06 kcal·mol^{-1}. These analytic potentials derived from high-accuracy ab initio calculations can readily be used in chemical dynamics simulations of collisions of rare gases with organic surfaces.

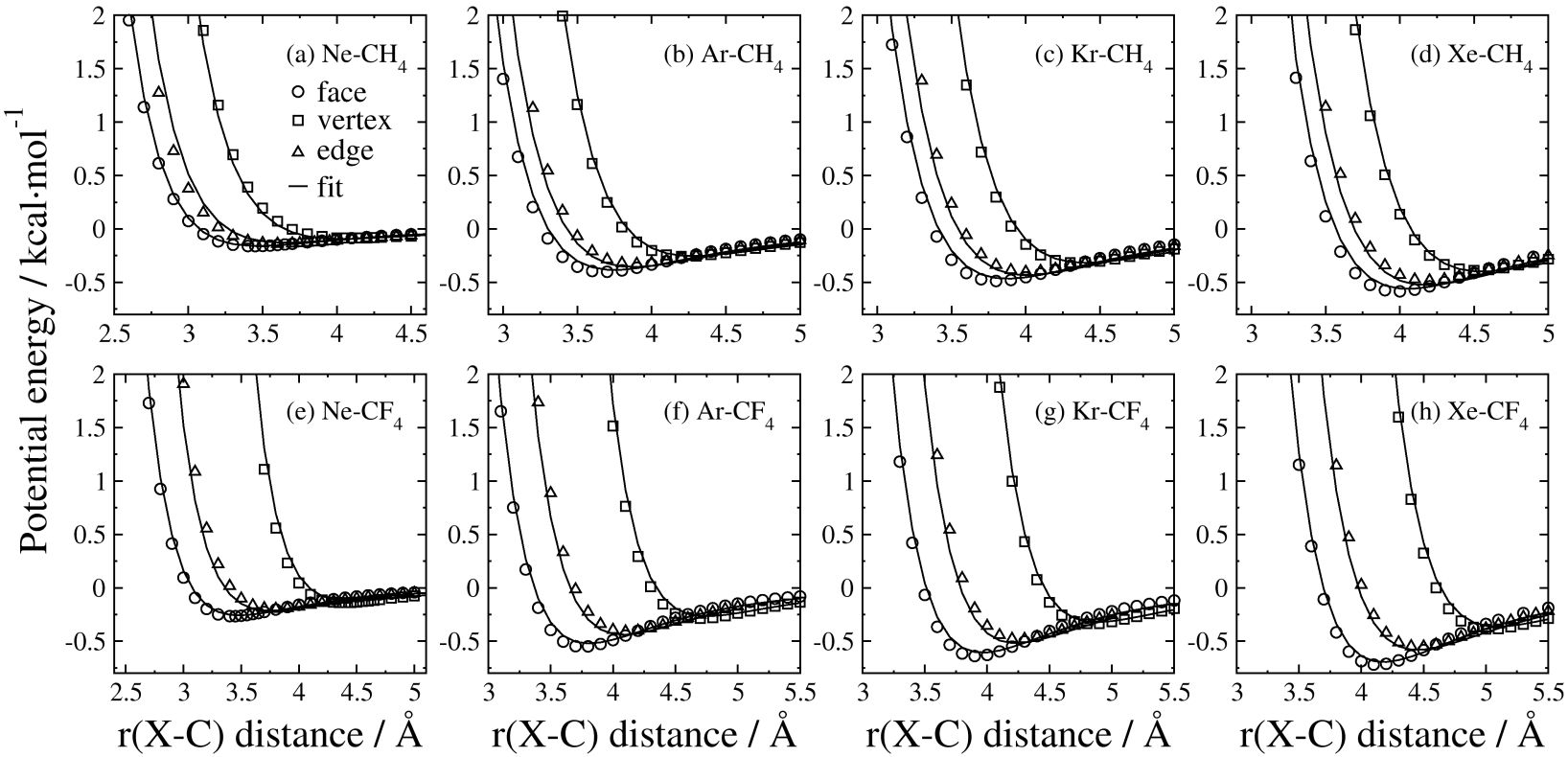

FIG. 4.13: Comparison of ab initio and analytic intermolecular potential-energy surfaces for the X–CY_4 pairs (X = Ne, Ar, Kr, Xe; Y = H, F). Ab initio values for each of the three approaches (facial, vertex, and edge) are indicated by open symbols and correspond to fp-CCSD(T)/CBS data. The corresponding fitted analytic values are shown as solid lines.

TABLE 4.6: Comparison of ab initio and analytic energy and geometry of the van der Waals minima along the facial, vertex, and edge approaches in rare-gas–hydrocarbon (fluorocarbon) systems.[a]

		Rg-CH_4			Rg-CF_4		
		facial	vertex	edge	facial	vertex	edge
Ne-CX_4	ab initio	0.16 (3.45)	0.09 (4.05)	0.13 (3.65)	0.27 (3.45)	0.14 (4.40)	0.20 (3.80)
	fit	0.16 (3.47)	0.09 (4.11)	0.14 (3.63)	0.26 (3.45)	0.12 (4.44)	0.21 (3.74)
Ar-CX_4	ab initio	0.40 (3.70)	0.26 (4.25)	0.33 (3.90)	0.55 (3.75)	0.29 (4.70)	0.41 (4.10)
	fit	0.38 (3.75)	0.25 (4.28)	0.36 (3.87)	0.52 (3.80)	0.27 (4.75)	0.44 (4.08)
Kr-CX_4	ab initio	0.49 (3.80)	0.32 (4.35)	0.40 (4.00)	0.64 (3.90)	0.33 (4.85)	0.48 (4.25)
	fit	0.47 (3.87)	0.32 (4.40)	0.43 (4.01)	0.61 (3.96)	0.32 (4.88)	0.52 (4.23)
Xe-CX_4	ab initio	0.58 (4.05)	0.39 (4.50)	0.48 (4.20)	0.72 (4.10)	0.39 (5.05)	0.55 (4.45)
	fit	0.56 (4.05)	0.40 (4.55)	0.53 (4.18)	0.70 (4.17)	0.36 (5.09)	0.58 (4.45)

[a]Energies below the asymptote in kcal·mol^{-1}. Values between parentheses correspond to the rare-gas–C distance in Å. The ab initio data correspond to fp-CCSD(T)/CBS values.

4.4. CONCLUDING REMARKS

We have carried out an extensive electronic-structure study of the interaction potentials between the Ne, Ar, Kr, and Xe rare gases and the CH_4 and CF_4 molecules. Our calculations using the MP2 and CCSD(T) methods in combination with correlation-consistent basis sets show that, as expected, both the van der Waals wells and the repulsive walls of the intermolecular potentials occur at longer rare-gas–hydrocarbon separations with increasing rare-gas atomic number. An interesting result of the calculations is that that the depths of the van der Waals wells increase linearly with the rare-gas atomic number. Fluorination of the hydrocarbon results in a slightly deeper van der Waals well along the facial approach, which occurs at longer rare-gas–molecule separations. Otherwise, the dependence of the potential-energy surface on the rare gas is analogous to that in the counterpart rare-gas–CH_4 systems. Investigation of the dependence of the intermolecular potential-energy curves on the ab initio level indicates that increasingly large basis sets lead to increased attraction between the approaching species, with MP2 calculations only slightly overestimating the attraction predicted by CCSD(T) in all six rare-gas–molecule pairs studied here.

We learn that the focal-point approach to estimate CCSD(T) energies from MP2 calculations works remarkably well for rare-gashydrocarbon systems. Use of this approximation enables attractive savings in the computational time required to obtain complete-basis set estimates at the CCSD(T) level.

Motivated by recent experiments on rare-gas/S-(CH_2)-CF3 SAM collisions, we have further calculated intermolecular potential-energy curves for the approach of the aforementioned rare gases to the CH_3CH_3, CH_3CF_3, and CF_3CF_3 molecules to learn whether a dipole at the terminus of the S-(CH_2)-CF_3 SAMs might affect the interactions between the rare gases and the surface. Our calculations at the fp-CCSD(T)/aug-cc-pVTZ level indicate that introducing a dipole in the hydrocarbon molecule has no tangible effect on the rare-gas/hydrocarbon potential-energy surfaces studied. Debye and London theories indicate that dispersion interactions dominate the attractive region of the potential energy surface, effectively swamping out influence of the dipole.

Using the ab initio information at the fp-CCSD(T)/CBS level, we have derived analytic potential-energy surfaces based on two-body Buckingham potentials. The analytic potentials accurately reproduce the ab initio data in all six rare-gas–hydrocarbon (–fluorocarbon) systems considered in this work.

In Chapter 5, we make use of the analytic potentials described in this chapter to simulate the scattering of rare gases from regular and fluorinated alkanethiol self-assembled monolayers.

REFERENCES

[1] D. M. Hirst, *Potential energy surfaces: molecular structure and reaction dynamics* (Taylor and Francis, London, 1985).

[2] J. N. Murrell, S. Carter, S. Frantos, P. Huxley, and A. J. C. Varandas, *Molecular potential energy functions* (John Wiley & Sons Inc., New York, 1984).

[3] S. L. Mielke, K. A. Peterson, D. W. Schwenke, B. C. Garrett, D. G. Truhlar, J. V. Michael, M.-C. Su, and J. W. Sutherland, Phys. Rev. Lett. **91**, 063201 (2003).

[4] M. E. Saecker, S. T. Govoni, D. V. Kowalski, M. E. King, and G. M. Nathanson, Science **252**, 1421 (1991).

[5] M. E. King, G. M. Nathanson, M. A. Hanning-Lee, and T. K. Minton, Phys. Rev. Lett. **70**, 1026 (1993).

[6] G. M. Nathanson, P. Davidovits, D. R. Wornsop, and C. E. Kolb, J. Phys. Chem. **100**, 13007 (1996).

[7] K. D. King, M. E. Fiehrer, G. M. Nathanson, and T. K. Minton, J. Phys. Chem. A **101**, 6556 (1997).

[8] S. R. Cohen, R. Naaman, and J. Sagiv, Phys. Rev. Lett. **58**, 1208 (1987).

[9] S. F. Shuler, G. M. Davis, and J. R. Morris, J. Chem. Phys. **116**, 9147 (2002).

[10] B. S. Day, G. M. Davis, and J. R. Morris, Anal. Chim. Acta **496**, 249 (2003).

[11] B. S. Day, S. F. Shuler, A. Ducre, and J. R. Morris, J. Chem. Phys. **119**, 8084 (2003).

[12] B. S. Day and J. R. Morris, J. Phys. Chem. B **107**, 7120 (2003).

[13] M. K. Ferguson, J. R. Lohr, B. S. Day, and J. R. Morris, Phys. Rev. Lett. **92**, 073201 (2004).

[14] K. D. Gibson, N. Isa, and S. J. Sibener, J. Chem. Phys. **119**, 13083 (2003).

[15] N. Isa, K. D. Gibson, and S. J. Sibener, J. Chem. Phys. **120**, 2417 (2004).

[16] K. D. Gibson, N. Isa, and S. J. Sibener, J. Phys. Chem. A **110**, 1469 (2005).

[17] B. S. Day and J. R. Morris, To be submitted (2006).

[18] M. R. Morris, J. Riederer, D. E., B. E. Winger, R. G. Cooks, T. Ast, and C. E. D. Chidsey, Int. J. Mass Spectron. Ion Processes **122**, 181 (1992).

[19] A. L. L. East and W. D. Allen, J. Chem. Phys. **99**, 4638 (1993).

[20] A. G. Csaszar, W. D. Allen, and H. F. Schaefer III, J. Chem. Phys. **108**, 9751 (1998).

[21] T. H. Dunning Jr., J. Chem. Phys. **90**, 1007 (1989).

[22] D. E. Woon and T. H. Dunning Jr., J. Chem. Phys. **98**, 1358 (1993).

[23] A. K. Wilson, D. E. Woon, K. A. Peterson, and T. H. Dunning Jr., J. Chem. Phys. **110**, 7667 (1999).

[24] K. A. Peterson, D. Figgen, E. Goll, H. Stoll, and M. Dolg, J. Chem. Phys. **119**, 11113 (2003).

[25] Basis sets were obtained from the Extensible Computational Chemistry Environment Basis Set Database, Version 02/25/04, as developed and distributed by the Molecular Science Computing Facility, Environmental and Molecular Sciences Laboratory which is part of the Pacific Northwest Laboratory, P.O. Box 999, Richland, Washington 99352, USA, and funded by the U.S. Department of Energy. The Pacific Northwest Laboratory is a multi-program laboratory operated by Battelle Memorial Institute for the U.S. Department of Energy under contract

DE-AC06-76RLO 1830.

[26] A. Halkier, T. Helgaker, P. Jorgensen, W. Klopper, H. Koch, J. Olsen, and A. K. Wilson, Chem. Phys. Lett. **286**, 243 (1998).

[27] S. F. Boys and F. Bernardi, Mol. Phys. **19**, 553 (1970).

[28] M. J. Frisch, G. W. Trucks, H. B. Schlegel, G. E. Scuseria, M. A. Robb, J. R. Cheeseman, J. A. Montgomery, Jr., T. Vreven, K. N. Kudin, J. C. Burant, et al., *Gaussian 03, revision c.02* (2004).

[29] T. D. Crawford, C. D. Sherrill, E. F. Valeev, J. T. Fermann, R. A. King, M. L. Leininger, S. T. Brown, C. L. Janssen, E. T. Seidl, J. P. Kenny, et al. (PSI 3.2, 2003).

[30] D. Gao, L. Chen, Z. Li, F.-M. Tao, and Y.-K. Pan, Chem. Phys. Lett. **277**, 483 (1997).

[31] G. Liuti, F. Pirani, U. Buck, and B. Schmidt, Chem. Phys. **126**, 1 (1988).

[32] T. G. A. Heijmen, T. Korona, R. Moszynski, P. E. S. Wormer, and A. van der Avoird, J. Chem. Phys. **107**, 902 (1997).

[33] Y. Liu and W. Jager, J. Chem. Phys. **120**, 9047 (2004).

[34] Q. Wen and W. Jager, J. Chem. Phys. **124**, 014301 (2006).

[35] The calculations involve the removal of basis set superposition error using the counterpoise method.

[36] G. Vayner, Y. Alexeev, J. Wang, T. L. Windus, and W. L. Hase, J. Phys. Chem. A **110**, 3174 (2006).

[37] Y. F. Miura, M. Takenaga, T. Koini, M. Graupe, N. Garg, J. Graham, R. L., and T. R. Lee, Langmuir **14**, 5821 (1998).

[38] M. Graupe, M. Takenaga, T. Koini, J. Colorado, R., and T. R. Lee, J. Am. Chem. Soc. **121**, 3222 (1999).

[39] J. Colorado, R. and T. R. Lee, Langmuir **19**, 3288 (2003).

[40] E. G. Shafrin and W. A. Zisman, J. Chem. Phys. **61**, 1046 (1957).

[41] P. Debye, Phys. Z. **21**, 178 (1920).

[42] F. London, Z. Phys. **63**, 245 (1930).

[43] *http://webbook.nist.gov/chemistry.*

[44] R. H. Orcutt and R. H. Cole, J. Chem. Phys. **46**, 697 (1967).

[45] T. M. Miller and B. Bederson, Adv. At. Mol. Phys. **13**, 1 (1977).

[46] The value used for the polarizability of CF_3CH_3 was obtained from MP2/aug-cc-pvtz calcula-

tions.

[47] L. Sun, P. de Sainte Claire, O. Meroueh, and W. L. Hase, J. Chem. Phys. **114**, 535 (2001).

Chapter 5

Experimental and theoretical studies of the effect of mass on the dynamics of gas/organic-surface energy transfer

Reproduced in part with permission from W. A. Alexander, B. S. Day, H. J. Moore, T. R. Lee, J. R. Morris, and D. Troya, *J. Chem. Phys.* **128**, 014713 (2008). Copyright 2008 American Institute of Physics.

5.1. INTRODUCTION

A detailed characterization of the collsion dynamics between gas-phase species and organic surfaces is essential to understanding the interfacial behavior of organic surfaces. Early molecular-beam scattering studies by the Nathanson group investigated the dynamics of energy transfer in collisions of atomic gases and small molecules (Ne, Ar, Xe, SF_6, CH_4, NH_3, and H_2O) with liquid organic surfaces.[1–4] They found the scattered gases' final translational-energy distributions to be bimodal, with a low-energy thermal desorption component well characterized by a Boltzmann distribution at or near the surface temperature. This low-energy component is attributed to collision events in which the gas traps for some time on the surface and eventually desorbs thermally. The high-energy component of the distribution is characterized by impulsive collision events in which the gas' brief encounter with the surface does not allow thermalization. The consensus in the field has since been that in most cases the dynamics of gas/organic-surface collisions can be understood as the competition between two main mechanisms: impulsive scattering and trapping desorption. While impulsive scattering is reminiscent of direct gas-phase collisions, trapping enables enhanced gas/surface energy transfer and allows for thermal accommodation of the gas on the surface.

Among the liquid surfaces investigated in the work of the Nathanson group are squalane (2,6,10,15,19,23-hexamethyltetracosane) and perfluoropolyether (PFPE). These two liquids served as models of hydrocarbon and fluorocabon surfaces, respectively. Comparison of the scattering properties of these two liquids revealed that gas/surface energy transfer depends critically on liquid composition, and only secondarily on the varying chemical and physical

properties of the probe gases.[1,2] Overall, the results show that energy transfer from the scattered gases to the squalane surface is more efficient than with the PFPE surface. Moreover, while an increase in projectile mass led to an increase in energy transfer, the underlying surface effects persisted.[2,4] Those efforts have further shown that energy transfer is insensitive to gas identity for gases with similar masses; high incident energy Ne, CH_4, NH_3, and H_2O give similar overall energy transfer profiles on the same organic surface.[3,4] Even SF_6, with 15 vibrational and three rotational modes available in which to deposit energy during collision, closely mimics the energy transfer behavior of Xe.[2]

More recently, the Nesbitt group, via high-resolution direct infrared absorption spectrometry and laser dopplerimetry techniques, have studied CO_2 scattering from the same squalane and PFPE liquid surfaces and their results agree well with the findings of the Nathanson group.[5] Final translational-energy distributions were well characterized by separation into thermal desorption and impulsive scattering components, and overall energy transfer from CO_2 to the squalane surface was found to be more efficient than transfer to PFPE. These experiments also showed that energy transfer in the impulsive scattering channel is highly efficient and nearly the same from both surfaces, despite differences in surface properties and a marked difference in overall energy transfer to the two surfaces.[5] This agrees well with the finding that thermal roughening of the surfaces does not alter energy transfer in impulsive events.[6]

Although the previous experiments indicate that the chemical and physical structure of the organic liquid affects gas/surface energy transfer, the independent effects of mass, structure, and chemical properties of the surface on the energy-transfer dynamics remain to be deciphered. The specific role of gas and surface masses has been an important component in understanding collision dynamics since the early developments of hard-cube models of gas-surface scattering.[7] The hard-cube model is based on the assumption that the component of the gas' momentum parallel to the surface is conserved during collsion. The perpendicular component of momentum is altered via and impulsive hard-wall collision with a cube vibrating at the surface temperature. Borne out from the model is the fact that energy transfer is maximal when the gas/surface mass ratio, $\mu = \frac{m_{gas}}{m_{surface}}$, equals one. Under the assumption of energy and momentum conservation, the fractional energy transfer to the surface for a normal incidence angle can be written as $\frac{\Delta E}{E_{coll}} = \frac{4\mu}{(\mu+1)^2}$, where ΔE is the change in energy of the gas, and E_{coll} is the incident gas energy. By fitting the value of the mass ratio, μ,

to experimental data this relationship has been used to obtain an "effective" surface mass, which gives some idea of the collective response of the surface in collisions. The hard-cubes model and its various extentions have been widely applied to describe experimentally observed trends in gas-surface scattering from metals and other inorganic surfaces.[8,9] While the model performs well for smooth, hard surfaces - giving quantitative agreement with experiment for systems in which its use is optimal[10] - it is not well known if the same descriptions of collision dynamics are applicable to softer, organic solids, such as polymers. Saecker and Nathanson have applied a hard-cubes description to the abovementioned scattering studies of rare gases with squalane and PFPE.[4] For Ne scattering, they find the ratio of the effective surface masses to be m_s(PFPE):m_s(squalane) = 1:0.69. This same ratio for Ar scattering is 1:0.75, implying that Ar interacts with a larger portion of the squalane surface in impulsive collisions than does Ne. These trends follow the intuitive picture of the hard-cube model, but the liquid surfaces are highly amorphous and dynamic so the extracted effective surface mass values likely have little meaning.

A strategy to separate the individual contributions of mass, structure, and chemical properties of the surface is to use self-assembled monolayers. Self assembly of alkanethiols on metal surfaces provides a convenient way to to model organic surfaces with control over the molecular-level structure, chemical properties, and mass of the surface.[11] These properties of alkanethiol SAMs have enabled detailed studies of rare-gas/organic-surface energy transfer that augment the abovementioned efforts with organic liquids. Several experiments have investigated the scattering of Ar from a variety of SAMs of different lengths and functionalization at the surface terminus,[12–14] and the scatttering of Ne, Ar, and Xe, from regular alkanethiol SAMs.[15–17] Xe scattering off regular SAMs has also been used to induce structural changes in the organic monolayers.[18–20] At a theoretical level, molecular-dynamics simulations have unveiled a wealth of details about the mechanisms governing scattering of rare gases from SAMs.[21–26]

Recently, CF_3-terminated alkanethiol SAMs have been synthesized in the Lee group.[27] These surfaces have nearly identical structure to the regular CH_3-SAMs, only differing in the chemical composition of the terminal group of the surface. Therefore, comparison of the interfacial behavior of CF_3- and CH_3-SAMs can be used to learn the effect of fluorination on the properties of an organic surface, absent significant structural effects. Lee and coworkers have performed extensive studies of wetting behavior on CH_3- and CF_3-SAMs and find that

nonpolar hydrocarbon liquids are more wetting on CH_3-SAMs, while polar liquids are more wetting on CF_3-SAMs.[27,28] Polar aprotic liquids were not only more wetting on CF_3-SAMs, but also displayed an "odd-even" effect as the alkyl chain length was varied. This behavior was attributed to the presence of a strong dipole at the SAM terminus resulting from charge separation of the $-CH_2-CF_3$ moiety. This dipole also influences the surface potential, as evidenced by CF_3-SAMs having a substantially higher frictional response than CH_3-SAMs as measured by atomic force and interfacial force microscopies.[27,29] Studies employing ultraviolet photoelectron spectroscopy have also shown the surface potentials to be measurably different for these two SAMs.[30]

Additionally, Wysocki and co-workers have investigated CH_3- and CF_3-SAMs using low-energy ion-surface collisions.[31] Replacing the methyl terminus with a trifluoromethyl group results in more efficient conversion of translational energy to internal vibrational modes in the polyatomic probe gases. Further fluorination of the alkyl chains showed minimal additional enhancement of energy transfer, suggesting that interaction with the outermost CX_3 group is most influential in dictating energy conversion.[31] Electron energy transfer (ion neutralization) was also found to be drastically decreased on the fluorinated surface relative to the hydrogenated surface. The trends with CH_3- and CF_3-SAMs agree well with earlier studies of similarly functionalized Langmuir-Blodgett films.[32]

The experiments by the Lee and Wysocki groups reveal that fluorination of the terminal methyl unit of alkanethiolate SAMs has a profound effect on the interfacial behavior of the surfaces. In the work described below, we examine the scattering of rare gases from CH_3- and CF_3-SAMs adsorbed on gold to provide an atomic understanding of the distinct properties of these two surfaces. As mentioned above, unlike hydrogenated and fluorinated organic liquids,[1] these organic surfaces have identical structures below the terminal groups[27] and therefore the differences in their interfacial behavior[28,31] can be attributed primarily to the properties of these exposed groups. In particular, we aim at addressing the effect of mass on gas/organic-surface energy transfer, which has not been directly and specifically probed in the prior studies with organic liquids. The remainder of this paper is as follows: Details of our experimental and theoretical approach are described in Section 5.2, the main results of our scattering study are presented in Section 5.3, the results are given in-depth discussion in Section 5.4, and our concluding remarks are included in Section 5.5.

5.2. EXPERIMENTAL AND THEORETICAL DETAILS

5.2.1. Molecular-beam scattering

As in our previous studies, the SAMs were prepared via spontaneous chemisorption of the corresponding alkanethiol from ∼1mM ethanolic solutions onto clean gold surfaces.[12–14,33] The substrates used in this study were prepared by Au evaporation onto Cr-coated glass slides (EMF Corp.) and were cleaned in pirahna solution (70% H_2SO_4 / 30% H_2O_2) prior to use. Previous work using SAMs prepared on both gold-coated glass and gold-coated mica slides found the scattering results to have an insignificant dependence on the underlying substrate used for the monlayer, despite the differences in the polycrystalline structure of the two gold surfaces.[12] Pentadecanethiol (CH_3-$(CH_2)_{14}$-SH) was obtained from Aldrich and used as received. 15,15,15-Trifluoropentadecanethiol (CF_3-$(CH_2)_{14}$-SH) was prepared as described by Lee and coworkers according to established procedures.[34] After immersion in the solutions for at least 24 h, the slides were removed, rinsed with copious amounts of ethanol, dried under a stream of nitrogen, and were tranferred via a load-lock system into the scattering chamber. The main UHV chamber operates at a base pressure of $<5\times10^{-10}$ torr, which rises to $\sim1\times10^{-9}$ torr during a scattering experiment.

Atomic beams of Ne, Ar, and Kr seeded in either H_2 (Ne) or He (Ar, Kr) were created via standard supersonic expansion techniques.[35] To match the collision energies of each rare gas, we progressively diluted a small volume of the rare gas with H_2 or He, while monitoring the pulsed beam's peak arrival time with a mass spectrometer (Stanford Research Systems) located in the beam path, until we obtained the desired energy. The resulting beams, ∼0.5% Ne in H_2, ∼0.5% Ar in He, and ∼6% Kr in He, yield peak incident energies of 60 kJ·mol^{-1} (full width at half maximum (FWHM)=17, 11, and 10 kJ·mol^{-1} for Ne, Ar, and Kr beams, respectively).

Details of our scattering experiment have been presented elsewhere.[12] Briefly, the well-collimated pulsed beam of rare gas enters an ultrahigh-vacuum chamber containing the SAMs at room temperature. After collision, the recoiling rare-gas atoms are detected with an Extrel mass spectrometer (tuned to m/e=20.0, 40.0, and 84.0 amu for Ne, Ar, and Kr beams, respectively). The spectrometer records the flight times of the rare gas atoms as they travel from a slotted chopper wheel to the surface and subsequent scattering from the

surface into the ionizer. This time-of-flight data is corrected for the chopper-to-surface flight time and other experimental timing offsets. The resulting time-of-flight distribution, $N(t)$, is converted to a final translational-energy distribution using the relation $P(E) \sim t^2 N(t)$. translational-energy distributions. Therefore, our experiments measure the amount of energy that the rare gas possesses after collision with the organic monolayer, providing direct information about gas/surface energy exchange.

The beam source and mass spectrometer are geometrically situated such that the angle between the incident beam and the mass spectrometer is fixed (60°). The angle between the atomic beam and the surface normal (incidence angle, θ_i) is 30°, and the surfaces are laser aligned such that flight times are measured at the specular angle (final angle, θ_f=30°). As our surface mount accomodates two surfaces, we 'are able to rapidly perform scattering experiments with both the CH_3- and CF_3-terminated SAMs under the same UHV and beam conditions. Switching between the two surfaces requires only a small translation of the manipulator.

5.2.2. Molecular dynamics trajectories

To provide insight into the atomic-scale scattering dynamics, we simulated collisions of Ne, Ar, and Kr with both SAMs using classical trajectories. The potential-energy surfaces employed to evolve the trajectories have been described in detail in our prior work on Ar+CH_3-SAM collisions.[25,26] Briefly, we divide the potential into two terms: the potential describing the organic monolayer (SAM potential hereafter), and the potential for the rare-gas/SAM interactions (gas/SAM potential hereafter). The OPLS force field is used for the SAM, as this standard force field bears out the experimental structure of the SAMs, including a 30° tilt of the chains.[36] The gas/surface potential is described using two-body Buckingham potentials derived from highly-accurate ab initio calculations of rare-gas/hydrocarbon pairs.[37] Specifically, the intermolecular energies of Ne, Ar, and Kr in various approaches to the CH_4 and CF_4 molecules were calculated at the focal-point coupled-cluster with single, double, and perturbative triple excitations level with extrapolation to the complete basis set limit (fp-CCSD(T)/CBS). These high-quality points of the intermolecular potential-energy surface were then used to fit pairwise Buckingham potentials. Detailed information about the fitting procedure and the obtained parameters can be found in Chapter 4.

Using these potential-energy surfaces, we calculated batches of ∼3000 trajectories for each rare-gas/SAM combination. For comparison with experiment, the initial angle between the rare-gas' velocity vector and the surface normal was fixed to 30°. The initial conditions of the surface were selected according to a thermal distribution at 300 K. At the beginning of each trajectory, the rare gas was placed 11.5 Å away from the impact point along its incident velocity vector (∼10 Å away from the closest surface atom). The trajectories were stopped post-collision when the gas either recoiled to a distance of 12 Å from the closest atom of the surface, or, in the case of long-trapping times, after 15 ps. Those trajectories stopped as a result of long trapping times are assumed to be fully thermalized with the surface and are randomly assigned final energies, E'_T, based on a Boltzmann distribution at the surface temperature and with a final angle, θ_f, from a cosine distribution. The fractions of trajectories that do not desorb after 15 ps are 0.6, 0.0, 15.4, 6.9, 24.2, and 18.6% for the Ne/CH_3-, Ne/CF_3, Ar/CH_3-, Ar/CF_3-, Kr/CH_3-, and Kr/CF_3-SAM systems, respectively.

From the initial and final coordinates and momenta of the rare gas, we calculated final translational-energy distributions, and scattering-angle-dependent average final translational energies. Examination of the coordinates and momenta during the trajectory was used to provide mechanistic understanding of the collisions.

5.3. RESULTS

We show in Fig. 5.1 the experimental final translational-energy distributions ($P(E'_T)$) for Ne, Ar, and Kr after collision with CH_3- and CF_3-SAMs at E_{coll}=60 kJ·mol^{-1} with a 30° incidence angle. Fig. 5.1(a) indicates that Ne transfers substantially more energy to the CH_3-SAM than to the CF_3-SAM, suggesting that the more massive surface inhibits energy transfer. The same trend is observed for Ar scattering (Fig. 5.1(b)), but to a much lesser extent than for Ne. In addition, we see that Ar transfers much more energy to either SAM than Ne. This can be appreciated in the shape of the final translational-energy distribution. In comparing Ne to Ar for either SAM surface, we see that the distributions narrow, with an increase in the low-energy peak and a decrease in the high-energy tail. For Kr (Fig. 5.1(c)), the difference between CH_3- and CF_3-SAMs reduces even further, such that the energy distributions overlap. We also see that there is slightly more energy transfer in Kr collisions than in Ar collisions. In effect, the translational-energy distributions become narrower for

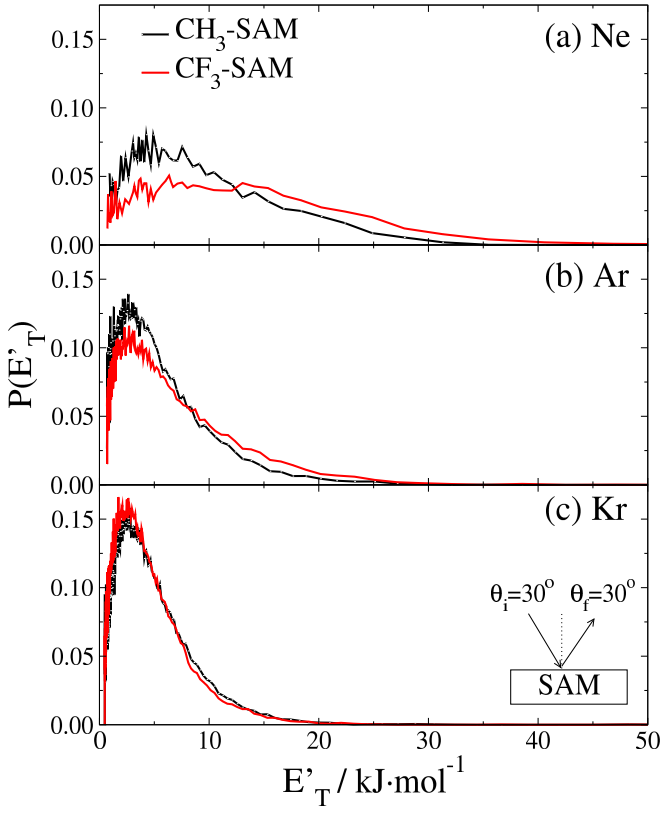

FIG. 5.1: Measured final translational-energy distributions in collisions of rare gases with the CH_3- and CF_3-SAMs at E_{coll}=60 kJ·mol^{-1} and $\theta_i = 30°$. (a) Ne, (b) Ar, (c) Kr.

Kr, with an increase in the low-energy peak that corresponds to enhanced thermalization. Nevertheless, it should be noted that the difference between the final translational-energy distributions is much smaller than between the distributions of Ar and Ne.

We show in Fig. 5.2 the calculated final-energy distributions for scattering of Ne, Ar, and Kr from CH_3- and CF_3-SAMs at E_{coll}=60 kJ·mol^{-1} and θ_i =30°. Although the initial conditions are chosen to match experiments, the total number of simulations that can be performed is limited; therefore, the final-energy distributions are integrated over all final scattering anglesi and scattering planes in contrast with the θ_f=30° detection angle in the in-plane forward scattering direction used in the experiment. The calculated distributions reproduce the experimental trend: while there is a sizable difference in the scattering of Ne from CH_3- and CF_3-SAMs, the differences in the amount of energy transferred to the two SAMs decrease with increasing mass of the projectile. For Kr, the distributions for CH_3- and CF_3-SAMs virtually match. For the CF_3-SAM surface, we see that, as seen in the experiment, the final translational-energy distributions become narrower in the Ne→Ar→Kr

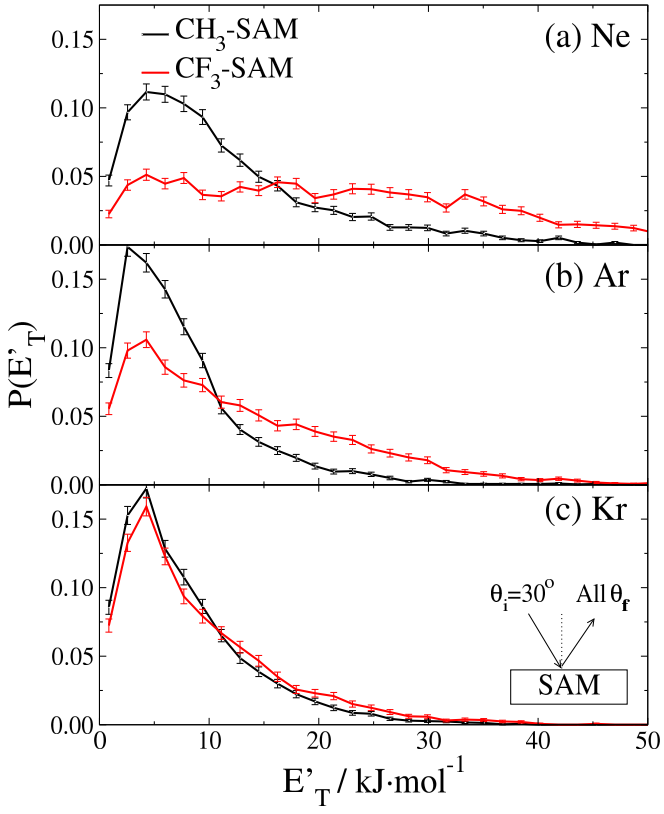

FIG. 5.2: Calculated final translational-energy distributions in collisions of rare gases with the CH_3- and CF_3-SAMs at E_{coll}=60 kJ·mol^{-1} and $\theta_i = 30°$. (a) Ne, (b) Ar, (c) Kr.

sequence. The peak at low energies, which is traditionally attributed to thermal scattering, increases in the same order for both surfaces.

In an effort to establish direct quantitative comparison between theory and experiment, we have calculated a large batch of Ne+CH_3-SAM trajectories (10,000 total trajectories) and calculated the energy distribution of the Ne atoms that scatter in range of $\pm 10°$ with respect to the experimental detection polar scattering angle (30°) and within $\pm 30°$ of the in-plane-forward direction, which is where the detector is located in the experiment. A comparison of this angle-restricted analysis and experiment is displayed in Fig. 5.3. The figure shows quantitative agreement between theory and experiment. Similar comparisons between angle-restricted calculations and experiment were carried out for the rest of the gas/SAM systems with significantly fewer trajectories ($\sim$3000). Although the error bars in the calculations are large, we find an overall good agreement between theory and experiment but not always quantitative. These results indicate that the potential-energy surfaces and SAM model used in the simulations adequately mimic the true properties of the systems.

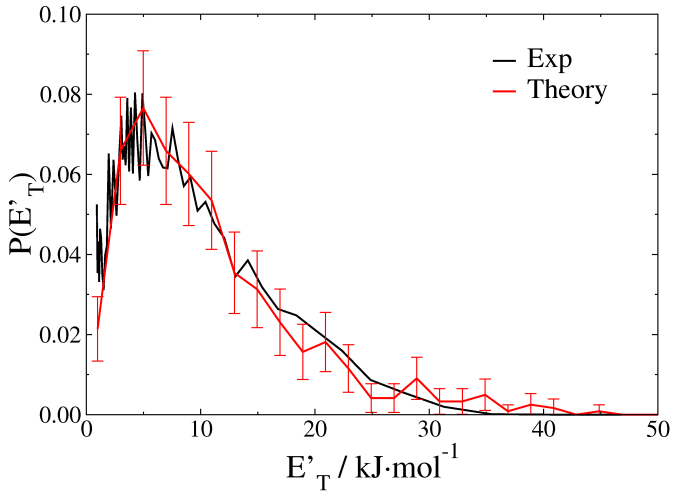

FIG. 5.3: Comparison of measured and calculated final translational-energy distributions in Ne/CH_3-SAM collisions at E_{coll}=60 kJ·mol^{-1} and θ_i=30°. In the experiments, the energy distributions are measured in the in-plane-forward direction at a polar scattering angle of θ_f=30° from the surface normal. The theoretical distribution has been calculated from trajectories scattering in a ±30° window for the in-plane-forward scattering plane and a polar scattering angle in the 20°-40° range. The distributions are normalized to unit area.

Therefore, we can use simulations to provide additional information about the scattering dynamics not readily available from our experimental measurements.

To understand further the experimental results, Fig. 5.4 shows the calculated average final translational energies as a function of the polar scattering angle. The figure reveals that the calculated average energies at θ_f=30^o (experimental detection angle) reproduce the experimental trend: the differences in the average energy of the rare gas recoiling from CH_3- or CF_3-SAMs diminish as the mass of the incident gas increases. Much as is seen in the experiments, while the difference between the results of CF_3- and CH_3-terminated SAMs at θ_f=30^o is sizeable for Ne collisions, the final average final translational energies overlap for Kr.

Analysis of the calculated polar-scattering-angle dependent final translational energies reveals that the amount of energy transferred to CH_3- and CF_3-SAMs depends on the final recoil angle of the rare gas. Ne transfers less energy to the CF_3-SAM than to the CH_3-SAM regardless of the scattering angle, and the amount of energy retained by the rare gas increases for larger final scattering angles. For instance, the average energy for near-perpendicular

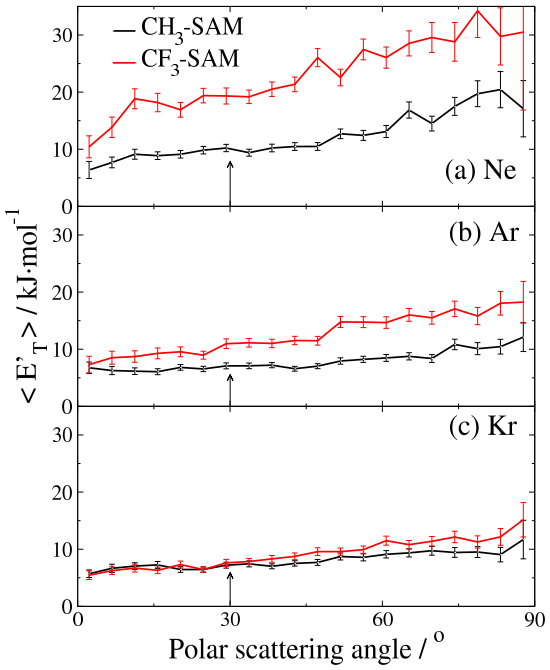

FIG. 5.4: Calculated average final translational energies as a function of the scattering angle in collisions of rare gases with CH_3- and CF_3-SAMs at E_{coll}=60 kJ·mol^{-1}. (a) Ne, (b) Ar, (c) Kr. The arrows correspond to the specular scattering angle, at which the experimental results were obtained.

scattering is ∼20 kJ·mol^{-1} smaller than for near-parallel scattering for the CF_3-SAM, and ∼15 kJ·mol^{-1} smaller for the CH_3-SAM. In contrast, the amount of energy transferred to CH_3- and CF_3-SAMs is essentially the same for Kr scattering and depends very slightly on the final scattering angle. In this case, the difference between near-perpendicular and near-parallel average final energies reduces to ∼10 kJ·mol^{-1} in the CF_3-SAM and ∼5 kJ·mol^{-1} in the CH_3-SAM. The results for Ar lie nicely between the two extremes of Ne and Kr.

Figure 5.4 also reveals that energy transfer from the rare gas to the organic monolayer is very efficient. The collisions that exhibit the least energy transfer correspond to Ne scattering from the CF_3-SAM in a direction near-perpendicular to the surface normal (parallel to the surface). However, even in this extreme case, Ne transfers on the average about half of its initial translational energy to the SAM. For Kr, only a quarter of the collision energy is retained even when Kr desorbs parallel to the surface. On the other hand, the atoms desorbing in a direction perpendicular to the surface (parallel to the surface normal) only possess thermal energy at the surface temperature. An exception to this occurs in Ne

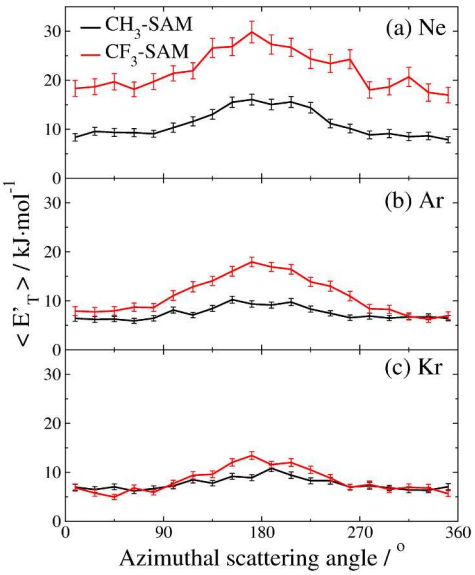

FIG. 5.5: Calculated average final translational energies as a function of azimuthal angle in collisions of rare gases with CH_3- and CF_3-SAMs at E_{coll}=60 kJ·mol^{-1}. (a) Ne, (b) Ar, (c) Kr.

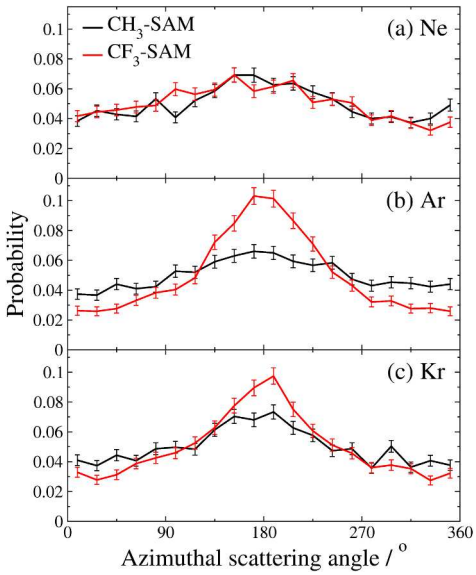

FIG. 5.6: Calculated azimuthal angle distributions in collisions of rare gases with the CH_3- and CF−3-SAMs at E_{coll}=60 kJ·mol^{-1} and θ_i=30°. (a) Ne, (b) Ar, (c) Kr. The distributions are normalized to unit area.

scattering from the CF_3-SAM surface, where complete thermalization does not seem to be allowed, even when Ne recoils perpendicular to the surface (Fig. 5.4(a)).

We have also investigated the dependence of the amount of energy transfer on the azimuthal scattering angle (angle formed by the projections of the initial and final rare-gas velocity vectors on the surface plane.) Regardless of the rare-gas/SAM pair, we see that trajectories exhibiting in-plane-forward scattering are associated with minimum energy transfer, as seen before in earlier Ar+CH_3-SAM studies.[25] Specifically, rare gases recoiling in the in-plane-forward direction possess roughtly twice more energy thand in the in-plane-backward direction for all of the rare-gas/SAM combinations studied in this work (See Figure 5.5). Examination of the azimuthal scattering probability distributions (Fig. 5.6) indicates that irrespective of the rare-gas/SAM pair, most trajectories undergo in-plane-forward scattering. This result is important because our molecular-beam measurements only detect flux scattered in the in-plane-forward direction.

Further analysis of the simulations reveals that, in accord with previous studies, the gas/surface collisions follow the two main mechanisms: direct impulsive scattering and

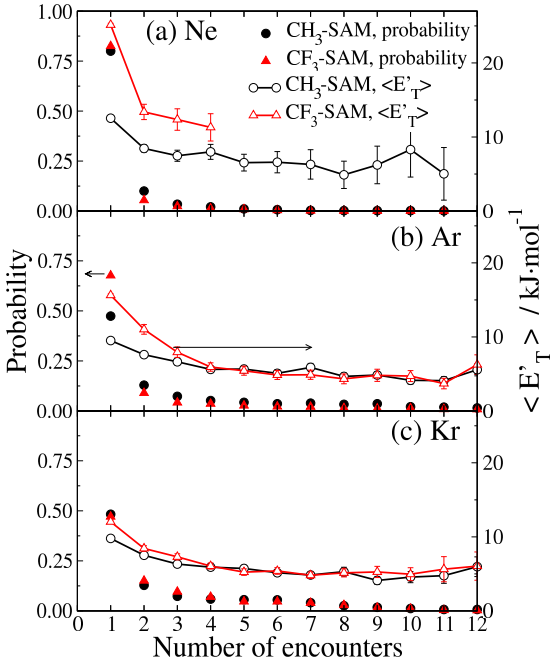

FIG. 5.7: Calculated probability distribution of number of gas-surface encounters and average final translational energy as a function of the number of encounters in collisions of rare gases with the CH_3- and CF_3-SAMs at E_{coll}=60 kJ·mol^{-1}. (a) Ne, (b) Ar, (c) Kr.

trapping-desorption. To separate these two pathways, we study the dynamics as a function of the number of collisions or encounters between the gas and the surface. We define that an encounter between the gas and the surface takes place when there is a minimum in the coordinate of the rare gas along the surface normal. For the purpose of our analysis, we define that direct impulsive scattering occurs when there is only one minimum in the rare-gas coordinate along the surface-normal axis (i.e., the rare gas hits the surface only once). Figure 5.7 displays the probability distribution of gas-surface collisions (left axis), and the average final translational energy (right axis), as a function of the number of encounters. Figure 5.7(a) shows that in most of the Ne collisions (∼80%), there is only one encounter between the gas and the surface for both CH_3- and CF_3-SAMs. Therefore, direct impulsive scattering dominates over trapping-desorption for both SAM surfaces. Remarkably, the number-of-encounters probability distributions overlap for both SAMs, implying that the difference in the final translational-energy distributions for Ne recoiling from these two SAMs is not due to a change in the number of encounters of the gas with the surface. Instead, Fig. 5.7(a) shows that the energy transferred per collision determines the outcome.

For instance, Ne transfers much less energy (∼30% less) to the CF_3-SAM than to the CH_3-SAM in the first encounter. For trajectories that exhibit more than one encounter between Ne and the surface, the energy retained by Ne is significantly larger if it recoils from the CF_3-SAM than from the CH_3-SAM. This result, that Ne transfers less energy to the more massive surface, agrees well with the prediction of elementary hard-cubes models that energy transfer decreases with increasing effective surface mass.[38] A more detailed study of the performance of the hard-cube model in rare-gas/SAM collisions is presented later.

Analysis of the mechanism of Ar collisions (Fig. 5.7(b)) reveals significant differences with respect to Ne. First, Ar has a larger probability of colliding more than once on the SAMs than Ne. Second, Ar has a notably larger probability of experiencing multiple encounters with the CH_3-SAM (∼50%) than with the CF_3-SAM (∼30%). Therefore, the mechanisms of Ar energy exchange on both surfaces seem to be slightly different. Third, although, as seen in the Ne data, there is less energy transfer from Ar to the CF_3-SAM than to the CH_3-SAM, the amount of energy transferred in the first encounter between Ar and the SAMs is larger than in the case of Ne. For instance, the final average energy of Ne in single-encounter collisions with the CF_3-SAM is ∼25 kJ·mol^{-1}, but decreases to ∼15 kJ·mol^{-1} with Ar. For the CH_3-SAM, the average final energy in single-encounter collisions is 12.5 kJ·mol^{-1} for Ne and 9.5 kJ·mol^{-1} for Ar. In fact, energy transfer in Ar collisions with SAMs is so much more efficient than with Ne that Ar is thermalized after three encounters with the surface ($< E'_T > \sim$ 5 kJ·mol^{-1} for four or more encounters, Fig. 5.7(b)) for both the CH_3- and CF_3-SAMs. In Ne/CF_3-SAM collisions there is no thermalization, and only a very small fraction ($<<$ 5%) of Ne/CH_3-SAM collisions fully thermalize (Fig. 5.7(a)).

The results for Ar indicate that the decreased energy transfer of Ar to the CF_3-SAM with respect to the CH_3-SAM is due to (i) an enhanced trapping of Ar on the CH_3-SAM, and (ii) a more efficient transfer of energy to the CH_3-SAM than to the CF_3-SAM in single-encounter collisions. Although energy transfer from Ar to the CF_3-SAM is limited in comparison with the CH_3-SAM, it is appreciably more efficient than Ne/CF_3-SAM energy transfer. Therefore, the differences between the final-energy distributions of Ar in collisions with CH_3- and CF_3-SAMs are smaller than those of Ne. As we shall see later, these differences between the scattering of Ne and Ar can be understood mostly as a simple kinematic effect.

For Kr, we find that the microscopic details of the collisions with CH_3- or CF_3-SAMs are nearly identical. For instance, the number-of-encounters probability distributions (Fig.

5.7(c)) overlap. This implies that the mechanism of the collisions is the same for both surfaces. The only difference between the two SAMs is that the average energy retained by Kr in single-encounter collisions is slightly larger for CF_3-SAMs. Figure 5.4(c) shows that this is due to trajectories in which Kr recoils in a direction near perpendicular to the surface normal. At smaller final scattering angles, including the experimental detection angle, the dynamics of Kr/CH_3-SAM and Kr/CF_3-SAM collisions are indistinguishable. The changes in the dynamics when going from Ar to Kr are minor for the CH_3-SAM but notable for the CF_3-SAM. In particular, we see a marked decrease in the probability for single-encounter collisions and an increase in the amount of energy transferred in single-encounter collisions. Therefore, while the differences between the CH_3- and the CF_3-SAMs are appreciable for Ar, they essentially disappear for Kr.

5.4. DISCUSSION

In this section, we discuss the origin of the differences in the scattering of Ne, Ar, and Kr from the same organic surface, and the differences in the scattering of the same rare gas from the CH_3- and CF_3-SAMs. Since the structures of the CH_3- and CF_3-SAMs are similar, the differences in the energy-transfer dynamics for different rare gases or surfaces must emerge from the change in the collision kinematics (i.e., mass) and/or changes in the gas/SAM and SAM potential-energy surfaces (PESs). In the following, we use simulations to address the individual effect of the changes in potential-energy surface with changes in the rare gas or the surface, and the effect of mass. We follow this with a brief discussion of the applicability of a hard-cubes model description of these systems.

5.4.1. Potential-energy surface effects

To quantify the changes in the rare-gas/SAM PES upon changing the rare gas or fluorinating the surface, we examine high-level ab initio calculations of rare-gas/CX_4, X=H,F pairs.[37] Focal-point coupled-cluster calculations including single, double, and perturbative triple excitations extrapolated to the complete basis-set limit (fp-CCSD(T)/CBS) indicate that the depths of the absolute van der Waals wells of the Y/CH_4 pairs are 0.7, 1.7, and 2.0 kJ·mol^{-1} for Y=Ne, Ar, and Kr, respectively. The absolute well depths for the Y/CF_4

pairs are 1.1, 2.3, and 2.7 kJ·mol^{-1}, respectively. Two main conclusions can be extracted from these high-accuracy electronic-structure calculations. First, the long-range attraction between either of the SAMs and the rare gases increases in the Ne→Ar→Kr order, as expected from the increase in polarizability of the rare gases in that order. Second, the interactions of fluorinated alkanes with rare gases are slightly more attractive than those of regular alkanes. This result is also expected from the more diffuse character of the electronic cloud in fluorinated alkanes and the consequent increase in polarizability.

Aside from enhancing the long-range attractions between the gas and the surface, the selective fluorination at the SAM terminus also induces a strong dipole moment in each of the CF_3-SAM chains due to the difference in electronegativity between the terminal -CF_3 moiety and the last -CH_2- group of the SAM. Although this surface dipole has been shown to affect the surface free energy,[28] ab initio calculations indicate that the interactions between rare gases and CF_3-SAMs are dominated by dispersion interactions and the effect of the surface dipole is minimal.[37] In particular, the ab initio well depth or Ar approaching the fluorinated side of a CH_3CF_3 molecule is identical to the well between Ar and the CF_3CF_3 molecule along the same approach. Analogously, the ab initio calculations do not show any difference between the approach of Ar to the hydrogenated side of the CH_3CF_3 molecule or to CH_3CH_3.

To ascertain whether the changes in the dynamics of Ne, Ar, and Kr scattering off the same surface are due to the changes in the gas/SAM potential-energy surface, we have performed simulations of Ne/CF_3-SAM collisions with two different gas/SAM potentials. Figure 5.8 shows the final translational-energy distributions in collisions of Ne with the CF_3-SAM at E_{coll}=60 kJ·mol^{-1} and θ_i=30° using the regular Ne/CF_3-SAM gas/SAM potentials, and the more attractive Kr/CF_3-SAM gas/SAM potentials. Note that in the simulation involving the Kr/CF_3-SAM potentials, the initial conditions of the trajectories and the mass of the projectile are identical to those of the regular Ne/CF_3-SAM simulations, so the difference in the scattering dynamics are solely due to the gas/SAM potential.

The final translational-energy distributions of regular Ne/CF_3-SAM collisions and Ne/CF_3-SAM collisions integrated using Kr/CF_3-SAM potentials in Figure 5.8 are very similar. Quantitatively, the average fraction of energy transfer ($\frac{E_{coll}-<E'_T>}{E_{coll}}$) in Ne/$CF_3$-SAM collisions calculated using the Kr/CF_3-SAM potentials is in good agreement with the result obtained using the regular Ne/CF_3-SAM potentials (0.64 vs 0.62, respectively). These

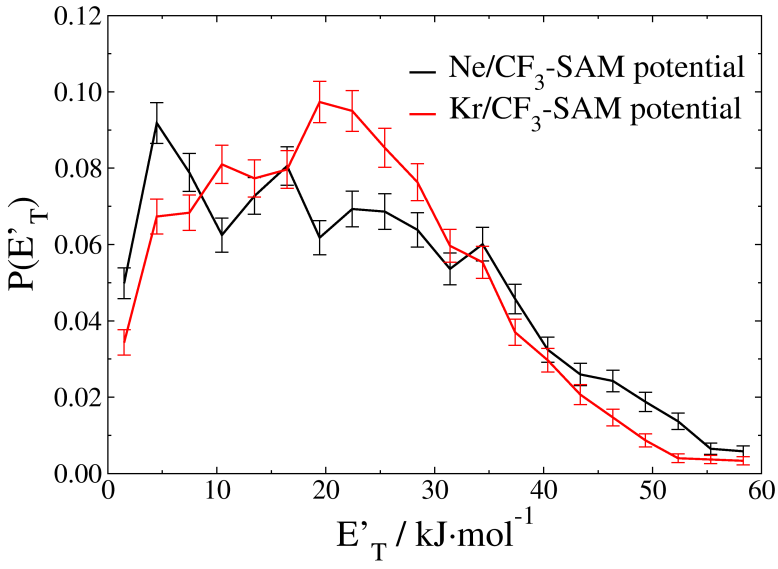

FIG. 5.8: Calculated final translational-energy distributions in collisions of Ne with the CF_3-SAM at E_{coll}=60 kJ·mol^{-1} and θ_i=30°. Effect of varying the gas/surface intermolecular potential.

results indicate that the more attractive character of the Kr/CF_3-SAM potential has little influence in the different dynamics of Ne and Kr collisions with SAMs.

We now address the effect of the change in the gas/SAM and SAM potential-energy surface upon fluorination on the dynamics of rare-gas/SAM collisions. For this purpose, we have integrated a batch of Ne/CF_3-SAM trajectories at E_{coll}=60 kJ·mol^{-1} and θ_i=30° in which the gas/SAM potential is assumed to be that of the Ne/CH_3-SAM, and the SAM potential is assumed to be that of the CH_3-SAM. Figure 5.9 shows the final translationl-energy distribution of such simulation compared with the distribution obtained in regular Ne/CF_3-SAM calculations. Both translational-energy distributions overlap within statistical uncertainties. Quantitatively, the average fraction of energy transfer in these calculations (0.64) agrees well with the result using the regular gas/surface and SAM potentials (0.62). These results indicate that the changes to both the gas/surface and surface potentials upon fluorination also play a minor role in the dynamics of rare-gas/SAM collisions at the initial conditions explored in this work.

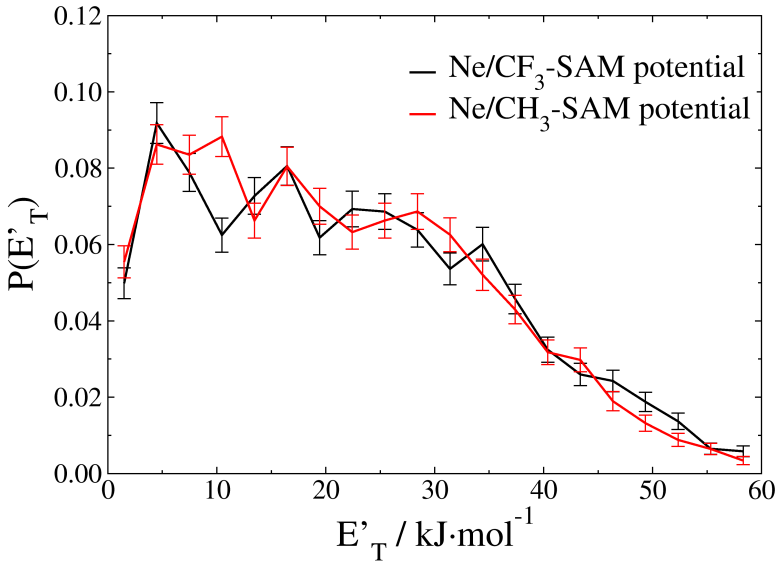

FIG. 5.9: Calculated final translational-energy distributions in collisions of Ne with the CF_3-SAMs at E_{coll}=60 kJ·mol^{-1} and θ_i=30°. Effect of varying the SAM intramolecular potential.

5.4.2. Kinematic effects

The above analysis has verified that the differences in the potential-energy surface when changing the rare gas or fluorinating the SAM terminus only have a minor effect on the dynamics. We now focus on determining if kinematic effects alone are responsible for the observed scattering trends. We first study the effect of making the surface terminus heavier upon fluorination. To this end, we compare in Figure 5.10 the final translational-energy distributions of Ne scattering at 60 kJ·mol^{-1} and θ_i=30^o from a regular CH_3-SAM and from an isotopomeric SAM in which the mass of the H atoms at the methyl terminus is that of F atoms. The gas/surface and SAM potentials are identical in both simulations, and correspond to the potentials for the Ne/CH_3-SAM system. The figure shows a sharp difference in the amount of energy transfer with a change in the mass of the terminus. The average fraction of energy transfer with the regular SAM is 0.81, and that with the heavy SAM is 0.64. Also included in the figure is the final translational-energy distribution obtained in the regular Ne/CF_3-SAM simulations. The Ne/heavy-CH_3-SAM distribution is in excellent agreement with the Ne/CF_3-SAM distribution. Therefore, a simple change in the mass of the surface terminus greatly limits gas/surface energy transfer in Ne collisions and accounts for the the differences between the dynamics of Ne scattering off fluorinated

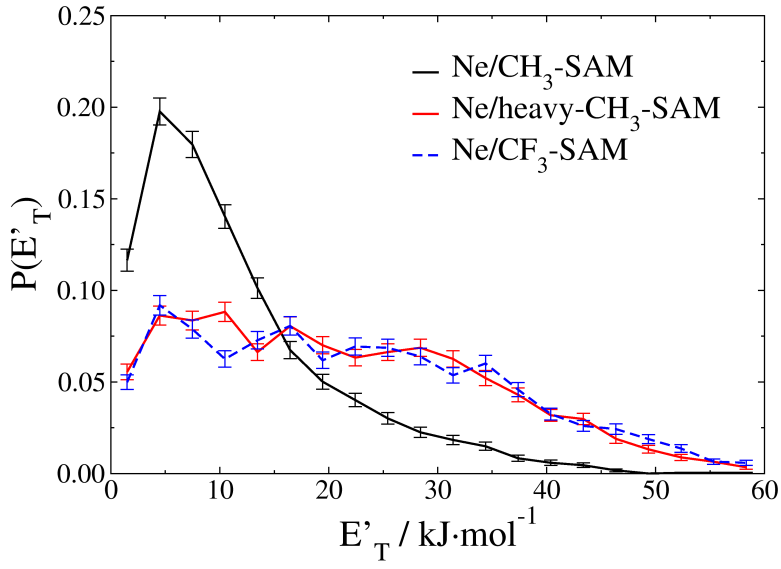

FIG. 5.10: Calculated final translational-energy distributions in collisions of Ne with the indicated SAMs at E_{coll}=60 kJ·mol^{-1} and θ_i=30°. Effect of varying the mass. The "heavy" CH_3-SAM corresponds to a CH_3-SAM in which the mass of the H atoms of the CH_3 terminus is replaced by that of F atoms in the simulations.

and regular surfaces seen in the experiment (Fig. 5.1(a)).

To delve further into the effect of kinematics on the dynamics of rare-gas/SAM collisions, we have calculated energy transfer in Ne/CF_3-SAM collisions at 119 kJ·mol^{-1} and compared it with the results for Ar/CF_3-SAM at 60 kJ·mol^{-1}. In both simulations, the rare gas has the same momentum, so the comparison will further address the role of initial momentum on gas/organic-surface energy exchange. Figure 5.11 shows the fraction of energy transfer probability distributions. The distributions are in good agreement with each other, indicating that energy transfer under these two different sets of initial conditions is very similar. The average fraction of energy transfer in Ne/CF_3-SAM collisions at 119 kJ·mol^{-1} (0.78) and in Ar/CF_3-SAM collisions at 60 kJ·mol^{-1} (0.79) are also in excellent agreement. We therefore conclude that kinematic effects alone are able to explain the changes in rare-gas/SAM dynamics for different rare gases, and CH_3- or CF_3-SAMs.

The observed energy transfer behavior in these systems displays the intuitive trends expected from a hard-cubes scattering model. Looking at the rare gas scattering results, and recalling that energy transfer is maximal when $\mu = 1$, the trends are quite easily explained. The mass of Kr is a close match to that of a CF_3- group, and is practically equal

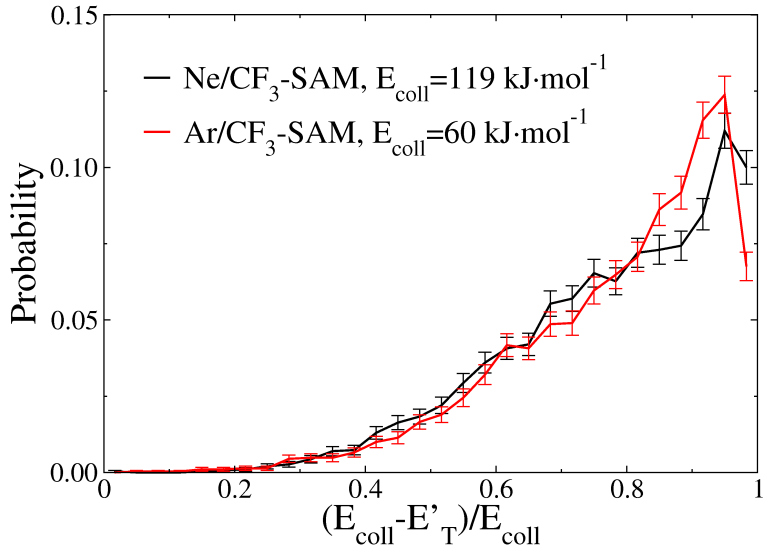

FIG. 5.11: Calculated fraction of energy transfer probability distributions in collisions of Ne and Ar with the CF_3-SAM in which the rare gases have equal initial momenta. For Ne and Ar, E_{coll}=119 kJ·mol^{-1} and 60 kJ·mol^{-1}, respectively. θ_i=30°.

to the mass of a CF_3CH_2- group, therefore μ should be close to unity and energy transfer should be very efficient. Ne's mass is quite different from that of a CF_3- group, μ is much less than 1, and energy transfer is limited. However, Ne sees a fairly good mass match with the CH_3-SAM and energy transfer is efficient. One curious result from the simulations is that for trajectories in which the rare gas only encounters the CF_3-SAM one time, Kr leaves the surface with slightly more energy (9.8 kJ·mol^{-1}) than Ar (9.5 kJ·mol^{-1}). In this case, it seems that Kr is much more massive than the limiting effective mass of the CH_3-SAM surface, making μ substantially greater than 1 and hindering efficient energy transfer. Ar seems to have a slightly better mass match with the CH_3-SAM and hence energy transfer is more efficient. It is seen then that these systems can be qualitatively described quite satisfactorily within the framework of a hard-cubes model.

The result that mass governs the extent of energy transfer between rare gases and CH_3- and CF_3-SAM surfaces provides a microscopic rationalization of the experimental results in Fig. 5.1. These results indicate that while there is a large difference in energy transfer to the CH_3- and CF_3-SAM in collisions of Ne at 60 kJ·mol^{-1}, these differences essentially disappear for collisions of Kr at 60 kJ·mol^{-1}. The fact that changes in the gas mass or surface mass alone are able to reproduce this trend suggests the presence of a kinematic barrier for

gas/surface energy transfer. In order for a SAM to absorb the energy of an impinging gas-phase species, low-frequency, large-amplitude surface modes need to be excited.[24] These modes are primarily chain wags and torsions, and in order for them to be excited, the SAM chains need to move laterally. The excitation received by the SAM is then dissipated to chains adjacent to the impact region. The heavier CF_3-SAM therefore possesses a higher inertial barrier for energy transfer than the lighter CH_3-SAM, as lateral motion of the heavier chains is more difficult. The relatively small momentum of Ne at 60 kJ·mol^{-1} is not large enough to excite the absorbing modes in the CF_3-SAM as efficiently as in the CH_3-SAM. The lack of efficient Ne/SAM energy transfer in the initial gas/surface collision results in mostly impulsive scattering of the gas. In contrast, the momentum of Kr at 60 kJ·mol^{-1} is large enough to efficiently excite surface modes in both CH_3- and CF_3-SAM surfaces, even though the CF_3-SAM possesses a higher kinematic barrier for energy transfer. Energy transfer is very efficient in the initial collision, resulting in an increased probability of trapping-desorption. The results for Ar scattering lie between those of Ne and Kr: while energy transfer is more efficient than in Ne, the inertial barrier for energy transfer to the heavier surface can still be realized.

5.5. CONCLUDING REMARKS

The dynamics of energy transfer in collisions of Ne, Ar, and Kr with regular and ω-fluorinated alkanethiolate monolayers on Au(111) have been investigated with the goal of determining the role that mass plays in gas/organic-surface energy transfer. Molecular-beam scattering experiments indicate that while 60 kJ·mol^{-1} Ne transfers more energy to CH_3-SAMs than to CF_3-SAMs, 60 kJ·mol^{-1} Kr transfers equal amounts of energy to both organic surfaces. Extensive molecular-dynamics simulations have been carried out to elucidate the microscopic origin for this behavior. The calculated final translational-energy distributions reproduce the experimental trends, lending confidence to the accuracy of the simulations.

High-quality ab initio calculations show that the long-range attractions between the rare gases and the SAMs increase in the Ne→Ar→Kr order, as expected. In addition, ω-fluorination of the SAMs enhances the attractions between the gases and the surface. Molecular-dynamics simulations have been carried out to investigate the effect of the differences in the potential-energy surface on the dynamics. Interestingly, the simulations reveal

that the differences in the potential-energy surface play only a minor role in the changing scattering dynamics when going from Ne, to Ar and Kr on a particular SAM, and when going from the CH_3-SAM to the CF_3-SAM for a particular gas. Instead, our simulations reveal that changes in the impinging gas' mass, or the surface mass capture the differences in the dynamics of these systems.

The fact that mass governs the extent of energy transfer in collisions of rare gases with CH_3- and CF_3-SAMs therefore enables us to rationalize the experimental finding that Ne transfers different amounts of energy to the CH_3- and CF_3-SAMs, while Kr transfers the same amount of energy to these SAMs. In order for SAMs to efficiently absorb energy from an impinging gas species, the chains of the SAM need to move laterally so that neighboring chains can dissipate the energy of the collision. Heavier chains require larger momentum transfer from the colliding gas to exert this lateral motion which creates and inertial barrier for energy transfer. The momentum of 60 kJ·mol^{-1} is not large enough to displace the CF_3-SAM chains as much as the CH_3-SAM chains, and this results in limited energy transfer to the heavier SAM. Kr at 60 kJ·mol^{-1} possesses enough momentum to equally excite the absorbing modes in each SAM, and energy transfer for both SAMs is similar. It is found that the same hard-cubes model of scattering developed for use with metals and other hard inorganic solid surfaces is sufficient to describe the dynamic trends for the softer SAM systems studied.

In subsequent chapters, we examine energy transfer from molecules to the model organic surfaces employed in this chapter. In particular, elucidation of the role played by the internal modes of the gas-phase species on heterogeneous energy transfer helps to further our understanding of gas/organic-surface collisions.

REFERENCES

[1] M. E. King, G. M. Nathanson, M. A. Hanning-Lee, and T. K. Minton, Phys. Rev. Lett. **70**, 1026 (1993).

[2] M. E. Saecker, S. T. Govoni, D. V. Kowalski, M. E. King, and G. M. Nathanson, Science **252**, 1421 (1991).

[3] M. E. Saecker and G. M. Nathanson, J. Chem. Phys. **99**, 7056 (1993).

[4] M. E. Saecker and G. M. Nathanson, J. Chem. Phys. **100**, 3999 (1993).

[5] B. G. Perkins and D. J. Nesbitt, J. Phys. Chem. B **110**, 17126 (2006).

[6] M. E. King, M. E. Saecker, and G. M. Nathanson, J. Chem. Phys. **101**, 2539 (1994).

[7] E. K. Grimmelmann, J. C. Tully, and M. J. Cardillo, J. Chem. Phys. **72**, 1039 (1980).

[8] J. N. Smith, Surf. Sci. **34**, 613 (1973).

[9] S. T. Ceyer and G. A. Somorjai, Annu. Rev. Phys. Chem. **28**, 477 (1977).

[10] Y. Watanabe, H. Yamaguchi, M. Hashinokuchi, K. Sawabe, S. Maruyame, Y. Matsumoto, and K. Shobatake, Eur. Phys. J. D **38**, 103 (2006).

[11] J. C. Love, L. A. Estroff, J. K. Kriebel, R. G. Nuzzo, and G. M. Whitesides, Chem. Rev. **105**, 1103 (2005).

[12] B. S. Day and J. R. Morris, J. Phys. Chem. B **107**, 7120 (2003).

[13] B. S. Day, S. F. Shuler, A. Ducre, and J. R. Morris, J. Chem. Phys. **119**, 8084 (2003).

[14] M. K. Ferguson, J. R. Lohr, B. S. Day, and J. R. Morris, Phys. Rev. Lett. **92**, 073201 (2004).

[15] N. Isa, K. D. Gibson, and S. J. Sibener, J. Chem. Phys. **120**, 2417 (2004).

[16] K. D. Gibson, N. Isa, and S. J. Sibener, J. Chem. Phys. **119**, 13083 (2003).

[17] K. D. Gibson, N. Isa, and S. J. Sibener, J. Phys. Chem. A **110**, 1469 (2006).

[18] D. P. Fogarty and S. A. Kandel, J. Chem. Phys. **124**, 111101 (2006).

[19] D. P. Fogarty and S. A. Kandel, J. Chem. Phys. **125**, 174710 (2006).

[20] D. P. Fogarty, N. A. Kautz, and S. A. Kandel, Surf. Sci. **601**, 2117 (2007).

[21] S. B. M. Bosio and W. L. Hase, J. Chem. Phys. **107**, 9677 (1997).

[22] T.-Y. Yan and W. L. Hase, Phys. Chem. Chem. Phys. **4**, 901 (2000).

[23] T.-Y. Yan and W. L. Hase, J. Phys. Chem. B **106**, 8029 (2002).

[24] T.-Y. Yan, N. Isa, K. D. Gibson, S. J. Sibener, and W. L. Hase, J. Phys. Chem. A **107**, 10600 (2003).

[25] B. S. Day, J. R. Morris, and D. Troya, J. Chem. Phys. **122**, 214712 (2005).

[26] B. S. Day, J. R. Morris, W. A. Alexander, and D. Troya, J. Phys. Chem. A **110**, 1319 (2006).

[27] M. Graupe, T. Koini, H. I. Kim, N. Garg, Y. F. Miura, M. Takenaga, S. S. Perry, and T. R. Lee, Coll. Surf. A **154**, 239 (1999).

[28] M. Graupe, M. Takenaga, T. Koini, R. Colorado, and T. R. Lee, J. Am. Chem. Soc. **121**, 3222 (1999).

[29] J. E. Houston, C. M. Doelling, T. K. Vanderlick, Y. Hu, G. Scoles, I. Wenzl, and T. R. Lee,

Langmuir **21**, 3926 (2005).

[30] D. M. Alloway, M. Hofmann, D. L. Smith, N. E. Gruhn, A. L. Graham, R. Colorado, V. H. Wysocki, T. R. Lee, P. A. Lee, and N. R. Armstrong, J. Phys. Chem. B **107**, 11690 (2003).

[31] D. L. Smith, V. H. Wysocki, R. Colorado, O. E. Shmakova, M. Graupe, and T. R. Lee, Langmuir **18**, 3895 (2002).

[32] C. Gu, V. H. Wysocki, A. Harada, H. Takaya, and I. Kumadaki, J. Am. Chem. Soc. **121**, 10554 (1999).

[33] B. S. Day and J. R. Morris, J. Chem. Phys. **122**, 234714 (2005).

[34] M. Graupe, T. Koini, V. Y. Wang, G. M. Nassif, R. Colorado, R. J. Villazana, H. Dong, Y. F. Miura, O. E. Shmakova, and T. R. Lee, J. Fluorine Chem. **93**, 107 (1999).

[35] D. R. Miller, in *Atomic and Molecular Beam Methods*, edited by G. Scoles (Oxford University Press, New York, 1988), vol. 1, p. 14.

[36] J. Hautman and M. L. Klein, J. Chem. Phys. **91**, 4994 (1989).

[37] W. A. Alexander and D. Troya, J. Phys. Chem. A **110**, 10834 (2006).

[38] G. M. Nathanson, Annu. Rev. Phys. Chem. **55**, 231 (2004).

Preface: Molecular gas scattering

In Chapters 4 and 5, we described our efforts in characterizing the energy exchange dynamics when a model organic surface is impinged upon by the simplest case of gas-phase partners, rare-gases. This approach allowed us to investigate the collision dynamics of gas/organic surface systems as a function of gas and surface masses in absence of rovibrational degrees of freedom. In the following chapters, we extend our studies of non-reactive gas/organic-surface collisions (inelastic scattering studies) to include small polyatomic molecules. Comparison of the differential behavior of small polyatomics scattering from SAM surfaces with the previously observed rare-gas scattering behavior enables us to infer the participation of internal rotational and vibrational degrees of freedom in the energy transfer characteristics during collision. As before, experimental molecular beam scattering experiments are performed to yield final translational-energy distributions, and these are compared with calculated distributions obtained from classical dynamics trajectories integrated with potential energy surfaces derived from highly-accurate ab initio data. The level of agreement with experiment gives us confidence in using simulations to study properties of the collision dynamics not currently attainable with our experimental setup.

Within Chapter 6, we explore the influence that the polar/apolar character of the gas-phase and surface has on overall energy transfer. In a collaborative effort, we performed ab initio calculations to approximate the maximal van der Waals attractions of various gas-phase species with a simple SAM mimic, and correlated these well depths with the molecular beam scattering experiments of Megan Bennett. The molecular beam scattering experiments explored collisions of 60 kJ·mol Ne, CD_4, ND_3, and D_2O with long-chain CH_3-, NH_2-, and OH-terminated self-assembled monolayers (SAMs). Time-of-flight measurements for the scattered gases reveal the extent of energy exchange and the propensity for a gas to thermally accommodate with the surface during a collision. Of the four gases studied, Ne transfers the least amount of translational energy into the monolayers. Overall, the trend in final translational energies follow the order Ne $\geq$ CD_4 $\geq$ ND_3 $\geq$ D_2O for scattering from all three SAMs. The observed trend in the energy exchange is due to a combination of factors that include differences in the internal degrees of freedom and the gas/surface attractive forces. The thermal accommodation efficiencies of the four gases follow the opposite trend. Thermalization for the Ne atoms is nearly negligible for all three monolayers, whereas D_2O

and ND_3 approach near complete accommodation on the OH- and NH_2-SAMs. The overall energy exchange and thermal accommodation efficiencies also depend markedly on the terminal group of the SAM. For Ne scattering, the trend for the overall energy transfer follows: CH_3- >NH_2- >OH-SAMs. In contrast, the overall D_2O energy transfer is greater when colliding with the polar SAMs than the non-polar, CH_3-SAM. Together, the results show that the extent of energy transfer depends on a balance between the rigidity of the surface, as affected by intra-surface hydrogen bonding, and the strength of the gas-surface attractive forces. The experimental scattering study, and a preliminary version of the calculations discussed in Chapter 6, formed the basis for Megan Bennett's Master's thesis. This work resulted in a paper in the Journal of Physical Chemistry C.[1]

The remainder of the section on polyatomic scattering (Chapters 7-10) focuses on a detailed examination of the collision dynamics of two common diatomic molecules, N_2 and CO, impinging upon the CH_3- and CF_3-SAM surfaces. Chapter 7 details our derivation of gas/SAM intermolecular potentials for use in subsequent scattering studies, along with similar discussion and investigation into the potential energy surfaces as was presented in Chapter 4 for the rare-gas systems. While the methods for arriving at analytic potential energy surfaces for the N_2 and CO/SAM interactions was analogous to that employed in the rare-gas studies, the seemingly miniscule change in complexity when going from atomic to diatomic species made the fitting procedures especially fickle. The heterogeneity of the CO molecule made for subtle differences in the respulsive walls and attractive wells based on relative CO–CX_4 geometries that was quite hard to realize with the Buckingham form. Patience and finesse eventually paid off, and we were able to derive high-quality analytic potentials that are some of the best currently attainable through feasible means of calculation.

In Chapter 8, we make a comparison study of N_2 and CO scattering from the CH_3- and CF_3-SAMs. Experimentally determined final translational-energy distributions are obtained at E_{coll}=43 and 60 kJ·mol^{-1} for both gases and directly compared. Additionally, classical trajectories were performed, validated via comparison with experiment, and used to examine other aspects of the energy transfer dynamics not attainable in experiment, such as final rovibrational populations. No ascertainable difference was noted between the N_2 and CO scattering. This was not overly surprising as the main difference between the two molecules is the existence of a very small dipole moment (0.11 Debye) in CO. As such, we chose to focus on the (slightly) more interesting case of CO scattering for more in-depth study of

diatomic/organic-surface collision dynamics.

We present an expanded experimental and theoretical study of the dynamics of collisions of the CO molecule with the SAM surfaces in Chapter 9, with the main goal of investigating the influence of rovibrational degrees of freedom on the collision dynamics. Experimentally, we scatter CO at 60 kJ·mol^{-1} and 30° incident angle from regular (CH_3-terminated) and ω-fluorinated (CF_3-terminated) alkanethiol self-assembled monolayers (SAMs) and measure the time-of-flight distributions at the specular angle after collision. At a theoretical level, we carry out classical-trajectory simulations of the same scattering process using CO/SAM potential-energy surfaces derived from ab initio calculations. Calculated state-to-state energy-transfer properties indicate that the collisions are notably vibrationally adiabatic. Similarly, translational energy transfer from and to CO rotation is relatively weak. The trends are examined as a function of collision energy and incident angle to provide a deeper understanding of the factors governing state-to-state energy transfer in gas/organic-surface collisions.

Finally, in Chapter 10, we present a classical-trajectory study of CO collisions with regular (CH_3-terminated) and ω-fluorinated (CF_3-terminated) alkanethiol self-assembled monolayers (SAMs) with a focus on analyzing the stereodynamics properties of the collision. The CO molecule is scattered with incident angles of either 30° or 60° with respect to the surface normal and with 60 kJ·mol^{-1} collision energy and we analyze final translational and rotational energy, mechanism of the collisions, and orientation and alignment of the rotational angular momentum. Analysis of the alignment of the final rotational angular momentum in collisions involving initially rotationally cold CO indicates a slight preference for "cartwheel" and "corkscrew" rotational motions. In contrast, collisions of initially excited CO slightly favor "helicopter" motion of the recoiling molecule. Moreover, studies of final orientation reveal that, while cartwheel "topspin" motion is favored for collisions in which initially cold CO becomes rotationally excited, no preferred handedness is observed when CO leaves the surfaces with "helicopter" motion. Analysis of trajectories involving initially rotationally excited CO in which the initial rotational angular momentum is aligned and/or oriented shows a non-negligible effect of the initial rotational motion on the dynamics of energy transfer. For instance, CO approaching the SAMs with helicopter motion retains a larger fraction of its initial rotation than molecules colliding with cartwheel-type motions. Conservation of the alignment and orientation of the initial rotational angular momentum vector is also

enhanced with helicopter motion relative to cartwheel or random motions. The calculated trends in the stereodynamic properties for the two SAMs indicate that the CH_3-SAM is effectively more corrugated than the CF_3-SAM.

Two papers based on the CO/SAM scattering investigations described in Chapters 7-10 have been published. A paper focusing on scalar energy-transfer phenomena (see Chapter 9), as well as derivation of the analytical potentials (see Chapter 7) was published in the Journal of Chemical Physics.[2] The stereodynamics study (see Chapter 10) has been published in the Journal of Physical Chemistry A.[3]

[1]M. E. Bennett, W. A. Alexander, J. W. Lu, D. Troya, and J. R. Morris *J. Phys. Chem. C* **112**, 17272 (2008).

[2]W. A. Alexander, J. R. Morris, and D. Troya, *J. Chem. Phys.* **130**, 084702 (2009).

[3]W. A. Alexander, J. R. Morris, and D. Troya, *J. Phys. Chem. A* **113**, 4155 (2009).

Chapter 6
Correlation of potential energy surface characteristics with scattering behavior from polar and nonpolar surfaces

Reproduced in part with permission from M. E. Bennett, W. A. Alexander, J. W. Lu, D. Troya, and J. R. Morris, *J. Phys. Chem. C* **112**, 17272 (2008). Copyright 2008 American Institute of Physics.

6.1. INTRODUCTION

The dissolution of gas phase molecules into a hydrocarbon liquid or the uptake of a vaporous species onto a solid organic surface depends on the physical and chemical properties of the interface that govern the motions of the molecules as they collide. Pioneering molecular beam scattering experiments by Saecker and Nathanson have provided detailed insight into the roles of gas-surface collision energy, dipole-dipole interactions, and surface free energy in determining the outcome of collisions of atomic and small polyatomic gases on liquid organic surfaces.[1] Their studies of Ne, CH_4, NH_3, and D_2O impinging on liquid glycerol and squalane show that the molecules recoil from the surfaces with energies that are well described by separation into two channels corresponding to impulsive scattering and trapping desorption. The final energy distributions of molecules that scatter impulsively from the surfaces of the two liquids are found to depend largely on the kinematics of the system. However, the extent of trapping on the surfaces depends markedly on the gas-surface attractive forces and the rigidity of the liquid. For example, they find that high energy, $\sim$55 kJ·mol^{-1}, D_2O molecules trap much more readily on glycerol, a hydrogen bonding liquid, than on squalane, a pure hydrocarbon. In contrast, Ne appears to trap more readily on the hydrocarbon liquid than on the stiff hydrogen-bonding surface of glycerol. Overall, these studies have correlated the enthalpies and free energies of solvation with the final energy distributions of the gases to show that the "like dissolves like" principle can be used to predict the relative energy transfer and rate of approach to thermal equilibrium for gas-liquid collisions.[1] The studies described herein are designed to explore whether similar principles can be extended to understand the

dynamics of gases colliding with solid organic materials, where the interfacial region is more static, the microscopic structure is different, and the energetic degrees of freedom of the surface are altered significantly relative to those of a liquid.

The following studies examine collisions of the non-polar gases, Ne and CD_4, and polar gases, ND_3 and D_2O, with model organic surfaces composed of ω-functionalized alkanethiol self-assembled monolayers (SAMs) on gold. Alkanethiol SAMs on gold provide the opportunity to study gas-surface scattering dynamics on well-organized, atomically flat systems where the chemical groups of interest are located precisely at the gas-surface interface. Pure hydrocarbon surfaces are created by using long-chain CH_3-terminated SAMs and polar hydrogen-bonding groups are placed at the interface by employing NH_2- and OH-terminated SAMs. Previous studies using reflection-absorption infrared spectroscopy, scanning-tunneling microscopy, and molecular dynamics simulations indicate that these monolayers are very similar in their packing density and chain orientation.[2–7] Simulations performed by Hase and co-workers[8] and Klein et al.[2,3,9] show that the terminal groups of the OH-SAM are more closely spaced as they move together to form an extended hydrogen-bonding network that binds nearly every hydroxyl group within the monolayer.

The choice of incident gases was made based on the wide range of properties exhibited by these four gases, while maintaining their similar sizes and masses, thereby enabling the correlation of observed trends in the scattering dynamics to chemical or physical characteristics rather than to structural influences. For instance, the polarizabilities of the gases vary from 2.6 $Å^3$ for CH_4 to as low as 1.3 $Å^3$ and 0.4 $Å^3$ for H_2O and Ne, respectively. The trend for dipole moment strength is just the opposite, as it ranges from 0 Debye for Ne and CH_4, to 1.8 Debye for H_2O. By using molecular beam scattering experiments of these gases on polar and non-polar SAMs, we aim to develop an understanding for how the attractive and repulsive forces between gases and solid organic surfaces affect energy transfer and the propensity for a gas to accommodate on a surface. Specifically, we aim to explore whether the same principles that govern gas/surface energy transfer and trapping probabilities on liquids can be extended to describe collisions on solid organic surfaces. Overall, this work is focused on studying the interplay between surface rigidity, as provided by polar hydrogen bonding groups, that limits energy transfer into the material and strong gas/surface attractive interactions that may ultimately enhance the extent of energy transfer and thermal accomodation.

6.2. EXPERIMENTAL SCATTERING

We extensively detail the experimental setup in Chapter 2, so only details specific to this work are given here. Atomic/molecular beams of 60 kJ·mol^{-1} Ne, CD_4, and ND_3 were made by expanding ∼2% mixtures of each gas in H_2 through our 0.05 mm nozzle beam source chamber. The D_2O beam was created by bubbling the carrier gas through the liquid at 20°C. Reasons for use of deuterated molecules are twofold: 1) deuteration of the molecules gives them all the same mass, eliminating the (albeit small) mass differences as a variable in the differential scattering dynamics, and 2) the background noise in the mass spectrometer is much smaller at m/e=20.0 amu than at the hydrogenated masses (H_2O is an especially significant background gas in our chamber). The peak energy of each beam was carefully tuned to the 60 ± 1 kJ·mol^{-1} collision energy (FWHM ∼ 10 kJ·mol^{-1}) by precisely controlling the mixing ratio.

Time-of-flight profiles for the four gases were obtained after collision with three different self-assembled monolayers: CH_3-, NH_2- and OH-SAMs. Synthesis and characterization of these surfaces is explained in detail in Chapter 2. The TOF spectra were subsequently transformed into final translational-energy distributions, and are plotted in Figure 6.1. Accomodation fractions and average final translational energies for all twelve systems are summarized in Table 6.1.

Overall, the data in Figure 6.1 and Table 6.1 show that energy transfer from the impinging gaseous species is very efficient in collision with all three surfaces, with final average translational energies decreasing in the order Ne→CD_4 →ND_3 →D_2O on all surfaces. We see that the non-polar gases retain more of their initial translational energy after collision. Additionally, Ne and CD_4 show much hotter final translational-energy distributions when scattering from the hydrogen-bonding surfaces than when scattering from the methyl SAM. This is due in part to the glassy, hydrogen bonding network that forms at the interface of these monolayers.[8] This difference is eliminated when scattering the polar gases. In fact, D_2O has the largest TD component and lowest average final energy when scattering from the OH-SAM. The increased propensity for energy exchange and surface accomodation for the polar gases is attributable in part to the increased dipolar interactions they experience when interacting with the polar, hydrogen bonding surfaces. We attempt to explain this behavior in some detail in the remainder of this chapter. Our discussion, interpretation, and

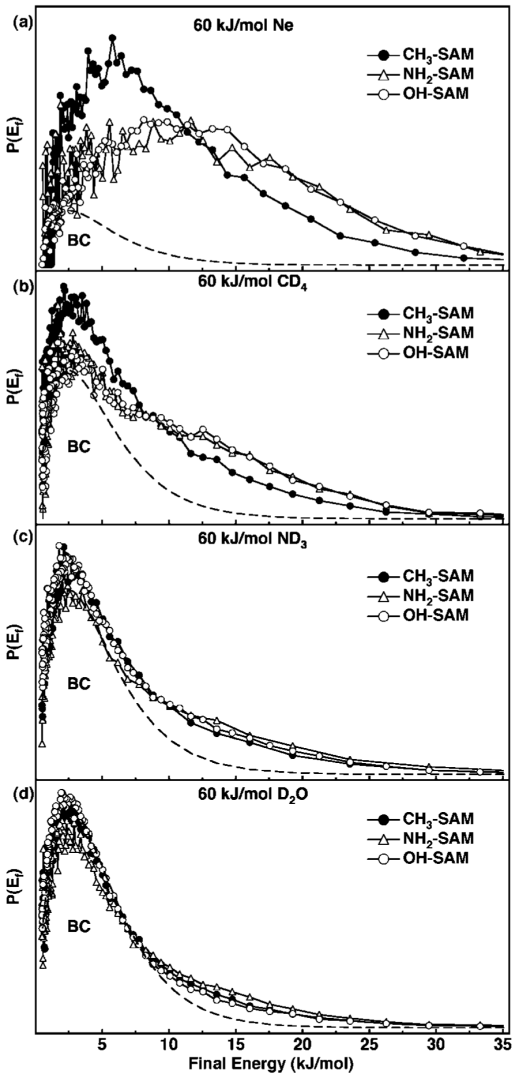

FIG. 6.1: Experimentally determined final translational-energy distributions for (a) Ne, (b) CD_4, (c) ND_3, and (d) D_2O scattering from CH_3, NH_2, and OH-SAMs. The dashed line in each panel represents the best fit for a Boltzmann distribution to the OH-SAM data at the temperature of the surface. Adapted from Ref. 10.

rationale for these differences seen in Figure 6.1 and 6.1 for the scattering behavior is aided by the use of ab initio calculations.

6.3. GAS/SURFACE POTENTIAL ENERGY CALCULATIONS

The extent of gas/surface energy exchange in interfacial collisions depends significantly on the rigidity and mass of the surface as well as the attractive forces between the impinging gas and the terminal groups of the surface. For the systems explored in the study, the attractive forces are expected to span a large range from the dispersion interactions that govern the attractions of the nonpolar gases with the CH_3-SAM, to strong hydrogen bonding interactions between the polar gases and the polar terminal groups of the OH- and NH_2-SAMs. Although the general trend in these attractive forces can be estimated from the

TABLE 6.1: Summary of 60 kJ·mol^{-1} Ne, CD_4, ND_3, and D_2O scattering from CH_3-, NH_3-, and OH-SAMs.[a]

	CH_3-SAM (α / <E'$_T$>)	NH_2-SAM (α / <E'$_T$>)	OH-SAM (α / <E'$_T$>)
Ne	0.39±0.01 / 10.6±0.2	0.30±0.01 / 14.1±0.2	0.22±0.01 / 14.4±0.2
CD_4	0.70±0.02 / 7.8±0.2	0.60±0.02 / 9.5±0.2	0.53±0.02 / 9.7±0.2
ND_3	0.78±0.02 / 7.0±0.2	0.72±0.02 / 8.4±0.2	0.78±0.02 / 7.6±0.2
D_2O	0.79±0.01 / 6.7±0.2	0.79±0.01 / 7.4±0.2	0.89±0.01 / 6.4±0.2

[a]The accomodation fraction, α, is the fractional area of the final translational-energy distribution fit by a Boltzmann component.

polarity and polarizability of the gases, we present a more rigorous determination of the potential using ab initio calculations.

Since it is impractical to map the entire gas/surface potential energy surface (PES) for every possible molecular orientation and impact parameter, we have focused on characterization of the minimum-energy gas/surface potential wells for Ne, CH_4, NH_3, and H_2O gases approaching a simple model of each SAM. The model SAMs are composed of a triad of molecules that are arranged to approximate the structure of the termini of three adjacent chains in an ideal CH_3-, NH_2-, or OH-SAM. Namely, the internuclear axes are 5.0 Å away from each other, and the three C (and N or O) atoms form an angle of 60°. Geometries for each of the gas/surface-mimic pairs were optimized at the MP2/aug-cc-pVDZ level of theory using the GAUSSIAN03 suite of programs.[11] The geometries and depths of the potential wells for each system were subsequently corrected for basis-set superposition error (BSSE) by applying the counterpoise method.[12] To preserve the 5.0 Å separation between chains and 60° arrangement, the heavy atoms of the surface mimic molecules (both C atoms in the CH_3-SAM mimic, C and O in the OH-SAM mimic, and C and N in the NH_2-SAM mimic) are held fixed during the optimization. All other variables are optimized.

Figure 6.2 illustrates the calculated optimized geometries for all twelve gas/surface-mimic systems explored in this work. For example, included in the figure are the minimum energy structures for an ammonia molecule approaching an NH_2-SAM (h) and an OH-SAM (i). The structures exhibited reveal that ammonia can establish three hydrogen bonds with either the NH_2- or OH-SAM. The extensive hydrogen bonding can lead to significant potential energy

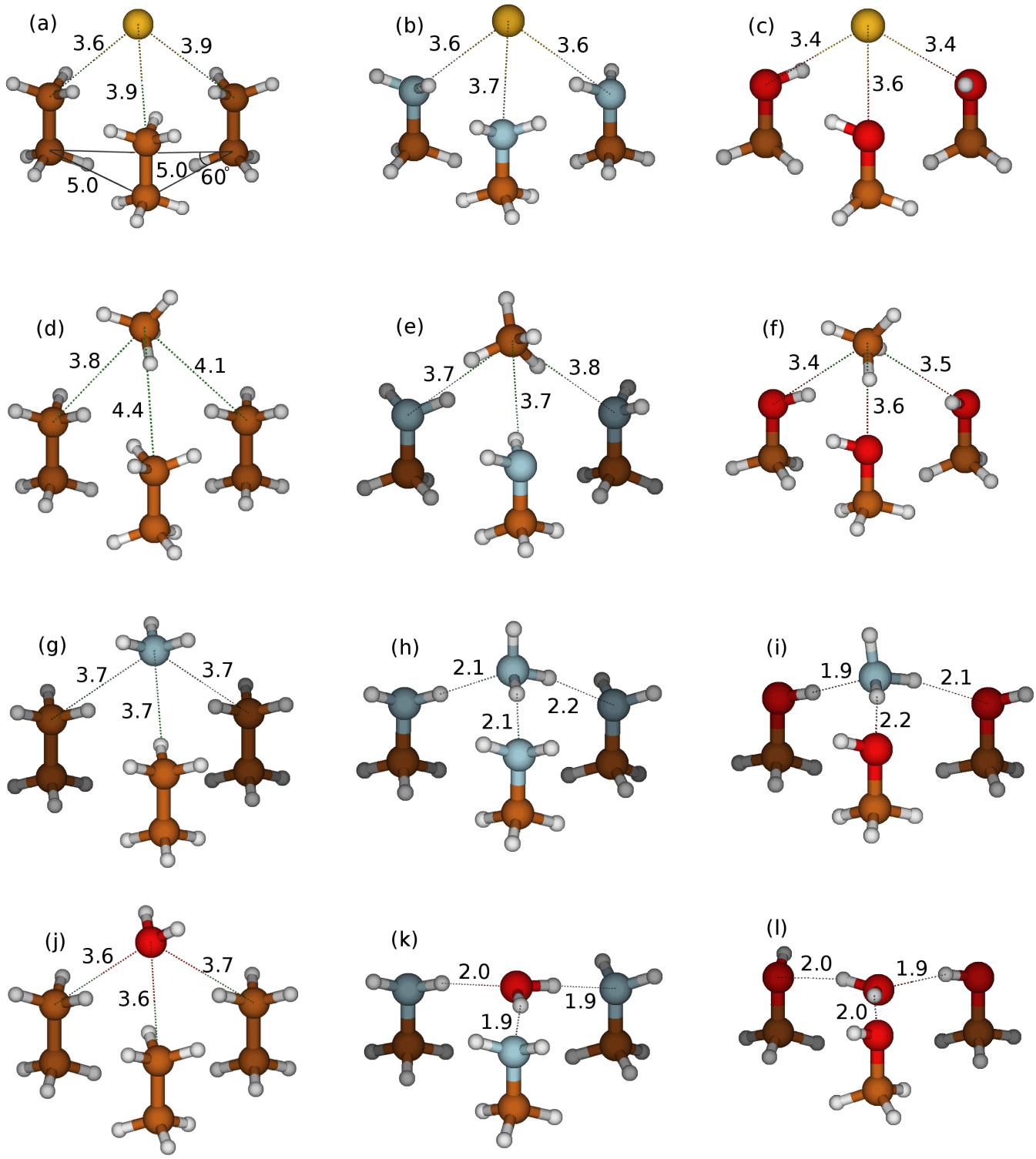

FIG. 6.2: Optimized geometries for the twelve gas/surface-mimic systems investigated in this work. Interatomic distances are given in Å.

TABLE 6.2: Energy of the potential-energy minima of gas/surface mimic pairs.[a]

	CH_3CH_3	CH_3NH_2	CH_3OH
Ne	0.3	0.5	0.6
CH_4	3.1	5.5	6.9
NH_3	6.1	33.5	49.0
D_2O	5.0	62.0	61.0

[a] Energies below the asymptote in $kJ \cdot mol^{-1}$ for the optimized geometry for each gas interacting with a model SAM, as described in the text.

wells. The counterpoise-corrected MP2/aug-cc-pVDZ minimum energy for the structure shown in Figure 6.2 is 33.5 $kJ \cdot mol^{-1}$ for NH_3 interacting with three methylamine molecules and is even greater, 49.0 $kJ \cdot mol^{-1}$, when it interacts with three methanol molecules. Similar calculations were performed for all 12 gas/surface combinations explored in the scattering experiments. The results are provided in Table 6.2.

Analysis of the well depths for a particular surface mimic reveals that the attractive forces generally increase in the following order: Ne $<CH_4 <NH_3 <H_2O$. In addition, the well depths for a particular gas approaching the three surfaces show the general trend of increasing in the order CH_3-SAM $<NH_2$-SAM <OH-SAM. However, Ne interacts relatively weakly with all three surfaces and its minimum energy is nearly independent of the surface terminal group. CH_4 interacts slightly more strongly than Ne with all of the surfaces due to its increased polarizability. The well depths of the interactions with the NH_2-SAM and OH-SAM are only slightly larger than for the CH_3-SAM. The depths of the potential wells for NH_3 increase with respect to CH_4 for all of the surface mimics examined. The difference with CH_4 is small for the CH_3-SAM but noticeable for the polar surfaces, with increases of over 25 $kJ \cdot mol^{-1}$ due to the presence of strong hydrogen bonds between NH_3 and the surface mimics. Finally, H_2O shows a well very similar to that of NH_3 for the CH_3-SAM, but remarkably deeper wells for the polar surfaces. The deeper well for H_2O relative to NH_3, for polar surfaces, is also reflected in the fact that the enthalpy of solvation for water in methanol (-47 $kJ \cdot mol^{-1}$) is nearly four times that of ammonia in methanol (-12 $kJ \cdot mol^{-1}$).[13] Overall, the calculations indicate that the hydrogen bonding ability of the H_2O and NH_3 molecules results in sharply enhanced interactions with the hydrogen bonding SAMs. Quantitatively, Figure 6.2 shows that H_2O and NH_3 can form up to three hydrogen bonds with the polar surfaces, leading to

a very stable complex. Earlier calculations of the minimum-energy structure of H_2O and a slightly different model of the OH-SAMs also showed the ability of a single water molecule to form three hydrogen bonds with the SAM.[14]

We note that caution should be exercised when using calculations of NH_3 or H_2O interacting with methylamine and methanol molecule triads to better understand the actual interactions of these gases with NH_2- of OH-SAMs. For instance, the locations of the backbones of the surface-mimic molecules are fixed so that they are parallel and 5.0 Å away from each other. Although 5.0 Å is the average separation between the chains in a SAM grown on Au(111), in the actual SAMs there is a degree of mobility that lifts the 5.0 Å constraint. Therefore, gas-phase molecules approaching a SAM will likely not encounter chain termini separated by exactly 5.0 Å and the interaction energies will be different from those reported here. Another point to consider is that it has been shown that OH-SAMs form extensive hydrogen bonding networks. Therefore, when a hydrogen bonding gas-phase molecule, such as ND_3 or D_2O, approaches a SAM possessing intrasurface hydrogen bonding, such as the NH_2- or OH-SAM, it is expected that the approaching molecule will compete with surface molecules adjacent to the impact site for hydrogen bonds. This effect will probably impair the idealized structures depicted in Figure 6.2, where no intrasurface hydrogen bonding is allowed. Furthermore, it should be noted that the structures and energies in Figure 6.2 and Table 6.2 correspond to the potential minima on the three surfaces. However, during actual collisions the system visits a variety of other regions of the highly multidimensional potential energy surfaces, which have not been described here. Despite these caveats, the PES calculations do highlight physically releveant trends that can serve as an approximation to the trends of the actual potentials. Below, the theoretical results are used to help construct an understanding of the dynamics that lead to the final energy distributions presented in Figure 6.1 and Table 6.1.

6.4. DISCUSSION

Gas-surface energy exchange and thermal accommodation have been explored for collisions of small polar and nonpolar molecules with ω-functionalized self-assembled monolayers. In general, we find that the final energy distributions are very broad, usually spanning over 20 kJ·mol^{-1} in energy. The large distribution of final energies is due to the variety of possi-

ble impact parameters and molecular orientations for the impinging molecules. In addition to the broad nature of the final energy distributions, the data reveal that overall energy transfer is extensive for every gas studied. Figure 6.1a shows that, for Ne, the $P(E'_T)$ distribution peaks at 6 kJ·mol^{-1} and that virtually no atoms escape the surface (at 30° to the normal) with greater than 40 kJ·mol^{-1} of energy. Previous experimental and theoretical studies have shown that the extensive energy transfer is due to the large number of energy-absorbing low-energy modes available within the surface, such as chain wagging motions, torsions, and vibrations.[15] However, the dynamics also depend markedly on the chemical and physical properties of the specific gas/surface interface. We find that the nonpolar gases, Ne and CD_4, transfer more energy to the nonpolar CH_3-terminated surface than to the polar, NH_2- and OH-SAMs. In contrast, the polar gases, D_2O and ND_3, have a larger tendency to thermally equilibrate with all of the surfaces studied. The following sections highlight the observed trends and provide a detailed discussion, augmented by potential-energy calculations, of the properties that control the extent of energy exchange and thermal accommodation in these gas/surface collisions.

6.4.1. Monolayer rigidity: Ne and CD_4 scattering

Table 6.2 shows that the Ne PES minima for all three SAMs are relatively small and that they are all very similar, two characteristics that make Ne an excellent probe of monolayer rigidity, as influenced by the outermost functional groups. For such small potential energy wells, the dynamics are dominated by single collision events with residence times of only 0.75 to 1 ps for the initial conditions of our experiment.[15–20] Such short interaction times for Ne limit the number of atoms along the alkane chains that can participate in the energy exchange event and the dynamics are governed by interactions with the terminal groups on these organic surfaces.[15–20] In addition, the nearly identical (within 0.3 kJ·mol^{-1}) Ne PES minima for all three surfaces enables one to attribute differences in the scattering dynamics to differing intramonolayer properties of the surfaces, rather than the gas/surface forces.

As described previously, the three SAMs employed in this work exhibit similar structures. For each SAM, the sulfur atoms are separated by 5.0 Å , the alkane chains are packed in an all-trans configuration, and the chains are tilted from the surface normal by 30°. However, the termini of the polar NH_2- and OH-SAMs tilt toward one another to form hydrogen bonds that

extend throughout the monolayer. Molecular dynamics simulations show that the hydrogen bonding network is so extensive that nearly every OH group in an OH-SAM participates as a hydrogen bond donor and acceptor.[2,3,8,9] Our results for Ne scattering suggest that this network has a significant effect on the final energy distributions for gas/surface collisions.

Figure 6.1 shows that the dynamics for Ne scattering from the OH- and NH_2-SAMs differ significantly from the non-hydrogen bonding CH_3-SAM. Specifically, the 60 kJ·mol^{-1} incident Ne atoms recoil from the CH_3-SAM with an average of only 10.6 kJ·mol^{-1} of energy, while Ne scatters from the polar SAMs with greater than 14 kJ·mol^{-1} of final translational energy. This difference is likely the result of the hydrogen bonding network that renders the polar SAMs more rigid than the nonpolar CH_3-SAM. These results are similar to prior observations for Ar scattering from a variety of ω-functionalized monolayers. Previous experimental studies suggested that the hydrogen bonding network that forms between alkane chains in OH-, NH_2-, and COOH-SAMs creates a more rigid collision partner by restricting the types of low-energy extended motions that facilitate energy transfer on non-hydrogen bonding CH_3- or $C(O)OCH_3$-SAMs.[21–26] The role of intramonolayer hydrogen bonding in gas/surface collisions has also been explored through theoretical studies of Ar impinging on OH- and CH_3-SAMs.[8] As observed for the Ne scattering data presented here, the molecular dynamics investigations demonstrate that the OH-SAM is significantly more rigid than the nonpolar CH_3-SAM.[8]

The overall dynamics governing CD_4 scattering from the CH_3-, NH_2-, and OH-SAMs mirror the dynamics for Ne scattering. However, the overall energy transfer is much greater than that for Ne scattering. In fact, the $P(E'_T)$ distributions for scattering from each SAM display a maximum intensity close to 2.5 kJ·mol^{-1}, the peak of a Boltzmann distribution at the temperature of the surface. The CD_4/SAM potential energy minimum is deeper than the Ne/SAM potential. The greater gas/surface attraction leads to more efficient energy transfer and, most likely, a significant amount of trapping followed by full thermal accommodation on the surfaces, as indicated by the much larger BC fractions of CD_4 with respect to Ne (see Table 6.1). Despite the larger potential and significant thermal accommodation for CD_4 scattering on all surfaces, the effect of relative rigidity of the polar SAMs continues to play a significant role in the energy exchange for CD_4.

An interesting final observation about the polar SAMs is that, according to the results of the molecular-beam experiments, the NH_2- and OH-SAMs have similar rigidities. For

instance, the final translational energies of Ne scattering off these two surfaces are within experimental error bars of one another (14.1 ± 0.5 and 14.4 ± 0.5 kJ·mol^{-1} for Ne/NH_2-SAM and Ne/OH-SAM, respectively, Table 6.1). Given that the initial collision energy is the same in both experiments and that the difference in the potential energy surfaces seems to be very small (the well depth in the Ne–CH_3NH_2 system is only 0.15 kJ·mol^{-1} shallower than that in the Ne–CH_3OH system at the MP2/aug-cc-pVDZ level, see Table 6.2), the scattering results imply that the physical properties of the surfaces are very similar.

6.4.2. Gas/surface attractive forces: ND_3 and D_2O scattering

The observed trends in the scattering dynamics for the polar gases, ND_3 and D_2O, are markedly different than the trends for Ne and CD_4. We find that nearly the entire $P(E'_T)$ for the polar gases can be described by a Boltzmann distribution at the surface temperature. That is, very few molecules that collide with the NH_2- or OH-SAMs escape without first thermally equilibrating on the surface. The PES calculations show that the large thermal components are due to the significant attractive forces between the polar gases and the functional groups at the interface. Large attractive forces enhance the overall energy exchange in two ways. First, during the approach to the surface, the molecules gain kinetic energy as they traverse the potential energy well. The PES calculations suggest that water molecules may gain as much as 60 kJ·mol^{-1} if the potential energy minimum conformation is achieved. Even if the impinging molecules do not fall directly into the absolute minimum, the attractive character of the gas/surface interactions will result in an acceleration of the gases prior to collision. This acceleration results in a total kinetic energy immediately before impact that can be notably larger than the nominal energy of our beams. The molecules then collide with the surface to transfer some fraction of their total energy. Following collision, the molecules again traverse the potential energy well and decelerate as they recoil from the surface. The net result of the well is to enhance the fraction of incident energy, 60 kJ·mol^{-1}, that is transferred to the surface. Second, the residence time on the surface for trapped molecules is exponentially proportional to the well depth. Longer residence times result in more collisions, which facilitate energy transfer and thermal accommodation. Our results indicate that these two effects are sufficient enough for ND_3 and D_2O collisions with the OH- and NH_2-SAMs to result in near complete thermal accommodation for both sur-

faces. Furthermore, it appears that the rigid nature of the intramonolayer hydrogen bonding network of these SAMs is countered by the strong attractive forces. Molecules that would otherwise skip impulsively off the rigid surfaces are instead pulled into the well, where they dissipate their remaining excess energy through multiple collisions.

Although attractive forces dominate the dynamics for the polar SAMs, the nonpolar CH_3-SAM also produces final energy distributions that are composed primarily of low-energy molecules that appear thermal in nature. As for Ne scattering, the relatively large BC intensity for ND_3 and D_2O scattering from the CH_3-SAM is due to the flexible nature of the chains within this monolayer that serve as an excellent energy sink for facile dissipation of the translational energy of the impinging gases. In addition, the BC fractions of ND_3 and D_2O are larger than those for CD_4 and Ne because, as reported in Table 3, the polar molecules establish stronger interactions with the CH_3-SAM than CD_4 and Ne.

Our observed trends in the scattering dynamics are very similar to those for previous molecular beam experiments involving collisions on polar and nonpolar liquid surfaces. Nathanson et al. reported that the final energy distributions for 55 kJ·mol^{-1} NH_3 and D_2O scattering from liquid glycerol and squalane are both composed of large trapping-desorption components and that trapping is most likely for D_2O impinging on the polar liquid, glycerol.[1] Furthermore, their studies revealed that the opposite trend applies to the nonpolar gases. Specifically, the high-energy impulsive channel is much more prominent in the final energy distributions for Ne and CH_4 scattering from the hydrogen bonding glycerol liquid than for these gases scattering from the pure hydrocarbon liquid.[1] Our results suggest that, for both SAMs and liquid surfaces, the interfacial hydrogen bonding network that can form between polar surface groups creates a more rigid or glassy surface and makes thermal accommodation and trapping of nonpolar gases less likely than for collisions on nonpolar hydrocarbon surfaces.

6.4.3. Impulsive scattering

While the extent of overall energy transfer follows trends that can be understood based on minimum energy arguments and surface rigidity, the differences between the energy distributions of the impulsively scattered molecules do not follow such trends. We have examined the final translational-energy distributions for only the impulsively scattered D_2O

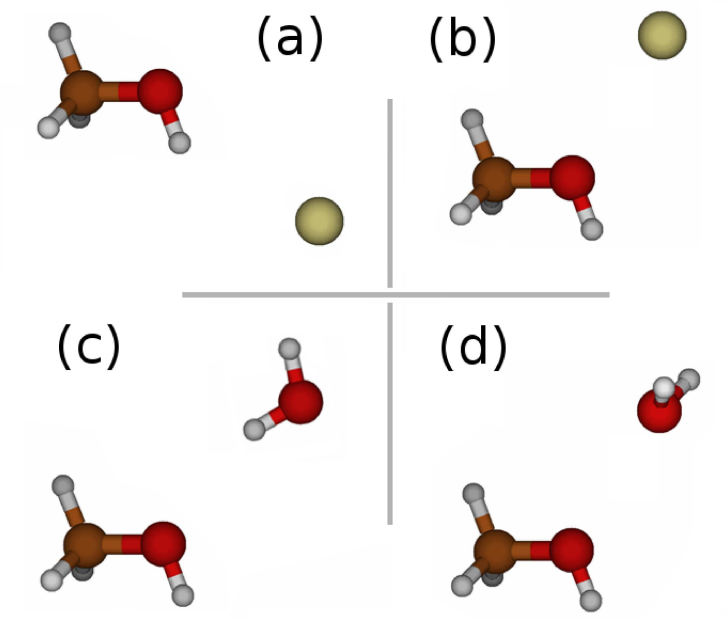

FIG. 6.3: Approach geometries used to investigate the directional nature of the dipolar interaction for the H_2O–O(H)CH_3 system, in comparison with Ne–O(H)CH_3.

and Ne off the OH-SAM. Although these gases represent the extremes in terms of their polarity and hydrogen bonding ability, the final energy distributions are nearly identical for E'$_T$ >12 kJ·mol^{-1}. This observation suggests that both gases experience similar dynamics for collisions that lead to the highest energy scattering. We find similar results for CD_4 and ND_3, suggesting the remarkable result that the dynamics for high-energy scattering depend little on the complexity of the gas. In addition, this result suggests that the potential energy surfaces that govern the dynamics of collisions leading to the highest final energies (i.e., single impulsive collision events) are very similar. If the potential energy wells were significantly different, simple kinematic descriptions of the dynamics show that the fractional energy transfer would be greatest for the molecule with the deepest well by a factor of $(1 + \frac{V}{E_{coll}})$, where V is the well depth.[27] Therefore, one may hypothesize that there exist particular orientations of the impinging D_2O molecule that exhibit a similar potential energy as Ne when it approaches the OH-SAM. It may be that these approach geometries are responsible for the similar impulsive scattering distributions, for E'$_T$ >12 kJ·mol^{-1}.

Not unexpectedly from the highly directional nature of dipole-dipole interactions, calculations show that the H_2O/OH-SAM PES depends markedly on the orientation of the water

molecule. Strong hydrogen bonding interactions and deep wells of 60 kJ·mol^{-1} occur for the approach geometry depicted in Figure 6.2, but the PES for the water molecule orientated with its lone pair toward one of the oxygen atoms of the SAM mimic exhibits a very small potential energy well. We speculate that the orientation of the D_2O molecules that scatter from the surface with the highest final energies are those that approach the OH-SAM with an orientation that leads to weak attractions or even a purely repulsive interaction with the terminal groups of the monolayer. We show in Figure 6.3 the geometry of the optimized Ne– and H_2O–$O(H)CH_3$ complexes, (a) and (c). These complexes give van der Waals well depths of 0.5 and 19.8 kJ·mol^{-1}, respectively. While the depth of the Ne well is due to its relatively weak polarizability, in H_2O–$O(H)CH_3$, water donates a hydrogen bond, making the complex substantially more stable. However, if H_2O approaches with its lone pairs directed toward the CH_3OH oxygen (d), the interaction is entirely repulive. Also included in the figure is Ne approaching CH_3OH along the same intermolecular axis, (b), which results a meager van der Waals well depth of 0.4 kJ·mol^{-1}. Therefore, incident water molecules that are oriented with the oxygen atom directed toward the O atom of the OH groups of the surface experience similar energy exchange as Ne atoms, because the PES well depths for Ne and D_2O, in this particular orientation, are similar. Similar calculations (not shown) with ammonia displayed the same behavior as for the H_2O–$O(H)CH_3$ system.

An important difference between Ne and D_2O is that the latter can gain rovibrational energy during the collision. Previous studies have demonstrated the important role that internal excitation of a gas-phase molecule can play during interfacial energy exchange. Hase and co-workers and Nesbitt and co-workers have recently shown that translational-to-vibrational (T→V') energy transfer is very inefficient in collisions with organic surfaces, but translational-to-rotational (T→R') energy transfer readily occurs.[28–32] In fact, they find that for CO_2 colliding with a liquid hydrocarbon, fluorocarbon, and model SAM, the molecules that do not trap on the surface scatter with rotational temperatures that can be as high as the final translational temperature. In the work presented here, if rotational excitation in D_2O arises at the expense of translational energy, this effect should be reflected in differences between the final energy distributions for the polyatomic gases and Ne. However, similar translational-energy distributions are seen for impulsively scattered D_2O and Ne. Therefore, either rotational excitation is limited for impulsively scattered D_2O, rotational excitation comes at the expense of energy transfer to the surface, or the molecules for which T→R'

energy transfer occurs are scattered to final angles not sampled by the fixed angle detector used in this work. We examine in subsequent chapters the influence of rovibrational modes on energy transfer in scattering of the diatomic molecules, N_2 and CO.

6.5. SUMMARY

Molecular beam studies of the energy exchange in collisions of Ne, CD_4, ND_3, and D_2O with CH_3-, NH_2-, and OH-SAMs have been conducted to explore how polar and nonpolar gases interact with hydrogen bonding and pure hydrocarbon organic surfaces. The experiments show that the model OH-, NH_2-, and CH_3-terminated self-assembled monolayer surfaces are all efficient energy sinks for impinging gases. Greater than 50% of the incident translational energy of each gas (60 kJ·mol^{-1}) is transferred into the low-energy modes of the monolayer for every system studied. The overall extent of energy transfer and full thermal accommodation depends on a balance between the rigidity of the SAM and the gas/surface attractive forces. The nonpolar gases, Ne and CD_4, show that the NH_2- and OH-SAMs are more rigid collision partners than the hydrocarbon CH_3-SAM. This result, in accord with previous rare gas scattering experiments and molecular dynamics simulations,[8,21–26] is due to the intramonolayer hydrogen bonding network that forms between the surface OH groups. The network serves to anchor the terminus of each monolayer chain, thereby restricting many of the low-energy motions within the monolayer that are responsible for the more extensive energy transfer into the CH_3-SAM. However, the polar gases, ND_3 and D_2O, have a deep enough potential energy well to become trapped very efficiently on the OH- and NH_2-SAMs and transfer essentially all of their collision energy, despite the rigidity of the monolayers.

In addition to studying the energy transfer of small gases scattering from solid organic surfaces, these experiments further enable direct comparisons to the dynamics of the same gases when they collide with liquids. Previous experiments that probed collisions of Ne, CH_4, NH_3, and D_2O with liquid glycerol, a hydrogen bonding liquid, and squalane, a liquid hydrocarbon,[1] have revealed unique insight into the first steps of gas solvation into a liquid. These studies correlated the enthalpies and free energies of solvation with the final energy distributions of the gases to show that the "like dissolves like" principle can be used to predict the relative energy transfer and rate of approach to thermal equilibrium. The overall trends in the extent of energy exchange and the thermal accommodation fractions for the

gas/liquid collisions are remarkably similar to the dynamics of the same gases scattering from well-ordered, densely packed self-assembled monolayers. The similarities suggest that the structure of an organic surface is not as important as the character of the interfacial functional groups in determining the final trends in the overall scattering dynamics. Furthermore, the comparison implies that SAMs may be a good model of liquid organic surfaces for exploring general trends in gas/surface collision dynamics.

Acknowledgments

A large portion of the work presented in this chapter formed the basis of Megan E. Bennett's Masters thesis.

REFERENCES

[1] M. E. Saecker and G. M. Nathanson, J. Chem. Phys. **99**, 7056 (1993).

[2] J. Hautman, J. P. Bareman, W. Mar, and M. L. Klein, J. Chem. Soc., Faraday Trans. **87**, 2031 (1991).

[3] M. Sprik, E. Delamarche, B. Michel, U. Rothlisberger, M. L. Klein, and H. Wolf, Langmuir **10**, 4116 (1994).

[4] L. H. Dubois, B. R. Zegarski, and R. G. Nuzzo, J. Am. Chem. Soc. **112**, 570 (1990).

[5] R. G. Nuzzo, B. R. Zegarski, and L. H. Dubois, J. Am. Chem. Soc. **109**, 733 (1987).

[6] A. Ulman, Chem. Rev. **96**, 1533 (1996).

[7] G. E. Poirier, E. D. Pylant, and J. M. White, J. Chem. Phys. **104**, 7325 (1996).

[8] U. Tasic, B. S. Day, T.-Y. Yan, J. R. Morris, and W. L. Hase, J. Phys. Chem. C **112**, 176 (2008).

[9] H. Klein, N. Battaglini, B. Bellini, and P. Dumas, Mater. Sci. Eng., C **2002**, 279 (2002).

[10] M. E. Bennett, W. A. Alexander, J. Lu, D. Troya, and J. R. Morris, J. Phys. Chem. C **112**, 17279 (2008).

[11] M. J. Frisch, G. W. Trucks, H. B. Schlegel, G. E. Scuseria, M. A. Robb, J. R. Cheeseman, J. A. Montgomery, Jr., T. Vreven, K. N. Kudin, J. C. Burant, et al., *Gaussian 03, revision c.02* (2004).

[12] S. F. Boys and F. Bernardi, Mol. Phys. **19**, 553 (1970).

[13] V. Majer and V. Svoboda, *Enthalpies of Vaporization of Organic Compounds: A Critical Review and Data Compilation* (Blackwell Scientific Publications, Oxford, UK, 1985).

[14] P. G. Silvestrelli, F. Ancillotto, F. Toigo, C. Sbraccia, T. Ikeda, and M. Boero, ChemPhysChem **6**, 1889 (2005).

[15] T.-Y. Yan and W. L. Hase, J. Phys. Chem. B **106**, 8029 (2002).

[16] T.-Y. Yan, W. L. Hase, and J. C. Tully, J. Chem. Phys. **120**, 1031 (2004).

[17] T.-Y. Yan, N. Isa, K. D. Gibson, S. J. Sibener, and W. L. Hase, J. Phys. Chem. A **107**, 10600 (2003).

[18] T.-Y. Yan and W. L. Hase, Phys. Chem. Chem. Phys. **4**, 901 (2000).

[19] T.-Y. Yan, W. L. Hase, and J. R. Baker, J. Chem. Phys. **329**, 84 (2000).

[20] B. S. Day, J. R. Morris, and D. Troya, J. Chem. Phys. **122**, 214712 (2005).

[21] M. K. Ferguson, J. R. Lohr, B. S. Day, and J. R. Morris, Phys. Rev. Lett. **92**, 073201 (2004).

[22] B. S. Day, G. M. Davis, and J. R. Morris, Anal. Chim. Acta. **496**, 249 (2003).

[23] B. S. Day, S. F. Schuler, A. Ducre, and J. R. Morris, J. Chem. Phys. **119**, 8084 (2003).

[24] J. R. Lohr, B. S. Day, and J. R. Morris, J. Phys. Chem. B **105**, 15469 (2005).

[25] J. R. Lohr, B. S. Day, and J. R. Morris, J. Phys. Chem. A **110**, 1645 (2006).

[26] G. Bracco, J. Acker, M. D. Ward, and G. Scoles, Langmuir **18**, 5551 (2002).

[27] M. Head-Gordon, J. C. Tully, C. T. Rettner, C. B. Mullins, and D. J. Auerbach, J. Chem. Phys. **94**, 1516 (1991).

[28] B. G. Perkins, Jr., T. Haber, and D. J. Nesbitt, J. Phys. Chem. B **109**, 16396 (2005).

[29] B. G. Perkins, Jr. and D. J. Nesbitt, J. Phys. Chem. B **110**, 17126 (2006).

[30] B. G. Perkins, Jr. and D. J. Nesbitt, J. Phys. Chem. A **111**, 7420 (2007).

[31] A. M. Zolot, W. W. Harper, B. G. Perkins, Jr., P. J. Dagdigian, and D. J. Nesbitt, J. Chem. Phys. **125**, 021101 (2006).

[32] E. Martinez-Nunez, A. Rahaman, and W. L. Hase, J. Phys. Chem. C **111**, 354 (2007).

Chapter 7

Theoretical study of the N_2 and CO–CH_4, –CF_4 intermolecular potential-energy surfaces

Reproduced in part with permission from W. A. Alexander, J. R. Morris, and D. Troya, *J. Chem. Phys.* **130**, 084702 (2009). Copyright 2009 American Institute of Physics.

7.1. INTRODUCTION

As was described in Chapter 4, the ability of a chemical dynamics simulation to reliably predict experimental properties is highly dependent on the quality of the potential-energy surface used when integrating the equations of motion. One common practice in developing intermolecular potential-energy surfaces has been to use information gained from crossed-beams experiments.[1–4] While these gas-phase-based potentials have been shown to give qualitative agreement with scattering experiment, they are usually not sufficient to give predictive, quantitative results. Another approach to building intermolecular potential-energy surfaces is fitting multiparametric analytic functions to high-quality ab initio data.[5–12] Advances in computational technology allow the affordable calculation of highly-accurate ab initio datasets for systems of increasing size and complexity. If a method is used which introduces minimal errors in the fitting process, these high-quality ab initio data can be used to construct predictive potential-energy surfaces.

Within this chapter, we detail our efforts in the derivation of accurate analytic potential energy surfaces for use in chemical-dynamics simulations of diatomic molecules with hydrocarbon and fluorocarbon surfaces. As the energy transfer dynamics of rare gases impinging on organic surfaces is nearing a nearly complete level of understanding within the scientific community, research in gas/organic-surface scattering has begun to shift toward diatomic and polyatomic molecule scattering, with an emphasis on obtaining state-to-state information.[13–22] Study of the scattering dynamics of inert diatomic molecules from organic surfaces extends our previous investigations of rare-gas scattering. With diatomic molecules, we can examine the influence of rovibrational degrees of freedom on the collision dynamics and how these additional energy modes manifest deviation from rare-gas scattering behavior.

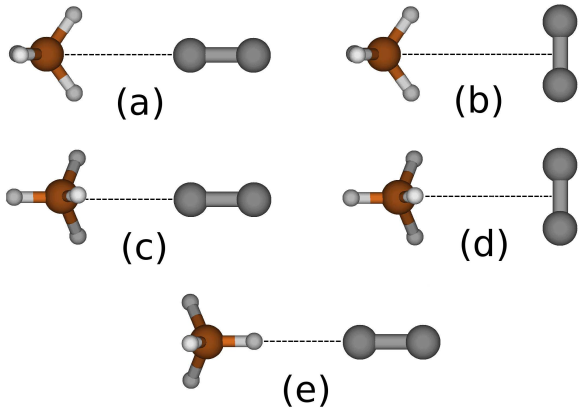

FIG. 7.1: Schematic of the N_2–CX_4 (X = H, F) orientations investigated with ab initio calculations in this work.

In this work, we present accurate ab initio calculation of the N_2 and CO-CH_4 and CF_4 systems. The ab initio data are used to derive pair-wise analytic potential-energy surfaces that can be used in dynamics simulations of collisions of N_2 and CO with regular and fluorinated alkanethiol SAMs. In addition, the N_2 potentials have been designed to be additionally accurate at hyperthermal collision energies such as those important in gas/surface collisions in low-earth orbit.

7.2. ELECTRONIC STRUCTURE CALCULATIONS

7.2.1. Computational details

We have calculated intermolecular potential-energy curves for the N_2 and CO–CH_4, –CF_4 systems by scanning the X–CY_4 (X=N_2, CO; Y=H, F) center-of-mass coordinate from the asymptote to repulsive energies of about 1300 kJ·mol^{-1} for N_2 and 200 kJ·mol^{-1} for CO. The separation between the points of the scan is 0.1 Å. The equilibrium tetrahedral geometry of the CH_4 and CF_4 molecules, as well as the equilibrium N_2 and CO bond lengths, have been held fixed throughout the scans (r(C-H)=1.089 Å, r(C-F)=1.330 Å, r(N-N)=1.098 Å, and r(C-O)=1.128 Å). Our approach and methods follow those described in Chapter 4 in which we presented a detailed study of the Ne, Ar, Kr, and Xe–CH_4, –CF_4 intermolecular potential energy surfaces. In that study, three approaches ("facial", "vertex", and "edge") were investigated. In this work, we have investigated a total of five and nine different

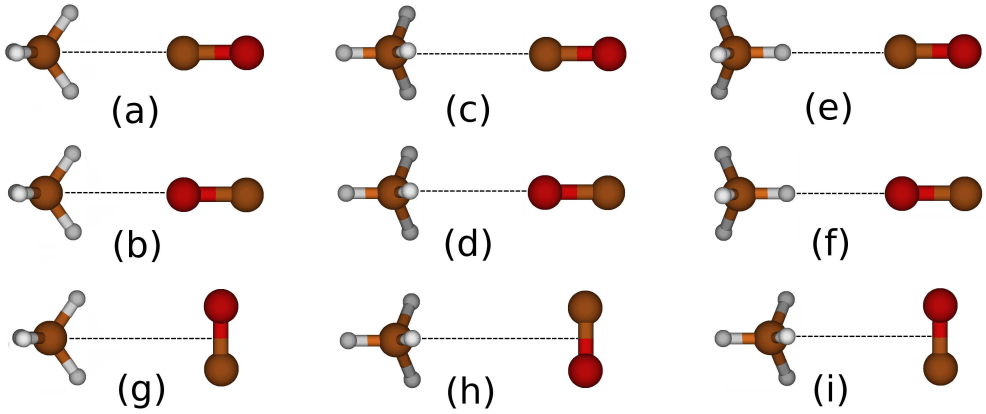

FIG. 7.2: Schematic of the CO–CX_4 (X = H, F) orientations investigated with ab initio calculations in this work. Carbon atoms are brown and oxygen atoms are red.

approaches of N_2 and CO, respectively, to CH_4 and CF_4, which are depicted in Figures 7.1 and 7.2, respectively.

For N_2, we have calculated three approaches, a, c, and e (see Fig. 7.1) in which the nitrogen molecule approaches the CX_4 molecule collinearly to the scan axis, and two approaches, b and d, in which the nitrogen approaches perpendicularly to the N_2–CX_4 scan axis. Approaches a and b are the diatomic analogs of the rare-gas "edge" approaches, c and d correspond to "facial", and e to the "vertex" approaches. Similarly, for CO, (see Fig. 7.2), in approaches a-f, the CO molecule approaches the CX_4 molecule collinearly to the scan axis, while in g-i, the CO molecule approaches perpendicularly to the scan axis. Approaches a, b, and g are "edge" analogs, c, d, h, and i correspond to "facial", and e, and f to "vertex" approaches.

The electronic Schrödinger equation has been solved at each step of the scans using second-order Möller-Plesset perturbation theory in combination with the double, triple, and quadruple-ζ family of correlation-consistent basis sets of Dunning,[23–25] augmented with diffuse functions (aug-cc-pVDZ, aug-cc-pVTZ, and aug-cc-pVQZ, respectively). Coupled cluster calculations with explicit single and double excitations and perturbative treatment of triple excitations (CCSD(T)) have also been carried out with the aug-cc-pVDZ basis set. The focal-point approach of Allen and co-workers[26,27] has been used to estimate CCSD(T) energies with the aug-cc-pVTZ and aug-cc-pVQZ basis sets from MP2 calculations with those basis sets. (Hereafter, focal-point CCSD(T) energies will be referred to as fp-CCSD(T).)

The focal-point approach has been extensively examined in Chapter 4 and its legitimacy has been demonstrated by our group and others in the description of rare-gas–hydrocarbon systems[28–30] (see Chapter 4). Complete basis set (CBS) estimates are obtained for both MP2 and fp-CCSD(T) calculations using the two-point extrapolation procedure of Halkier et al.[31] We have removed the basis-set superposition error using the standard counterpoise method[32] in all of the points of the calculated potential-energy surfaces. The electronic-structure calculations have been carried out with the Gaussian03 suite of programs.[33]

7.2.2. Ab initio intermolecular potentials for N_2 and CO–CH_4, –CF_4

We display in Figure 7.3 intermolecular potential-energy curves for approach (d) of the N_2–CF_4 system, which gives the deepest van der Waals well, as function of intermolecular distance calculated with a variety of ab initio levels. The intermolecular potential-energy curves show the expected features of a steep repulsive wall at short distances, and a shallow attractive well at longer separations due to stabilizing intermolecular interactions. An examination of the dependence of the N_2–CH_4 intermolecular potential on the basis set reveals that, for MP2 calculations, an increase in the size of the basis set results in lower intermolecular energies. In addition, the location of the van der Waals wells occur at shorter N_2–molecule distances with larger basis sets. The MP2 method converges quickly with increasing basis set size, so the difference between aug-cc-pVDZ and aug-cc-pVTZ energies is larger than that between the aug-cc-pVTZ and aug-cc-pVQZ data. The root-mean-square deviation (RMSD) between MP2/aug-cc-pVDZ and aug-cc-pVTZ energies is 3.06 kJ·mol^{-1} for the overall 150 points calculated for the five approaches of the N_2–CH_4 system that result in energies less than ∼200 kJ·mol^{-1}, while the RMSD between aug-cc-pVTZ and aug-cc-pVQZ data decreases to 0.89 kJ·mol^{-1}.

Comparison of the CCSD(T) and MP2 data with the aug-cc-pVDZ basis set reveals how treating electron correlation influences the characteristics of the potential-energy surface. We find the differences between MP2 and CCSD(T) data to be small, with a RMSD of 1.74 kJ·mol^{-1} over all approaches. The differences between these two methods is especially small in the region of the energy minima. For instance, CCSD(T) predicts the well depth of approach (d) to vary by less than 0.3 kJ·mol^{-1} from the MP2 estimate.

The RMSD analysis here has focused on the region of the intermolecular potential im-

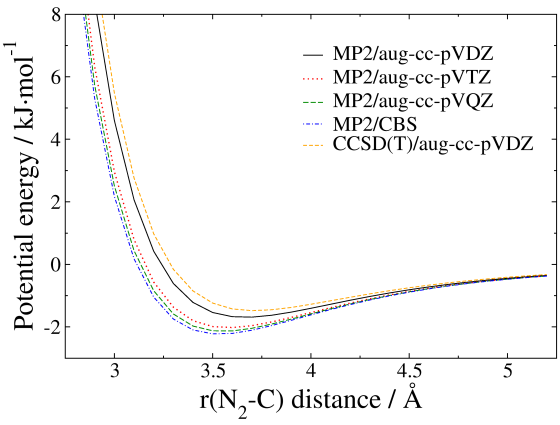

FIG. 7.3: Calculated intermolecular potential energy for the N_2–CH_4 system as a function of N_2 center-of-mass–C distance. Displayed curves are for the (d) approach orientation (see Fig. 7.1).

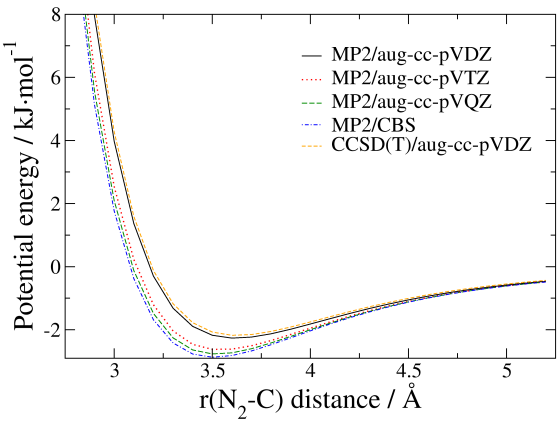

FIG. 7.5: Calculated intermolecular potential energy for the N_2–CF_4 system as a function of CO center-of-mass–C distance. Displayed curves are for the (d) approach orientation (see Fig. 7.1).

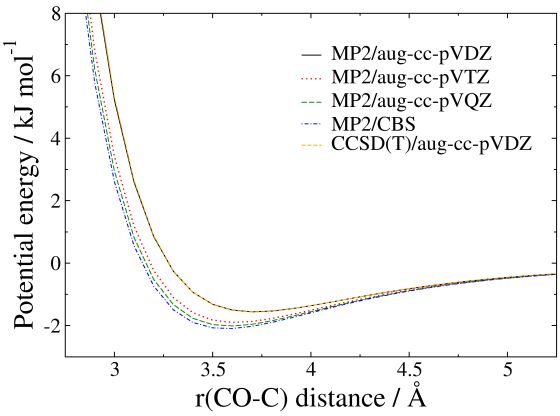

FIG. 7.4: Calculated intermolecular potential energy for the CO–CH_4 system as a function of CO center-of-mass–C distance. Displayed curves are for the (i) approach orientation (see Fig. 7.2).

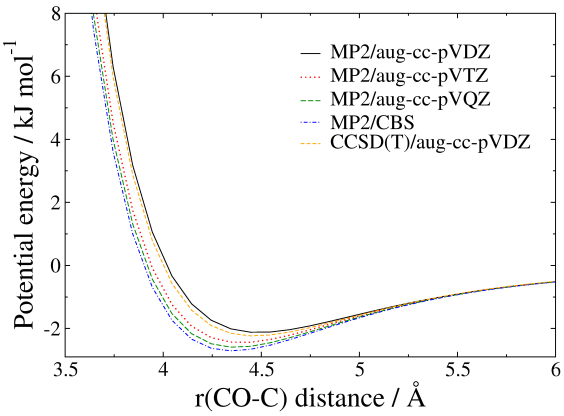

FIG. 7.6: Calculated intermolecular potential energy for the CO–CF_4 system as a function of CO center-of-mass–C distance. Displayed curved are for the (c) approach orientation (see Fig. 7.2).

MP2/CBS corresponds to a complete basis set limit estimate based on MP2 energies.

portant and accessible in our molecular-beam experiment. However, the potential curves have been carried out to repulsive energies of up to 1300 kJ·mol^{-1} (∼12 eV), which is the energetic regime important for collisions occuring at the surface of spacecraft in low earth

orbit. All of these points have been included in the analytic fits described later. Inclusion of all points up to 1300 kJ·mol^{-1} increases the RMSDs to 15.66, 4.16, and 3.59 kJ·mol^{-1} for the MP2/aug-cc-pVDZ:aug-cc-pVTZ, MP2/aug-cc-pVTZ:aug-cc-pVQZ, and MP2/aug-cc-pVDZ:CCSD(T)/aug-cc-pVDZ comparisons, respectively.

Figure 7.4 shows the intermolecular potential-energy curve of the CO–CH_4 approach, (i), that yields the deepest well as a function of the separation between the centers of mass of the ineracting molecules as predicted by various ab initio methods. The same general features are seen in the CO-CH_4 system as were observed with N_2, a steep repulsive wall at short distances and a shallow attractive well at longer separations. Increasing in basis set size lowers the calculated intermolecular energies and shifts the location of the van der Waals wells to shorter CO–molecule distances. The root-mean-square deviation (RMSD) between MP2/aug-cc-pVDZ and aug-cc-pVTZ energies is 3.12 kJ·mol^{-1} for the overall 270 points calculated in the nine approaches of the CO–CH_4 system, while the RMSD between aug-cc-pVTZ and aug-cc-pVQZ data decreases to 0.90 kJ·mol^{-1}. The MP2 and CCSD(T) methods with the aug-cc-pVDZ basis gives a minor RMSD of 0.70 kJ·mol^{-1} over all approaches, with characteristic deviations in the well minimum of only 0.01 kJ·mol^{-1} [approach (i)] between the MP2 and CCSD(T) methods.

We present in Figure 7.5 [7.6] the intermolecular potential-energy trace that corresponds to the N_2–CF_4 [CO–CF_4] approach, (d) [(c)], with the deepest van der Waals well as a function of ab initio method. The fluorinated systems behave analogously to the methane systems with respect to the size of basis set; larger basis sets lead to deeper van der Waals minima with shorter gas–C separation distances. Over all approaches, the RMSD between MP2/aug-cc-pVTZ and aug-cc-pVQZ results is 3.35 [3.05] kJ·mol^{-1}, decreasing to 1.21 [1.15] kJ·mol^{-1} between the MP2/aug-cc-pVTZ and aug-cc-pVQZ data sets. The differences between the CCSD(T) and MP2 methods are also minor, with a RMSD of 1.27 [0.60] kJ·mol^{-1} for all approaches. In general, the CF_4 van der Waals wells are deeper and at larger intermolecular distances than the analogous CH_4 potential, although this is not rigorously true for all approaches. For instance, N_2–CH_4 yields its deepest well (1.96 kJ·mol^{-1} at 3.60 Å) in a facial approach with the N_2 internuclear axis perpendicular to the scan axis, while N_2–CF_4 yields its deepest well (2.77 kJ·mol^{-1} at 4.04 Å) in a parallel facial orientation.

While the above analysis for the N_2–CF_4 system has considered the overall 140 points that result in energies less than ∼200 kJ·mol^{-1}, as with the CH_4 system, we have carried

TABLE 7.1: Parameters of the Buckingham potential describing the N_2–CX_4 (X = H,F) interactions.[a]

pair	A_{ij}	B_{ij}	C_{ij}
N-H	3366.087	3.281	-10.617
N-C(H)	39318.987	3.371	-1304.885
N-F	40563.816	3.736	-292.613
N-C(F)	11605.192	3.443	-315.400

[a]Units are such that if internuclear distances are given in Å, then the potential energy is in kcal·mol^{-1}.

out calculations up to hyperthermal energies for inclusion in the analytic fits described later. When considering all points up to 1300 kJ·mol^{-1}, the RMSDs increase to 22.00, 6.28, and 11.69 kJ·mol^{-1} for the MP2/aug-cc-pVDZ:aug-cc-pVTZ, MP2/aug-cc-pVTZ:aug-cc-pVQZ, and MP2/aug-cc-pVDZ:CCSD(T)/aug-cc-pVDZ comparisons, respectively. From these ab initio data we have obtained fp-CCSD(T)/CBS energies that will be used in the fit.

7.3. ANALYTIC INTERMOLECULAR POTENTIAL-ENERGY SURFACES

7.3.1. Intermolecular potentials for the N_2–CX_4 (X=H, F) systems

The analytic intermolecular potential-energy surfaces are constructed as a sum of two-body functions, where each two-body term is expressed as a Buckingham potential of the form:

$$V_{ij} = A_{ij}\, e^{-B_{ij}\, r_{ij}} + \frac{C_{ij}}{r_{ij}^6} \tag{7.2}$$

where r_{ij} is the internuclear distance between the atoms of each pair, and A_{ij}, B_{ij}, and C_{ij}, are adjustable parameters specific to each pair of atoms. For both the N_2–CH_4 and N_2–CF_4 systems there are two pairs of atoms, arising from N atom with the C orH(F) atoms of the CH_4(CF_4) molecules. We have used a nonlinear least-squares procedure to obtain the values of the A_{ij}, B_{ij}, and C_{ij} parameters that minimize the relative differences between analytic energies obtained with the Buckingham potentials and the fp-CCSD(T)/CBS data.

Each of the fits includes a total of about 170 points distributed roughly evenly between the five approaches and covers regions of the potential-energy surface from the asymptote

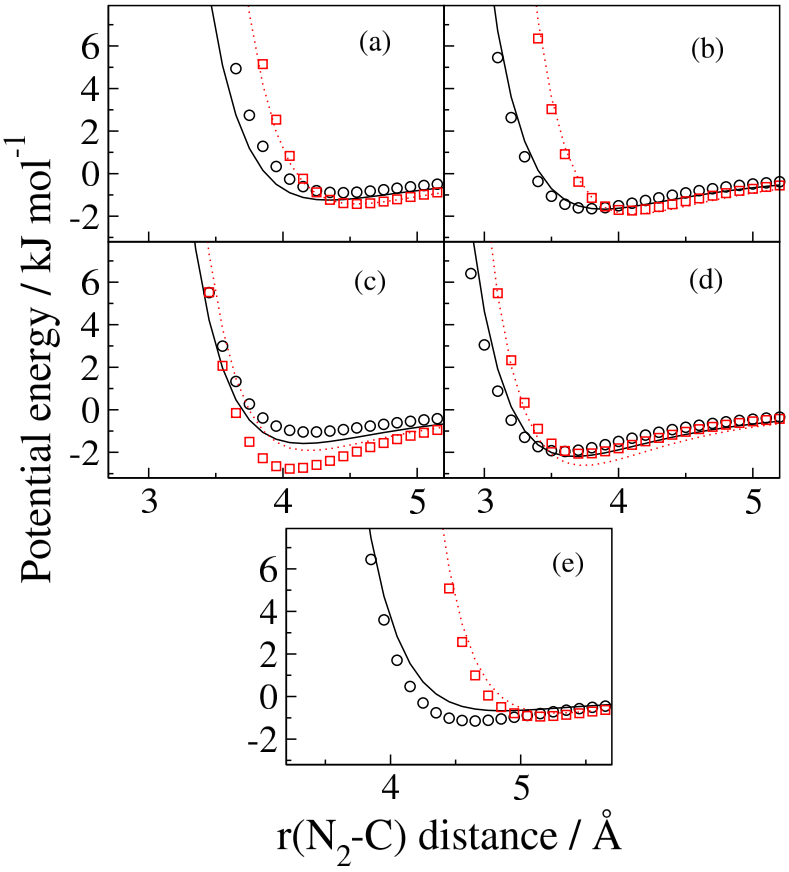

FIG. 7.7: Comparison of fp-CCSD(T)/CBS and analytic intermolecular potential-energy surfaces for the N_2–CH_4 and –CF_4 systems. (a)-(e) correspond to the approach geometries shown in Figure 7.2. ∘ N_2–CH_4, ab initio data; — N_2–CH_4, fit; □ N_2–CF_4, ab initio; ··· N_2-CF_4, fit

up to 13 eV (∼1300 kJ·mol^{-1}). This represents a substantially higher repulsive energy than that attainable for investigation in our scattering experiment. However, we decided to build a potential that would be able to be used at high collision energies for use in simulations of high-energy collision processes such as those that would occur on the surface of spacecraft in low-earth orbit. Notes about the fitting procedure are as follows: Care was given in the fits to ensure that the Ae^{-Br} term is repulsive and that the second term, C/r^6, is attractive. These constraints help to ensure that the potential is well-behaved for geometries outside of those explicitly inlcuded in the fit. Neither allowing the inverse r^6 term to vary its exponent, nor incoporation of additional D/r^n terms led to significant improvements in the quality of fit. Particular emphasis was given to the description of the repulsive wall region by weighting points greater than 20 kcal·mol^{-1} by a factor of 20.0. Additionally, for points between 0.10

TABLE 7.2: Comparison of ab initio and analytic energy and geometry of the van der Waals mimima for N_2–CH_4, –CF_4 systems.[a]

	N_2–CH_4		N_2–CF_4	
approach[b]	ab intio	fit	ab initio	fit
a	0.90 (4.44)	1.24 (4.34)	1.43 (4.44)	1.43 (4.44)
b	1.65 (3.80)	1.67 (3.90)	1.74 (4.10)	1.90 (4.10)
c	1.04 (4.24)	1.59 (4.14)	2.77 (4.04)	1.90 (4.14)
d	1.96 (3.60)	2.19 (3.70)	2.06 (3.70)	2.61 (3.70)
e	1.15 (4.64)	0.67 (4.94)	0.94 (5.14)	0.78 (5.24)

[a]Energies below the asymptote in kJ·mol^{-1}. Values between parentheses correspond to the distance between the centers of mass of the N_2–CX_4 pairs in angstroms. The ab initio data correspond to fp-CCSD(T)/CBS values.

[b]The approach geometries are depicted in Figure 7.2

and -0.10 kcal·mol^{-1}, absolute, as opposed to relative, differences were taken for our fitting procedure.

The optimum parameters of the Buckingham potential we obtained for the systems studied in this work are shown in Table 7.1. A direct comparison between the analytic and ab initio data for the five approaches to each N_2-CX_4 (X = H, F) pair is displayed in Figure 7.7. The table shows that the N_2–CX_4 center-of-mass separation at the minima furnished by the analytic potential-energy surface is generally within 0.15 Å of the fp-CCSD(T)/CBS estimates. Average deviations for the N_2–CH_4 and N_2–CF_4 systems are 0.09 and 0.10 Å, repectively, with approaches A (N_2–CH_4) and E (N_2–CF_4) having the largest discrepancies of 0.34 and 0.18 Å, respectively. The agreement between the analytic and ab initio well minima is overall quite good, with average deviations of only 0.25 kJ·mol^{-1} for all approaches, and with a maximum deviation of 0.92 kJ·mol^{-1} for approach C (N_2–CF_4).

7.3.2. Intermolecular potentials for the CO–CX_4 (X=H, F) systems

Using the highest-level ab initio information for the CO–CH_4, CO–CF_4 systems (fp-CCSD(T)/CBS), we have constructed two-body analytic potentials that can be used to

TABLE 7.3: Parameters of the Buckingham potential describing the CO–CX_4 (X = H,F) interactions.[a]

pair	A_{ij}	B_{ij}	C_{ij}	n_{ij}
C-H	10561.1	3.687	-239.429	6.379
O-H	163266.2	4.545	-12598.797	10.070
C-F	55797.7	3.849	-1750.947	7.22
O-F	86837.9	3.930	-346.116	6.857
C-C(H)	163265.8	4.037	-22898.515	9.569
O-C(H)	64909.9	3.865	-0.917	1.549
C-C(F)	4073.1	3.023	-151582.132	16.046
O-C(F)	24750.9	3.453	-1257.451	6.012

[a]Units are such that if internuclear distances are given in Å, then the potential energy is in kcal·mol^{-1}.

TABLE 7.4: Comparison of ab initio and analytic energy and geometry of the van der Waals mimima for CO–CH_4, –CF_4 systems.[a]

	CO–CH_4		CO–CF_4	
approach[b]	ab intio	fit	ab initio	fit
a	0.85 (4.74)	0.82 (4.44)	1.30 (4.84)	1.10 (4.74)
b	1.00 (4.18)	1.19 (4.08)	1.54 (4.28)	1.72 (4.28)
c	0.94 (4.54)	0.84 (4.24)	2.85 (4.34)	1.74 (4.34)
d	1.17 (3.98)	1.35 (3.98)	2.70 (3.88)	2.14 (3.98)
e	1.31 (4.84)	0.81 (4.74)	0.83 (5.44)	0.47 (5.54)
f	1.12 (4.48)	0.81 (4.58)	1.04 (4.88)	0.97 (4.98)
g	1.77 (3.80)	1.34 (3.80)	1.66 (4.10)	1.80 (4.10)
h	2.05 (3.60)	1.49 (3.60)	1.93 (3.80)	2.66 (3.70)
i	2.10 (3.60)	1.49 (3.60)	1.82 (3.80)	2.63 (3.70)

[a]Energies below the asymptote in kJ·mol^{-1}. Values between parentheses correspond to the distance between the centers of mass of the CO–CX_4 pairs in angstroms. The ab initio data correspond to fp-CCSD(T)/CBS values.

[b]The approach geometries are depicted in Figure 7.2

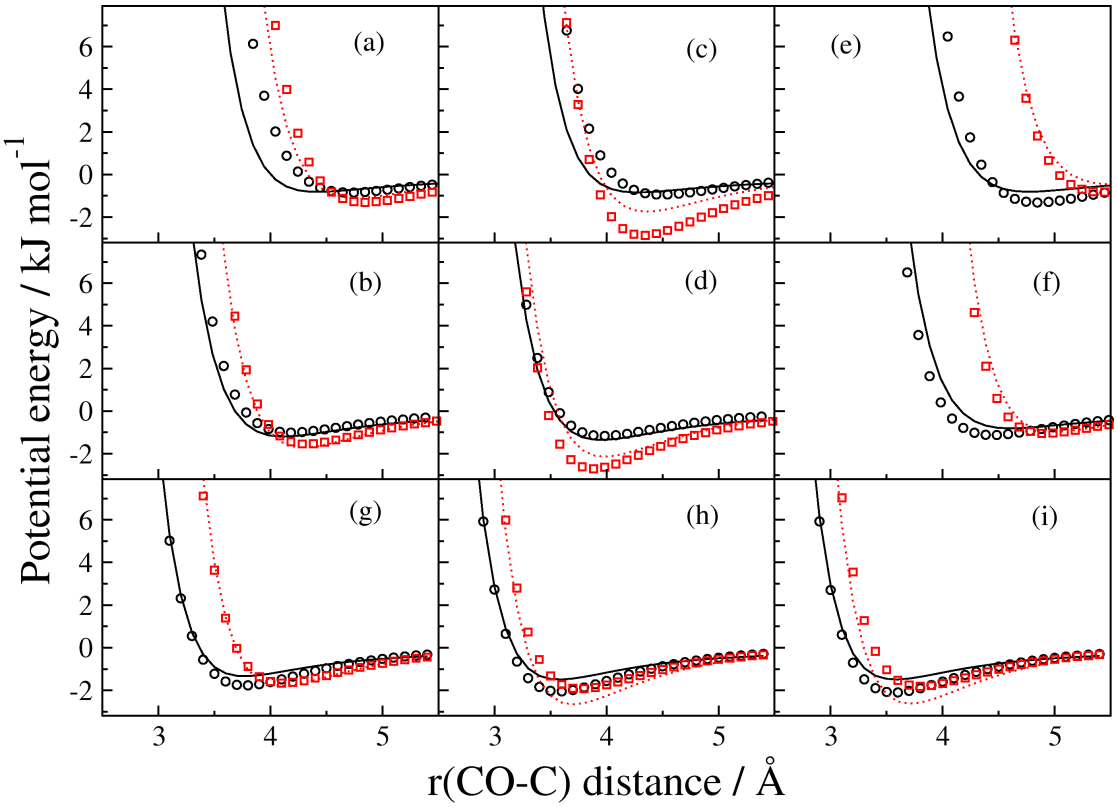

FIG. 7.8: Comparison of fp-CCSD(T)/CBS and analytic intermolecular potential-energy surfaces for the CO–CH_4 and –CF_4 systems. (a)-(i) correspond to the approach geometries shown in Figure 7.2. ∘ CO–CH_4, ab initio data; — CO–CH_4, fit; □ CO–CF_4, ab initio; ··· CO-CF_4, fit

describe the CO/CH_3-SAM and CO/CF_3-SAM gas/surface potential-energy surface. The potentials are sum of two-body functions, where each two-body term is expressed as a Buckingham potential of the form:

$$V_{ij} = A_{ij}\, e^{-B_{ij}\, r_{ij}} + \frac{C_{ij}}{r_{ij}^{n_{ij}}} \tag{7.3}$$

where r_{ij} is the internuclear distance between the atoms of each pair, and A_{ij}, B_{ij}, C_{ij}, and n_{ij} are adjustable parameters specific to each pair of atoms. For both CO–CH_4 and CO–CF_4 systems there are four pairs of atoms, arising from the interactions of the C atom of CO with the C or H(F) atoms of the CH_4(CF_4) molecules, and the O atom of CO with the same atoms of CH_4(CF_4). We have used a nonlinear least-squares procedure to obtain the values of the A_{ij}, B_{ij}, C_{ij}, and n_{ij} parameters that minimize the relative differences between analytic energies obtained with the Buckingham potentials and the fp-CCSD(T)/CBS data for the hundreds of points contained in the potential-energy-surface scans described before.

The two-body Buckingham potentials provide an adequate representation of all nine approaches of CO to the CH_4 and CF_4 molecules. However, we note that in relation to our previous work on rare gas-hydrocarbon systems,[28,29] the added complexity of the diatomic molecule results in slightly less accuracy in fitting the Buckingham potential. Each of the fits includes a total of about 270 points distributed roughly evenly between the nine approaches and covers regions of the potential-energy surface from the asymptote up to $\sim$200 kJ·mol^{-1}. Particular emphasis was given to the description of the repulsive region by giving points >80 kJ·mol^{-1} increased weight during the fit. These points were weighted by factors of 2.0 and 5.0 for the CO–CH_4 and CO–CF_4 systems, respectively. Additionally, for points between 0.40 and -0.40 kJ·mol^{-1}, absolute, as opposed to relative, differences were taken for our fitting procedure. This procedure ensured a minimization of root-mean-square deviation (RMSD) values in the repulsive region of the potenial, while maintaining a good fit globally for the nine approaches. The average relative errors between fp-CCSD(T)/CBS calculations and our fitted values in the repulsive region are 22.7 and 12.4% for the CO–CH_4 and CO–CF_4 systems, respectively. Average absolute deviations in the region of the attractive well are 0.22 and 0.31 kJ·mol^{-1}, for the same systems.

The optimum parameters of the Buckingham potential we obtained for the systems studied in this work are shown in Table 7.3. A direct comparison between the analytic and ab initio data for the nine approaches to each CO–CX_4 (X = H, F) pair is displayed in Figure 7.8, and the location and depth of the van der Waals wells for all approaches are shown in Table 7.4. The table shows that the CO–CX_4 center-of-mass separation at the minima furnished by the analytic potential-energy surface is generally within 0.10 Å of the fp-CCSD(T)/CBS estimates. Average deviations for the CO–CH_4 and CO–CF_4 systems are 0.10 and 0.07 Å, repectively, with approaches (a) and (c) for the CO–CH_4 system both having the largest discrepancies of 0.30 Å. The agreement between the analytic and ab initio well minima is overall quite good, with average deviations of only 0.39 kJ·mol^{-1} for all approaches for both systems, and with a maximum deviation of 1.11 kJ·mol^{-1} for approach (c) (CO–CF_4). We note that these discrepancies are substantially smaller than the collision energy of the scattering calculations (60 kJ·mol^{-1}), and therefore their effect should be minor.

TABLE 7.5: Comparison of calculated and experimental N_2 spectroscopic parameters.[a]

parameter	Calculated	Experiment[b]
ω_e	2358.58607	2358.57
$\omega_e\chi_e$	17.4083	14.3241
B_e	1.99785	1.99824
α_e	0.019819	0.0173
D_e	5.733838×10^{-6}	5.73727×10^{-6}

[a] Units are cm^{-1}. [b] From Ref. 35.

TABLE 7.6: Comparison of calculated and experimental CO spectroscopic parameters.[a]

parameter	Calculated	Experiment[b]
ω_e	2168.892	2169.756
$\omega_e\chi_e$	12.84978	13.28803
B_e	1.931583	1.931602
α_e	0.016300	0.017505
D_e	6.128×10^{-6}	6.1216×10^{-6}

[a] Units are cm^{-1}. [b] From Ref. 36.

7.4. MORSE POTENTIALS FOR N_2 AND CO STRETCHING

Although we have presented here a chapter detailing our derivation of intermolecular potential-energy surfaces for the N_2 and CO–CX_4 (X=H,F) systems, we also need an accurate description of the intramolecular potential for both the gas-phase diatomic molecules and the SAM surface to obtain accurate scattering behavior. The SAM surface intramolecular potential is built with standard molecular-mechanics force fields and is detailed in Chapter 3. Within this section, we describe the fitting of analytic N_2 and CO intramolecular potentials.

A standard Morse function is used to describe the N_2 molecular stretch potential:

$$V_{CO} = D[1 - e^{-\beta(r-r_e)}]^2 \tag{7.4}$$

where D, β, and r_e are the bond dissociation energy, curvature of the potential well at its minimum, and the equilibrium bond length, respectively. D and r_e are taken to be 955.88 kJ·mol^{-1} and 1.0977 Å,[34] respectively. The value of β=2.68908 Å^{-1} was determined by fitting to established experimental values of N_2's spectroscopic constants.[35] The resulting spectroscopic constants obtained with our Morse potential are compared to reference values in Table 7.5. As can be seen from the data in the table, spectroscopic constants calculated from our Morse potential parameters are in excellent agreement with experiment

To appropriately describe the CO molecule, D and r_e are taken to be 1094.83 kJ·mol^{-1} and 1.128 Å.[37] The value of β=2.28656 Å^{-1} was determined by fitting to established experimental values of CO's spectroscopic constants.[36] The resulting fundamental frequency and rotational constant obtained for the CO Morse potential are ω_e=2168.892 cm^{-1} and

B_e=1.931583 cm^{-1}, which are in excellent agreement with the experimental values of ω_e=2169.756 cm^{-1} and B_e=1.931602 cm^{-1}.[36]

7.5. CONCLUDING REMARKS

Analytic potential-energy surfaces required to carry out N_2 and CO/SAM scattering simulations have been derived from extensive electronic-structure calculations of the interaction potentials between N_2 and CO and the CH_4 and CF_4 molecules. Highly-accurate focal point-CCSD(T) calculations extrapolated to the complete basis set limit have been performed along five (nine) approaches of N_2 (CO) to the CH_4 and CF_4 molecules to obtain a good coverage of the global potential-energy surfaces. Using our ab initio information at that level, we have derived analytic potential-energy surfaces based on two-body Buckingham potentials. The analytic potentials accurately reproduce the ab initio data and result in a model applicable to N_2 and CO interactions with alkanes and fluoroalkanes. In the subsequent three chapters, we use these analytic potentials to perform molecular-dynamics simulations of N_2 and CO scattering from CH_3- and CF_3-SAMs.

REFERENCES

[1] B. S. Day, J. R. Morris, and D. Troya, J. Chem. Phys. **122**, 214712 (2005).

[2] K. D. Gibson, N. Isa, and S. J. Sibener, J. Phys. Chem. A **110**, 1469 (2006).

[3] G. Liuti, F. Pirani, U. Buck, and B. Schmidt, Chem. Phys. **126**, 1 (1988).

[4] B. P. Reid, M. J. O'Loughlin, and R. K. Sparks, J. Chem. Phys. **83**, 5656 (1988).

[5] S. B. M. Bosio and W. L. Hase, J. Chem. Phys. **107**, 9677 (1997).

[6] T.-Y. Yan, W. L. Hase, and J. R. Barker, Chem. Phys. Lett. **329**, 84 (2000).

[7] T.-Y. Yan and W. L. Hase, Phys. Chem. Chem. Phys. **4**, 901 (2000).

[8] T.-Y. Yan, N. Isa, K. D. Gibson, S. J. Sibener, and W. L. Hase, J. Phys. Chem. A **107**, 10600 (2003).

[9] X. Huang, B. J. Braams, and J. M. Bowman, J. Phys. Chem. A **110**, 445 (2006).

[10] X. Zhang, B. J. Braams, and J. M. Bowman, J. Chem. Phys. **124**, 021104 (2006).

[11] Z. Jin, B. J. Braams, and J. M. Bowman, J. Phys. Chem. A **110**, 1569 (2006).

[12] X. Zhang, S. Zou, L. B. Harding, and J. M. Bowman, J. Phys. Chem A **108**, 8980 (2004).

[13] B. G. Perkins, Jr., , T. Haber, and D. J. Nesbitt, J. Phys. Chem. B **109**, 16396 (2005).

[14] B. G. Perkins, Jr. and D. J. Nesbitt, J. Phys. Chem. B **110**, 17126 (2006).

[15] B. G. Perkins, Jr. and D. J. Nesbitt, J. Phys. Chem. A **111**, 7420 (2007).

[16] B. G. Perkins, Jr. and D. J. Nesbitt, J. Phys. Chem. B **112**, 507 (2008).

[17] B. G. Perkins, Jr. and D. J. Nesbitt, Proc. Natl. Acad. Sci. **105**, 12684 (2008).

[18] A. J. Kenyon, A. J. McCaffery, C. M. Quintella, and M. D. Zidan, J. Chem. Soc., Faraday Trans. **89**, 3877 (1993).

[19] A. J. Kenyon, A. J. McCaffery, C. M. Quintella, and M. D. Zidan, Faraday Discuss. **96**, 245 (1993).

[20] P. A. J. Bagot, C. Waring, M. L. Costen, and K. G. McKendrick, J. Phys. Chem. C **112**, 10868 (2008).

[21] E. Martinez-Nunez, A. Rahaman, and W. L. Hase, J. Phys. Chem. C **111**, 354 (2007).

[22] J. J. Nagueira, S. A. Vazquez, O. A. Mazyar, W. L. Hase, B. G. Perkins, Jr., D. J. Nesbitt, and E. Martinez-Nunez, J. Phys. Chem. A **113**, in print (2009).

[23] T. H. Dunning, Jr., J. Chem. Phys. **90**, 1007 (1989).

[24] D. E. Woon and T. H. Dunning, Jr., J. Chem. Phys. **98**, 1358 (1993).

[25] A. K. Wilson, D. E. Woon, K. A. Peterson, and T. H. Dunning, Jr., J. Chem. Phys. **110**, 7667 (1999).

[26] A. L. L. East and W. D. Allen, J. Chem. Phys. **99**, 4638 (1993).

[27] A. G. Csaszar, W. D. Allen, and H. F. Schaefer, III, J. Chem. Phys. **108**, 9751 (1998).

[28] W. A. Alexander and D. Troya, J. Phys. Chem. A **110**, 10834 (2006).

[29] U. Tasic, P. Hein, and D. Troya, J. Phys. Chem. A **111**, 3618 (2007).

[30] J. R. Cooper and N. Moazzen-Ahmadi, J. Chem. Phys. **444**, 28 (2007).

[31] A. Halkier, T. Helgaker, P. Jorgensen, W. Klopper, H. Koch, J. Olsen, and A. K. Wilson, Chem. Phys. Lett. **286**, 243 (1998).

[32] S. F. Boys and F. Bernardi, Mol. Phys. **19**, 553 (1970).

[33] M. J. Frisch, G. W. Trucks, H. B. Schlegel, G. E. Scuseria, M. A. Robb, J. R. Cheeseman, J. A. Montgomery, Jr., T. Vreven, K. N. Kudin, J. C. Burant, et al., *Gaussian 03, Revision C.02*, Gaussian, Inc., Wallingford, CT, 2004.

[34] J. M. L. Martin, J. Chem. Phys. **97**, 5012 (1192).

[35] K. P. Huber and G. Herzberg, *Molecular Spectra and Molecular Structure: IV. Constants of Diatomic Molecules* (Van Nostrand Reinhold, New York, 1979).

[36] A. LeFloch, Mol. Phys. **72**, 133 (1991).

[37] *http://webbook.nist.gov/chemistry.*

Chapter 8

Experimental and theoretical study of collision energy on CO and N_2 scattering from CH_3- and CF_3-terminated alkanethiolate self-assembled monolayers

Reproduced in part with permission from W. A. Alexander, J. R. Morris, and D. Troya, *J. Chem. Phys.* **130**, 084702 (2009). Copyright 2009 American Institute of Physics.

8.1. INTRODUCTION

A detailed understanding of how gas-phase species exchange energy upon collision with organic surfaces is essential for a full characterization of gas/surface interfacial chemistry. The study of translational energy transfer from an impinging gas-phase species to an organic surface is of fundamental importance as the gas-phase species in many heterogeneous chemical processes must accommodate thermally on the surface before finding the proper transition-state geometry for subsequent reaction to occur.[1] These Langmuir-Hinselwood-type processes may be highly dependent on the initial collisional impact with the organic surface and the surface's ability to dissipate excess energy into bath modes. Early molecular-beam scattering studies by Nathanson and co-workers, in which they scattered various small-molecule and atomic gases from a variety of organic liquids, have provided some of the most detailed insight into gas/surface collision dynamics.[2–5] They found the scattered gases' final translational-energy distributions to be bimodal, with a low-energy thermal desorption component characterized by a Boltzmann distribution at the surface temperature. The high-energy component of the distribution was attributed to impulsive collision events in which the gas' brief encounter with the surface limits energy transfer and thermalization. The consensus has since been that, in most cases, the dynamics of gas/organic surface collisions can be understood by two main mechanisms: impulsive scattering and trapping desorption. Among the liquids studied by Nathanson and co-workers are squalane (2,6,10,15,19,23-hexamethyltetracosane), glycerol, and perfluoropolyether (PFPE). Compar-

ison of the scattering properties of these liquids reveals a critical dependence on liquid composition, while the varying chemical and physical properties of the impinging probe gases play only a secondary role in the dynamical outcome.[2,3] Their studies examined translational energy exchange as a result of collision, and revealed that accommodation decreases with an increase in collision energy. Overall, energy transfer and accommodation fractions for the probe gas to the surface were seen to increase when scattering from the squalane surface relative to the glycerol and PFPE. While kinematics plays the major role in the differences between scattering dynamics of squalane and PFPE, squalane and glycerol should behave similarly, as they have similar effective surface masses. However, the glycerol hydroxyl groups can participate in hydrogen bonding, forming a rigid, glassy network that effectively limits energy transfer into the low-energy, high amplitude motions that have been shown to be important for efficient dissipation of the collision energy. (We investigated the effect of hydrogen-bonding networks on energy-transfer dynamics in collisions of small molecules with polar SAM surfaces in Chapter 6, and our results generally agree with those of Nathanson.) Overall, PFPE is the most rigid surface and yields the smallest accommodation fractions, with squalane being the most accommodating, and glycerol showing intermediate behavior.

CO_2 scattering from the PFPE surface with a collision energy of $\sim$44 kJ·mol^{-1} also showed evidence for nonequilibrium dynamics with a two-channel model of thermal and impulsive scattering in the work of Perkins and Nesbitt.[6] Doppler profiles were well modeled by assuming that the translational-energy distributions of impulsively-scattered molecules are determined by a single superthermal temperature. Rotational-state measurements indicated that the rotational temperature of impulsively-scattered CO_2 molecules was essentially the same as their translational temperature.[7] Further studies probed the effect of collision energy on final translational and rotational energy distributions.[6] As collision energy was increased from 6.7 to 44 kJ·mol^{-1}, scattered CO_2 showed an increase in average translational and rotational energy, and in the fraction of impulsively-scattered molecules. Additionally, CO_2 was found to have an increased impulsive-scattering component when scattering from PFPE relative to squalane.[6]

Use of SAMs has enabled detailed studies of gas/organic-surface energy transfer that augment the above-mentioned efforts with organic liquids. Of the gas/SAM scattering studies, those involving rare-gas collisions are the most mature. Rare-gas/SAM studies have investigated a wide range of properties, and some have looked at the influence of initial collision

energy on the energy transfer dynamics.[8–12] Collectively, these studies show that an increase in the incident translational energy results in an increase in the impulsive-scattering component, and a decrease in accommodation. At the theoretical level, complementary molecular dynamics simulations have unveiled a wealth of details concerning the mechanisms governing the scattering of rare gases from SAMs. Of particular importance are the pioneering studies of Hase and co-workers.[13–17] Their work demonstrated, among other effects, that the scattered molecules that give rise to the low energy, trapping-desorption component of the final translational-energy distribution are not only composed of trapped gases, but that an impinging gas may transfer enough energy in just one encounter to appear "thermal." This study had the additional impact of determining that atoms interacting with the surface through an impulsive-scattering mechanism may have more than one encounter with the surface (a few surface hops) and still retain large fractions of their incident energy and memory of their direction of travel.

When an atom collides with a surface, the only energy transfer allowed is from the impinging gas's collisional energy to the surface degrees of freedom. Use of gas-phase polyatomic molecules in gas/surface collision studies brings added degrees of freedom that potentially can be involved in energy transfer and reveal richer collision dynamics than that of rare-gas systems. Understanding how gas/surface energy transfer dynamics is influenced by the addition of rovibrational degrees of freedom in the scattered molecule is of relevance in light of recent experiments by Nesbitt et al., described above, and those of Lohr and co-workers, who scattered HCl from hydroxyl- and methyl-terminated monolayers.[18,19] These efforts drew inspiration from work in the late 1980's by Cohen et al., who investigated O_2 and NO scattering from amphiphillic monolayers with incident collision energies (E_{coll}) of $\sim$9 kJ·mol^{-1}.[8] Those studies revealed that O_2 retained a larger fraction of its translational energy when scattering from a perfluorinated acid ester (PFAE) monolayer than when scattering from an n-octadecyltrichlorosilane (OTS) SAM and seemed to follow rare-gas trends. NO scattering from these monolayers showed a reversal of trends in overall energy transfer. A subsequent study of NO scattering at higher collision energies ($\sim$10-50 kJ·mol^{-1}) revealed that as the collision energy was increased, the properties of the recoiling NO varied. While scattering at E_{coll} $\sim$9 kJ·mol^{-1} showed greater translational energy loss in collision with the PFAE surface,[8] scattering at E_{coll} $\sim$28 kJ·mol^{-1} showed enhanced energy transfer when colliding with the OTS surface.[20] Furthermore, for collisional energy in excess of $\sim$30 kJ·mol^{-1},

the authors found PFAE and OTS to elicit nearly the same behavior. This trend can be explained as follows. At low collision energies (i.e. 9 kJ·mol^{-1}), long-range attractive forces are influential in the outcome of collision. The increased dipolar attractions between the NO and PFAE surface allow for greater thermalization and energy transfer of NO to the PFAE surface in comparison to the OTS surface. Apolar O_2 scattering at the same conditions does not experience an enhanced dipolar environment and its scattering outcome is determined by kinematic aspects of the collision. As NO collision energy increases, kinematics overcomes the attractive forces and dominates the dynamics. Finally, at higher collision energy, the momentum of NO is high enough such that the inertial barrier to energy transfer imposed by the increase in surface mass due to fluorination is overcome and the two surfaces act similarly.

One limitation with the gas/liquid studies by Nesbitt and co-workers is that the probed surfaces vary in their supramolecular structure and, as a result, separation of chemical and structural effects on the dynamics is difficult. The above-mentioned use of SAMs by Cohen et al. ameliorates some of these difficulties, but the OTS and PFAE surfaces still vary greatly in their chain tilts, packing densities, and intrachain twist angles. The use of SAMs built from CH_3- and CF_3-terminated alkanethiols on gold substrates solves this problem. These two surfaces have identical structure[21–25] [other than the slightly different C-X (X=H, F) bond lengths] and therefore any differences in scattering dynamics from these surfaces can be attributed primarily to the exposed groups.

In this work, we investigate the dynamics of N_2 and CO scattering from CH_3- and CF_3-SAM surfaces using classical-trajectory simulations and molecular-beam scattering experiments with the main goal of understanding the effect of initial collision energy of the gas-phase species on gas/organic-surface energy transfer, as well as the influence of surface mass (via fluorination) on the dynamics. Several are the reasons for our choice of N_2 and CO as the impinging gas-phase molecules. First, N_2 and CO are diatomic molecules, which represent a natural first step in the transition from atomic to polyatomic scattering. Second, they are closed-shell species, which precludes reaction with the SAM surfaces at the conditions of this study and therefore permits a convenient characterization of inelastic energy transfer. The fact that they are closed-shell species also facilitates the electronic-structure calculations required to derive accurate potential-energy surfaces for the molecular-dynamics calculations involved in this work (see Chapter 7).

8.2. CLASSICAL-TRAJECTORY CALCULATIONS

Using the analytical potential-energy surfaces described in Chapter 7, we have performed classical-trajectory calculations of collisions of the N_2 and CO molecules with both regular (CH_3-terminated) and ω-fluorinated (CF_3-terminated) alkanethiol self-assembled monolayers. Our trajectory integration scheme is detailed in Chapter 3, so only a brief description of details relevant to this work is provided here.

We have integrated batches of 2000 trajectories for N_2 and CO with E_{coll}=43, 60, and 86 kJ·mol^{-1}. (10000 trajectories are included for the CO systems at E_{coll}=60 kJ·mol^{-1}.) Initial conditions for the N_2 and CO molecules were determined via quasi-classical sampling of the ground vibrational and rotational states as implemented in the VENUS96 computer program.[26] At the beginning of each trajectory, the molecule was placed above the surface, at a separation of at least 10 Å from the closest surface atom. The initial conditions (coordinates and momenta) of the surface are taken as intermediate steps of a 0.5 ns canonical simulation of the SAM at 300 K. In the scattering calculations, we use SAMs composed of 36 thiolate chains (S-$(CH_2)_{11}$-CH_3 or S-$(CH_2)_{11}$-CF_3 for CH_3- and CF_3-SAMs, respectively) that are replicated in two dimensions using the periodic-boundary-conditions algorithm of the TINKER package of programs.[27] The initial azimuthal angle formed by the incident gas velocity vector and the tilt direction of the SAM chains is randomly selected to establish fair comparison with experiment. The initial spatial orientation of N_2 and CO was randomly assigned via rotation through random Euler's angles.

The trajectories were stopped post-collision when the gas either recoiled to a distance of 12 Å from the closest atom of the surface, or, in the case of long-trapping times, after 15 ps. Those trajectories stopped as a result of long trapping times are assumed to have the gas molecule fully thermalized with the surface, and the molecules are randomly assigned final translational-energies, E'_T, and rovibrational states, v', j' based on Boltzmann distributions at the surface temperature and a final polar angle, θ_f, based on a random distribution.

From the initial and final coordinates and momenta of the molecule, scattering properties including final translational-energy distributions and rotational state distributions were determined. Examination of the coordinates and momenta during the trajectory was used to provide mechanistic understanding of the collisions.

8.3. EXPERIMENTAL DETAILS

As in our previous studies, the SAMs were prepared via spontaneous chemisorption of the corresponding alkanethiol from ∼1 mM ethanolic solutions onto clean gold surfaces.[12,28–31] The substrates used in this study were prepared by Au evaporation onto Cr-coated glass slides (EMF Corp.) and were cleaned in pirahna solution prior to use. Previous work using SAMs prepared on both gold-coated glass and gold-coated mica slides found the scattering results to have an insignificant dependence on the underlying substrate used for the monlayer, despite the differences in the polycrystalline structure of the two gold surfaces.[28] Hexadecanethiol (CH_3-$(CH_2)_{15}$-SH) was obtained from Aldrich and used as received. 16,16,16-Trifluorohexadecanethiol (CF_3-$(CH_2)_{15}$-SH) was prepared as described by Lee and coworkers according to established procedures.[21] After immersion in the solutions for at least 24 h, the slides were removed, rinsed with copious amounts of ethanol, dried under a stream of nitrogen, and transferred via a load-lock system into the scattering chamber. The main ultrahigh-vacuum (UHV) chamber operates at a base pressure of $<5\times10^{-10}$ torr, which rises to $\sim1\times10^{-9}$ torr during a scattering experiment.

Molecular beams of ^{13}CO and $^{15}N_2$ seeded in H_2 were created via standard supersonic expansion techniques.[32] Isotopically labeled, 99% pure, ^{13}CO and $^{15}N_2$ were obtained from Cambridge Isotopes and used to distinguish the scattered molecules from background N_2 in our chamber. The incident translational-energy profile was characterized by monitoring the pulsed beam's peak arrival time with a mass spectrometer (Stanford Research Systems) located in the beam path. The resulting beams, ∼4% probe gas in H_2, yielded peak incident energies of 43 and 60 kJ·mol^{-1} with full width at half maximum values of ∼16 kJ·mol^{-1}. Attempts were made to obtain an 86 kJ·mol^{-1} CO beam, but the necessary dilution resulted in negligible signal intensity and the efforts were abandoned. No attempts were made to bring the N_2 beam to this higher energy as the signal-to-noise ratio was already poor at 60 kJ·mol^{-1} and further dilution would not have yielded useful data.

Details of our scattering experiment have been presented in Chapter 2. Briefly, the well-collimated pulsed beam of molecules enters an ultrahigh-vacuum chamber containing the SAMs at room temperature. After collision, the recoiling gas-phase molecules are detected with an Extrel mass spectrometer tuned to m/e=29.0 (^{13}CO) and 30.0 ($^{15}N_2$) amu. The spectrometer records the flight times of the molecules as they travel from a slotted

chopper wheel to the surface and subsequently scatter from the surface into the ionizer. These time-of-flight data are corrected for the chopper-to-surface flight time and other experimental timing offsets. The resulting time-of-flight distribution, $N(t)$, is converted to a final translational-energy distribution using the relation $P(E) \sim t^2 N(t)$. Therefore, our experiments measure the amount of translational energy that the molecule possesses after collision with the organic monolayer, providing direct information about gas/surface energy exchange.

The beam source and mass spectrometer are geometrically situated such that the angle between the incident beam and the mass spectrometer is fixed (60°). The angle between the molecular beam and the surface normal (incident angle, θ_i) is 30°, and the surfaces are laser aligned such that flight times are measured at the specular angle (final angle, θ_f=30°). The collection angle of the mass spectrometer is ±0.5° within the plane of the molecular beam. As our surface mount accommodates two surfaces, we are able to rapidly perform scattering experiments with both the CH_3- and CF_3-terminated SAMs under the same UHV and beam conditions. Switching between the two surfaces requires only a small translation of the sample holder.

8.4. RESULTS AND DISCUSSION

8.4.1. Similarity between N_2 and CO scattering dynamics

In Figure 8.1 we plot the experimental final translational-energy distributions that result when scattering $^{15}N_2$ and ^{13}CO from CH_3- and CF_3-SAMs at E_{coll}= 43 and 60 kJ·mol^{-1} with a 30° incident angle. These results are summarized in Table 8.1. The experimental data indicate that N_2 and CO transfer more energy to the CH_3-SAM than to the CF_3-SAM. This different behavior of CH_3- and CF_3-SAMs agrees with recent results of scattering of rare gases from these two surfaces[31] and can be traced to a purely kinematic effect. For translational energy to be transferred from the diatomic molecule to the SAMs, lateral movement of the SAM chains is required to dissipate the energy from the collision into the surface. The heavy terminal groups in the CF_3-SAM induce a larger inertial barrier to this lateral movement than in the CH_3-SAM. As such, it is expected that energy transfer to the CF_3-SAM surface will be decreased relative to the CH_3-SAM surface. Figure 8.1 reveals

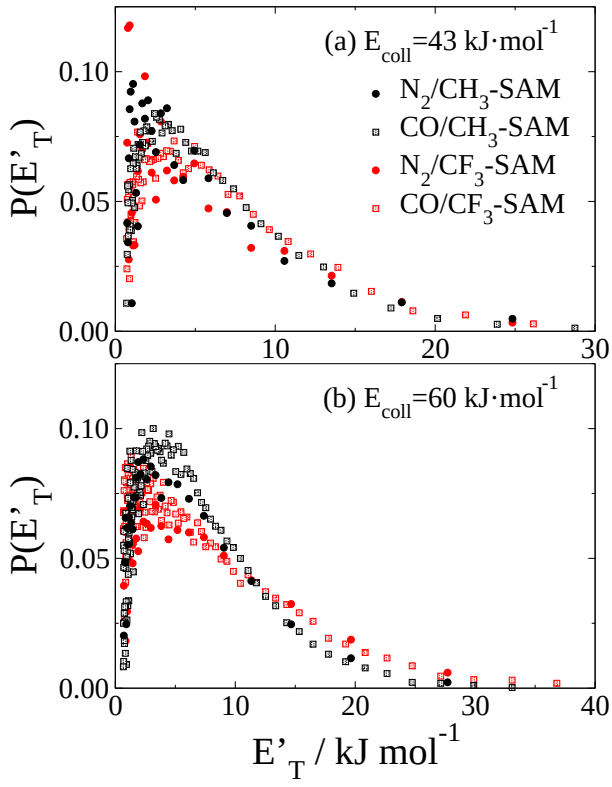

FIG. 8.1: Measured final translational-energy distributions in collisions of N_2 and CO with CH_3- and CF_3-SAMs with collision energies of (a) 43 and (b) 60 kJ·mol^{-1}.

that diatomics scattering from a CF_3-SAM at either 43 or 60 kJ·mol^{-1} and 30° retain more of their initial energy than from a CH_3-SAM at the same initial conditions, confirming the expectations of the kinematic model emerging from earlier rare-gas/SAM studies. On average, N_2 loses ∼86% and ∼82% of its translational energy, while CO loses ∼87% and ∼83%, when colliding with the CH_3- and CF_3-SAMs, respectively, at 60 kJ·mol^{-1}.

Perhaps unsurprisingly, N_2 and CO display very similar energy transfer characteristics as evidenced by the data in Figure 8.1 and Table 8.1. Average total translational-energy transfer fractions are within 1% of each other for N_2 and CO scattering from either monolayer, with N_2 consistently having a slight propensity to leave the surface with higher translational energy, although the differences in final average translational energy are within our experimental error. The small increase in the depth of the CO van der Waals well in comparison to N_2 (see Chapter 7) may be influential enough to affect the overall collision dynamics, but such an effect would be minor at the collision energies probed in this study. Indeed, we do see that the slightly deeper CO/SAM potential wells might (as deduced in comparison of N_2–

TABLE 8.1: Experimentally determined average final energy transfer properties as a function of collision energy in collisions of N_2 and CO with CH_3- and CF_3-SAMs.[a]

Gas	E_{coll}[b]	$<E'_T>$
	CH_3-SAM	
N_2	43	7.5
CO	43	7.3
N_2	60	8.5
CO	60	7.8
CO[b]	103	9.0
	CF_3-SAM	
N_2	43	9.2
CO	43	8.1
N_2	60	10.8
CO	60	10.1
CO[b]	103	12.3

[a] Energies in kJ·mol^{-1}. [b] Scattering of 103 kJ·mol^{-1} CO is discussed in Section 8.4.4. Signal-to-noise ratio for these data was large; therefore large errors should be expected. CO scattering from an OH-SAM results in $<E'_T>$=12.6 kJ·mol^{-1}.

and CO–CX_4 (X=H,F) electronic structure calculations) manifest in the experimentally observed energy transfer behavior, leading to increased accomodation for the CO systems. We expect this effect to become more important at lower collision energies, where the potential well plays an increasing role in the collision dynamics.

8.4.2. Comparison between theory and experiment

In Figure 8.2 we compare experimental and calculated final translational-energy distributions for (a) N_2 and (b) CO scattering from the CH_3- and CF_3-SAMs at E_T=60 kJ·mol^{-1} and θ_i=30°. Although the initial conditions of the trajectories were chosen to correspond with experiments, the total number of simulations that can be performed is limited; therefore, the calculated distributions are integrated over final scattering angles and scattering planes, in constrast to the θ_f=30° detection angle in the in-plane, forward scattering direction used in

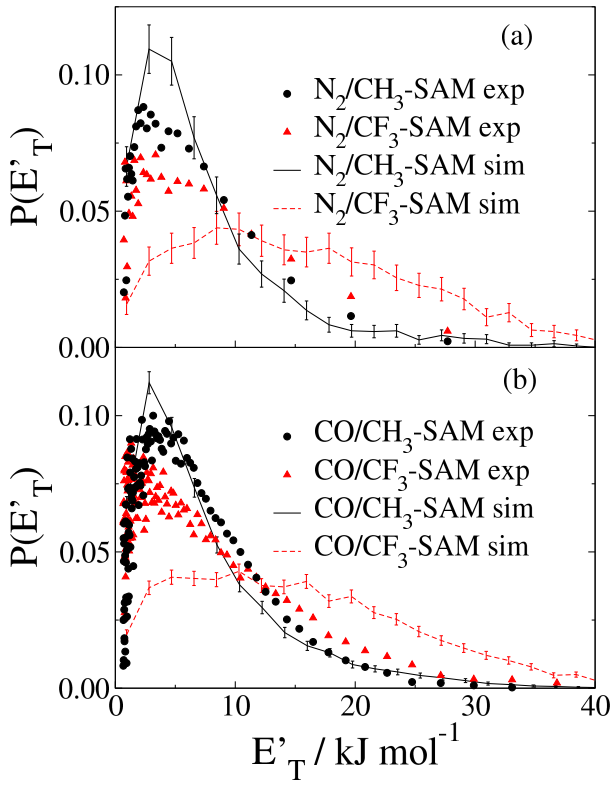

FIG. 8.2: Measured (symbols) and calculated (lines) final translational-energy distributions for collisions of (a) N_2 and (b) CO with the indicated SAMs at E_{coll}=60 kJ·mol^{-1} and θ_i=30°. Note that the experimental distributions correspond to those molecules which scatter from the SAM in a ±1° acceptance window in the in-plane, forward-scattering specular direction (θ_f=30°), while the calculated distributions include the scattering flux integrated over all final angles. The distributions are normalized to unit area.

the experiment. Nevertheless, the calculated distributions reproduce the experimental trend of the gases transferring more of its translational energy when colliding with the CH_3-SAM than with the CF_3-SAM. Average translational energy transfer from N_2 is ∼88% and ∼73% and from CO is ∼87% and ∼75% in collision with CH_3- and CF_3-SAMs, respectively, for 60 kJ·mol^{-1} collision energy. Similar agreement between experiment and theory is seen for the 43 kJ·mol^{-1} systems. (Here we note that the trends for scattering from the CH_3-SAM is reversed from that seen in experiment, with CO having a slightly higher final translational energy than N_2. This emphasizes the fact that, at the probed collision energies, differences in the van der Waals well depth are washed out by the similar repulsive interactions experienced during collision.) More translational energy is retained in the simulated collisions than

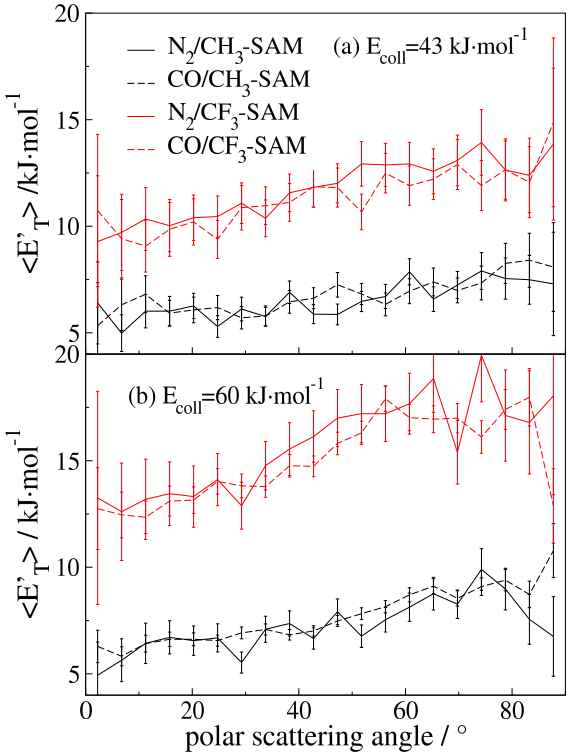

FIG. 8.3: Calculated average final translational energies as a function of the final scattering angle in collisions of N_2 and CO with the indicated SAMs at E_{coll} = 43 and 60 kJ·mol^{-1} and θ_i=30°.

seen in experiment, an effect that has been seen in previous studies of rare gas scattering from SAMs.[9,11,14,16,31,33] This known discrepancy is partially attributable to the fact that real SAM surfaces have defects due to step edges in the underlying gold substrate, boundaries between rotational domains, and pinhole vacancies.[34] However, the major reason for the difference is that in our experiment, θ_f is fixed at 30 °, but our calculated distributions include trajectories recoiling at all final scattering angles.

To understand further the experimental results and attempt to establish a more adequate comparison between theory and experiment, Figure 8.3 shows the calculated average final translational energies as a function of the polar scattering angle. The figure reveals that the calculated average energies at θ_f=30° (experimental detection angle) reproduce the experiments. We limit discussion of these angular-resolved results to the CO/SAM systems with E_{coll}=60 kJ·mol^{-1}. Quantitatively, for CO, the calculated fractions of energy transfer obtained by grouping trajectories scattered in the θ_f=20-40° range are 0.89 for the CH_3-SAM and 0.79 for the CF_3-SAM, which are in good agreement with the corresponding experimental results (0.87 and 0.83, respectively). This agreement between theory and experiment

indicates that the potential-energy surfaces and SAM model used in the simulations adequately mimic the true properties of the systems.

Figure 8.3 also shows that the amount of translational energy retention depends on the final recoil angle of the gas. In both surfaces, CO recoling at large scattering angles retains more of its initial translational energy than at small angles. This result can be substantiated by the ∼5-7 kJ·mol^{-1} difference in CO's final translational energy between near-perpendicular ($\theta_f \sim 0°$) and near-parallel ($\theta_f \sim 90°$) scattering for both surfaces. Another interesting result displayed in Figure 8.3 is that CO loses more translational energy upon collision with the CH_3-SAM than with the CF_3-SAM regardless of scattering angle. Specifically, the average final translational energy for scattering from the CF_3-SAM is ∼10 kJ·mol^{-1} larger than when scattering from the CH_3-SAM over the entire angular range. Similar trends are seen at 43 kJ·mol^{-1} and for N_2. Additionally, the results for CO and N_2 scattering from the same surface at with the same collision energy agree within the error of the calculations over all but the most extreme scattering angles.

8.4.3. The effect of collision energy

In Figure 8.4, we plot the calculated final translational-energy probability distributions for N_2 and CO (v=0,j=0) scattering from the CH_3- and CF_3-SAMs with E_{coll}=43, 60, and 86 kJ·mol^{-1} and θ_i= 30°. Scattering properties for these initial conditions are summarized in Table 8.2. Over this range of collision energies, energy transfer out of translation is very efficient when scattering from the CH_3-SAM, and a large fraction of trajectories lose enough energy to thermalize with the surface. On average, 0.84, 0.87, and 0.89 of CO's initial translational energy is lost upon collision with the CH_3-SAM at E_{coll}=43, 60 and 86 kJ·mol^{-1}, respectively. As collision energy increases, the distributions shift slightly to higher values, with a proportional decrease in the low-energy scattering component. This effect is illustrated in Figure 8.5, in which we plot final translational-energy distributions for the CO/CF_3-SAM system as a function of collision energy. This result of increasing final translation with initial collision energy points to the presence of T→T' energy correlation, and agrees with the recent measurements of the Nesbitt group on CO_2/liquid scattering.[6] T→T' energy retention is more apparent in CO scattering from the CF_3-SAM, for which the final translational energy of CO roughly doubles (11.4 to 21.4 kJ·mol^{-1}) when the initial

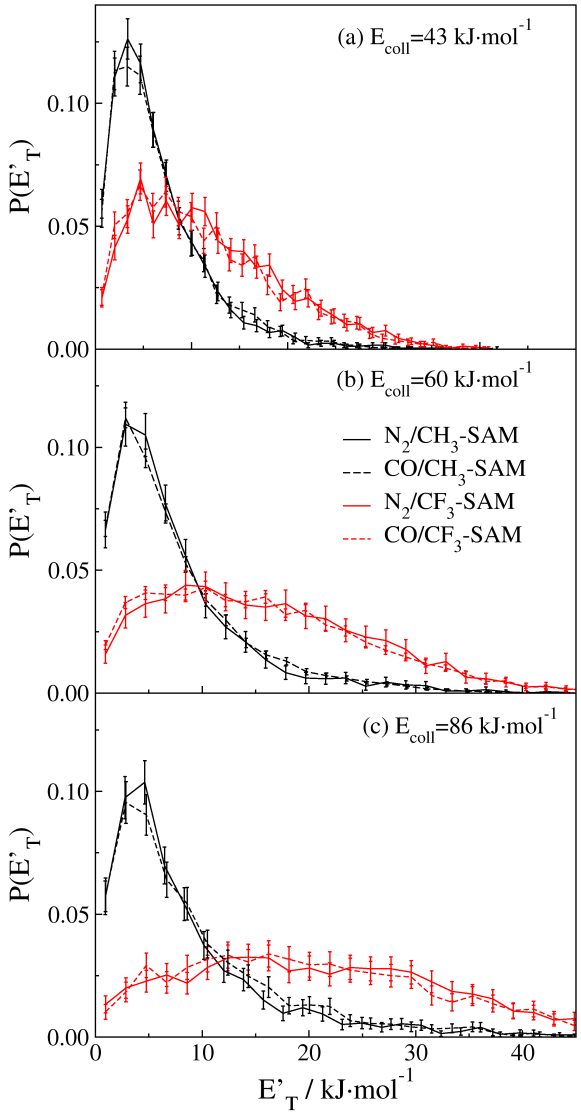

FIG. 8.4: Calculated N_2 and CO final translational-energy distributions as a function of collision energy. θ_i=30°. E_{coll}= (a) 43, (b) 60, and (c) 86 kJ·mol^{-1}.

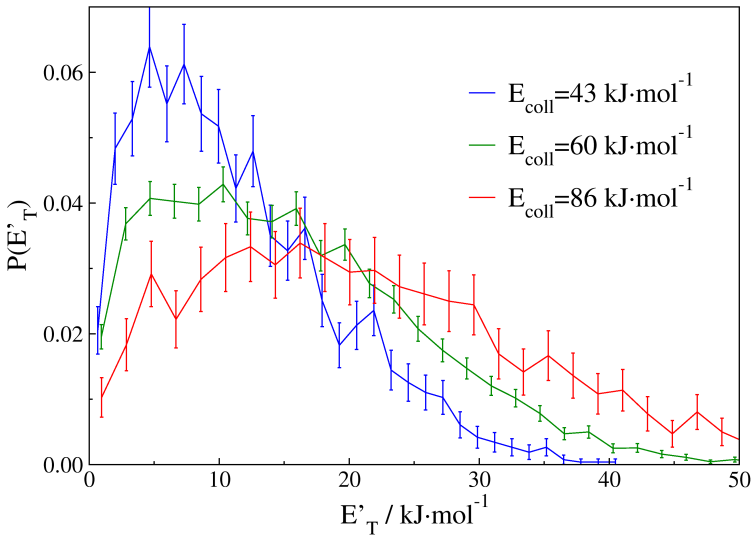

FIG. 8.5: Calculated final translational-energy distributions for the CO/CF_3-SAM system as a function of collision energy

collision energy is doubled (43 to 86 kJ·mol^{-1}). N_2 scattering results parallel those of CO and need no further dicussion.

Table 8.2 also lists the final average rotational energy of the scattered molecules at the three collision energies. The values in the table indicate a certain degree of energy transfer from initial CO translation to final CO rotation (T→R' energy transfer): as collision energy increases, final rotational energies increase for CO scattering from either surface. This result

TABLE 8.2: Scattering properties as a function of collision energy in collisions of N_2 and CO with CH_3- and CF_3-SAMs.[a]

Gas	E_{coll}[b]	<E'$_T$ >[c]	<E'$_{ROT}$ >[d]	<θ_f >[e]	% direct[f]	% long[g]
			CH_3-SAM			
N_2	43	6.5(9.1)	2.8(3.4)	45.8	27.1	32.8
CO	43	6.7(7.8)	2.9(3.3)	46.3	32.7	35.9
N_2	60	7.4(11.3)	3.3(4.2)	47.5	30.6	29.7
CO	60	7.8(10.7)	3.5(4.5)	46.5	39.6	30.4
N_2	86	8.7(13.2)	3.9(5.2)	47.2	36.0	24.4
CO	86	9.4(13.1)	5.0(5.8)	46.0	47.3	25.2
			CF_3-SAM			
N_2	43	11.9(14.3)	3.8(4.0)	47.0	67.2	8.7
CO	43	11.4(13.9)	4.0(4.6)	47.8	63.3	10.4
N_2	60	16.0(18.3)	4.9(5.2)	46.2	76.6	6.2
CO	60	14.9(17.6)	5.2(5.7)	46.4	73.5	7.5
N_2	86	21.9(23.9)	6.6(6.8)	46.1	84.9	2.9
CO	86	21.4(23.5)	6.6(6.9)	46.6	83.6	3.3

[a]30° incident angle; rovibrational states: v=0, j=0; Energies are in kJ· mol^{-1}. Values within parentheses correspond to averages considering only those molecules undergoing a direct mechanism.

[b]Initial gas translational energy in kJ·mol^{-1}.

[c]Average final gas translational energy in kJ·mol^{-1}.

[d]Average final gas rotational energy in kJ·mol^{-1}.

[e]Average polar scattering angle in degrees.

[f]Percentage of trajectories experiencing only one turning point.

[g]Percentage of trajectories that do not desorb the surface after 15 ps.

also agrees with the measurements of CO_2 scattering from liquids.[6] Even though the average final CO rotational energy increases with collision energy, the fraction of translational energy disposal into CO rotation, as a fraction of the whole, decreases with increasing collision energy. For instance, when CO scatters from the CF_3-SAM with E_{coll}=43, 60, and 86 kJ·mol^{-1}, <E'$_{ROT}$>= 4.0, 5.2, and 6.6 kJ·mol^{-1}, respectively, which correspond to 9.3, 8.7, and 7.7% of the collision energy. Rotational distributions are plotted in Figure 9.2. Again,

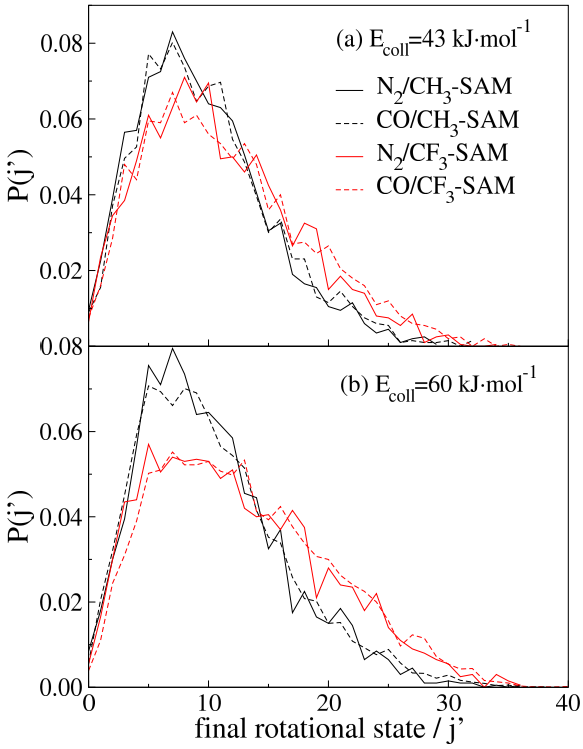

FIG. 8.6: Calculated final rotational distributions for N_2 and CO scattering at 43 and 60 kJ·mol^{-1} from CH_3- and CF_3-SAMs.

N_2 shows nearly identical behavior to CO scattering.

We now turn our attention to examining the effect of collision energy in the scattering mechanism. As discussed above, separation of trajectories into direct and indirect pathways is an important measure, as the different average final scattering characteristics are determined mainly by molecules which experience only a few encounters with the surface. A telling rubric of this effect is the percentage of direct trajectories, which increases from 33% to 47% for CO scattering from CH_3-SAMs at E_{coll}=43 and 86 kJ·mol^{-1}, respectively (see Table 8.2). The enhancement of a direct mechanism with increasing collision energy can also be observed in the percentage of trajectories that remain trapped on the CH_3-SAM surface after 15 ps, which clearly decreases with collision energy. These trends in the evolution of the collision mechanism with collision energy also apply to the CF_3-SAM, but direct processes are even more dominant for this more rigid surface. For instance, the percentage of direct trajectories is almost twice as large for the CF_3-SAM, and the percentage of trajectories in which CO remains trapped on this surface for more than 15 ps is at least three times smaller than on the CH_3-SAM surface. These results provide a mechanistic rational-

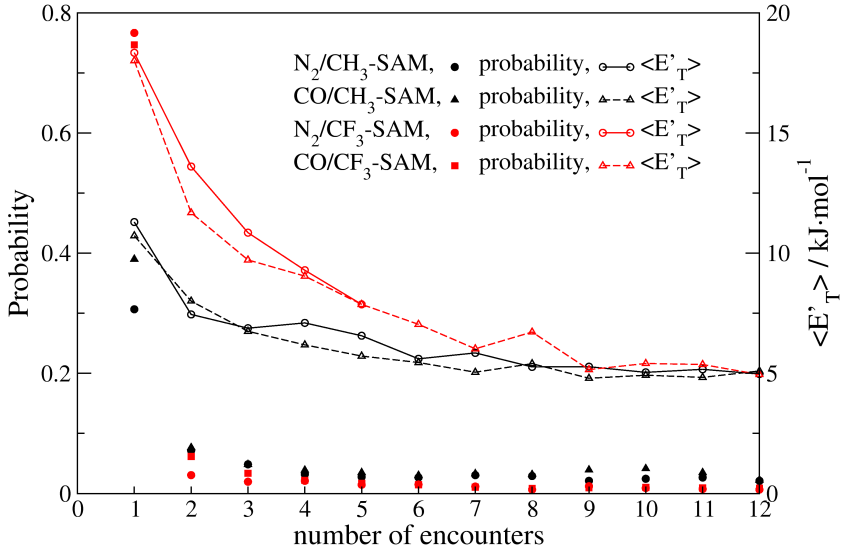

FIG. 8.7: Calculated probability and average final translational-energy distributions as a function of number of encounters with the CH_3- and CF_3-SAM surfaces for E_{coll}=60 kJ·mol^{-1}.

ization of the well-known larger rigidity of fluorinated surfaces with respect to less massive hydrogenated surfaces. As the CF_3-SAM is more rigid, the CO projectile transfers less of its initial energy to the surface on the first impact, and retains enough energy to overcome the attractive interactions with the surface that would result in subsequent collisions and ultimately trapping. Therefore, the larger rigidity of the CF_3-SAM promotes a direct mechanism in comparison with the CH_3-SAM. With regards to N_2 scattering, trends are similar to CO, with the largest deviations seen in the probability of interaction through a direct mechanism. Overall, these deviations are slight and reenforce the notion that N_2 and CO show similar mechanistic behavior.

With regards to N_2 scattering, trends are similar to CO, with the most notable deviation seen in the probability of interaction through a direct mechanismbut actually show noticeable deviation in the direct and long-trapping fractions. While the fraction of direct trajectories increases on both surfaces with increasing E_{coll}, on the CH_3-SAM CO shows more direct scattering, while on the CF_3-SAM, N_2 interacts in a direct mechanism more often. This shown in Figure 8.7 for E_{coll}=60 kJ·mol^{-1}. Single encounter collisions are more probable for CO scattering from the CH_3-SAM than for N_2, but on average, N_2 transfers slightly less energy out of translation, regardless of the number of encounters. On the CF_3-SAM, N_2 interacts with the surface only once with a slightly higher probability than CO. N_2 again

retains more of its initial translational energy than CO after any number of encounters with the surface. Examination of the long trapping fractions provides further evidence for CO dipole enhanced TD fractions presented in discussion of the experimetnal scattering results. The long trapping fractions are greater for CO scattering than N_2 over all studied incident conditions. Evidence for this behavior can also be seen in the number-of-encounters probabillity distributions, where the probability that CO interacts with the surface >8 times is always greater than for N_2.

Over the entire range of incident energies, we see that less than 4% of the total trajectories penetrate the surface below the average height of the terminal carbon of the SAM chains. Penetration on the CH_3-SAM shows a slight increase from 2.5 (1.7)% for E_{coll}=43 kJ·mol^{-1} to 5.8 (3.8)% for E_{coll}=86 kJ·mol^{-1} for CO (N_2) scattering. Of these penetrating trajectories, nearly half proceed through a direct scattering process (ballistic penetration). No penetration was seen under any circumstances for scattering from the CF_3-SAM. This behavior is in direct contrast with previous studies of rare gas/SAM collisions that showed penetration to be common on the CH_3- and CF_3-SAM surfaces. For instance, recent work has shown that ∼27% and ∼22% of Ne and Ar atoms impinging on the CH_3-SAM at 60 kJ·mol^{-1} penetrate the surface, respectively.[31] Penetration into the CF_3-SAM was also seen for the rare gases, although to a lesser extent than on the hydrogenated surface. Repulsive steric effects, due to the increased molecular size of the molecules relative to the rare gases, preclude penetration of CO and N_2 into the SAM surface.

In addition to investigating the effect of collision energy on the amount of energy going into the various products degrees of freedom and on the mechanism of the collisions, we have also studied whether the recoil direction of the molecule is influenced by the initial collision energy. Examination of polar-angle distributions shows that collision energy has virtually no effect on the recoil direction of the scattered diatomic. Evidence for insensitivity of the angular properties to collision energy is given by the average final polar scattering angle (angle formed by the gas' final velocity vector and the surface normal) in Table 8.2. Clearly, the average angles do not change within statistical uncertainty in the range of collision energies explored.

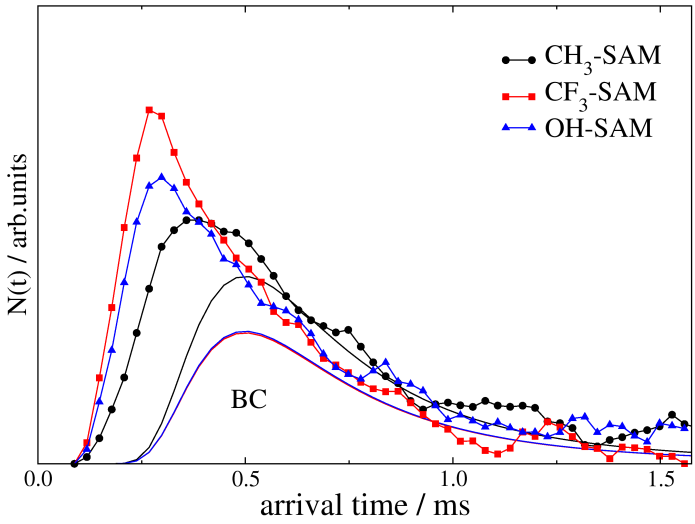

FIG. 8.8: Time of flight distributions for ^{13}CO scattering from CH_3- CF_3-, and OH-SAMs with E_{coll}=103 kJ·mol^{-1}. Lines with symbols are the total distribution, while the regular lines are Maxwell-Boltzmann fits to the low-energy component of the data (BC). Note that to eliminate noise, we have plotted here ten-point running averages of the raw experimental data.

8.4.4. Correlation with gas/liquid scattering

In relation to the nature of the gas/liquid interfaces studied in the work of Nathanson and co-workers described above, CH_3-SAMs are analogous to squalane, OH-SAMs to glycerol, and CF_3-SAMs to PFPE (perfluorinated SAMs (PF-SAMs) are more suitable analogs, but the SAM structures of PF-SAMs vary from the standard 30° chain tilt angle and 4.98 Å lattice spacing). Time-of-flight profiles of 103 kJ·mol^{-1} ^{13}CO scattering from these three SAM surface are shown in Figure 8.8. From the figure, it is plain to see that the Boltzmann component is greatly increased when scattering from the CH_3-SAM in relation to the other surfaces. While differences in the accommodating nature of the glycerol and PFPE were seen in Nathanson's studies, no significant difference in accommodation fraction is seen for the CF_3- and OH-SAMs. The effects of increased rigidity due to fluorination, and polar hydrogen-bonding character seem to be in balance at this collision energy for CO.

8.5. CONCLUDING REMARKS

The energy transfer dynamics in collisions of N_2 and CO with regular and ω-fluorinated alkanethiolate mononlayers have been investigated via a combined theory-experiment approach. Good agreement between experiment and theory is seen, demonstrating the validity of our computational model to properly describe the N_2 and CO/SAM systems. Experimentally, we scattered N_2 and CO at various collision energies and obtained final translational-energy probability distributions. CO and N_2 are seen to have nearly identical energy transfer characteristics as implied by the similarity of the distributions.

Analytic potentials were used in molecular-dynamics simulations of N_2 and CO molecular scattering from CH_3- and CF_3-SAMs. Energy transfer out of initial translation is very efficient in collisions with the SAMs over the range of incident conditions examined, and this energy transfer is notably larger for the CH_3-SAM than for the CF_3-SAM. These calculated trends agree with molecular-beam scattering experiments, particularly when the analysis is performed with trajectories that scatter at final angles representative of the experiment.

Increasing collision energy moderately increases both the final translational energy of the scattered molecule and its rotational excitation on both surfaces. This is shown to be connected to an increase in the fraction of trajectories that undergo a direct mechanism with collision energy.

Subsequent chapters will investigate the effect of rovibrational degrees of freedom, incident angle, and orientation and alignment of diatomic molecules on gas/SAM collision dynamics.

REFERENCES

[1] G. A. Somorjai, *Principles of Surface Chemistry* (Prentice Hall, Inc., Englewood Cliffs, New Jersey, 1972).

[2] M. E. King, G. M. Nathanson, M. A. Hanning-Lee, and T. K. Minton, Phys. Rev. Lett. **70**, 1026 (1993).

[3] M. E. Saecker, S. T. Govoni, D. V. Kowalski, M. E. King, and G. M. Nathanson, Science **252**, 1421 (1991).

[4] M. E. Saecker and G. M. Nathanson, J. Chem. Phys. **99**, 7056 (1993).

[5] M. E. Saecker and G. M. Nathanson, J. Chem. Phys. **100**, 3999 (1993).

[6] B. G. Perkins, Jr. and D. J. Nesbitt, J. Phys. Chem. B **110**, 17126 (2006).

[7] B. G. Perkins, Jr., T. Haber, and D. J. Nesbitt, J. Phys. Chem. B **109**, 16396 (2005).

[8] S. R. Cohen, R. Naaman, and J. Sagiv, Phys. Rev. Lett. **58**, 1208 (1987).

[9] K. D. Gibson, N. Isa, and S. J. Sibener, J. Phys. Chem. A **110**, 1469 (2006).

[10] K. D. Gibson, N. Isa, and S. J. Sibener, J. Chem. Phys. **119**, 13083 (2003).

[11] N. Isa, K. D. Gibson, and S. J. Sibener, J. Chem. Phys. **120**, 2417 (2004).

[12] B. S. Day and J. R. Morris, J. Chem. Phys. **122**, 234714 (2005).

[13] T.-Y. Yan, W. L. Hase, and J. R. Barker, Chem. Phys. Lett. **329**, 84 (2000).

[14] T.-Y. Yan and W. L. Hase, Phys. Chem. Chem. Phys. **4**, 901 (2000).

[15] T.-Y. Yan and W. L. Hase, J. Phys. Chem. B **106**, 8029 (2002).

[16] T.-Y. Yan, N. Isa, K. D. Gibson, S. J. Sibener, and W. L. Hase, J. Phys. Chem. A **107**, 10600 (2003).

[17] S. B. M. Bosio and W. L. Hase, J. Chem. Phys. **107**, 9677 (1997).

[18] J. R. Lohr, B. S. Day, and J. R. Morris, J. Phys. Chem. B **109**, 15469 (2005).

[19] J. R. Lohr, B. S. Day, and J. R. Morris, J. Phys. Chem. A **110**, 1645 (2006).

[20] S. R. Cohen, R. Naaman, and J. Sagiv, J. Chem. Phys. **88**, 2757 (1988).

[21] M. Graupe, T. Koini, V. Y. Wang, G. M. Nassif, R. Colorado, R. J. Villazana, H. Dong, Y. F. Miura, O. E. Shmakova, and T. R. Lee, J. Fluorine Chem. **93**, 107 (1999).

[22] M. Graupe, M. Takenaga, T. Koini, R. Colorado, and T. R. Lee, J. Am. Chem. Soc. **121**, 3222 (1999).

[23] J. E. Houston, C. M. Doelling, T. K. Vanderlick, Y. Hu, G. Scoles, I. Wenzl, and T. R. Lee, Langmuir **21**, 3926 (2005).

[24] D. M. Alloway, M. Hofmann, D. L. Smith, N. E. Gruhn, A. L. Graham, R. Colorado, V. H. Wysocki, T. R. Lee, P. A. Lee, and N. R. Armstrong, J. Phys. Chem. B **107**, 11690 (2003).

[25] D. L. Smith, V. H. Wysocki, R. Colorado, O. E. Shmakova, M. Graupe, and T. R. Lee, Langmuir **18**, 3895 (2002).

[26] W. L. Hase, R. J. Duchovic, X. Hu, A. Komornicki, K. F. Lim, D. h. Lu, G. H. Peslherbe, K. N. Swamya, S. R. V. Linde, A. Varandas, et al., Quantum Chemistry Program Exchange Bulletin **16**, 671 (1996).

[27] J. W. Ponder and F. M. Richards, J. Comput. Chem. **8**, 1016 (1987).

[28] B. S. Day and J. R. Morris, J. Phys. Chem. B **107**, 7120 (2003).

[29] B. S. Day, S. F. Shuler, A. Ducre, and J. R. Morris, J. Chem. Phys. **119**, 8084 (2003).

[30] M. K. Ferguson, J. R. Lohr, B. S. Day, and J. R. Morris, Phys. Rev. Lett. **92**, 073201 (2004).

[31] W. A. Alexander, B. S. Day, H. J. Moore, T. R. Lee, J. R. Morris, and D. Troya, J. Chem. Phys. **128**, 014713 (2008).

[32] D. R. Miller, in *Atomic and Molecular Beam Methods*, edited by G. Scoles (Oxford University Press, New York, 1988), vol. 1, p. 14.

[33] B. S. Day, J. R. Morris, and D. Troya, J. Chem. Phys. **122**, 214712 (2005).

[34] C. Vericat, M. E. Vela, and R. C. Salarezza, Phys. Chem. Chem. Phys. **7**, 3258 (2005).

Chapter 9

Classical trajectory study of CO collisions with CH_3- and CF_3-terminated self-assembled monolayers

Reproduced in part with permission from W. A. Alexander, J. R. Morris, and D. Troya, *J. Chem. Phys.* **130**, 084702 (2009). Copyright 2009 American Institute of Physics.

9.1. INTRODUCTION

Understanding how gas/surface energy transfer dynamics is influenced by the addtion of rovibrational degrees of freedom in the scattered molecule is of relevance in light of recent experiments by Nesbitt et al., described below and those of Lohr and co-workers, who scattered HCl from hydroxyl- and methyl-terminated monolayers.[1,2] When an atom collides with a surface, the only energy transfer allowed is from the impinging gas' collisional energy to the surface degrees-of-freedom. Polyatomic molecules bring added rovibrational degrees-of-freedom that can potentially be involved in energy transfer and reveal richer collision dynamics than those of rare gas systems.

In Chapter 8, we investigated the effect of incident translational energy on the scattering dynamics of two common diatomic molecules, CO and N_2, in collision with CH_3- and CF_3-SAM surfaces. It was shown that overall energy transfer to these surfaces is quite efficient, with energy transfer and accomodation being increased on the hydrogenated surface. Increasing the incident collision energy resulted in and increase in the fraction of molecules that interact with the surface in a direct or impulsive scattering (IS) mechanism and a concomitant decrease in the fraction of impinging molecules which thermally accomodate with the surface. Trends seen with collision energy are in line with findings of previous groups, including the gas/liquid scattering studies of Nathanson.[3–6]

Since the Nathanson group's pioneering work, at least three other groups have investigated small-molecule scattering from the squalane and PFPE liquid surfaces.[7–14] Collectively these studies agree with the findings of Nathanson of bimodal final translational-energy distributions and the different scattering behavior in collisions on hydrogenated or fluorinated surfaces. Additionally, however, these studies have been able to investigate state-to-state

energy transfer by resolving the rovibrational state populations of the recoiling gas species. McCaffery and co-workers recorded quantum state distributions of I_2 before and after collision with squalane and PFPE via laser-induced fluorescence (LIF) techniques.[7,8] They found squalane to be superior to PFPE at trapping I_2 at the surface and vibrationally warming the initially cold vibrational (and rotational) distributions of the incident beam. The impulsive scattering component displayed less overall warming in the scattered rovibrational distributions, with I_2 coming off the surface rotationally hotter when scattering from PFPE. The McKendrick group also used LIF to investigate OH radicals scattering from the same surfaces[14] and they too observed bimodal scattering behavior. Squalane was found to absorb OH translational energy and accomodate the OH on the surface better than in collisions with PFPE. Final rotational distributions of OH scattered from PFPE were found to be hotter than those with squalane. The results of both groups' LIF studies are consistent with the findings of the Nathanson group.

As discussed in the previous chapter, CO_2 scattering from the PFPE surface also showed evidence for a two-channel model of thermal and impulsive scattering.[10] Doppler profiles were well modeled by assuming that the translational-energy distributions of impulsively scattered molecules are determined by a single superthermal temperature. Rotational-state measurements indicated that the rotational temperature of impulsively-scattered CO_2 molecules was essentially the same as their translational temperature.[9] In addition to their studies of collision energy,[10] the effect of incident collision angle[11] and surface temperature[12] on final translational and rotational energy distributions was examined. The CO_2 vibrational modes were shown to warm only slightly as a result of collision, indicating that the impinging gas-phase species have a finite interaction time with the surface well below that required for the usually large number of encounters required for vibrational excitation. Variation of the incident angle from θ_i=0° (incidence normal to the surface) to 60°, in CO_2 collisions with the PFPE surface revealed that while final average translational and rotational energies increased with a more glancing angle, final vibrational energies remained constant. The fraction of molecules that thermalize with the surface as a result of collision decreased with increasingly glancing incident angles, as expected.

Cohen et al. investigated the influence of NO collision energy on final rotational distributions.[15] They found that, while on average the amount of translational energy lost could account for the rotational energy gain, there was essentially no difference in the final

translational-energy distributions of scattered NO with final j states of 1.5 or 25.5 for either monolayer. As such, direct coupling between translational and rotational modes cannot be governing rotational excitation in this system under the probed initial conditions. Scattering from PFAE resulted in increased population in high rotational modes relative to OTS. The Nesbitt group also reported increased population in high rotational states when scattering CO_2 from PFPE relative to squalane.[10] The only theoretical study that has involved state-to-state resolution until now is for CO_2 scattering from perfluorinated SAMs.[12,13,16]

As mentioned previously, the use of SAMs built from CH_3- and CF_3-terminated alkanethiols on gold substrates overcomes the difficulty of separating supramolecular structure effects present in liquid surfaces from the chemical and physical properties of the exposed groups at the interface. The two surfaces have identical structure[17–21] [other than the slightly different C-X (X=H, F) bond lengths] and therefore any differences in scattering dynamics from these surfaces can be attributed primarily to the exposed groups.

Within this chapter, we investigate the dynamics of CO scattering from CH_3- and CF_3-SAM surfaces using classical-trajectory simulations with the aim of understanding what influence internal degrees of freedom of the gas-phase species play in gas/organic-surface energy transfer. Additionally, we have investigated the influence of the impinging gas species' angle of incidence on the enrgy transfer dynamics. Finally, the mass of CO is almost perfectly intermediate between that of Ne and Ar. Therefore, comparison of CO scattering with that of Ne and Ar from the same surface can be used to infer the involvement of its internal degrees of freedom in the energy-transfer dynamics.

9.2. COMPUTATIONAL DETAILS

Our computational approach is analogous to that taken in Chapter 8. Details of the production of initial conditions and propagation scheme are included in Chapter 3, and analytical PESs used for the studies contained in this chapter are extensively discussed in Chapter 7.

We have integrated batches of 2000 trajectories for each set of collision energy (E_{coll}), CO rovibrational state (v,j), and incident angle (θ_i) explored in this work. Initial conditions for the CO molecule were determined via quasi-classical sampling of selected vibrational and rotational states as implemented in the VENUS96 computer program.[22] To examine the

influence of rovibrational excitation, we have integrated trajectories with j=0, 7, 14, and 28 and with v=0 and 1. The effect of incident angle has been studied by calculating trajectories with θ_i=30° or 60°, and all trajectories examined in this chapter have E_{coll}=60 kJ·mol^{-1}.

At the beginning of each trajectory, CO was placed above the surface, at a separation of at least 10 Å from the closest surface atom. The trajectories were stopped post-collision when the gas either recoiled to a distance of 12 Å from the closest atom of the surface, or, in the case of long-trapping times, after 15 ps. Those trajectories stopped as a result of long trapping times are assumed to be fully thermalized with the surface and are randomly assigned final translational energies, E'_T, and rovibrational states, v', j' based on Boltzmann distributions at the surface temperature and a final polar angle, θ_f, based on a random distribution.

From the initial and final coordinates and momenta of the CO molecule, scattering properties including final translational-energy distributions, and CO rotational state distributions were determined. Examination of the coordinates and momenta during the trajectory was used to provide mechanistic understanding of the collisions.

9.3. RESULTS AND DISCUSSION

In the previous chapter we analyzed the ability of our simulations to reproduce experimentally observed scattering behavior. Satisfactory agreement with experiment was seen, which allows us to use simulations to investigate aspects of the collisions not currently obtainable with our experimental setup. While the previous chapter focused on the similarities of N_2 and CO scattering from CH_3- and CF_3-SAMs and the influence of collision energy on energy transfer dynamics, in this chapter we examine CO scattering exclusively. An in-depth study of rovibrational effects and the influence of incident angle follows a comparison of CO scattering with our previous work with rare gas scattering.

9.3.1. Comparison with rare gas scattering

Recently, we undertook a rigorous study of rare gas scattering from SAM surfaces to investigate the effect of gas mass and surface mass on the gas/surface energy-transfer dynamics.[23] (These efforts were detailed in Chapter 5.) Ne, Ar, and Kr were scattered at E_{coll}=60

kJ·mol^{-1} from CH_3- and CF_3-terminated SAMs and the extent of energy transfer was determined by experimental and theoretical methods. Initial translational energy retention was seen to decrease in the Ne→Ar→Kr sequence on both surfaces and this result was demonstrated to be entirely attributable to the increase in the gas mass along that series. Other effects, such as the difference in the potential-energy surfaces, were shown to have a negligible effect in the scattering properties at 60 kJ·mol^{-1}. Comparison of the current CO scattering data with the rare-gas results should therefore enable us to learn the influence of the added complexity of a diatomic molecule on energy transfer to organic surfaces in relation to atomic scattering.

Experimentally, the average final translational energies of Ne, CO, and Ar scattering from the CH_3-SAM with $\theta_i = \theta_f = 30°$ and E_{coll}=60 kJ·mol^{-1} are 10.3, 7.8, and 6.1 kJ·mol^{-1}, respectively. The corresponding final energies for scattering from the CF_3-SAM are 14.4, 10.1, and 7.4 kJ·mol^{-1}. These results show that the scattering properties of CO are roughly intermediate between those of Ne and Ar. This is the expected result according to kinematic considerations, because the mass of ^{13}CO (29.0 amu) is intermediate between that of Ne (20.2 amu) and Ar (39.9 amu). However, a close inspection of the data suggests that the final energy of CO is closer to that of Ar than Ne. Additional insight into this result can be gained from Figure 9.1, where we show calculated final translational-energy distributions of CO scattering from CH_3- and CF_3-SAMs at E_T=60 kJ·mol^{-1} and θ_i= 30° compared with our previous results for Ne and Ar. Note that these calculated distributions show all the CO flux, and not only that at $\theta_f = 30°$, as measured in the experiment. As described before, if the scattering behavior of CO from SAMs is dominated by the system kinematics, the CO final translational-energy distributions should fall nicely between those of Ne and Ar. Fig. 9.1(a) shows that the expectations from purely kinematic considerations are not fully realized for CO scattering from the CH_3-SAM. Instead, the CO retains less of its initial translational energy than it should according to its mass (intermediate between Ne and Ar) and the CO distributions overlap with those of Ar. Quantitatively, 0.81, 0.87, and 0.87 of the gases' translational energy is lost in Ne, CO, and Ar collisions with the CH_3-SAM, respectively (E'$_T$=11.4, 7.8, and 7.8 kJ·mol^{-1}). It therefore seems that scattering of CO from the CH_3-SAM at all final angles is not entirely governed by kinematic effects. Other effects, such as the internal excitation of CO, or the differences in the gas/surface potential-energy surface seem to play a role.

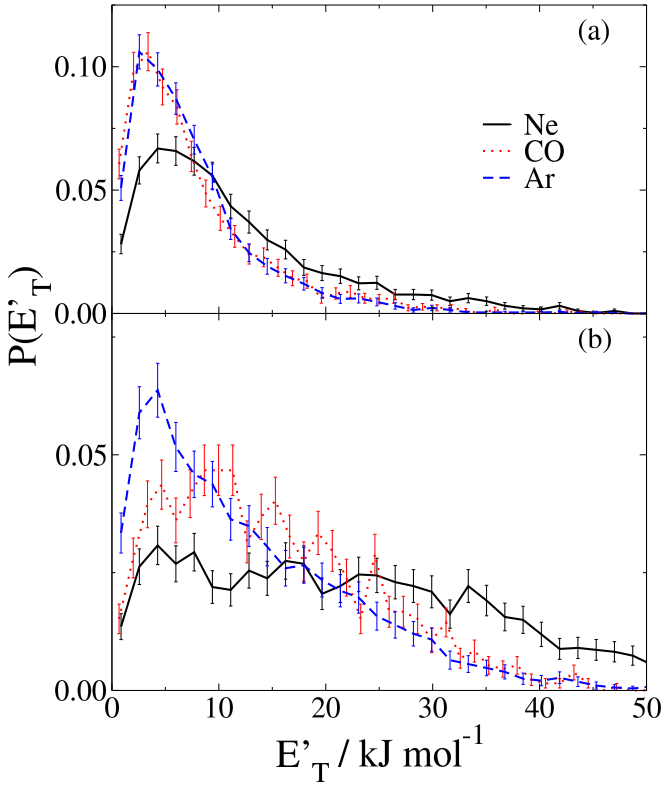

FIG. 9.1: Calculated final translational-energy distributions for collisions of Ne, CO, and Ar with (a) CH_3- and (b) CF_3-SAMs at E_{coll}=60 kJ·mol^{-1} and θ_i=30°. The distributions are normalized to unit area. Data for Ne and Ar are from Ref. 23.

Figure 9.1(b) shows that scattering of Ne, CO, and Ar from the CF_3-SAM produces results that show better agreement with what would be expected if kinematic effects alone control energy transfer. Energy transfer fractions are 0.63, 0.75, and 0.79 (E'_T=22.2, 15.0, and 12.6 kJ·mol^{-1}) for the same gases colliding with the CF_3-SAM. Even though the CO results are intermediate between that of Ne and Ar, the average properties are distinctly closer to those of Ar than to Ne. While the larger rigidity of the CF_3-SAMs seems to enable kinematics to play a more prominent role in determining the outcome of the collisions than in the case of the CH_3-SAMs, properties other than the system kinematics might play a role in the dynamics.

As a first approximation to what role differences in the gas/surface potential play in the dynamics of CO scattering, in comparison with Ne and Ar, we show in Table 9.1 the ab initio energy and geometry of the van der Waals minima of gas–CX_4 (X=H,F) systems, averaged over all computed approach geometries. For the rare gases, as mass increases, the well depth

TABLE 9.1: Comparison of intermolecular interaction parameters for CO– and rare-gas–CH_4 and –CF_4 systems.

	mass (amu)	$\alpha/4\pi\epsilon_o$ [a]	r_w [b]	Y-CH_4 well[c]	Y-CF_4 well[c]
Ne	20.18	0.39	1.54	0.53 (3.73)	0.84 (3.88)
CO	28.01	1.97	2.16	1.37 (4.20)	1.74 (4.37)
Ar	39.95	1.63	1.88	1.38 (3.95)	1.74 (4.18)

[a]Polarizability volume in $10^{-30}m^3$.

[b]van der Waals radii in Å as reported in Ref. 24. For CO, this value is calculated as $\frac{1}{2}(r_{w,O}+r_{w,C}+r_{e,CO})$.

[c]Energies below the asymptote in $kJ{\cdot}mol^{-1}$ of the Y-CH_4 and Y-CF_4 attractive potential-energy wells (Y=Ne, CO, Ar). Values in parentheses correspond to the gas-CX_4 (X=H,F) center-of-mass distance in Å. The results for Ne and Ar are an average over three approaches from Ref. 23, and the results for CO are an average over the nine approaches calculated in this work.

increases, and its location is shifted to longer intermolecular distances. However, with the increased polarizablity (relative to the rare gases) and the addition of a small dipole moment, CO does not follow straight mass trends. As can be seen from the table, the average energy minima for CO–CX_4 is nearly the same as for the Ar–CX_4 systems, with the well minima location occuring at ∼0.3 Å longer distances. This increase in well depth likely results in an enhancement of CO accomodation and energy transfer on the CH_3-SAM surface than would be expected from a solely kinematic effect. A similar effect has been seen in comparison of Ar and HCl scattering from CH_3- and OH-SAMs.[1] While a simple kinematic argument would predict Ar and HCl to have similar energy transfer dynamics, in the experiments HCl was seen to thermalize much more readily than Ar on both surfaces, while showing identical energy transfer characteristics in molecules which undergo impulsive scattering. Therefore, even though kinematics seem to dictate the outcome of direct scattering processes, the increased attractions between the HCl molecule and the surface enhanced overall energy transfer to the surfaces.

The above analysis only discusses the departure of CO scattering results from the kinematic expectations based on the features of the potential-energy surface. However, the participation of the internal degrees of freedom of CO in the energy-exchange dynamics might also play an important role. In the following, we present an analysis of CO/SAM

energy transfer focusing on the transfer of energy from and to CO's rovibrations. Since our molecular beam instrument does not currently have the capability to select initial rovibrational states of the CO molecule or probe them after collision with the surface, we use molecular-dynamics simulations to perform these state-to-state studies. The satisfactory reproduction of the available experimental data concerning CO translation (see Chapter 8) lends confidence to the accuracy of the simulations.

9.3.2. The effect of initial CO rovibrational excitation

We have investigated the influence of initial CO rovibrational excitation on the energy transfer dynamics by integrating batches of trajectories in which the initial conditions for CO correspond to selected rovibrational states. Our goal is to characterize the correlation between initial CO rovibration and energy disposal into the various products degrees of freedom, including CO rotation (R→R' and V→R' energy retention and transfer), CO vibration (V→V' and R→V' energy retention and transfer), and final translation (R→T' and V→T' energy transfer). A summary of the scattering properties for all of the CO initial rovibrational states probed in this work can be seen in Table 9.2.

Figure 9.2 shows the final CO rotational distributions as a function of initial rotational excitation with E_{coll}=60 kJ·mol^{-1} and θ_i=30°. Also plotted in the figure is a Boltzmann distribution of rotational states for CO at the surface temperature of 300 K. As can be seen from the plot, in every case CO recoils from the surface with a rotational distribution hotter than a Boltzmann distribution at the temperature of the surface. This is true also for trajectories started with CO(j=0), which indicates that some of the initial translational energy of CO is transferred to final CO rotation (T→R' energy transfer). Rotational distributions are peaked at higher j values for the CF_3-SAM than with the CH_3-SAM, with average final j values being ∼3 rotational states higher after scattering from the fluorinated surface. The result that fluorinated surfaces promote rotational excitation has been seen before in experimental studies of NO colliding with perfluorinated acid ester and n-octadecyltrichlorosilane SAMs,[15] and with I_2,[7,8] CO_2,[10] and OH[14] colliding with liquid squalane and perfluoropolyether. In those prior experiments, the larger rigidity of fluorinated surfaces was claimed to be responsible for the enhanced rotational excitation of the scattering gases. We note that while those experiments were carried out for a unique set of initial states of the impinging gas,

TABLE 9.2: Scattering properties as a function of initial CO rovibrational state in collisions of CO with CH_3- and CF_3-SAMs.[a]

Surface	v	j	E_{VIB}[b]	E_{ROT}[c]	$<E'_T>$[d]	$<E'_{VIB}>$[e]	$<E'_{ROT}>$[f]	% direct[g]	% long[h]
CH_3-SAM	0	0	12.9	0.0	7.8(10.7)	13.9	3.5(4.5)	38.3	30.4
	0	7	12.9	1.3	7.8(11.1)	13.9	3.6(4.5)	39.8	30.2
	0	14	12.9	4.9	7.8(10.7)	13.9	4.1(5.7)	40.9	29.1
	0	28	12.9	18.7	9.2(13.1)	13.9	6.6(9.4)	42.8	26.8
	1	0	38.6	0.0	7.9(10.8)	39.7	3.3(4.0)	41.5	30.2
CF_3-SAM	0	0	12.9	0.0	14.9(17.6)	13.5	5.2(5.7)	73.5	7.5
	0	7	12.9	1.3	16.2(18.6)	13.6	5.3(5.8)	75.5	6.6
	0	14	12.9	4.9	16.7(19.2)	13.6	6.2(6.6)	75.7	6.4
	0	28	12.9	18.7	19.0(21.4)	13.6	11.7(12.4)	79.3	4.3
	1	0	38.6	0.0	15.3(17.6)	39.9	5.1(5.4)	75.8	6.3

[a]30° incident angle; 60 kJ·mol^{-1} collision energy. Values within parenteses correspond to averages considering only those molecules undergoing a direct mechanism.
[b]Initial CO vibrational energy in kJ·mol^{-1}.
[c]Initial CO rotational energy in kJ·mol^{-1}.
[d]Average final CO translational energy in kJ·mol^{-1}.
[e]Average final CO vibrational energy in kJ·mol^{-1}.
[f]Average final CO rotational energy in kJ·mol^{-1}.
[g]Percentage of trajectories experiencing only one turning point.
[h]Percentage of trajectories that do not desorb the surface after 15 ps.

the calculated distributions in Figure 9.2 indicate that CO results with larger rotational excitation when colliding with a fluorinated surface regardless of its initial level of internal excitation prior to collision.

A result of interest in both Figure 9.2 and Table 9.2 is that there is a positive correlation between initial and final CO rotational excitation on both surfaces (R→R' energy retention). While this positive correlation is barely perceptible when comparing the rotational distributions of CO(j=0) or CO(j=7) scattering, it becomes prominent for larger initial CO excitation (CO(j=14) and CO(j=28)). From an energetic perspective, we see that even though the average final rotational energy of the scattered CO increases with increasing

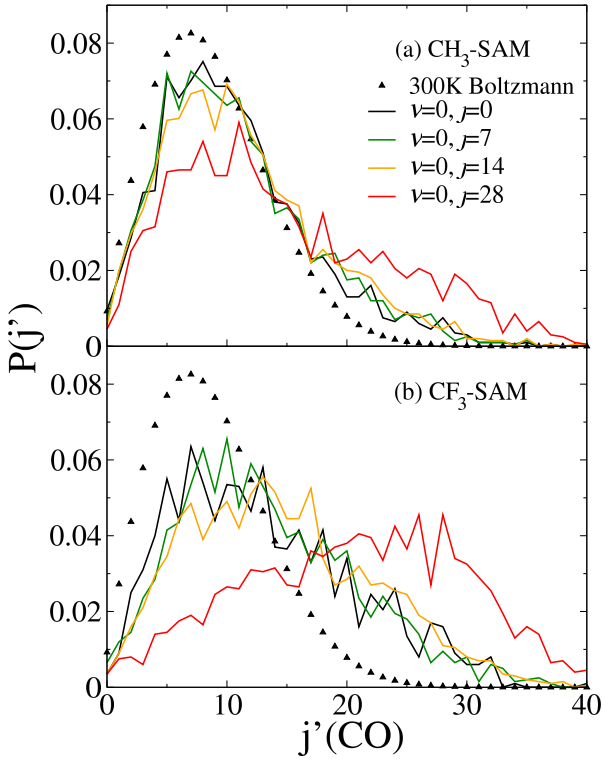

FIG. 9.2: Final CO rotational distributions for various initial rotational states when scattering from (a) CH_3- and (b) CF_3-SAMs at E_{coll}=60 kJ·mol^{-1} and θ_i=30°.

initial CO rotational energy, the correlation is very weak. For instance, while the initial rotational energy increases by ∼14 kJ·mol^{-1} when going from j=14 to j=28 initial states, the final CO rotational energy increases by only ∼3 kJ·mol^{-1}.

Table 9.2 also shows that while rotational excitation is gained in collisions started with low CO rotational states (j=0,7), there is a net loss of rotational energy in collisions started with CO in rotational states j=14 and 28. For instance, for CO impinging on the surfaces in the j=28 state, the average fraction of rotational energy loss, $\frac{E_{ROT}-<E'_{ROT}>}{E_{ROT}}$, is 0.65 for the CH_3-SAM and 0.37 for the CF_3-SAM, indicating that the surfaces act as an effective sink of rotational excitation. The fact that rotational energy is gained during collision for initial low (j=0,7) states but lost for high (j=14,28) states is due to the direction and magnitude of the torques acting on the CO molecule when it collides with the the surface. At j=0 or 7, the initial rotational angular momentum is zero or very small, so any torque applied to the CO molecule by the surface during collision will result in a transformation of the initially large linear momentum of CO into rotational angular momentum. This leads to a gain in

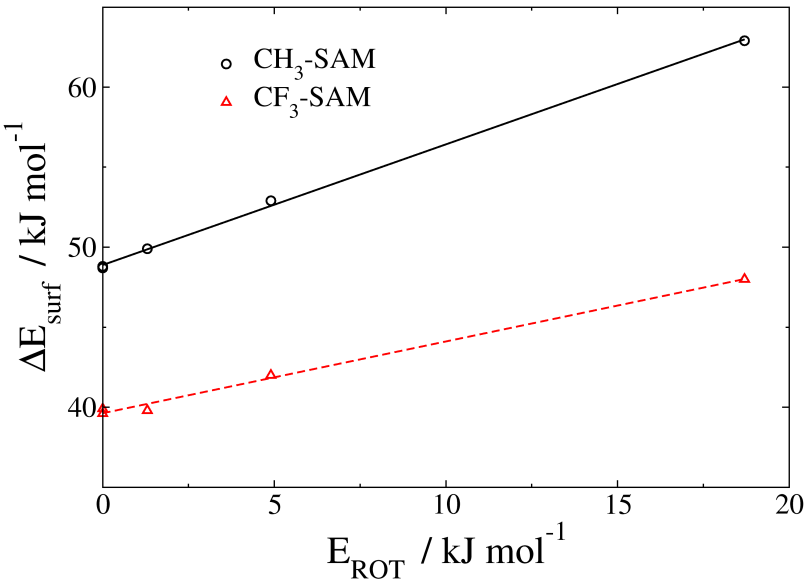

FIG. 9.3: Total energy deposited into the indicated SAM surfaces as a function of initial rotational energy. E_{coll}=60 kJ·mol^{-1} and θ_i=30°.

rotational energy. At high j states, CO impacts the surface with both large initial linear momentum and rotational angular momentum. Depending on the molecular orientation and direction of rotation of CO at the moment of impact, the surface will induce a torque opposite to the direction of rotation or in the direction of rotation. If the torque occurs in a direction opposite to that of initial rotation, rotational energy will be lost. If the torque is applied in the direction of rotation, a small fraction of the initial CO linear momentum will be transformed into rotational momentum, and this will increase slightly the rotational excitation. The fact that CO molecules initially in j=14 and 28 state lose a significant fraction of energy to the surface therefore indicates that, on average, the torque applied on the CO molecule by the surface is opposite to the direction of rotation. However, the small population beyond j'=28 in the rotational distributions of Fig. 9.2 indicates that some of the orientations are appropiate for the transformation of linear momentum into rotational angular momentum even if the initial rotational angular momentum is large.

A demonstration that the surfaces act as effective sinks of initial CO rotational excitation is given in Figure 9.3, where we show the energy transferred to the surface (ΔE_{surf}) as a function of the initial CO rotational energy. (ΔE_{surf} is calculated as the balance between the initial and final CO energies: $\Delta E_{surf} = E_{coll}+E_{VIB,CO}+E_{ROT,CO}-E'_T-E'_{VIB,CO}-E'_{ROT,CO}$.) The figure shows a linear dependence between initial CO rotation and the energy absorbed

by the surface, which supports the notion of a strong $R \rightarrow E_{surf}$ energy transfer. The figure also reveals that the slope of the CH_3-SAM line is notably steeper than that of the CF_3-SAM. This result implies that the CH_3-SAM is a more efficient absorber of CO rotational energy and further indicates that the more rigid SAM inhibits transfer of not only translational but also rotational energy from the gas species to the surface.

Regarding energy transfer from CO initial rotation to final translation (R→T' energy transfer), Table 9.2 shows that there is a positive correlation between these energy modes for both surfaces. However, the correlation is also weak. Quantitatively, an increase of 18.7 kJ·mol^{-1} in initial CO rotational excitation when going from j=0 to j=28 results in a meager 1.4 kJ·mol^{-1} increase in the average final translational energy of CO for the CH_3-SAM. For the CF_3-SAM the correlation is notably stronger, with the final translational energy of CO increasing by 5.1 kJ·mol^{-1} for the same increase in initial CO rotational energy.

Table 9.2 also shows data that help provide fundamental mechanistic undestanding of the different interfacial behavior of CH_3- and CF_3-SAMs, including the percentage of trajectories that undergo a direct mechanism and the percentage of trajectories that remain trapped for a very long time on the surface. In this work, we consider that the collision mechanism is direct if CO collides with the surface only once. The calculation of the number of collisions between CO and the surface is carried out by examining the behavior of CO's center-of-mass coordinate along the surface-normal axis during the collisions. If that coordinate exhibits only one minimum, the trajectory is considered to be direct. On the other hand, trajectories accounted for in the '% long' column in Table 9.2 are those in which CO did not desorb from the surface after 15 ps. Included parenthetically in Table 9.2 are average final translational and rotational energies for those collisions in which CO undergoes a direct mechanism. Overall, scattering via a direct pathway results in ∼30 and 7% increases in final rotational energy compared to all flux for CO colliding with the CH_3– and CF_3–SAMs, respectively. This increase is greater (∼40 and 15% for CH_3– and CF_3–SAMs, respectively) when analyzing final translational energy. While analysis of only directly scattered trajectories mimics the trends seen in final rotational and translational energies for all CO flux, analysis of trajectories that experience multiple encounters with the SAM surface does not bear out these overall trends. We observe total thermalization of translational energy by the time trajectories experience 5-7 encounters with the surface. In fact, if the average final translational energy is computed using only those trajectories experiencing more

than 5 encounters, the resulting value is 5.4 ± 0.3 kJ·mol^{-1} under all conditions explored in Table 9.2. As such, the trends in final rotational and translational energy for increasing initial rotational excitation, and the differences in scattering behavior must be a result of molecules colliding in a direct mechanism. An additional conclusion can be drawn from the analysis of the two indicators of the reaction mechanism (% direct and % long in Table 9.2) — initial CO rotation has only a mild effect on the microscopic mechanism of the collisions. For instance, the percentage of direct (single-turning-point) collisions increases very slightly (∼5%) with increasing initial CO rotation from j=0 to j=28 on both CH_3- and CF_3-SAMs. Regarding the the percentage of trajectories in which CO spends more than 15 ps on the surface, Table 9.2 shows that trajectories started with j=28 only have a slightly smaller probability of remaining trapped on the surface for a long time than trajectories started with lower CO rotation.

The data in Table 9.2 show that there is no apparent transfer of energy from initial CO rotation to final CO vibration (R→V' energy transfer) with either surface. To further investigate the role of CO vibration, we have computed batches of trajectories with CO initially in the v=1, j=0 state scattering off both SAM surfaces. The calculations do not reveal any evidence for CO gaining or losing vibrational excitation during the collisions, therefore, the CO/SAM collisions can be considered vibrationally adiabatic. This vibrational adiabaticity points toward the presence of perfect V→V' energy retention, and complete absence of V→R', and V→T' energy transfer.

The result that CO rotation is actively involved in the scattering process, while CO vibration is not, can be traced to the different timescales of interaction required for rotational and vibrational energy transfer as vibrational energy transfer usually requires many more encounters than are needed in energy transfer involving rotation. While the timescale of the CO/SAM collisions is long enough for rotational energy exchange to occur, it is short enough that energy in the vibrational modes is sequestered throughout the trajectory and does not participate in the dynamics of the collision process. Another interesting result connected to the vibrational adiabaticity of the collisions is that energy transfer to and from the remaining CO degrees of freedom (translation and rotation) seems completely unaltered by the presence of vibrational excitation in CO. As shown in Table 9.2, the final translational and rotational energies of CO are essentially the same for CO(v=0,j=0) and CO(v=1,j=0) scattering from either the CH_3- or CF_3-SAM at E_{coll}=60 kJ·mol^{-1} and $\theta_i = 30°$.

TABLE 9.3: Final CO properties as a function of the incident angle in collisions with CH_3- and CF_3-SAMs.[a]

Surface	θ_i	j	$<E'_T>$[b]	$<E'_{ROT}>$[c]	$<\theta_f>$[d]	% direct[e]	% long[f]
CH_3-SAM	30	0	7.8(10.7)	3.5(4.5)	46.5	39.6	30.4
	60	0	16.4(23.6)	3.8(4.4)	55.6	50.0	19.9
	30	28	9.2(13.1)	6.6(9.4)	47.3	42.8	26.8
	60	28	20.1(21.4)	9.1(9.4)	56.2	52.5	14.6
CF_3-SAM	30	0	14.8(17.6)	5.2(5.7)	46.4	73.5	7.5
	60	0	29.1(32.0)	5.1(5.2)	59.4	72.9	2.5
	30	28	19.0(21.4)	11.7(12.4)	47.2	79.3	4.3
	60	28	34.7(37.0)	12.6(12.8)	58.9	76.4	1.4

[a]60 kJ·mol^{-1} collision energy and v=0 CO vibrational state. Values within parenteses correspond to averages considering only those molecules undergoing a direct mechanism.

[b]Average final CO translational energy in kJ·mol^{-1}.

[c]Average final CO rotational energy in kJ·mol^{-1}.

[d]Average final polar scattering angle.

[e]Percentage of trajectories experiencing only one turning point.

[f]Percentage of trajectories that do not desorb the surface after 15 ps.

9.3.3. The effect of the angle of incidence

Until now, our discussion has focused on CO/SAM collisions in which the angle between the initial CO velocity vector and the surface normal was 30°. In this section, we examine the dependence of the scattering properties on the angle of incidence. The results for 30° incidence are compared with those at 60° incidence for collisions at E_{coll}=60 kJ·mol^{-1} and CO in ground vibrational state and ground or j=28 rotational state. The results are summarized in Table 9.3.

The first important result is that energy transfer out of initial translation is overall less efficient with θ_i=60° than with θ_i=30°. For instance, CO recoils with approximately twice the translational energy after impinging on the surfaces at the larger incident angle. This result has been observed before in other gas/SAM calculations[25] and in CO_2/liquid scattering

measurements,[11] and is commonly understood as due to the fact that the gas's momentum parallel to the surface is more difficult to transfer to the surface than perpendicular momentum.

Regarding energy transfer to CO rotation, the incident angle shows a different effect depending on the initial rotational excitation of CO. Table 9.3 indicates that, for CO(j=0), the rotational energy gained during the scattering process does not seem to depend on the initial angle on either SAM surface. On the other hand, trajectories started with CO(j=28) seem to lose slightly less of their initial rotational energy for the more glancing approach, particularly for the CH_3-SAM.

Even though the final CO translation and rotation increase with the incident angle, the increase in CO rotational excitation is much more moderate than the increase in the final translational energy of CO. Quantitatively, while the final translational energy of CO is roughly doubled when going from θ_i=30° to θ_i=60° for all of the conditions explored on both SAM surfaces, the amount of final CO rotation does not change or increases by at most 40% for the same change in initial angle. These data reveal the important result that the alignment of the initial velocity vector of the gas species with the surface has a marked effect on translational energy transfer but a minor effect on rotational energy transfer.

Regarding the effect of the angle of incidence on the mechanism of the collisions, our study shows a mild influence of this angle on the microscopic details of the CO collisions with the CH_3-SAM. This result can be substantiated by the percentage of trajectories undergoing a direct mechanism (single-turning-point collisions) in Table 9.3. Regardless of the initial rotational state of CO, changing the incident angle from 30° to 60° increases the probability of direct scattering from ∼40% to ∼50%. In addition, CO has a notably smaller probability of long trapping on the CH_3-SAM surface with the larger incident angle, as can be seen in the percentage of trajectories in which CO has not desorbed from the surface after 15 ps in Table 9.3. The trends in both the percentage of single-turning-point trajetories and long trapping indicate that larger incident angles promote direct processes in the CH_3-SAM. For the CF_3-SAM, the incident angle has a lesser effect on the probability of direct processes. Likely, the ridigity of this SAM has a prevalent effect on the mechanism over the incident angle, as can be seen from the relatively large percentage of single-turning-point trajectories and the small probability that the impinging molecule will trap for long times under all conditions explored in this work.

Finally, we have also examined the effect of the incident angle on the polar scattering angle. In contrast with the insensitivity of the polar-angle distributions on collision energy discussed before, the incident angle possesses a strong influence on the recoil angle of the scattered CO molecule. Table 9.3 shows the average final polar angles of CO as a function of the incident angle, rotational state, and SAM surface. Clearly, a larger incident angle results in a larger polar scattering angle. As mentioned before for θ_i=30°, the CO angular distributions do not seem to depend on the surface, and Table 9.3 shows that this happens also for θ_i=60°. Furthermore, for a particular incident angle and surface, the level of initial rotational excitation in CO does not seem to play a role in the angular distributions. Unsurprisingly, our studies reveal that this independence of the CO polar scattering angle on initial CO rotation also applies to initial CO vibration.

9.4. CONCLUDING REMARKS

The energy transfer dynamics in collisions of CO with regular and ω-fluorinated alkanethiolate mononlayers have been investigated via a classical trajectory approach with the goal of determining the role that rovibrational modes play in gas/organic-surface energy transfer.

Comparison of CO scattering with previous calculations of Ne and Ar scattering from the CH_3- and CF_3-SAM surfaces indicates that the amount of translational energy transfer for CO cannot be predicted solely based on kinematic factors. Other factors, such as the enhanced attractions of CO with the surface and the presence of internal modes play a role that cannot be predicted by atomic scattering. To shed light on this issue, we have used trajectory calculations to investigate the effect of initial CO internal excitation, along with collision energy and incident angle, on the dynamics of CO/SAM energy transfer.

Increasing the initial CO rotational energy produces a modest increase in the final translational and rotational excitation of CO. An interesting result is that while there is a net gain of CO rotational excitation during the collision if CO is initially rotationally cold, there is a net loss of rotational energy if CO impinges on the surfaces rotationally excited. In contrast with the involvement of CO rotation in the scattering process, the collisions are seen to be completely vibrationally adiabatic. There is no energy channeled to CO vibration at any of the conditions studied in this work. In addition, if trajectories are started with

vibrational excitation in CO, that excitation remains after collision.

An increase in the incident angle results in larger final CO translation, but has a very mild effect on CO rotation. The change in the initial angle of CO with the surface normal has a significant effect on the recoil angle of CO. More grazing collisions result in CO recoiling at larger angles with respect to the surface normal.

Within Chapter 10, we investigate the effect of orientation and alignment of diatomic molecules on gas/SAM collision dynamics. Additionally, in the future, we plan to study the influences that a large dipole in the diatomic (e.g. HCl), as well as hydrogen bonding character in the surface have on the scattering.

REFERENCES

[1] J. R. Lohr, B. S. Day, and J. R. Morris, J. Phys. Chem. A **110**, 1645 (2006).

[2] J. R. Lohr, B. S. Day, and J. R. Morris, J. Phys. Chem. B **109**, 15469 (2005).

[3] M. E. King, G. M. Nathanson, M. A. Hanning-Lee, and T. K. Minton, Phys. Rev. Lett. **70**, 1026 (1993).

[4] M. E. Saecker, S. T. Govoni, D. V. Kowalski, M. E. King, and G. M. Nathanson, Science **252**, 1421 (1991).

[5] M. E. Saecker and G. M. Nathanson, J. Chem. Phys. **99**, 7056 (1993).

[6] M. E. Saecker and G. M. Nathanson, J. Chem. Phys. **100**, 3999 (1993).

[7] A. J. Kenyon, A. J. McCaffery, C. M. Quintella, and M. D. Zidan, J. Chem. Soc., Faraday Trans. **89**, 3877 (1993).

[8] A. J. Kenyon, A. J. McCaffery, C. M. Quintella, and M. D. Zidan, Faraday Discuss. **96**, 245 (1993).

[9] B. G. Perkins, Jr., T. Haber, and D. J. Nesbitt, J. Phys. Chem. B **109**, 16396 (2005).

[10] B. G. Perkins, Jr. and D. J. Nesbitt, J. Phys. Chem. B **110**, 17126 (2006).

[11] B. G. Perkins, Jr. and D. J. Nesbitt, J. Phys. Chem. A **111**, 7420 (2007).

[12] B. G. Perkins, Jr. and D. J. Nesbitt, J. Phys. Chem. B **112**, 507 (2008).

[13] B. G. Perkins, Jr and D. J. Nesbitt, Proc. Natl. Acad. Sci. **105**, 12684 (2008).

[14] P. A. J. Bagot, C. Waring, M. L. Costen, and K. G. McKendrick, J. Phys. Chem. C **112**, 10868 (2008).

[15] S. R. Cohen, R. Naaman, and J. Sagiv, J. Chem. Phys. **88**, 2757 (1988).

[16] E. Martinez-Nunez, A. Rahaman, and W. L. Hase, J. Phys. Chem. C **111**, 354 (2007).

[17] M. Graupe, T. Koini, V. Y. Wang, G. M. Nassif, R. Colorado, R. J. Villazana, H. Dong, Y. F. Miura, O. E. Shmakova, and T. R. Lee, J. Fluorine Chem. **93**, 107 (1999).

[18] M. Graupe, M. Takenaga, T. Koini, R. Colorado, and T. R. Lee, J. Am. Chem. Soc. **121**, 3222 (1999).

[19] J. E. Houston, C. M. Doelling, T. K. Vanderlick, Y. Hu, G. Scoles, I. Wenzl, and T. R. Lee, Langmuir **21**, 3926 (2005).

[20] D. M. Alloway, M. Hofmann, D. L. Smith, N. E. Gruhn, A. L. Graham, R. Colorado, V. H. Wysocki, T. R. Lee, P. A. Lee, and N. R. Armstrong, J. Phys. Chem. B **107**, 11690 (2003).

[21] D. L. Smith, V. H. Wysocki, R. Colorado, O. E. Shmakova, M. Graupe, and T. R. Lee, Langmuir **18**, 3895 (2002).

[22] W. L. Hase, R. J. Duchovic, X. Hu, A. Komornicki, K. F. Lim, D. h. Lu, G. H. Peslherbe, K. N. Swamya, S. R. V. Linde, A. Varandas, et al., Quantum Chemistry Program Exchange Bulletin **16**, 671 (1996).

[23] W. A. Alexander, B. S. Day, H. J. Moore, T. R. Lee, J. R. Morris, and D. Troya, J. Chem. Phys. **128**, 014713 (2008).

[24] A. Bondi, J. Phys. Chem. **68**, 441 (1964).

[25] U. Tasic and D. Troya, Phys. Chem. Chem. Phys. **37**, 5776 (2008).

Chapter 10

Theoretical study of the stereodynamics of CO collisions with CH_3- and CF_3-terminated alkanethiolate self-assembled monolayers

Reproduced in part with permission from W. A. Alexander, J. R. Morris, and D. Troya, *J. Phys. Chem. A* **113**, 4155 (2009). Copyright 2009 American Chemical Society.

10.1. INTRODUCTION

Studying energy transfer in collisions of gases with surfaces yields information important to a fundamental understanding of gas/surface chemical dynamics. In effect, gas/organic-surface energy transfer is the essential first step in a variety of heterogeneous chemical reactions such as ozone depletion in the stratosphere,[1,2] degradation of satellite and spacecraft coatings in low-Earth orbit,[3,4] or the processing of organic aerosols,[5] to name a few. To thoroughly understand gas/organic-surface energy transfer, it is necessary to determine the role played by the various degrees of freedom involved in the collision process, including not only the surface modes responsible for energy absorption and dissipation, but also the translational, rotational, and vibrational modes of the scattering gas species. The role of the gas-phase species' translational energy in the absence of rovibrational influences has been elegantly investigated by many groups via molecular-beam and molecular-dynamics studies of rare gases colliding with organic liquids[6–9] and self-assembled monolayer (SAM) surfaces,[10–25] and of oxygen atom collisions with these surfaces.[26–29] Early efforts in atomic scattering from low-vapor pressure liquids such as squalane and perfluoropolyether (PFPE) revealed that, in many cases, the dynamics of gas/organic-surface collisions can be understood as a competition between two main mechanisms: impulsive scattering and thermal desorption.[6–9] The thermal-desorption component refers to collisions in which the impinging gas-phase species loses enough energy to thermalize with the surface before desorbing with a Boltzmann distribution of energies at the surface temperature. In contrast, impulsive scattering events are characterized by brief encounters with the surface that most often

limit energy transfer and thermalization, resulting in a second, high-energy component in the final translational-energy distributions. Comparison of the scattering properties of rare gases from squalane and PFPE revealed a critical dependence on liquid composition,[6,7] and subsquent studies showed surface roughness to play an important role in the scattering dynamics.[30]

The use of SAMs as model organic surfaces in studies of gas/surface collisions allows control over the supramolecular structure of the surface and its interfacial chemical characteristics. Pioneering studies by Cohen et al. in the late 1980's posited that the most important factors governing the collision dynamics of a particular gas with a SAM are 1) mass of the SAM terminus and 2) energy disposal into low-frequency, high amplitude modes of the SAM.[31,32] Subsequent studies have probed the influence that SAM terminal groups,[10,11,15–17] SAM packing density,[12,14] potential-energy surface considerations,[13,15,20] and incident gas identity[15,21–23,33] have on the scattering dynamics.

In comparison to monoatomic gas/organic-surface scattering, studies involving the scattering of small polyatomic gas-phase species from organic surfaces are not as abundant.[8,31–46] In addition, only a few of these studies have been able to investigate state-to-state energy transfer by resolving the rovibrational state populations of the recoiling gas species. State-resolved studies include those of Cohen et al., who scattered O_2 and NO from SAMs,[31,32] Kenyon et al., who scattered I_2 from liquids,[34,35] Perkins and Nesbitt, who investigated CO_2 scattering off squalane and PFPE,[37–41] and Bagot et al., who measured OH scattering properties from those same two organic liquids.[45] A collective conclusion of these studies was that the same two limiting impulsive-scattering and thermal-desorption mechanisms invoked to understand atomic scattering also apply to molecular scattering from organic surfaces. In the case of molecular scattering, this has been shown not only by analysis of the recoil energy of the gas molecules, but also by measurement of their internal-state distributions, in particular rotational distributions. The surface governs the competition between these two limiting mechanisms for a particular gas molecule, with fluorinated surfaces generally inducing more direct processes than hydrogenated surfaces.

An exciting new development in the quantum state-resolved gas/organic-liquid experiments mentioned above has been aimed at elucidating the stereodynamic properties of CO_2/PFPE collisions.[40] Use of differential absorption characteristics of circularly polarized light has revealed that CO_2 preferentially scatters from the surface with a forward

end-over-end top spin orientation, an effect that is enhanced as the final rotational state increases. Complementary molecular-dynamics simulations of CO_2 scattering from perfluorinated SAMs were shown to agree with the experimentally-observed orientational preference. To the best of our knowledge, this is the first time that stereodynamic effects have been measured in gas/organic-surface scattering. In contrast, analogous studies involving metal surfaces are prevalent in the literature.[47–54] Of particular relevance to the work presented herein are the studies of Hanisco et al. of CO scattering from the Ag(111) surface.[47,48] In that work, resonantly enhanced multiphoton ionization (REMPI) spectroscopy was used to investigate the influence of collision with the Ag surface on CO's final angular momentum alignment. A supersonic beam of rotationally cold (T_{ROT} <5K) CO was directed onto the Ag surface along the surface normal with ∼72 kJ·mol^{-1} collision energy, and the alignment of the rotational angular momentum of the backscattered CO was measured. While no efforts were taken to initially align the impinging CO molecules, cartwheel motion, in which the CO rotates in a plane perpendicular to the surface plane, was found to be preferred in the scattered flux, with the extent of alignment ranging from near zero for rotationally cold CO to up to 90% for high (j'>20) rotational states. The extent of alignment was also shown to increase with increasing collision energy. While scattering from Ag results in aligned CO molecules for high rotational energy levels, N_2 scattering at the same initial conditions showed pure cartwheel alignment for final rotational states as low as j'=12. The differences in the alignment of CO relative to N_2 were attributed to the greater anisotropy of the CO/Ag potential-energy surface relative to N_2/Ag. The interactions between the departing CO and the corrugated surface potential act to steer the departing molecules away from the perfect cartwheel alignment that would otherwise result from an isotropic gas/surface potential.

In the previous two chapters, we have investigated collisions of CO with CH_3- and CF_3-SAMs to probe the influence of incident energy, angle, and rovibrational state on the scattering dynamics.[36] Our results generally paralleled those of Nesbitt et al. on CO_2/liquid systems and additionally indicated that polyatomic scattering cannot adequately be described by simple kinematic models of gas/surface scattering in which the gas species is approximated by a structureless particle. In this work, we extend our study of CO scattering from CH_3- and CF_3-SAMs by examining collisional stereodynamics via classical-trajectory simulations. Our results are examined in reference to the previous CO/Ag work and will be compared to the recent work on CO_2/liquid systems to further our understanding of how

surface corrugation influences gas/surface collision dynamics.

10.2. COMPUTATIONAL DETAILS

The potential-energy surfaces used to evolve the CO/SAM trajectories are analogous to those employed in the previous chapters (see Chapter 8), so we mention here only those details specifically relevant to this study.

Using the analytical potential-energy surfaces described in Chapter 7, we have performed classical-trajectory calculations of collisions of the CO molecule with both regular (CH_3-terminated) and ω-fluorinated (CF_3-terminated) alkanethiol self-assembled monolayers. Generation of initial conditions and our propagation scheme is detailed in Chapter 3.

We integrated batches of trajectories with various initial conditions, including 60 kJ·mol^{-1} collision energy (E_{coll}), CO(v=0,j=0) or CO(v=0,j=28) rovibrational states, and 30° or 60° angle of incidence (θ_i). In addition, CO has been initially given either a random collision geometry, or assigned a specifically aligned/oriented approach geometry. The specifics of these initial collision geometries will be elaborated below. For random collision geometry, 10,000 trajectories have been calculated for each combination of surface, incident angle, and initial CO rotational state, and for the aligned/oriented approaches, 2,000 trajectories have been calculated for the same combinations. Overall, 136,000 trajectories have been calculated for the work contained in this chapter. Initial conditions for the CO molecule have been determined via quasiclassical sampling of selected vibrational and rotational states as implemented in the VENUS96 computer program.[55] At the beginning of each trajectory, CO has been placed above the surface at a separation of at least 10 Å from the closest surface atom. The initial conditions (coordinates and momenta) of the surface have been taken as intermediate steps of a 0.5 ns canonical simulation of the SAM at 300 K. The initial azimuthal angle formed by the incident CO velocity vector and the tilt direction of the SAM chains has been randomly selected.

The trajectories have been stopped post-collision when the gas either recoiled to a distance of 12 Å from the closest atom of the surface, or, in the case of long-trapping processes, if the CO molecule has not desorbed from the surface after 15 ps. The trajectories terminated as a result of long trapping times were assumed to be fully thermalized with the surface

and were randomly assigned final translational energy, E'$_T$, and rovibrational states, v', j' based on Boltzmann distributions at the surface temperature. However, since the degree of orientation and alignment of the final CO rotational angular momentum in these long-trapped trajectories cannot be predicted a priori, we have not included trajectories in which CO does not desorb the surface within our 15 ps time cutoff in the analysis of orientation and alignment of the final rotational angular momentum.

From the initial and final coordinates and momenta of the CO molecule, scattering properties including final translational-energy distributions, CO rotational state distributions, and alignment and orientation of the CO final rotational angular momentum with respect to various axes have been determined. Examination of CO's coordinates and momenta during the trajectories has been used to gain insight into the mechanism of energy exchange during the collisions.

10.3. COLLISION DYNAMICS OF CO IN THE v=0, j=0 STATE

10.3.1. Energy transfer

Full details of the scalar properties of gas/surface energy tranfer in CO/SAM collisions have been published elsewhere[36] and has been detailed in the previous two chapters. Here we provide only a brief discussion of the results that are essential to understand the stereodynamic properties of the collisions that we describe later.

Figure 10.1(a) shows the calculated final translational-energy distributions of CO after collision with CH_3- and CF_3-SAMs at E_{coll}=60 kJ·mol^{-1} and with incident angles of 30° and 60°. The average energies of these distributions are listed in Table 10.1 (<E'$_T$>). The data in the figure and table reveal that energy transfer from CO translation is very efficient in collisions with both surfaces, with the CH_3-SAM being a better energy absorber than the CF_3-SAM; at θ_i=30°, CO loses ∼87% and ∼75% of its translational energy in collision with the CH_3- and CF_3-SAMs, respectively. The distinct behavior of both surfaces seems even more pronounced at grazing incident angles: with θ_i=60°, CO loses ∼73% and ∼52% of its translational energy in collision with the same surfaces. The differential energy transfer behavior in collisions with these two surfaces has been examined in detail elsewhere[36] (see Chapters 8 and 9) and agrees with recent rare-gas scattering results from the same surfaces[15]

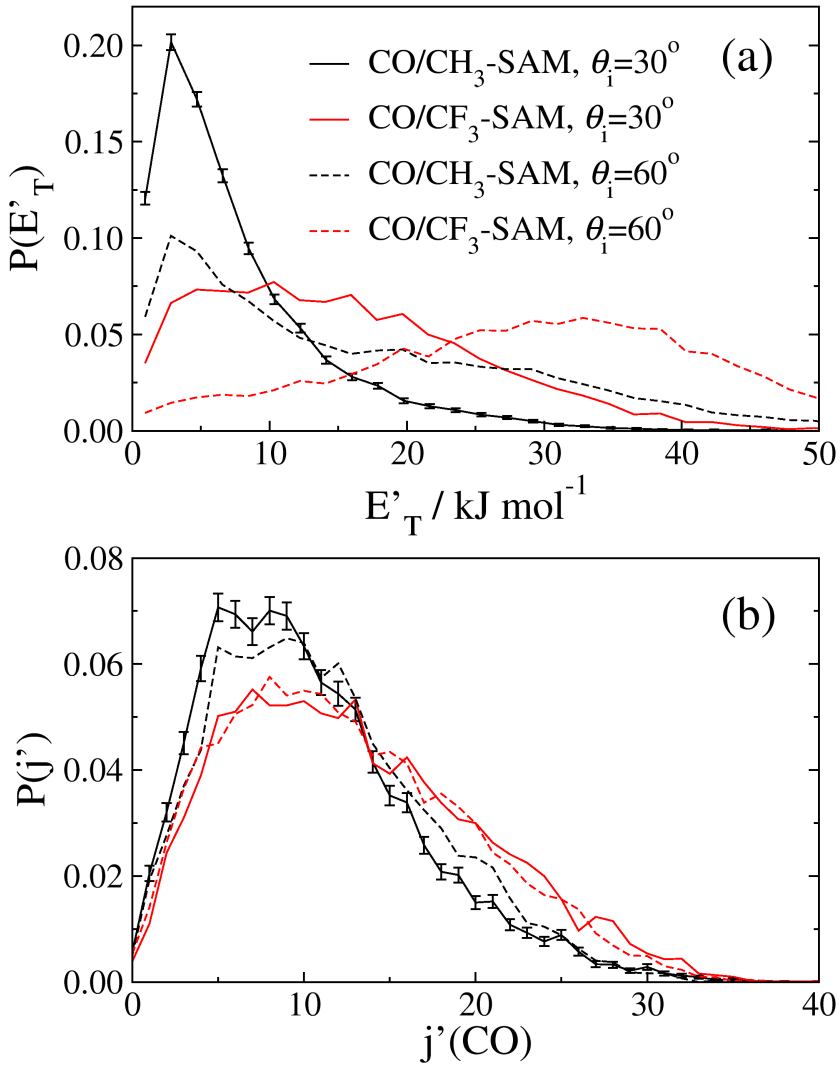

FIG. 10.1: Calculated (a) final translational-energy distributions and (b) final rotational state distributions in collisions of CO with CH_3– and CF_3–SAMs at E_{coll}=60 kJ·mol^{-1} with θ_i=30° and 60°. The distributions are normalized to unit area.

(see Chapter 5). The previous studies determined that surface mass controls the differences between these two SAMs and that the more massive surface impairs energy transfer from the impinging gas-phase projectile.[15,36] Another important result is that more grazing collisions cause CO to lose less energy to the surfaces, as can be expected from the notion that the gas species' momentum parallel to the surface is better conserved than its perpendicular momentum.

Table 10.1 shows additional information about the scattering process, including energy transfer to CO rotational degrees of freedom. The calculations reveal that CO becomes more

TABLE 10.1: Energy transfer properties in collisions of CO(v=0,j=0) with CH_3- and CF_3-SAMs.[a]

Surface	θ_i	$<E'_T>$[b]	$<E'_{ROT}>$[c]	% direct[d]	% long[e]
CH_3-SAM	30	7.7	3.4	39.0	30.5
	60	16.3	3.7	48.4	18.9
CF_3-SAM	30	15.5	5.1	74.7	6.7
	60	29.3	4.7	72.5	2.7

[a]60 kJ·mol^{-1} collision energy.

[b]Average final CO translational energy in kJ·mol^{-1}.

[c]Average final CO rotational energy in kJ·mol^{-1}.

[d]Percentage of trajectories experiencing only one turning point.

[e]Percentage of trajectories in which CO does not desorb the surface after 15 ps. Conservative estimates of the sampling error in average translational and rotational energies are 0.7 and 0.4 kJ·mol^{-1}, respectively. Estimated errors in the 'direct' and 'long' precentages are 2.0 and 0.5%, respectively. These estimated errors are applicable for these quantities throughout this study.

rotationally excited when scattering from the CF_3-SAM than from the CH_3-SAM, which is consistent with the larger rigidity of the heavier SAM. Increasing the incident angle from 30° to 60° results in little change in final rotational excitation. This is an interesting result, because in contrast, average CO final translational energies double on both surfaces. Figure 10.1(b) shows the full rotational distributions of CO for the four combinations of surface and incident angle calculated in this work. The figure cleanly shows the larger rotational excitation gained by CO in collisions with the CF_3-SAM surface in comparison with the CH_3-SAM surface and the mild effect of the incident angle. With respect to vibrational energy transfer, all of the collisions are seen to be vibrationally adiabatic, irrespective of initial vibrational (v=0 or 1) or rotational (j=0-28) excitation.

Regarding the collision mechanism, we list in Table 10.1 two indicators that help capture the broader aspects of the pathways followed by CO scattering from the SAMs studied here. First, we show the percentage of trajectories that experience only one encounter with the surface (% direct in Table 10.1). In this paper, we consider that a trajectory exhibits a direct mechanism when the CO center-of-mass coordinate along the surface-normal axis has only one turning point during the collision. Second, we show the percentage of trajectories in which CO does not desorb from the SAM surface after 15 ps (% long in Table 10.1). The

values of these scattering properties show that direct scattering is notably larger for the fluorinated SAM than for the regular SAM. On the other hand, long trapping on the surface is much larger for the CH_3-SAM. These results are clearly reflective of the well-known larger rigidity of the terminally-fluorinated SAM.

In summary, various dynamics properties indicate that the CF_3-SAM is a more rigid collision partner than the CH_3-SAM. This effect results in less translational energy transfer to the surface, more transfer to CO rotational energy, more direct collisions, and less long trapping for the CF_3-SAM than for the CH_3-SAM. In addition, more grazing collisions result in decreased translational energy transfer to the surface but do not affect substantially the amount of energy channeled into CO rotation. More grazing incidence also enhances direct collisions and diminishes long trapping on the surface.

10.3.2. Alignment and orientation of the final CO rotational angular momentum

We now investigate how the collision of CO(v=0,j=0) with a SAM drives rotational angular momentum alignment and orientation of the recoiling CO molecule. As mentioned in the introduction, some experiments can obtain information about the plane of rotation of a linear molecule (alignment)[51] and the handedness of the rotation (orientation).[40] However, simultaneous determination of both alignment and orientation is extremely difficult,[56] and this usually impairs a complete understanding and quantification of the type of rotational motion of the gas species after collision with a surface.

The ultimate goal of stereodynamics studies is to elucidate the exact type of rotational motion that a molecule possesses after collision with a surface and connect this information with the the gas/surface interaction. There are various limiting types of rotational motion with which a diatomic molecule can leave a surface. In terms of alignment, one can define four limiting rotational motions: cartwheel, helicopter, corkscrew (also termed propeller), and frisbee. A schematic of these rotational motions is depicted in Figure 10.2. As shown in the figure, the four limiting motions can be defined considering the relationship between the final rotational angular momentum of the molecule, **J'**, and the final center-of-mass velocity vector, **k'**, or the surface normal, **z**, in the case of helicopter motion. Alignment studies give insight into the plane in which the molecule rotates, but provide no information about the orientation or handedness of the rotation (clockwise or counterclockwise, exem-

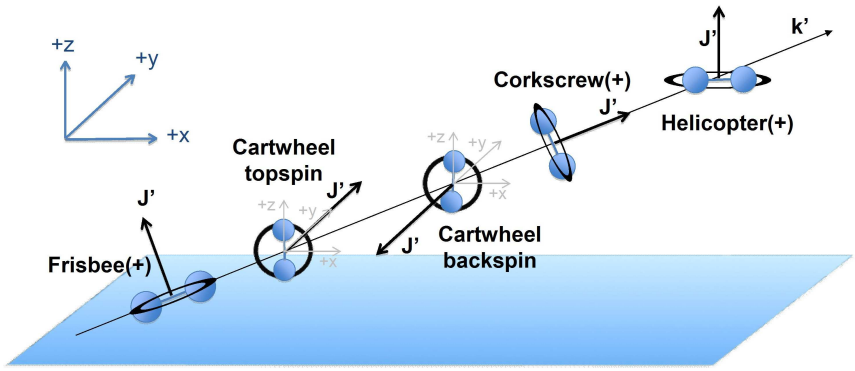

FIG. 10.2: Schematic of the various limiting rotational motions of a diatomic molecule scattering from a surface. Two orientations are shown for the cartwheel alignment.

TABLE 10.2: Average orientation and alignment moments of the final rotational angular momentum in collisions of CO(v=0,j=0) with CH_3- and CF_3-SAMs at E_{coll}=60 kJ·mol^{-1}.[a]

Surface	θ_i	$\frac{J'_x}{\lvert\mathbf{J'}\rvert}$	$\frac{3J'^2_x}{\lvert\mathbf{J'}\rvert^2}-1$	$\frac{J'_y}{\lvert\mathbf{J'}\rvert}$	$\frac{3J'^2_y}{\lvert\mathbf{J'}\rvert^2}-1$	$\frac{J'_z}{\lvert\mathbf{J'}\rvert}$	$\frac{3J'^2_z}{\lvert\mathbf{J'}\rvert^2}-1$
CH_3-SAM	30	-0.01(0.02)	0.00(-0.04)	0.04(0.18)	0.05(0.11)	0.00(0.02)	-0.04(-0.08)
	60	0.00(-0.02)	-0.03(-0.04)	0.06(0.23)	0.10(0.22)	-0.02(-0.01)	-0.07(-0.18)
CF_3-SAM	30	0.01(0.01)	-0.03(0.01)	0.04(0.11)	0.06(0.24)	0.00(0.01)	-0.02(-0.24)
	60	-0.01(-0.04)	0.00(0.01)	0.08(0.26)	0.11(0.33)	-0.01(-0.02)	-0.11(-0.33)

[a]Values between parentheses correspond to averages over trajectories in which CO results with a final rotational quantum number of 20 or larger. Conservative estimates of the sampling error in the orientation and alignment moments are 0.06 and 0.09, respectively. These estimated errors are applicable for these quantities throughout this study.

plified in Figure 10.2 by the topspin and backspin orientations possible in the limiting case of cartwheel alignment). Complete stereodynamics studies require determination of both the preferred alignment and orientation of the rotation. While, as mentioned before, simultaneous determination of alignment and orientation by experimental means is complicated, molecular-dynamics simulations can provide information of both alignment and orientation of gas-phase molecules after collision with a surface. This makes atomistic simulations an attractive tool to enhance our understanding of gas/surface dynamics.[52,54,57–59]

In an effort to establish comparison between our calculations on the CO/SAM system

and earlier measurements on CO/metal and CO_2/liquid systems, we show in Table 10.2 CO final rotational angular momentum orientation and alignment moments after collision with a SAM that can, in principle, be measured in an experiment. In classical mechanics, orientation moments can be calculated by obtaining the projections, J_i' of the rotational angular momentum vector **J'** on each of the axes of a frame of reference. In this work, we define a Cartesian frame of reference in the conventional way, i.e. by locating the SAM surface in the xy-plane and scattering CO in the xz-plane (see Fig. 10.2). In this Cartesian frame, the CO molecule is moving away from the surface after collision with positive velocity components in the z- and x-axis if the molecule scatters forward (the x-velocity component might be negative if CO recoils backwards). (Note that in experiment, in-plane scattering is usually measured exclusively, but in this work we examine all of the CO flux, including out-of-plane trajectories. However, we have verified that out-of-plane scattering is not highly probable in the calculations, so the results presented here are mostly due to in-plane scattering.) With this reference frame in mind, average $J_i'/|\mathbf{J'}|$ values provide information about the preferred handedness of the rotation (clockwise or counterclockwise) with respect to the specific i-axis. +1.0 or -1.0 values of the $J_i'/|\mathbf{J'}|$ ratio indicate exclusive handedness, and a value of 0.0 indicates no overall handedness. These calculated $J_i'/|\mathbf{J'}|$ factors are the classical analogues of the $A_1^{\{1\}}$ moment of the rotational angular momentum polarization distribution,[56] which is commonly reported in the experiment. On the other hand, average $3J_i'^2/|\mathbf{J'}|^2 - 1$ values provide information about alignment. A value of +2.0 for the $3J_i'^2/|\mathbf{J'}|^2 - 1$ alignment factor indicates that the molecule is exclusively rotating in a plane perpendicular to the i-axis. A value of -1.0 indicates rotation in a plane parallel to the i-axis, and a value of 0.0 indicates no preferred plane of rotation with respect to that axis. These calculated $3J_i'^2/|\mathbf{J'}|^2 - 1$ factors are the classical analogues of the popular $A_0^{\{2\}}$ moment of the rotational angular momentum polarization distribution that has been measured in various experiments, especially with respect to the z-axis (surface normal).[56]

The calculated average orientation and alignment moments calculated in this way are shown in Table 10.2. When the moments are calculated taking into consideration all of the CO flux (regardless of its final rotational excitation), their values are close to zero, suggesting that overall, rotational angular momentum polarization is weak in CO/SAM collisions. However, the situation changes when one performs the analysis for CO molecules that become highly rotationally excited (j'$\geq$20) as a result of the collision with the SAM surfaces

(values between parentheses in Table 10.2). For instance, the values of the $3J_y'^2/|\mathbf{J'}|^2 - 1$ moment are significantly larger than 0.0, which indicates a tendency of the CO molecule to rotate in the xz-plane (cartwheel rotation). This tendency toward cartwheel rotation is enhanced with more grazing collisions and for the heavier surface. In addition, the average values of $J_y'/|\mathbf{J'}|$ (orientation moment) are also significantly larger than 0.0, indicating a preferred handedness in the cartwheel rotation. This preferential handedness also increases with a more grazing incident angle, but does not depend very strongly on the surface. In this work, positive values of $J_y'/|\mathbf{J'}|$ represent topspin rotation (see Fig. 10.2). Therefore, the results in Table 10.2 suggest that cartwheel topspin rotation is slightly favored for highly rotationally excited CO.

A second result of interest in Table 10.2 is the presence of slight alignment with respect to the z-axis (surface normal). The average values of $3J_z'^2/|\mathbf{J'}|^2 - 1$ for rotationally excited CO show a small but noticeable deviation from 0.0 toward negative values. These results suggest a slight tendency for CO to avoid rotation in the SAM surface plane, which would correspond to helicopter motion. Instead, CO has a propensity to rotate in a plane containing the z-axis. Depending on the recoil angle, there are various motions that could satisfy this result, including cartwheel, which is consistent with the positive values of $3J_y'^2/|\mathbf{J'}|^2 - 1$, but also corkscrew, if the CO molecule is recoiling in a direction near-parallel to the SAM surface (see Fig. 10.2).

The presence of cartwheel alignment in our CO/SAM calculations agrees with the results of CO scattering from Ag(111).[48] Indeed, cartwheel alignment is the expected result for a homonuclear diatomic gas-phase species scattering from a flat, smooth surface, since the gas/surface forces that lead to rotational excitation are exclusively in the direction normal to the surface. This idealized surface model also predicts that the larger the rotational excitation, the larger the cartwheel alignment will be. With this model in mind, departure from pure cartwheel alignment in gas/surface scattering is an indication of the magnitude of tangential forces. These forces along the x- and y-directions can be traced to the corrugation of the surface (and therefore the gas/surface potential) so that the further the alignment is from pure cartwheel, the more corrugated the surface is. Whereas in the measurements of CO scattering from Ag(111) (normal incidence, $E_{coll} \sim 72$ kJ·mol^{-1}), the $3J_z'^2/|\mathbf{J'}|^2 - 1$ alignment moment was approximately -0.9 for j'=25 and larger, the most negative $3J_z'^2/|\mathbf{J'}|^2 - 1$ value obtained here is -0.33 for CO/CF_3-SAM collisions with θ_i=60° and E_{coll}=60 kJ·mol^{-1} for

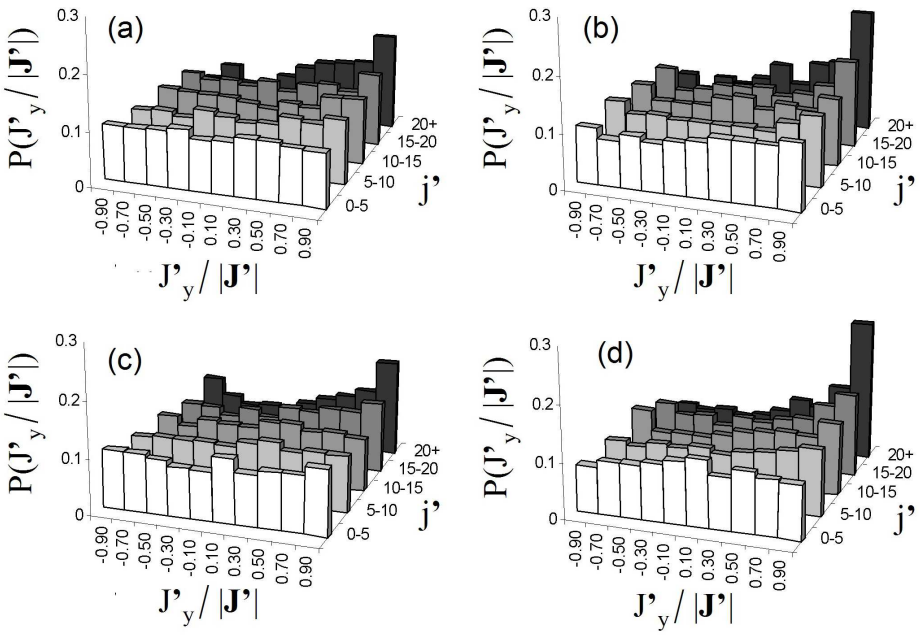

FIG. 10.3: Calculated J'$_y$/|**J'**| distributions as a function of final rotational state for CO(v=0,j=0) scattering with either θ_i=30°, (a) and (c); or θ_i=60°, (b) and (d) from the (a),(b) CH_3– and (c),(d) CF_3–SAM surfaces.

which the final rotational quantum state of CO is 20 or larger. This comparison of alignment moments with respect to the surface normal clearly shows that the SAM surfaces used in this work are much more corrugated than the Ag(111) metal surface.

Regarding orientation, while the CO experiments on silver did not report orientation moments, recent simulations by Perkins and Nesbitt of CO_2 scattering from a fully fluorinated SAM at E_{coll} = 43 kJ·mol^{-1} and θ_i=60°, performed to accompany experiments of CO_2 scattering from a perfluorinated liquid surface, reported an increased tendency toward topspin vs. backspin orientation by calculating $J'_y/|\mathbf{J'}|$ ratios.[40] Specifically, while CO_2 scattering with j'<10 does not show any orientational preference, up to ∼30% of trajectories in which CO_2 scatters with j'>50 have $J'_y/|\mathbf{J'}|$ values between 0.8 and 1.0. In an attempt to compare our results directly with those of CO_2 scattering from perfluorinated SAMs, we show in Figure 10.3 the evolution of the distribution of $J'_y/|\mathbf{J'}|$ orientation moments as a function of the level of rotational excitation in CO after collision with the CH_3- and CF_3-SAM at the two incident angles examined in this work. As can be seen in Fig. 10.3, at low values of j', the $J'_y/|\mathbf{J'}|$ distributions are largely isotropic for both surfaces at both angles, implying

no orientational preference. As j' increases, the distributions shift toward positive values of $J'_y/|\mathbf{J'}|$, indicating that CO scattering with large rotational excitation preferentially emerges with a topspin orientation. This result parallels the circular polarizance measurements of CO_2 scattering from PFPE, and is in good agreement with molecular dynamics simulations of CO_2 scattering from a perfluorinated SAM at E_{coll} ~43 kJ·mol^{-1} and θ_i=60°.[40] In fact, our calculations for CO/CF_3-SAM scattering at θ_i=60° also yield approximately 30% of the trajectories having $J'_y/|\mathbf{J'}|$ values between 0.8 and 1.0 (Fig. 10.3(d)). In an idealized model of a rotationless diatomic molecule undergoing collision with a flat, smooth surface exerting force only along the surface normal direction, symmetric topspin-backspin orientation would be expected. In addition, since momentum perpendicular to the surface normal is conserved in this ideal case, the orientational symmetry is preserved for all angles of incidence. The origin of this symmetry emerges from the equiprobable sampling of initial collision geometries in which the non-rotating diatomic axis is tilted up or down with respect to the surface normal. If the molecular axis is tilted up toward the surface normal, the trailing atom in a glancing approach collides first with the surface, and the subsequent torque from the repulsion in the surface-normal direction causes forward tumbling (topspin motion). Conversely, if the molecular axis prior to collision is tilted down, the leading atom collides first with the surface, and the torque experienced by the molecule causes it to tumble backwards (backspin motion). If the initial sampling of collision geometries is entirely random, the number of collisions in which the diatomic axis is tilted up or down prior to collision is identical, and therefore topspin-backspin symmetry should be expected. With this model in mind, the departure from topspin-backspin symmetry in the cartwheel alignment seen in this work is therefore indicative of the presence of gas/surface forces in directions other than the surface normal. In-plane gas/surface repulsions in the direction of travel will favor topspin rotation, and this is exactly what is observed in our calculations, as reflected in the $J'_y/|\mathbf{J'}|$ values of Table 10.2 and Fig. 10.3.

As mentioned before, Table 10.2 contains rotational angular momentum polarization moments that could be obtained in an experiment. While the analysis of the listed orientation and alignment moments reveals interesting information about the rotational motion of CO scattering from a SAM, an understanding of the precise types of motions and their handedness is limited using only those data. For instance, the contributions of corkscrew and frisbee motions cannot be determined from the data in the table because, unlike the helicopter and

cartwheel motions, these motions are not defined with respect to the chosen Cartesian reference frame, but with respect to the final velocity vector **k'**. Therefore, a knowledge of **k'**, i.e. the final polar-angle distribution, is necessary to investigate the presence of corkscrew or frisbee rotation. Since the negative values of $3J_z'^2/|\mathbf{J'}|^2 - 1$ (see Table 10.2) reveal that helicopter type scattering is negligible, we focus on analyzing our trajectory data in a way that will lead us to the determination of the relative contributions of cartwheel, corkscrew, and frisbee motions, and their handedness. This analysis is performed by calculating the angles between the final center-of-mass velocity of CO (**k'**), the surface normal (**z**), and the rotational angular momentum (**J'**) vectors.

Corkscrew-type motion occurs when the angle between the final CO rotational angular momentum vector **J'** and the final CO center of mass velocity vector **k'** is either 0° or 180° (see Fig. 10.2). On the other hand, frisbee motion occurs when the **k'** and **J'** vectors are perpendicular. In cartwheel motion, **k'** and **J'** are also perpendicular. Since frisbee and cartwheel alignments are indistinguishable via examination of only the **k'J'** angle, a second angle involving **J'** must be introduced to differentiate these two motions. In this work, we distinguish between frisbee and cartwheel motion by examining the angle between **J'** and a vector normal to the plane defined by the SAM surface normal vector **z**, and **k'**. (Recall that the **z** vector starts in the sulfur plane of atoms and points away from the SAM, i.e., in the +z direction, as noted in Fig. 10.2.) The vector normal to the plane defined by the **z** and **k'** vectors is calculated as the cross product of these two vectors, and will be referred to in this paper as **z**×**k'**. Assuming that the SAM surface is in the xy-plane, and that the recoiling CO molecule travels in the xz-plane with positive velocities in both the x- and z-axes, the vector **z**×**k'** is parallel to the y-axis, and points toward the +y direction. With this definition of the **z**×**k'** vector, we can distinguish cartwheel and frisbee motions by examining the angle formed by the **z**×**k'** and **J'** vectors. If the (**z**×**k'**)**J'** angle is 90°, then the motion is pure frisbee, and if the (**z**×**k'**)**J'** angle is 0° or 180°, the motion is pure cartwheel (see Figure 10.2).

With the angular analysis described above, one can also readily determine the handedness (orientation) of the corkscrew and cartwheel motions. In the corkscrew+ (clockwise) rotation, the **k'J'** angle is 0°, and in the corkscrew- (counterclockwise) rotation, the **k'J'** angle is 180°. Analogously, in the cartwheel topspin rotation, the (**z**×**k'**)**J'** angle is 0°, and in the cartwheel backspin rotation the (**z**×**k'**)**J'** angle is 180°. With these considerations in mind,

the probability of the various types of rotational motion of CO recoiling from SAMs can be elucidated by examining the probability distributions of the (**z**×**k'**)**J'** and **k'J'** angles.

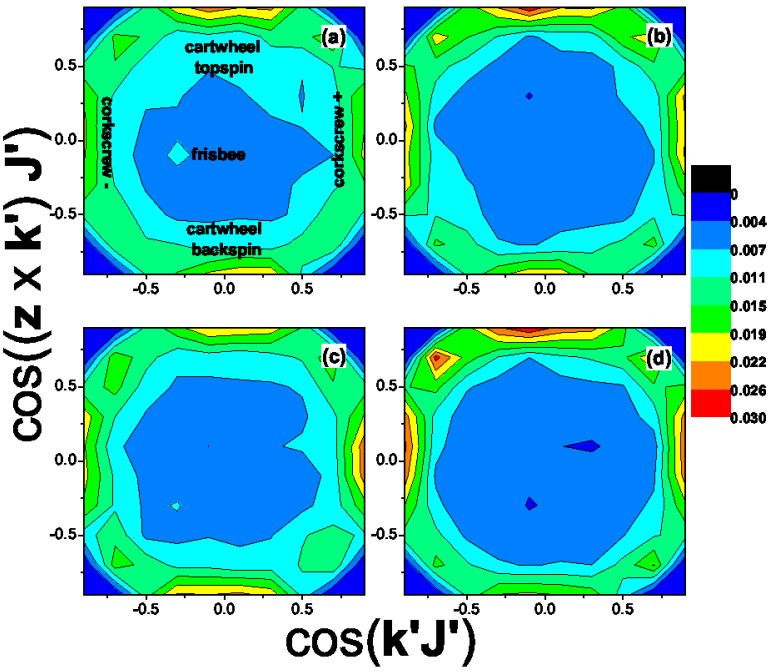

FIG. 10.4: Probability contours of CO scattering with given **k'J'** and (**z**×**k'**)**J'** angles in collisions with CH_3-, (a) and (b); and CF_3-SAMs, (c) and (d), at E_{coll}=60 kJ·mol^{-1} and v=0, j=0. The angle of incidence is 30° for (a) and (c), and 60° for (b) and (d). Contours are drawn from zero probability (blue) to probability 0.03 (maroon) at 0.00375 steps. Labels in panel (a) indicate the location of the limiting rotational motions.

Figure 10.4 shows contour plots for the probability of the recoiling CO molecules simultaneously having given (**z**×**k'**)**J'** and **k'J'** angles in collisions with SAMs at E_{coll}=60 kJ·mol^{-1}. CO is initially in its ground rovibrational state (v=0, j=0) before collision. Figure 10.4(a) displays the results for a CH_3-SAM with a 30° incident angle. The plot reveals small probability peaks in the cos(**k'J'**)=0.0 and cos((**z**×**k'**)**J'**)=+1.0 and -1.0 regions, which correspond to cartwheel topspin and backspin motions, respectively. These peaks have roughly the same intensity, indicating that topspin or backspin motions are nearly equally probable. Peaks in the regions of the graph corresponding to corkscrew+ and corkscrew- rotational motions (cos((**z**×**k'**)**J'**)=0.0 and cos(**k'J'**)=+1.0 or -1.0, respectively) are also appreciable, but their intensities are even smaller than those corresponding to cartwheel motions. There is no evidence for frisbee rotation. The probabilities for cartwheel, and especially corkscrew

motions are accentuated when CO impinges on the same surface at 60° (Fig. 10.4(b)). In addition, at this incident angle cartwheel topspin rotation seems slightly more favored than backspin rotation. This result indicates that more grazing collisions seem to provide enhanced alignment and orientation of the CO rotational angular momentum.

Much as in the case of the CH_3-SAM, the probability contours in CO/CF_3-SAM collisions at θ_i=30° also show a peak in the cartwheel and corkscrew regions (Fig. 10.4(c)). However, the intensity of the peaks in the corkscrew direction are comparable to those in the cartwheel regions. The description of the preferred alignment of CO's final rotational angular momentum is substantially different for collisions at 60° on the same CF_3-SAM surface (Fig. 10.4(d)) in three key ways. First, as with the CH_3-SAM results, the graph is more anisotropic at θ_i=60°, corroborating the idea that more grazing collisions enhance alignment. Second, there is a propensity toward cartwheel topspin over cartwheel backspin motion. The difference in the intensities of the topspin and backspin peaks is slightly larger than with the CH_3-SAM, suggesting that the heavier surface also enhances orientation. Finally, the cartwheel topspin peak is larger than the corkscrew peaks, which contrasts with the similar intensities seen at θ_i=30° on the same CF_3-SAM surface.

The emerging picture from Figure 10.4 is that when rotationally cold, but translationally hot, CO approaches a SAM surface with random collision geometry, scattered rotationally excited CO shows a weak but non-negligible degree of cartwheel and corkscrew alignment after collision. Alignment is increased for more grazing collisions and for the heavier surface, which also favors topspin vs. backspin orientation for cartwheel scattering.

Table 10.2 shows that both orientation and alignment are enhanced for rotationally excited CO. To verify this effect, we present in Figure 10.5 contour plots similar to those in Figure 10.4, but constructed with trajectories in which CO scatters with a final rotational quantum number j'≥20. The probability contour plots obtained with CO having high rotational excitation are notably more anisotropic than those considering all of the CO flux, suggesting that alignment and orientation of the rotational angular momentum is indeed enhanced if the rotational angular momentum is large. Aside from the larger anisotropy of the distributions, additional differences are evident. For instance, cartwheel topspin motion is clearly preferred over cartwheel backspin motion for both surfaces at the two incidence angles studied, including the CF_3-SAM at θ_i=30° (Fig. 10.5(c)), which exhibits topspin-backspin symmetry when considering all of the CO flux (Fig. 10.4(c)). In addition, Figure

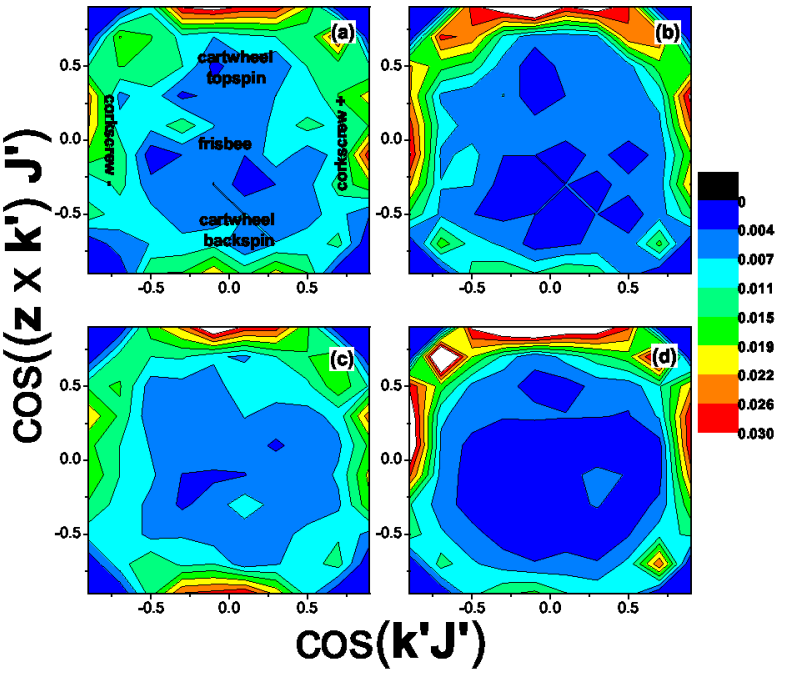

FIG. 10.5: Probability contours of CO scattering with given **k'J'** and (**z**×**k'**)**J'** angles in collisions with CH_3-, (a) and (b); and CF_3-SAMs, (c) and (d), at E_{coll}=60 kJ·mol^{-1} and v=0, j=0. Rotationally excited CO (j'≥20). The angle of incidence is 30° for (a) and (c), and 60° for (b) and (d). Contours are drawn from zero probability (blue) to probability 0.03 (maroon) at 0.00375 steps. Labels in panel (a) indicate the location of the limiting rotational motions. White areas indicate probabilities larger than 0.03.

10.5 shows that, for rotationally excited CO, cartwheel topspin motion is also more favored than corkscrew motions for both surfaces at both incident angles.

10.3.3. Stereodynamic properties of CO with initially aligned/oriented collision geometry

While there are clear trends in the final orientation and alignment of scattered CO molecules that approach the surface with a random collision geometry, we also find that the initial CO collision geometry has a significant effect on the outcome of the collision. To investigate this effect, we have integrated batches of trajectories in each of four different CO approach geometries for each of the four combinations of surface and incident angle studied in this work. Schematics of the initial collision geometries are given in Figure 10.6(a). In the

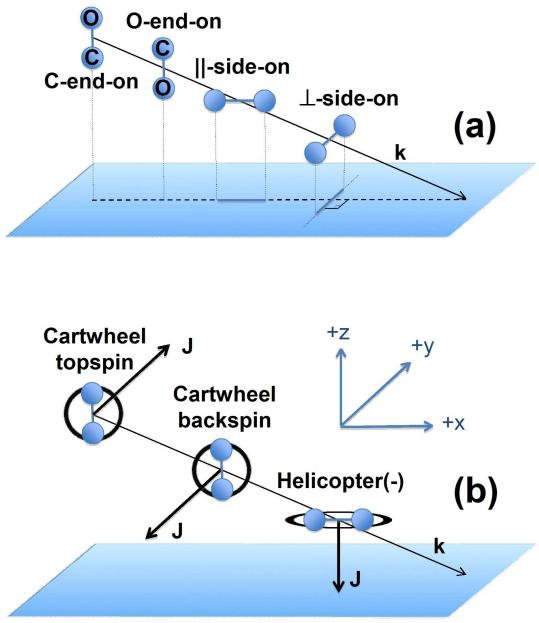

FIG. 10.6: Schematic of the various (a) initial collision geometries explored in CO(j=0)/SAM calculations and (b) initial rotational motions explored in CO(j=28)/SAM calculations.

first two approaches, the non-rotating CO molecule is aligned with its bond parallel with the surface normal, and with either the O or C atom located closest to the surface; we will refer to these as O–end-on and C–end-on collision geometries, respectively. In the other two approaches, which we refer to as ||–side-on and ⊥–side-on, the CO bond is perpendicular with the surface normal. In the ||–side-on approach, the CO bond is aligned parallel to the **k** vector projection on the xy-plane, which in this work corresponds to the SAM surface plane. Analogously, in the ⊥–side-on approach, CO is aligned with its bond perpendicular to this projection. We give a summary of the energy transfer properties for these collisions in Table 10.3. The average final translational energy, $<E'_T>$, values indicate that the initial collision geometry influences the translational energy transfer. Overall, the ||–side-on collision geometry results in larger final translational energy than the rest of the approaches, and this is especially evident for the CF_3–SAM surface and with a glancing angle of θ_i=60°. Under these conditions, we see that CO in a ||–side-on approach transfers significantly less collision energy than CO in a ⊥–side-on collision geometry. ||–side-on CO has its linear momentum directed along the -z and +x direction and its internuclear axis is aligned along the x-axis. ⊥–side-on CO also has its linear momentum directed along the -z and +x direction but the alignment of its internuclear axis along the y-axis makes it possible to interact with a larger

TABLE 10.3: Final CO properties for various initial CO collision geometries in collisions with CH_3- and CF_3-SAMs.[a]

Surface	approach	$<E'_T>$[b]	$<E'_{ROT}>$[c]	% direct[d]	% long[e]
		θ_i=30°			
CH_3–SAM	O–end-on	7.3	3.7	38.0	30.5
	C–end-on	7.1	4.2	38.2	30.5
	∥–side-on	7.8	3.1	38.5	31.1
	⊥–side-on	7.5	3.1	39.1	30.9
CF_3–SAM	O–end-on	11.8	8.4	55.2	9.6
	C–end-on	13.6	6.9	68.0	7.3
	∥–side-on	16.1	3.9	76.5	6.2
	⊥–side-on	10.2	2.9	63.5	13.2
		θ_i=60°			
CH_3–SAM	O–end-on	15.1	4.3	40.8	20.6
	C–end-on	14.8	4.7	42.7	21.1
	∥–side-on	17.3	3.1	51.9	17.4
	⊥–side-on	15.8	3.3	47.9	20.0
CF_3–SAM	O–end-on	25.7	6.8	54.3	4.5
	C–end-on	26.4	6.6	62.7	2.9
	∥–side-on	31.2	3.2	76.0	2.1
	⊥–side-on	22.8	2.8	61.8	8.4

[a]All trajectories calculated with E_{coll}=60 kJ·mol^{-1}, v=0, j=0.
[b]Average final CO translational energy in kJ·mol^{-1}.
[c]Average final CO rotational energy in kJ·mol^{-1}.
[d]Percentage of trajectories experiencing only one turning point.
[e]Percentage of trajectories that do not complete within 15 ps.

region of the SAM than the ∥–side-on approach, thereby enhancing energy transfer. This trend is backed by the substantially larger number of direct trajectories and smaller number of long-trapped trajectories for ∥–side-on trajectories. This result also suggests that thermal accomodation is favored for ⊥–side-on approach geometries.

Table 10.3 also shows the average final rotational energy of CO, $<E'_{ROT}>$for the four

collision geometries considered in this work. Comparison of these rotational energies immediately shows a marked difference between those approaches in which CO is aligned parallel (end-on), or perpendicular (side-on) to the surface normal. As one may intuitively expect, end-on approaches result in larger rotational excitation of CO molecules in comparison to side-on approaches in glancing collisions. This effect is greatest at θ_i=60°, where final rotational energy of end-on approaches is more than double that of side-on approaches. This result emerges from the fact that while in side-on approaches both atoms collide with the SAM at the same time on average, in end-on approaches, only one of the atoms initially collides with the surface directly. This atom experiences a repulsion from the surface in a direction opposite to the direction of travel, which results in a torque and rotational excitation. It is also interesting to note that for a perfectly flat and smooth surface, side-on approaches would not result in rotational excitation if the forces acting on each of the atoms of the gas-phase rotor are identical. The fact that we see rotational excitation for side-on approaches in this work is therefore either an indication of the degree of corrugation of the SAM surfaces investigated in this work or an indication of large differences in the C/SAM vs. O/SAM potential. While our previous work did reveal a slight difference in OC vs. CO approach geometry in the CO/SAM intermolecular potentials,[36] the difference is quite minor in comparison to the collision energy used in this work. Therefore, rotational excitation in side-on CO/SAM collisions is mainly due to surface corrugation.

Further insight into the dynamics of initially-aligned CO molecules scattering from SAM surfaces can be gained by examining the orientation and alignment of the final rotational angular momentum. Table 10.4 displays calculated orientation and alignment moments of the final rotational angular momentum vector as decribed before. We first note that, in contrast with the near-zero moments obtained for random collision geometry in Table 10.2, we observe significantly non-zero values in a number of moments when the molecules impinge with specifically aligned/oriented collision geometries. For the end-on approaches, large negative $3J_z'^2/|\mathbf{J'}|^2 - 1$ values coupled with large positive $3J_y'^2/|\mathbf{J'}|^2 - 1$ values indicate a strong preference for cartwheel alignment. Substantial positive $J_y'/|\mathbf{J'}|$ values further indicate that topspinning motion is preferred. This result bodes well with the expectation for a rotor traveling in the +x, -z direction and impinging end-on upon a corrugated surface that exerts a force in the -x, +z direction only on the atom that is closest to the surface. In this model, pure cartwheel topspin motion should be expected. Therefore, the result

TABLE 10.4: Average orientation and alignment factors of the final rotational angular momentum in collisions of CO(v=0,j=0) with CH_3- and CF_3-SAMs at E_{coll}=60 kJ·mol^{-1}.[a]

Surface	approach	$\frac{J'_x}{\lvert\mathbf{J}'\rvert}$	$\frac{3J'^2_x}{\lvert\mathbf{J}'\rvert^2}-1$	$\frac{J'_y}{\lvert\mathbf{J}'\rvert}$	$\frac{3J'^2_y}{\lvert\mathbf{J}'\rvert^2}-1$	$\frac{J'_z}{\lvert\mathbf{J}'\rvert}$	$\frac{3J'^2_z}{\lvert\mathbf{J}'\rvert^2}-1$
		θ_i=30°					
CH_3-SAM	O–end-on	.00(-.01)	.05(.14)	.17(.28)	.23(.41)	-.01(-.07)	-.27(-.55)
	C–end-on	.01(.05)	.07(.09)	.17(.34)	.21(.37)	.00(.01)	-.28(-.48)
	∥–side-on	.01(-.02)	-.21(-.52)	.01(-.04)	.17(.26)	.00(.00)	.04(.25)
	⊥–side-on	-.01(-.19)	.06(.08)	.04(.14)	-.09(-.31)	.01(.04)	.04(.23)
CF_3-SAM	O–end-on	.02(.03)	.23(.25)	.27(.37)	.46(.61)	.01(.01)	-.69(-.86)
	C–end-on	.02(.00)	.12(.14)	.30(.39)	.46(.65)	.00(.00)	-.58(-.78)
	∥–side-on	-.01(-.06)	-.44(-.55)	-.14(.01)	.35(.24)	.02(-.06)	.08(.30)
	⊥–side-on	.00(-.04)	.07(.20)	.08(.19)	-.27(-.39)	.01(-.01)	.20(.18)
		θ_i=60°					
CH_3-SAM	O–end-on	.02(-.09)	-.04(-.11)	.27(.63)	.36(.78)	.00(-.01)	-.32(-.67)
	C–end-on	.00(.03)	-.07(-.15)	.30(.61)	.32(.82)	.00(.00)	-.25(-.67)
	∥–side-on	.01(.06)	-.17(-.30)	-.08(.03)	.28(.47)	-.01(-.01)	-.10(-.17)
	⊥–side-on	-.01(-.03)	.12(-.04)	.10(.31)	-.15(-.06)	-.01(-.06)	.03(.10)
CF_3-SAM	O–end-on	.00(.00)	.15(-.01)	.41(.66)	.49(.83)	.01(.00)	-.64(-.82)
	C–end-on	-.01(-.02)	.10(-.07)	.38(.65)	.40(.83)	.00(.01)	-.50(-.76)
	∥–side-on	.01(.03)	-.40(-.36)	-.20(.03)	.48(.50)	.01(-.06)	-.06(-.14)
	⊥–side-on	.00(-.07)	.11(-.04)	.11(.34)	-.31(-.02)	.01(.04)	.20(.06)

[a]Values between parentheses correspond to averages over trajectories in which CO results with a final rotational quantum number of 20 or larger.

of $3J'^2_y/|\mathbf{J'}|^2 - 1$ being less than +2.0 and of $J'_y/|\mathbf{J'}|$ being less than +1.0 indicates forces acting in the y-direction, or in other words, surface corrugation orthogonal to the direction of travel. The finding that the degree of orientation and aligment is larger for the CF_3-SAM surface than for the CH_3-SAM surface can be explained as due to larger effective corrugation for the lighter surface.

Examination of the data for the side-on approaches enables further understanding of the

effect of a corrugated surface on the orientation and alignment of the rotational angular momentum of a scattering diatomic molecule. In a flat and smooth model surface, with spherically-symmetric forces about the surface normal, no rotational excitation should be expected in side-on collisions (in the limit of a homonuclear diatomic). Therefore, the presence of rotational excitation in our calculations must be due to surface corrugation, as mentioned above. In the case of a corrugated surface, if there were no forces orthogonal to the direction of travel, rotation with perfect cartwheel alignment should be expected for ∥-side-on collisions, and no rotational excitation (and therefore no alignment) would be possible for ⊥-side-on collisions. Tangential forces that emerge as a result of surface corrugation change these expected limiting trends. For instance, in a corrugated surface, tangential forces acting preferentially on one of the atoms will tend to promote helicopter motion in ∥-side-on collisions at the expense of cartwheel motion. Likewise, surface forces opposite to the direction of travel for a ⊥-side-on acting on only one of the atoms will also tend to produce helicopter motion. This is exactly what we see in the alignment and orientation moments of Table 10.4 for the two side-on approaches explored. For the ∥-side-on collision geometry, there is a tendency towards cartwheel alignment (positive values of $3J_y'^2/|\mathbf{J'}|^2 - 1$), which increases in molecules that are highly rotationally excited. However, cartwheel alignment is not perfect, which, as described before, is indicative of surface corrugation. The $3J_y'^2/|\mathbf{J'}|^2-1$ values are larger for the CF_3-SAM than for the CH_3-SAM, which reinforces the idea that the lighter surface is more corrugated. Interestingly, helicopter motion is also present for highly rotationally excited CO impinging in ∥-side-on collision geometry, further suggesting that strong surface forces orthogonal to the direction of travel act preferentially on one of the atoms. Regarding ⊥-side-on collisions, we see some tendency toward helicopter alignment from the positive values of the $3J_z'^2/|\mathbf{J'}|^2 - 1$ moment, which contrasts with the absence of cartwheel alignment (negative $3J_y'^2/|\mathbf{J'}|^2 - 1$ moments). Helicopter motion in ⊥-side-on collisions is again proof of unequal in-plane forces on the two atoms of CO.

10.4. COLLISION DYNAMICS OF CO IN THE v=0, j=28 STATE

The above discussion has focused on the stereodynamics of collisions of rotationally cold CO molecules with model organic surfaces. In the following, we turn our attention to collisions in which CO is initially rotationally excited. The presence of initial rotational

excitation enables us to select the type of rotational motion of the impinging CO prior to collision, and to investigate the effect of alignment and orientation of the initial rotational angular momentum on energy transfer and the mechanism of the collisions.

Our study is based on batches of trajectories of CO scattering from CH_3- and CF_3-SAM surfaces with θ_i=30° or 60° and E_{coll}=60 kJ·mol^{-1}. The CO was initially started in the v=0, j=28 state and with various initial alignments and orientations, which include cartwheel topspin, cartwheel backspin, helicopter(-), and random (see Fig. 10.6(b)). Cartwheel topspin and backspin motions are analogous to those described in Figure 10.2, with the only difference being that the initial rotational angular momentum **J** is parallel to the **z**×**k** vector (where **k** is the initial center-of-mass velocity vector of CO) instead of to the **z**×**k'** vector in Fig. 10.2. Helicopter(-) refers to the initial rotational motion in which CO approaches the surface rotating in a plane parallel to the SAM surface plane, with the initial rotational angular momentum pointing toward the surface. Calculations with molecules having initial helicopter motion but with an orientation such that the rotational angular momentum points away from the surface (helicopter(+)) gave results identical to those reported here for helicopter(-) and will not be reported. Due to this insensitivity of the dynamics to the handedness of the initial helicopter rotation, we will refer to helicopter(-) simply as helicopter hereafter.

10.4.1. Energy transfer

Table 10.5 shows energy transfer results for collisions of initially rotationally excited CO with the CH_3- and CF_3-SAM surfaces for both 30° and 60° incident angles. The average final translational energy, $\langle E'_T \rangle$, values indicate that the type of initial rotational motion has only a moderate effect on the final translational energy of CO. The largest differences in the four initial rotational motions investigated occur between the topspin and backspin cartwheel initial orientations. Collisions in which CO impinges having a cartwheel topspin rotational motion result in CO leaving the surface slightly faster than those in which CO is moving with cartwheel backspin motion, particularly for grazing incidence (60°). This result is rationalized by the fact that in topspin (backspin) motion, the atom closer to the SAM surface (and hence the atom which will participate in collision first) has its tangential rotational momentum pointed antiparallel (parallel) to the center-of-mass momentum in

TABLE 10.5: Energy transfer properties in collisions of CO(v=0,j=28) with CH_3- and CF_3-SAMs.[a]

Surface	Initial motion	$<E'_T>$[b]	$<E'_{ROT}>$[c]	% direct[d]	% long[e]
		θ_i=30°			
CH_3–SAM	random	9.0	6.8	43.8	25.7
	cartwheel topspin	9.7	6.8	45.8	24.5
	cartwheel backspin	8.8	7.5	43.3	25.5
	helicopter	9.3	7.9	44.4	24.5
CF_3–SAM	random	19.0	11.6	78.2	4.2
	cartwheel topspin	20.1	12.0	77.8	3.7
	cartwheel backspin	17.1	13.5	69.3	6.4
	helicopter	18.7	14.6	78.8	4.3
		θ_i=60°			
CH_3–SAM	random	20.4	9.2	53.2	14.4
	cartwheel topspin	23.6	7.2	55.5	11.1
	cartwheel backspin	18.3	7.8	53.0	15.6
	helicopter	20.5	12.0	53.8	13.6
CF_3–SAM	random	34.5	12.6	75.6	1.4
	cartwheel topspin	37.7	10.0	73.8	0.9
	cartwheel backspin	32.0	11.4	72.1	1.2
	helicopter	33.8	16.4	75.0	1.1

[a]60 kJ·mol^{-1} collision energy.
[b]Average final CO translational energy in kJ·mol^{-1}.
[c]Average final CO rotational energy in kJ·mol^{-1}.
[d]Percentage of trajectories experiencing only one turning point.
[e]Percentage of trajectories in which CO does not desorb the surface after 15 ps.

the xy-plane. For a backspinning molecule, this acts to increase the collisional momentum, yielding a harder hit with the surface and enhancing translational energy transfer to the surface. In the topspin case, the tangential rotational momentum decreases the collisional momentum, resulting in a softer encounter with the surface and decreased energy transfer. Irrespective of the individual values for the various initial rotational motions, the well-known trend that an increase in the incident angle and in the surface mass both impair translational

energy transfer seen before for CO(v=0,j=0) holds here for CO(v=0,j=28) collisions.

Table 10.5 also shows the average final rotational energy of CO, $<E'_{ROT}>$. These values are smaller than the initial CO rotational energy (18.7 kJ·mol^{-1} for j=28), implying a net loss of rotation during the collisions for all four combinations of surface and incident angle studied. This loss in rotation is caused by the torques elicited by the surface on the molecule upon collision, which tend to occur in a direction opposite to the molecular rotational motion. Comparison of the final rotational energy of CO for the various initial rotational motions studied reveals that helicopter motion is the most effective in preserving the initial rotation. This result can be understood by invoking a simplistic flat, smooth surface model and predicting deviations from that model when corrugation is present. The presence of only normal forces in a flat, smooth surface would permit a molecule scattering with initial helicopter motion to retain all of its rotational angular momentum, since there are no forces in the direction of rotation. Changes in the rotational angular momentum of a molecule approaching a surface with helicopter motion are therefore an indication of the degree of tangential forces. On the other hand, initial cartwheel rotations occur in a plane including the surface-normal axis, and therefore would be arrested in collision with this idealized surface even if there is no corrugation. The average final rotational energies in Table 10.5 and the rotational distributions in Figure 10.7 show the expected result that the amount of rotational excitation in helicopter CO is larger than in any of the other approaches examined.

Mechanistically, we see that initial rotational excitation results in both a larger percentage of direct processes and a smaller percentage of trajectories that trap on the surface for a long time when compared with the results obtained with rotationless CO in Table 10.1. It therefore seems that initial rotational excitation impairs slightly the gas/surface attractions that elicit non-direct processes, thereby promoting direct collisions.

10.4.2. Alignment and orientation of the final CO rotational angular momentum

Table 10.6 shows calculated orientation and alignment moments of the final rotational angular momentum with respect to the Cartesian reference frame defined in this work for collisions of rotationally excited CO (j=28) with the CH_3- and CF_3-SAMs. There are several differences between the values in Table 10.6 and those obtained for rotationless CO (Table

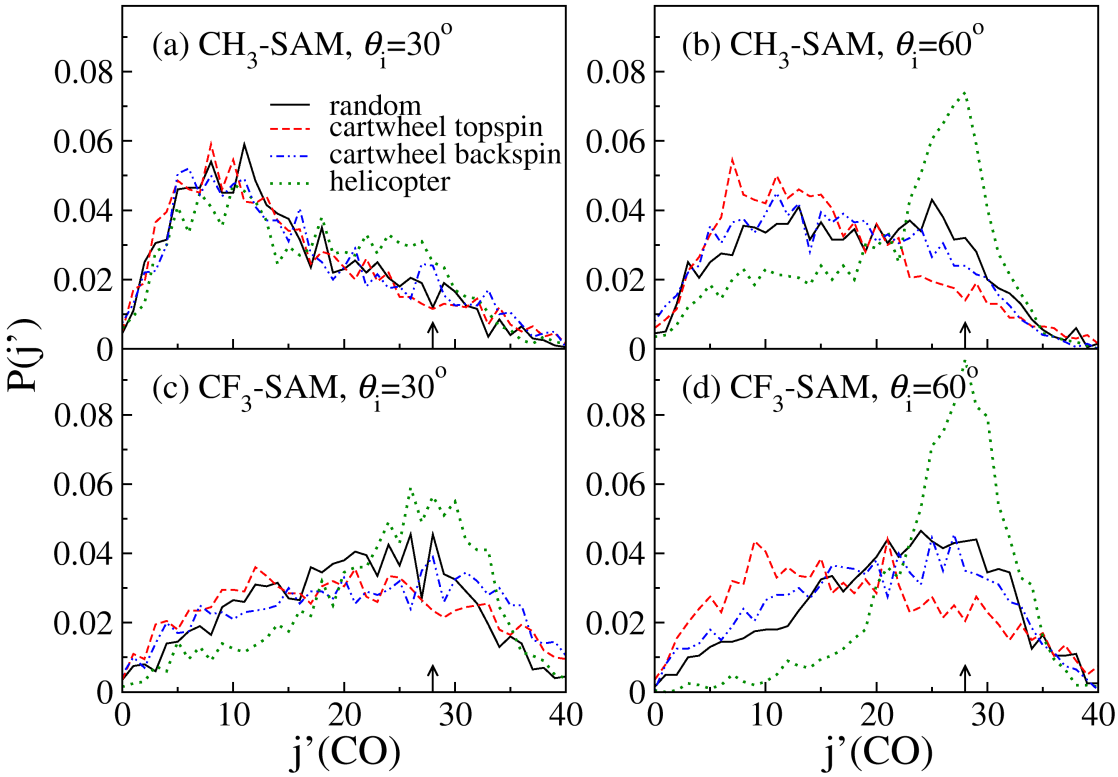

FIG. 10.7: Final rotational distributions for CO scattering from the CH_3- and CF_3-SAM surfaces as a function of initial rotational motion. (a) and (c), θ_i=30°; (b) and (d) θ_i=60°. (a) and (b), CH_3-SAM; (c) and (d) CF_3–SAM. CO is initially in the j=28 state, as indicated by the arrows in the figure.

TABLE 10.6: Average orientation and alignment moments of the final rotational angular momentum in collisions of CO(v=0,j=28) with CH_3- and CF_3-SAMs at E_{coll}=60 kJ·mol^{-1}.[a]

Surface	θ_i	$\frac{J'_x}{\|\mathbf{J}'\|}$	$\frac{3J'^2_x}{\|\mathbf{J}'\|^2}-1$	$\frac{J'_y}{\|\mathbf{J}'\|}$	$\frac{3J'^2_y}{\|\mathbf{J}'\|^2}-1$	$\frac{J'_z}{\|\mathbf{J}'\|}$	$\frac{3J'^2_z}{\|\mathbf{J}'\|^2}-1$
CH_3-SAM	30	0.00(-0.01)	-0.04(-0.09)	0.00(-0.02)	-0.03(-0.08)	0.00(0.02)	0.07(0.17)
	60	0.00(0.01)	-0.03(-0.07)	0.00(0.00)	-0.08(-0.14)	-0.01(0.00)	0.10(0.21)
CF_3-SAM	30	-0.01(-0.01)	-0.05(-0.08)	0.02(0.01)	-0.05(-0.09)	0.01(0.01)	0.09(0.17)
	60	-0.01(-0.02)	-0.06(-0.11)	0.01(0.02)	-0.05(-0.10)	0.01(0.01)	0.11(0.21)

[a]Values between parentheses correspond to averages over trajectories in which CO results with a final rotational quantum number of 20 or larger.

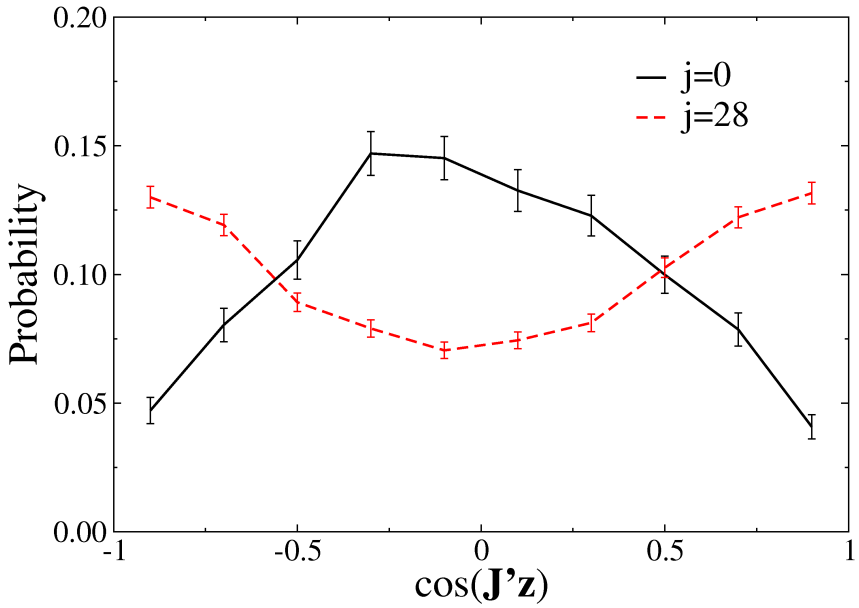

FIG. 10.8: Probability distributions of the angle formed between the final rotational angular momentum and the surface normal in collisions of CO(v=0, j=0 or 28) with a CF_3-SAM surface at E_{coll}=60 kJ·mol^{-1}, θ_i=30°. The distributions have been calculated with trajectories in which the final quantum state of CO is 20 or larger.

10.2). First, the presence of a modest alignment along the y-axis (cartwheel rotation) seen in Table 10.2 is not present for CO(j=28), even when we examine trajectories that retain a high level of rotational excitation. Instead, the values of $3J'^2_y/|\mathbf{J'}|^2-1$ are slightly negative, which indicates a slight tendency to rotate in a plane parallel to the y-axis (i.e., there is no tendency towards cartwheel rotation). This tendency increases when CO emerges rotationally excited, as indicated by the values between parentheses in Table 10.6. Second, there seems to be a small tendency to rotate in a plane perpendicular to the z-axis (helicopter motion), as indicated by the slightly positive values of the $3J'^2_z/|\mathbf{J'}|^2-1$ moment. Examination of the orientation moment in this axis ($J'_z/|\mathbf{J'}|$) reveals that the rotational motion does not have a dominant handedness (i.e., the average values of the orientation moment $J'_z/|\mathbf{J'}|$ are close to 0.0).

The conclusion stemming from Table 10.6 is that initial rotational excitation removes the slight tendency toward cartwheel topspin rotation seen in collisions with CO(j=0), and instead favors a helicopter motion. To illustrate this transition from a preference for rotation in a plane perpendicular to the SAM surface for CO(j=0) to in-plane rotation for CO(j=28),

we show in Figure 10.8 the probability distribution of the angle formed between the surface normal (**z**) and the final rotational angular momentum vector (**J'**) for CO collisions with the CF_3-SAM at 60 kJ·mol^{-1} and θ_i=30° with j=0 or 28. The figure only includes trajectories in which CO results with a rotational quantum number of 20 or larger. In perfect helicopter motion, the cosine of this angle is either -1.0 or +1.0, depending on the orientation of **J'**. On the other hand, in perfect cartwheel rotation, cos(**J'z**)=0.0. The figure clearly shows that initially rotationless CO tends to rotate in a plane perpendicular to the SAM surface plane after collision, while CO initially in j=28 favors rotation in the SAM surface plane. The preference for helicopter over cartwheel motion for initially rotationally excited CO can be explained as follows. For the j=0 case, molecules generally require an end-on molecular geometry to yield high (j'>20) rotational excitation, as is evidenced by the data in Table 10.3. Additionally, we have shown in Table 10.4 that molecules initially in an end-on approach geometry preferentially scatter with a cartwheel alignment. Although rotationally cold molecules whose approach geometry yields alignments other than cartwheel contribute to the trace in Fig. 10.8, their contribution is small, as fewer molecules obtain the necessary rotational momentum (j'≥20) to be included in the distribution than those exhibiting cartwheel alignment. Analogously, the reverse argument explains the behavior for the j=28 case in Fig. 10.8. Deactivation of the initial rotation is greatest when CO impinges with cartwheel motion. This effect will act to depopulate cartwheel alignment from the cos(**J'z**) distribution for j=28. On the other hand, CO(j=28) molecules impinging upon the surface with helicopter motion retain their high level of initial rotation (see Fig. 10.7 and Table 10.5) and conserve population of this alignment in the distribution.

We now turn our attention to the stereodynamics of collisions of CO(j=28) in which the *initial* rotational angular momentum is perfectly aligned and oriented in helicopter, cartwheel topspin, and cartwheel backspin motions (see Fig. 10.6b). To determine the correlation between initial and final CO angular momentum, we plot in Figure 10.9 cos(**JJ'**) probability distributions as a function of incident angle for the various initial CO rotational motions examined here. In the figure, population toward the +1.0 limiting value therefore corresponds to trajectories in which the CO rotational angular momentum alignment and orientation do not vary during collision. On the other hand, population toward -1.0 corresponds to trajectories in which the CO rotational angular momentum remains aligned, but changes orientation (becomes antiparallel with respect to the initial momentum) during the

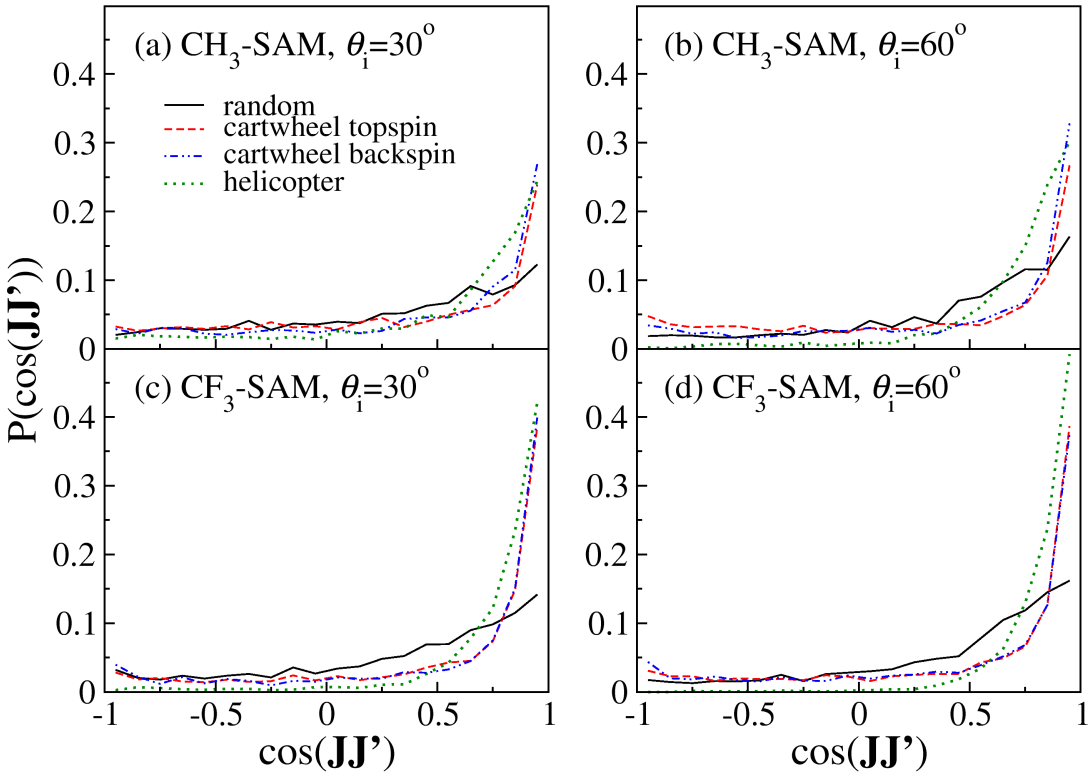

FIG. 10.9: Calculated cos(**JJ'**) distributions as a function of initial rotational motion for CO scattering with either θ_i=30°, (a) and (c); or θ_i=60°, (b) and (d). (a) and (b), CH_3-SAM; (c) and (d) CF_3-SAM. The CO is initially in the v=0, j=28 state.

collision. To help quantify the differences between the various initial motions, we show in Table 10.7 average values of cos(**JJ'**), which indicate the degree of orientation of the vectors, and of $3\cos^2(\mathbf{JJ'}) - 1$, which quantify their alignment. Values of $<\cos(\mathbf{JJ'})>$ close to +1.0(-1.0) indicate a large degree of parallel(antiparallel) orientation. On the other hand, values of $<3\cos^2(\mathbf{JJ'}) - 1 >$ close to +2.0 suggest a large degree of alignment, and values close to -1.0 are indicative of poor alignment between the **J** and **J'** vectors.

Some general trends can be drawn from the data in Figure 10.9 and Table 10.7. Regarding alignment, initial random rotational motion shows significantly poorer alignment of the **JJ'** vectors than any of the other initial rotations for collisions on both surfaces at both angles. This result likely emerges from the ability of random rotation to explore a broader region of the anisotropic gas/surface potential, which scrambles the initial rotational motion. Initial helicopter motion shows the best **JJ'** alignment, which is consistent with the notion that the absence of rotational motion in the surface-normal direction helps preserve the rotational

TABLE 10.7: Orientation and alignment coefficients between initial and final rotational angular momentum in collisions of CO(v=0,j=28) with CH_3- and CF_3-SAMs.[a]

Surface	Initial motion	<cos(**JJ**')>	<3cos^2(**JJ**')-1>
		θ_i=30°	
CH_3–SAM	random	0.28(0.65)	0.21(0.58)
	cartwheel topspin	0.31(0.84)	0.44(1.33)
	cartwheel backspin	0.40(0.85)	0.58(1.37)
	helicopter	0.51(0.80)	0.64(1.03)
CF_3–SAM	random	0.35(0.66)	0.31(0.59)
	cartwheel topspin	0.54(0.90)	0.86(1.52)
	cartwheel backspin	0.54(0.86)	0.93(1.37)
	helicopter	0.77(0.88)	1.08(1.35)
		θ_i=60°	
CH_3–SAM	random	0.42(0.61)	0.31(0.48)
	cartwheel topspin	0.31(0.86)	0.59(1.45)
	cartwheel backspin	0.45(0.90)	0.72(1.53)
	helicopter	0.71(0.84)	0.86(1.21)
CF_3–SAM	random	0.46(0.70)	0.39(0.71)
	cartwheel topspin	0.51(0.93)	0.84(1.65)
	cartwheel backspin	0.49(0.86)	0.84(1.43)
	helicopter	0.84(0.88)	1.23(1.37)

[a]60 kJ·mol^{-1} collision energy. Values between parentheses correspond to averages over trajectories in which CO results with a final rotational quantum number of 20 or larger.

angular momentum in this approach. Backspin and topspin motions provide **JJ'** alignments intermediate between random and helicopter initial motions, with backspin <3cos^2(**JJ'**)-1> values being generally larger than topspin. Regarding orientation, helicopter motion also shows the largest value of the orientation moment calculated here, which again is a consequence of the lower probability for this motion to experience surface forces opposite to the direction of rotation with respect to other initial motions. However, a difference

with the alignment trends described before is that random initial motion does not always provide the poorest degree of orientation. Instead, random and both cartwheel motions have comparable <cos(**JJ'**)> values for both surfaces and both angles, and these values are clearly smaller than those for helicopter motion. Finally, comparison between the surfaces shows that the CF_3-SAM surface promotes retention of the initial orientation and alignment of the rotational angular momentum vector, particularly in collisions at θ_i=60°. The dependence of the **JJ'** correlation with the incident angle and surface seems to be tied with the mechanism governing the collisions. The data in Table 10.5 show that direct collisions are favored at larger incident angles and with the more massive surface. This result nicely corroborates the intuitive trend that direct collisions, for which the gas/surface interaction is brief, better conserve initial alignment and orientation than non-direct collisions. In addition, the larger corrugation of the CH_3-SAM acts to scramble the initial rotational angular momentum to a larger extent than in the effectively smoother CF_3-SAM surface.

10.5. CONCLUDING REMARKS

A theoretical study of CO collisions with regular and ω-fluorinated alkanethiolate monolayers has been presented with a focus on understanding the collision stereodynamics. Rotationless CO scattering with initial random collision geometry from the CH_3- and CF_3-SAMs gains rotational excitation, but the alignment and orientation of the resulting rotational angular momentum is weak. Both alignment and orientation become more apparent when the analysis is restricted to trajectories in which CO gains large amounts of rotational excitation. The expected cartwheel topspin motion is evident in our analysis, but there is also a non-negligible contribution from unhanded corkscrew motion. The fact that cartwheel topspin motion is more prominent in collisions with the CF_3-SAM than with the CH_3-SAM suggests that the lighter SAM is effectively more corrugated than the terminally-fluorinated SAM.

Examination of the dynamics of various end-on and side-on initial approach geometries of rotationless CO indicate large corrugation of the model organic surfaces used in this work. The trend that end-on collisions result in more rotational excitation and stronger cartwheel topspin in the CF_3-SAM than in the CH_3-SAM provides further evidence of the larger effective corrugation of the latter surface.

Initial rotational excitation in CO scattering with random molecular orientation from the surfaces removes the tendency for final cartwheel topspin motion seen when CO impinges on the surfaces without rotational excitation. Instead, unhanded helicopter motion appears to be present in trajectories in which CO ends up rotationally excited after the collision. This result is rationalized as emerging from the better conservation of rotational angular momentum in gas/surface collisions in which CO is initially rotating in the surface plane. Conservation of initial CO rotational angular momentum is especially strong in the CF_3-SAM, reinforcing the notion that this surface is effectively smoother than the CH_3-SAM surface.

While this study has focused on relatively high-energy collisions of a weakly polar diatomic molecule with a surface, future studies will be aimed at understanding how stronger gas/surface forces, such as hydrogen bonding, govern the collision stereodynamics. In particular, if the gas/surface forces are comparable to the collision and initial rotational energy, steering effects that are not appreciable in the CO/SAM systems under the high-energy conditions of this work will likely change the dynamics and stereodynamics of the gas/organic-surface systems studied until now.

REFERENCES

[1] S. Solomon, Rev. Geophys. **37**, 275 (1999).

[2] D. R. Hanson and E. R. Lovejoy, J. Chem. Phys **100**, 6397 (1996).

[3] D. Troya and G. C. Schatz, Intl. Rev. Phys. Chem. **23**, 341 (2004).

[4] T. K. Minton, M. Tagawa, and G. M. Nathanson, J. Spacecr. Rockets **117**, 6239 (2002).

[5] G. B. Ellison, A. F. Tuck, and V. Vaida, J. Geophys. Res. Atmos. **104**, 11633 (1999).

[6] M. E. Saecker, S. T. Govoni, D. V. Kowalski, M. E. King, and G. M. Nathanson, Science **252**, 1421 (1991).

[7] M. E. King, G. M. Nathanson, M. A. Hanning-Lee, and T. K. Minton, Phys. Rev. Lett. **70**, 1026 (1993).

[8] M. E. Saecker and G. M. Nathanson, J. Chem. Phys. **100**, 3999 (1993).

[9] G. M. Nathanson, Annu. Rev. Phys. Chem. **55**, 231 (2004).

[10] B. S. Day and J. R. Morris, J. Phys. Chem. B **107**, 7120 (2003).

[11] B. S. Day, S. F. Shuler, A. Ducre, and J. R. Morris, J. Chem. Phys. **119**, 8084 (2003).

[12] B. S. Day and J. R. Morris, J. Chem. Phys. **122**, 234714 (2005).

[13] B. S. Day, J. R. Morris, and D. Troya, J. Chem. Phys. **122**, 214712 (2005).

[14] B. S. Day, J. R. Morris, W. A. Alexander, and D. Troya, J. Phys. Chem. A **110**, 1319 (2006).

[15] W. A. Alexander, B. S. Day, H. J. Moore, T. R. Lee, J. R. Morris, and D. Troya, J. Chem. Phys. **128**, 014713 (2008).

[16] U. Tasic, B. S. Day, T.-Y. Yan, J. R. Morris, and W. L. Hase, J. Phys. Chem. C **112**, 476 (2008).

[17] S. A. Vazquez, J. R. Morris, A. Rahaman, O. A. Mazyar, G. Vayner, S. V. Addepalli, W. L. Hase, and E. Martinez-Nunez, J. Phys. Chem. A **111**, 12785 (2007).

[18] S. B. M. Bosio and W. L. Hase, J. Chem. Phys. **107**, 9677 (1997).

[19] T.-Y. Yan and W. L. Hase, Phys. Chem. Chem. Phys. **4**, 901 (2000).

[20] T.-Y. Yan, N. Isa, K. D. Gibson, S. J. Sibener, and W. L. Hase, J. Phys. Chem. A **107**, 10600 (2003).

[21] N. Isa, K. D. Gibson, and S. J. Sibener, J. Chem. Phys. **120**, 2417 (2004).

[22] K. D. Gibson, N. Isa, and S. J. Sibener, J. Chem. Phys. **119**, 13083 (2003).

[23] K. D. Gibson, N. Isa, and S. J. Sibener, J. Phys. Chem. A **110**, 1469 (2006).

[24] D. P. Fogarty, N. A. Kautz, and S. A. Kandel, Surf. Sci. **601**, 2117 (2007).

[25] D. P. Fogarty and S. A. Kandel, J. Chem. Phys. **125**, 174710 (2006).

[26] D. Troya and G. C. Schatz, J. Chem. Phys. **120**, 7696 (2004).

[27] D. Troya and G. C. Schatz, European Space Agency SP **SP-540**, 121 (2003).

[28] M. Allan, P. A. J. Bagot, R. E. Westacott, M. L. Costen, and K. G. McKendrick, J. Phys. Chem. C **112**, 1524 (2008).

[29] M. Allan, P. A. J. Bagot, M. L. Costen, and K. G. McKendrick, J. Phys. Chem. C **111**, 14833 (2007).

[30] M. E. King, M. E. Saecker, and G. M. Nathanson, J. Chem. Phys. **101**, 2539 (1994).

[31] S. R. Cohen, R. Naaman, and J. Sagiv, Phys. Rev. Lett. **58**, 1208 (1987).

[32] S. R. Cohen, R. Naaman, and J. Sagiv, J. Chem. Phys. **88**, 2757 (1988).

[33] M. E. Bennett, W. A. Alexander, J. W. Lu, D. Troya, and J. R. Morris, J. Phys. Chem. C **112**, 17272 (2008).

[34] A. J. Kenyon, A. J. McCaffery, C. M. Quintella, and M. D. Zidan, J. Chem. Soc., Faraday

Trans. **89**, 3877 (1993).

[35] A. J. Kenyon, A. J. McCaffery, C. M. Quintella, and M. D. Zidan, Faraday Discuss. **96**, 245 (1993).

[36] W. A. Alexander, J. R. Morris, and D. Troya, J. Chem. Phys. **130**, 084702 (2009).

[37] B. G. Perkins, Jr., T. Haber, and D. J. Nesbitt, J. Phys. Chem. B **109**, 16396 (2005).

[38] B. G. Perkins, Jr. and D. J. Nesbitt, J. Phys. Chem. B **110**, 17126 (2006).

[39] B. G. Perkins, Jr. and D. J. Nesbitt, J. Phys. Chem. A **111**, 7420 (2007).

[40] B. G. Perkins, Jr and D. J. Nesbitt, Proc. Natl. Acad. Sci. **105**, 12684 (2008).

[41] B. G. Perkins, Jr. and D. J. Nesbitt, J. Phys. Chem. B **112**, 507 (2008).

[42] E. Martinez-Nunez, A. Rahaman, and W. L. Hase, J. Phys. Chem. C **111**, 354 (2007).

[43] J. R. Lohr, B. S. Day, and J. R. Morris, J. Phys. Chem. B **109**, 15469 (2005).

[44] J. R. Lohr, B. S. Day, and J. R. Morris, J. Phys. Chem. A **110**, 1645 (2006).

[45] P. A. J. Bagot, C. Waring, M. L. Costen, and K. G. McKendrick, J. Phys. Chem. C **112**, 10868 (2008).

[46] M. E. Saecker and G. M. Nathanson, J. Chem. Phys. **99**, 7056 (1993).

[47] T. F. Hanisco, C. Yan, and A. C. Kummel, J. Vac. Sci. Technol. A **11**, 2090 (1993).

[48] T. F. Hanisco, C. Yan, and A. C. Kummel, J. Chem. Phys. **97**, 1484 (1992).

[49] J. Kimman, C. T. Rettner, D. J. Auerbach, and J. A. Barker, Phys. Rev. Lett. **57**, 2053 (1986).

[50] C. T. Rettner, J. Kimman, and D. J. Auerbach, J. Chem. Phys. **94**, 734 (1991).

[51] D. C. Jacobs, K. W. Kolasinski, S. F. Shane, and R. N. Zare, J. Chem. Phys. **91**, 3182 (1989).

[52] D. P. Masson, T. F. Hanisco, W. L. Nichols, C. Yan, A. C. Kummel, and J. C. Tully, J. Chem Phys. **101**, 3341 (1994).

[53] G. O. Sitz, A. C. Kummel, and R. N. Zare, J. Chem. Phys. **89**, 2558 (1988).

[54] G. O. Sitz, A. C. Kummel, R. N. Zare, and J. C. Tully, J. Chem. Phys. **89**, 2572 (1988).

[55] W. L. Hase, R. J. Duchovic, X. Hu, A. Komornicki, K. F. Lim, D. h. Lu, G. H. Peslherbe, K. N. Swamya, S. R. V. Linde, A. Varandas, et al., Quantum Chemistry Program Exchange Bulletin **16**, 671 (1996).

[56] T. F. Hanisco, C. Yan, and A. C. Kummel, J. Phys. Chem. **96**, 2982 (1992).

[57] A. C. Kummel, G. O. Sitz, R. N. Zare, and J. C. Tully, J. Chem. Phys. **89**, 6947 (1988).

[58] D. C. Jacobs and R. N. Zare, J. Chem. Phys. **91**, 3196 (1989).

[59] H. R. Mayne, C.-Y. Kuan, and R. J. Wolf, Chem. Phys. Lett. **140**, 520 (1987).

Preface: Reactions at the gas/organic-surface interface

While much can be gained from study of energy transfer during inelastic scattering processes, future efforts should additionally address reactions at the gas/organic-surface interface. Installation of the RAIRS instrument on our molecular-beam chamber makes monitoring surface-bound products of reaction possible. While organic reactions are generally well understood in the solution phase, it is not clear that the extensive knowlege of solution-phase chemistry is applicable to gas/organic-surface processes. Our initial efforts in collision-energy promotion of gas/organic-surface reactions is described in Chapter 11. We directed high-energy alkynic beams at azide-terminated SAMs with the hope of observing a direct organic cycloaddition reaction as a result of collision. In addition to its importance as the poster child for 'click chemistry' in the organic-sythesis community, we chose azide-alkyne cycloaddition due to the energetic characteristics of the reaction. The reaction coordinate is characterized by a realtively early barrier of $\sim$20 kcal$\cdot$mol^{-1}, which is too high to be accessed thermally at the SAM surface temperature of 300K. As energy transfer in collisions of molecular-beams with SAMs is very efficient, with large fractions of impinging species thermalizing with the surface, the reaction should proceed only in a direct process at the point of impact, before the collision energy is lost to the surface. Such a reaction could be promoted by tuning the translational energy of the alkynic molecular beams. These exciting initial efforts indicated that the geometrical constraints imposed by the surface may be preventing reaction. Future work will continue to investigate this and other organic reactions at the gas/surface interface.

Chapter 11

Experimental and theoretical study of gas/surface reactions via a direct mechanism: 1,3-dipolar azide-alkyne cycloaddition

11.1. BACKGROUND

Since its introduction by Sharpless in 2001,[1] the methods described as "click chemistry" have permeated the polymer and organic synthetic communities.[2] The quintessential example of the so-called click reactions is the copper(I)-catalyzed azide-alkyne cycloaddition (CuAAC) reaction.[3] In the CuAAC reaction, a 1,2,3-triazole is formed by 1,3-dipolar cycloaddition of an azide and a terminal alkyne, which is activated by a Cu catalyst. The Cu catalyst is necessary for stereoselectivity as well as increasing the reaction rate.

The ubiquitous CuAAC reaction is amazingly robust and is routinely applied to organic synthesis, polymer and dendrimer chemistry, and adhesion processes, to name a few.[4] Such a coupling reaction is of interest to our studies as functionalization of ω-terminated SAMs represents a way to tailor the properties of the interface. Previous work in our group utilized carbamate chemistry to form various monolayers with buried hydrogen bonding networks.[5] Wöll and co-workers have examined functional group protection strategies for the synthesis of monolayers with species at the SAM terminus that would compete with the thiol headgroup absorption process.[6] The Chidsey and Hoffman groups first applied the azide-alkyne cycloaddition reaction to SAM surfaces on gold and silica substrates, respectively.[7–9] While the Chidsey studies utilized the CuAAC reaction,[8] the Hoffmann group was able to observe reaction (albeit not always to completion) without the need for the Cu catalyst.

Bertozzi and co-workers have recently developed a copper-free click chemistry approach that is competitive with CuAAC.[10] Their approach employs cyclooctane alkynes as reagents, which endows the molecules with about 18 kcal·mol^{-1} of ring strain. This strain effectively lowers the activation energy such that the reaction proceeds rapidly.[11] Additionally, they found that fluorine substituents at the β position of the alkyne leads to a sixty-fold increase in the reaction rate.

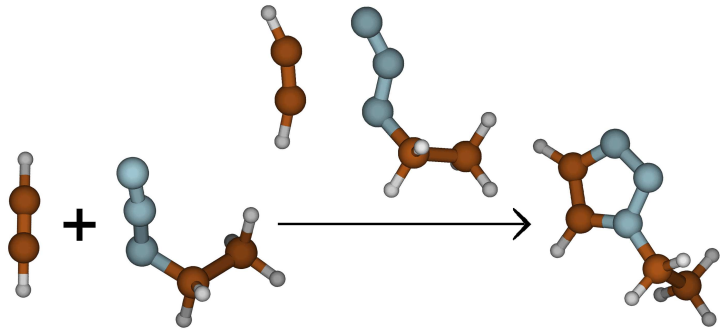

FIG. 11.1: 1,3-Dipolar cycloaddition reaction of acetylene with ethylazide to form 1-ethyl,1,2,3-triazole.

There is a fundamental interest in studying activated reactions at the gas/aruface interface. There exist many examples of translational energy being used to surmount reaction barriers in reactive gas/metal systems, but, to our knowledge, no one has observed this phenomenon in beam scattering experiments on organic surfaces. One can raise many fundamental questions about such a gas/organic-surface system. Will translational energy increase reactivity by helping to overcome the reactive barrier, or will the decrease in residence time actually hurt reactivity? Are organic reactions too geometrically constrained to proceed under our molecular-beam conditions? Will the reaction proceed faster due to an aligned distribution of functional groups positioned precisely at the interface? Within this chapter, we detail our investigations of 1,3-dipolar cycladdition reactions at the gas/surface interface, with the aim of providing insight into these questions. The topology of the azide-alkyne reactive PES shows an early barrier, which could make it possible for promotion of the reaction via translational excitation using molecular-beam techniques. We characterize the reaction of various alkyne gas species via electronic-structure calculations before outlining our molecular-beam exposure studies.

11.2. CALCULATION OF THE REACTION ENERGETICS

We have investigated the characteristics of the cycloaddition reaction coordinate for various azide-alkyne pairs. Specifically, we have located optimized geometries and energies for reactants, products, and transition states of the 1,3-dipolar cycloaddtion reaction of acetylene, **A**; 2-butyne, **B**; and 1,1,1,4,4,4-hexaflouro-2-butyne, **C** to ethylazide, **2**, using

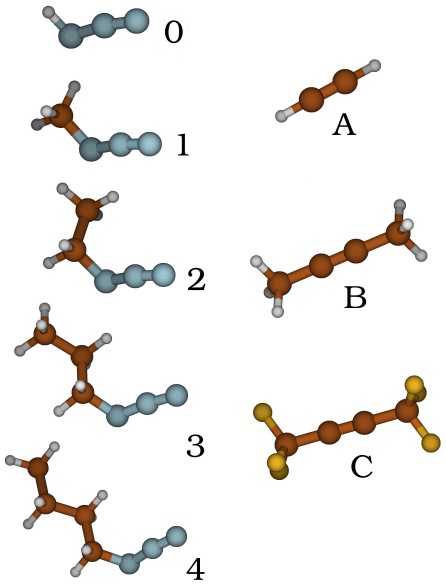

FIG. 11.2: Various reactant species investigated with electronic-structure calculations of the azide-alkyne 1,3-dipolar cycloaddition reaction. Hydrazoic acid, **0**; methylazide, **1**; ethylazide, **2**; propylazide, **3**; butylazide, **4**; acetylene, **A**; 2-butyne, **B**; and 1,1,1,4,4,4-hexafluoro,2-butyne, **C**.

electronic-structure calculations at various levels of theory. Reaction barriers and energies were also obtained for **A** in reaction with hydrazoic acid, **0**; methylazide, **1**; propylazide, **3**; and butylazide, **4**. All of these reactant species are depicted in Figure 11.2. Characterization of the reaction of **A** with **0**-**4** was carried out using density functional theory (DFT) at the B3LYP/6-31G* level to determine at what length of alkyl chain reaction barriers and energies converge. Results of these calculations are summarized in Table 11.1. From the data it is seen that, while energies vary notably from **0** to **1**, species **2** is within 0.1 kcal·mol^{-1} of the azide species with longer alkyl chain substituents, **3** and **4**. This result gives us confidence that reaction barriers and energies calculated using ethylazide, **2**, may produce data representative of longer chain azides, such as are used in the N_3-SAM.

We now investigate the differences in the reaction barrier and energy for species **A**-**C** undergoing cycloaddtion with **2**. The reaction coordinate diagrams for these three reactions are displayed in Figure 11.3, and our calculated results are summarized in Table 11.2. Examination of these data reveals that relative to **A**, addition of methyl groups, **B**, yields an increase in the barrier height, and a decrease in reaction enthalpy. However, if **A** is substi-

TABLE 11.1: Convergence of calculated reaction barriers and energies for acetylene undergoing 1,3-dipolar cycloaddition with alkylazides.[a]

Azide[b]	Barrier	Reaction energy
0	18.6 (16.9)	83.2 (71.8)
1	17.5 (16.2)	86.7 (74.9)
2	17.5 (16.3)	86.4 (74.6)
3	17.4 (16.3)	86.3 (74.5)
4	17.4 (16.3)	86.4[c](74.5)

[a]B3LYP/6-31G* zero-point corrected energies in kcal·mol^{-1}. Energies within parentheses are classical energies.

[b]Azide species as defined in Fig. 11.2.

[c]The butylazide product did not fully converge.

tuted with trifluoromethyl groups, **C**, the electron withdrawing nature of the fluorine atoms pulls electron density out of the alkyne bond, leading to a decrease in the reaction barrier and a concomitant increase in the overall exothermicity of reaction. According to the DFT calculations, the three alkyne gases are each separated from one another by 4-5 kcal·mol^{-1} (or ∼16-20 kJ·mol^{-1}) with the activation energy increasing in the order **3**→**1**→**2**. If the cycloaddition reaction proceeds through a direct mechanism and may be activated by translational excitation, the ∼5 kcal·mol^{-1} differences in reaction barriers should be large enough to facilitate translational-energy tuning of molecular beams to selectively promote reaction, since we are able to control the peak incident energy of our beams to within 1 kJ·mol^{-1} of a desired incident collision energy. As can be seen from Figure 11.3, the barrier for all three species is relatively early (i.e. the transition state resembles the reactants more closely than it resembles the product geometry). As such, translational energy should be able to drive the reaction over the transition state to form products in a direct process. In the next section, we outline our efforts in using translationally fast molecular beams to promote the 1,3-dipolar cycloaddition reaction on azide-terminated self-assembled monolayer surfaces.

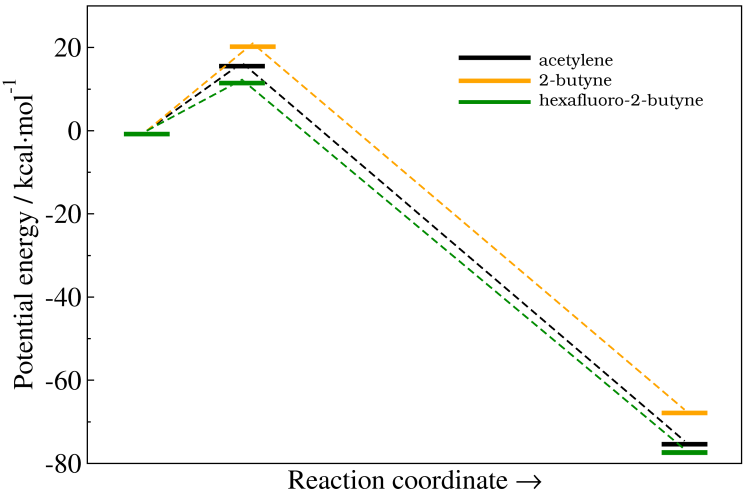

FIG. 11.3: Reaction coordinate diagram for the azide-alkyne 1,3-dipolar cycloaddition reactions. Energies obtained from B3LYP/6-31G* calculations.

TABLE 11.2: Reaction energies and barriers for the azide-alkyne 1,3-dipolar cycloaddition reactions of various alkynes with ethylazide[a].

	Reaction barrier			Reaction energy		
Alkyne[b]	**A**	**B**	**C**	**A**	**B**	**C**
B3LYP/6-31G*	16.3	21.0	12.3	74.6	67.1	76.6
MP2/aug-cc-pVDZ//						
B3LYP/6-31G*	10.6	12.6	–	75.5	75.4	83.9
MP2/aug-cc-pVDZ	8.6	8.3	–	74.9	74.6	82.9

[a] Classical energies in kcal·mol^{-1}. [b] Alkyne species as defined in Fig. 11.2.

11.3. EXPERIMENTAL SETUP AND RESULTS

As we have extensively detailed our experimental approach in Chapter 2, we present here only the specifics of this study. We have exposed azide-terminated monolayers to molecular beams of acetylene (C_2H_2) and 1,1,1,4,4,4-hexafluorobutyne (C_4F_6) with various collision energies. Pure, ∼5%, and ∼2% mixtures of C_2H_2 in H_2 give peak incident beam energies of 9, 41, and 81 kJ·mol^{-1} (see Figure 2.5) and will be referred to as 'pure', 'low', and 'high' energy C_2H_2 beams, respectively. Beams of C_4F_6 were also made. Mixtures of ∼5% and ∼2% C_4F_6 in H_2 yielded peak energies of 127 and 424 kJ·mol^{-1}, and will be referred to as 'low' and 'high' energy C_4F_6, respectively. While experiments with the above beams

have been carried out with a chopper wheel to produce a pulsed beam (see Chapter 2), we also have exposed N_3-SAMs to a continuous 424 kJ·mol^{-1} beam by removing the chopper wheel from the chamber. This beam we will refer to as the 'cw' C_4F_6 beam. The estimated flux for the pulsed beam is $\sim 1\times10^{13}$ molecules·s^{-1}cm^{-2} and for the cw beam is $\sim 1\times10^{15}$ molecules·s^{-1}cm^{-2}.

During bombardment by the alkynic beams, the SAM surface was interrogated using RAIRS as our primary means of determining whether reaction had occurred. The asymmetric N=N=N stretch gives an intense and well-resolved peak centered at 2104 cm^{-1} for our N_3-SAMs, and as reaction occurs to form the 1,2,3-triazole ring, this peak should decrease and eventually, as the reaction goes to completion, disappear.[8,9] XPS was used to obtain elemental concentrations of the monolayer before and after exposure to the beams. For the pulsed beams, we also monitored the time-of-flight profiles of the recoiling C_2H_2 or C_4F_6 molecules with mass spectrometry at m/e=26 or 93 amu, respectively. (The major fragment of C_4F_6 is the $CCCF_3$ ion, which is formed after loss of a CF_3 group upon ionization. The parent ion peak at 162 amu is very weak.) The resulting time-of-flight profiles (not shown) show extensive collisional-energy transfer to the surface. Average final translational energies for the pure, low, and high energy C_2H_2 beams were 5.5, 7.1, and 7.2 kJ·mol^{-1}, respectively. Thermal desorption fractions were $\sim$1.00, 0.86, and 0.82 for the same incident beams. Very high levels of thermalization were also observed for the C_4F_6 beams. TOF peak shapes did not noticably change over the course of any of our exposure experiments.

In Figure 11.4 are plotted the RAIR spectra of the N_3-SAM obtained before and after exposure to the molecular beam in the azide asymmetric stretch region. As can plainly be seen in the figure, no discernable decrease or broadening of the azide peak is observed. Even the 'cw' C_4F_6 beam, which allows a hundred-fold increase in flux, shows little to no change in signal. Under the conditions studied, no evidence for direct reaction was seen. Additionally, we note that evidence for a thermally-mediated reaction mechanism was also absent. This is an important result as the solution-phase cycloaddtion reaction does proceed thermally.

While we were not able to see evidence for reaction via mass spectrometry or RAIRS, the possibility exists that the reaction is proceeding, but with a low reaction probability. If only a few azide chains had reacted by the end of the exposure, the ensemble-averaged RAIR and TOF spectra may not be sensitive enough to detect such a small change in the surface. (We estimate that our RAIRS technique is sensitive only to processes that alter >5% of the

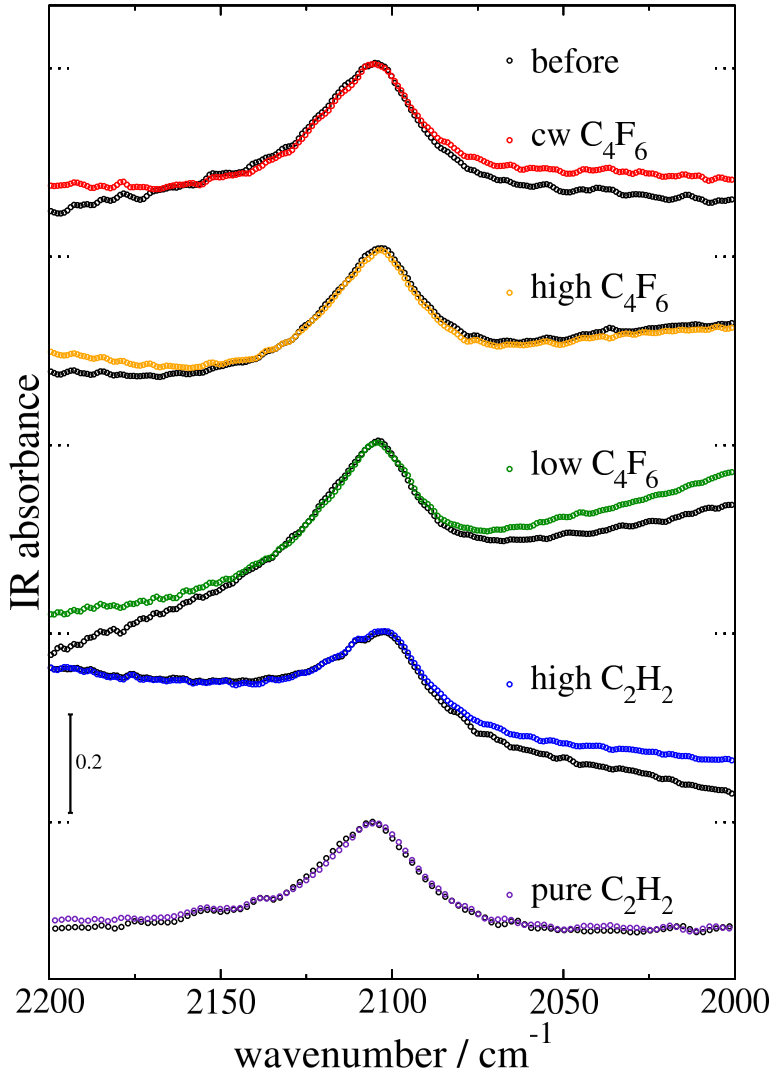

FIG. 11.4: RAIR spectra of the N_3-SAM IR signal due to the asymmetric azide stretch before (black) and after (colors) exposure to various alkynic molecular beams. Collision energies fo the 'pure', 'low', and 'high' C_2H_2 and C_4F_6 beams are defined in the text; 'cw' refers to a continuous (as opposed to pulsed) beam of the 'high C_4F_6' energy. Spectra have been shifted to match peak heights.

monolayer.) However, XPS is expected to be sensitive enough to detect changes in ∼1% of the surface groups, and use of XPS to interrogate the SAM surface before and after exposure to the flourinated alkyne should provide more definitive information on whether or not the cycloaddition reaction has occurred. Flourine has intense XPS signals due to the F 1s peak at binding energies of ∼689 eV and due to the F KLL Auger peak at ∼600 eV.[12] Cycloaddition of C_4F_6 to the N_3-SAM will light up these intense peaks. Additionally, changes should be

seen in the nitrogen and carbon regions of the XPS spectra as a result of reaction.[8,13] Shown in Figure 11.5 are XPS spectra of an N_3-SAM before and after exposure to the high energy C_4F_6 beam, compared with a CF_3-SAM for reference. The spectra indicate no evidence for reaction between the alkyne and azide species.

11.4. DISCUSSION

Our experimental results show resounding evidence that the cycloaddition reaction does not proceed under any of the investigated conditions, even with a constant flux of 10^{15} C_4F_6 molecules$\cdot s^{-1}$ bombarding the surface with over 4 eV of translational energy. (For reference, the entire 1 cm^2 sample spot contains $\sim 5\times10^{14}$ functional groups, based on the ideal packing density of 21.4 $Å^s\cdot$molecule^{-1}.) Based on our electronic-structure calculations, less than a quarter of this available translational energy would be needed to overcome the reaction barrier and form products. As the calculated barriers and reaction energies have been obtained in an effectively gas-phase, vacuum environment, they are not necessarily directly applicable to the N_3-SAM system — not only is the azide moiety tethered to the Au surface, which limits its available spatial orientation, the azide group is surrounded by the other tethered chains which may also confine its possible geometrical conformations. The nitrogen atoms in the azide tailgroup possess partial charges of alternating sign, which could serve to bring about attractive interchain interactions, making possible a coulombic-bonding network at the interface, or the charges may setup large inter-chain repulsions. In the former case, the azide-headgroups would tilt over to interact with neighboring chains, resulting in increased tilt angles relative to a straight-chain alkanethiol SAM. By tilting down, the azide groups would be in a position that would be conducive for impinging gas-phase alkynes to find the proper transition geometry in direct collision. However, in the latter case of chain-chain repulsion, the azide tailgroups would tilt toward the surface normal direction, minimizing repulsive energy, and result in a more highly "standing up" SAM. In this position, the azide species would not be in a very favorable position to promote direct cycloaddition upon alkyne collision.

We can ascertain which of these two limiting cases is most likely via molecular-dynamics simulation and inspection of our RAIR spectra. We have built model N_3-SAMs whose consituent united-atom chains have their azide tailgroups separated from the sulfur headgroups

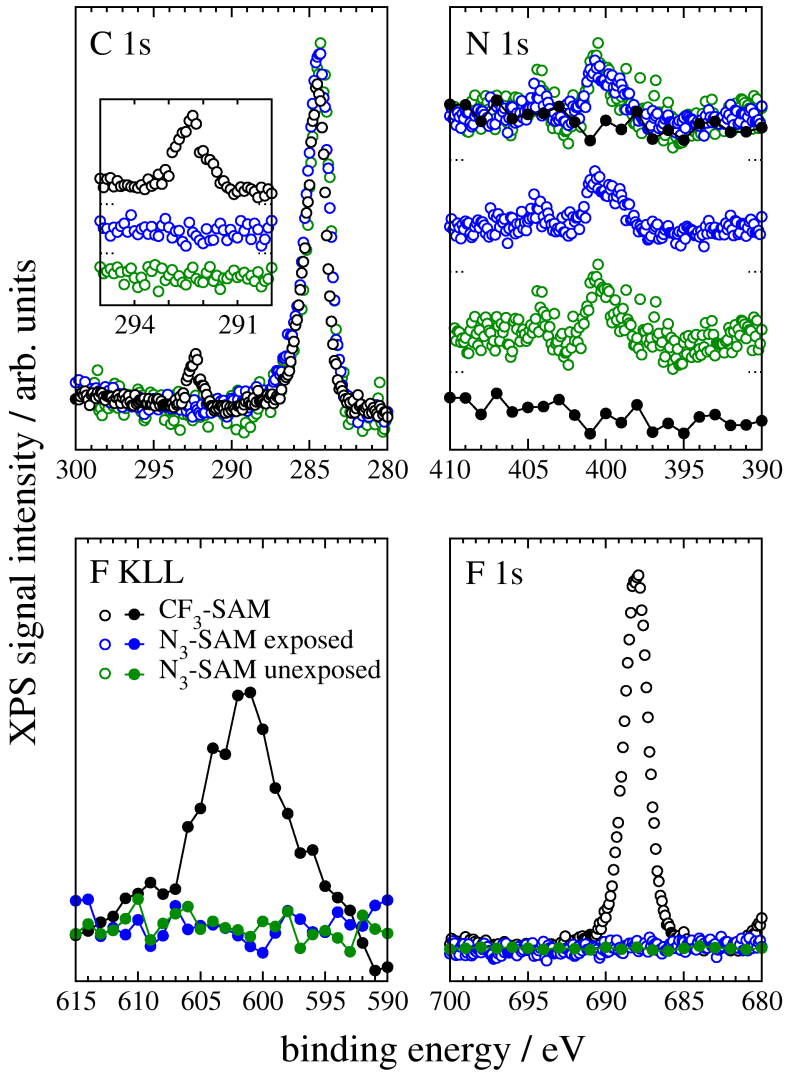

FIG. 11.5: XPS spectra of the carbon, nitrogen, and flourine regions for a CF_3-SAM compared to an N_3-SAM before and after exposure to high-energy C_4F_6 beams. Data are shown for the C 1s, N 1s, F 1s and F KLL regions. Intensities have been scaled relative to the Au $4f_{5/2}$ peak signal intesity, but relative intensities are not consistent between panels. For clarity, the N 1s spectra have been presented singly and superimposed on one another. Open symbols correpond to high-resolution (multiplex) data, and closed symbols with lines correspond to data obtained at low resolution (survey).

by either 8 (even) or 9 (odd) methylene units. We have utilized the same united-atom OPLSUA force field terms documented in Chapter 3 for description of CH_3-SAMs, with modifications for the azide group. The most important of these modifications is the incorporation of atomic partial charges into the SAM chains. We have used atomic partial

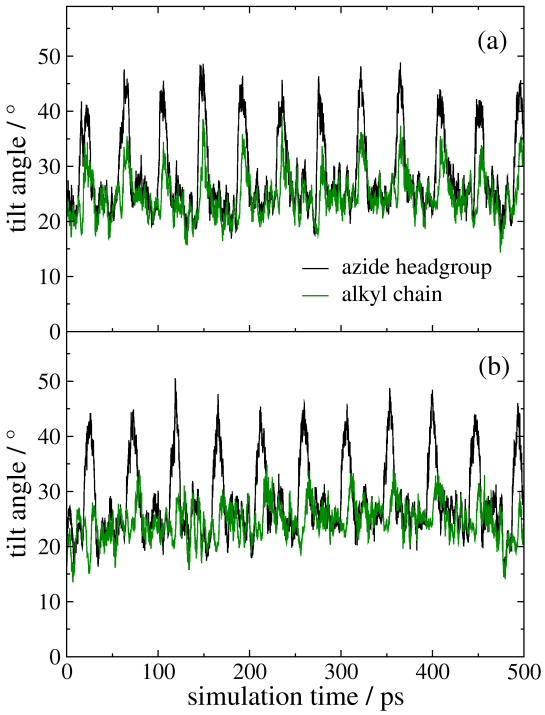

FIG. 11.6: Average tilt angle of the azide headgroup and methylene chains as a function of simulation time for N_3-SAMs. SAMs composed of both N_3-$(CH_2)_8$-S (a) and N_3-$(CH_2)_9$-S (b) chains were investigated.

charges (with charges on hydrogen summed into heavy atoms) obtained in our B3LYP/6-31G* calculations of the butylazide species and have assigned these unchanged to the 7 terminal united-atoms. The charges used were -0.273, 0.406, -0.306, 0.175, 0.039, 0.109, and -0.008 e, listed in order from the terminal N toward the interior of the SAM.[14] After a thermal equilibration at 300K, we ran a 500 ps canonical simulation and calculated the average tilt angle of the azide tailgroup and the interior alkyl chain relative to surface normal. Recall that CH_3-SAM has been shown experimentally to have an average tilt angle of $\sim$30°, and we determined an average chain-tilt angle of 29.9° with a similar molecular-dynamics simulation (see Chapter 3). The results of this study are plotted in Figure 11.6, which shows the average tilt angle for the azide tail group and the alkyl chains as a function of simulation time. Time- and ensemble-averaged values for the azide tilt angle are 28.2 and 28.4° from the surface normal for the even and odd chain lengths, respectively. Average values for the alkyl chains are 24.6 and 24.5° for the same surfaces. These values are significantly smaller than the 29.9° chain-tilt value obtained for a CH_3-SAM, and indicate that repul-

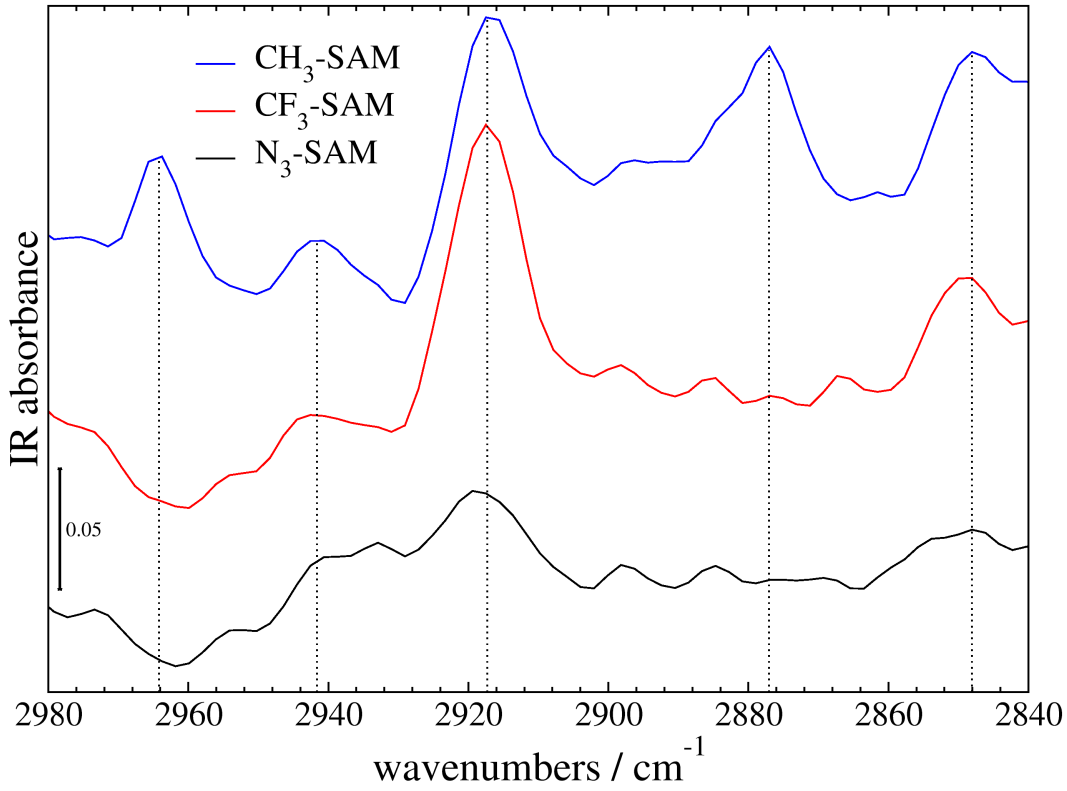

FIG. 11.7: RAIR spectra of the hydrocarbon region for CH_3-, CF_3-, and N_3-SAMs. Dotted lines indicate relevant peak positions (detailed in text) for the CH_3-SAM and are included as a guide for the eye.

sive interactions between the chains result in SAM chains that are more vertically oriented than in CH_3-SAMs. We also note that inspection of Fig. 11.6 reveals that these tilt-angles values fluctuate with about the same frequency as the CH_3-SAM, but with a much higher amplitude. The majority of the time, the tilt-angles hoover just above 20°, but make short fluctuations to values above 40°. However, even during these brief fluctuations to tilt angles closer to surface-parallel, the azide groups do not approach a beneficial geometry for cycloaddition (∼90°).

Due to the surface-selection rules of RAIRS, we can also ascertain information about the molecular orientation of the SAM chains by examining the RAIR signal from the methylene units. RAIRs only detects molecular motions whose transition dipole moment has some component along the surface-normal direction. Alkyl chains in an all-trans confirmation having a chain-tilt angle of near 0° have their methylene hydrogens oriented in such a way that the plane of the HCH unit is near-parallel to the SAM surface; consequently, alkyl chains

in a standing-up orientation have very small transition-dipole components in the surface-normal direction for the CH_2 stretches. As the chains tilt over toward surface parallel, the transition-dipole components grow in the z-axis and the RAIR signal due to the CH_2 stretches increases in intensity. Comparing intensities of the CH_2 stretches for CH_3- and N_3-SAMs can give us a handle on whether the N_3-SAM chains are more or less tilted than in CH_3-SAMs. In Figure 11.7 we show the RAIR spectra for CH_3-, CF_3-, and N_3-SAMs in the hydrocarbon stretching region. Characteristic peaks for the CH_3-SAM are seen at 2964, 2942, 2917, 2877, and 2848 cm^{-1} due to the CH_3 asymmetric, CH_3 fermi resonance, CH_2 asymmetric, CH_3 symmetric, and CH_2 symmetric stretches. The CH_2 stretches are also seen with approximately the same position and intensity for the CF_3-SAM, implying similar tilt angles. However, the N_3-SAM surface displays substantially less intense CH_2 stretching peaks than seen with the CH_3 and CF_3-SAMs. This implies that the N_3-SAM chains tilt less than the chains of the other monolayers, and corroborates the results seen in the molecular dynamics simulation. Further evidence for only a slight tilt of the N_3-SAM chains is given by the fact that the asymmetric azide peak itself is very intense, which would require the azide moiety to be aligned near the surface-normal axis.

Taken together, the data from RAIRS and the MD simulations indicate that the azide groups are located at the interface in a non-favorable orientation for reaction. Based on these studies, it seems that the cycloaddition reaction does not proceed to any observable extent due to geometric constraints imposed by the surface. With the azide groups arranged in a near-surface normal orientation, the direct, concerted reaction pathway is sterically hindered. While geometrical constraints seem to be governing the lack of reaction, alternative explainations include 1) the gas/surface interaction time may be too short for with the high-energy beams for the system to reach the transition state and proceed to products, and 2) the large amount of collisional energy available may simply send the system back toward reactants once the transition state geometry is achieved (in fact, the early barrier may encourage this).

11.5. SUMMARY

We have investigated the feasibility of translational-energy promotion of organic reactions at the gas/surface interface using the quintessential click chemistry reaction, 1,3-dipolar

azide-alkyne cycloaddition, as our exemplar. Our approach was to combine popular contemporary techniques from the molecular-beam and organic-sythesis communities (mode-selective reactivity and click chemistry, respectively) to study reactions at the gas/surface interface. Electronic structure calculations reveal that the reaction energetics and potential energy surface topology along the minimum energy reaction coordinate should be conducive to promotion of this reaction using translational energy. Azide-terminated SAMs were exposed to high-energy molecular beams of alkyne species and the reaction progress was monitored using reflection absorbsion infrared spectroscopy to interrogate the SAM surface, and mass spectrometry time-of-flight techniques to infer any changes in the gas/surface collision mechanism as a result of surface modification. Both techniques revealed no evidence for reaction as a result of exposure. XPS gave further confirmation that cycloaddition of the impinging gas-phase species had failed. Combined results of molecular-dynamics simulations and RAIRS indicate that the azide tailgroups are oriented at the interface with an unfavorable orientation for the reaction to proceed. Future experiments with this system will include: 1) confirmation that the alkynic gases used will indeed react with the N_3-SAM surface in solution, and 2) scattering from surfaces in which we have introduced disorder into the azide monolayer via mixed monolayer approaches and/or surface heating.

REFERENCES

[1] H. C. Kolb, M. G. Finn, and K. B. Sharpless, Angew. Chem. Intl. Ed. Engl. **40**, 2004 (2001).

[2] C. Hawker, V. V. Fokin, M. G. Finn, and K. B. Sharpless, Aust. J. Chem. **60**, 381 (2007).

[3] C. W. Tornoe, C. Christensen, and M. Meldal, J. Org. Chem. **67**, 3057 (2002).

[4] R. A. Evans, Aust. J. Chem. **60**, 384 (2007).

[5] M. K. Ferguson, E. R. Low, and J. R. Morris, Langmuir **20**, 3319 (2004).

[6] K. Rajalingam, A. Bashir, M. Badin, F. Schroder, N. Hardman, T. Strunskus, R. A. Fischer, and C. Woll, ChemPhysChem **8**, 657 (2007).

[7] J. P. Collmann, N. K. Devaraj, and C. E. D. Chidsey, Langmuir **20**, 1051 (2004).

[8] J. P. Collmann, N. K. Devaraj, T. P. A. Eberspecher, and C. E. D. Chidsey, Langmuir **22**, 2457 (2006).

[9] T. Lummerstorfer and H. Hoffmann, J. Phys. Chem. B **108**, 3963 (2004).

[10] J. M. Baskin, J. A. Prescher, S. T. Laughlin, N. J. Agard, P. V. Chang, I. A. Miller, A. Lo, J. A. Codelli, and C. R. Bertozzi, Proc. Natl. Acad. Sci. **104**, 16793 (2007).

[11] N. J. Agard, J. A. Prescher, and C. R. Bertozzi, J. Am. Chem. Soc. **126**, 15046 (2004).

[12] G. N. Robinson, A. Freedman, and R. L. Graham, Langmuir **11**, 2600 (1995).

[13] R. L. Graham, C. D. Bain, H. A. Biebuyck, P. Laibinis, and G. E. Whitesides, J. Phys. Chem. **97**, 9456 (1993).

[14] Similar results were obtained with inclusion of partial charges on only the azide nitrogens.

Chapter 12

Summary and concluding remarks

12.1. GENERAL COMMENTS

The goal of the research presented in this dissertation is to further our understanding of energy transfer dynamics at the gas/organic-surface interface. A full understanding of chemical reaction dynamics at the gas/organic-surface interface requires knowledge of energy transfer processes that happen as a result of a gas-phase species colliding with the surface. The extent of energy transfer between the various degrees of freedom of the surface and the impinging species determines the propensity for gas accomodation and subsequent chemical reaction. Energy transfer in the initial gas/surface impact can also reveal information regarding the likelihood for reaction via a direct mechanism. In this dissertation, we have examined the influence of mass and rovibrational motion on the energy-transfer dynamics of gas-phase species scattering from model organic surfaces using theory and experiment. From an experimental prespective, self-assembled monolayers are attractive organic-surface models due to their reproducible, well-characterized structure, which makes alteration of the gas/organic-surface interface amenable through standard organic synthetic techniques. Supersonic beams of rare gases and diatomic molecules were directed onto CH_3- and CF_3-SAM surfaces in ultrahigh vacuum, and time-of-flight profiles were recorded for the scattered species. This allows us a direct probe of the gas's translational energy loss/gain as a result of collision. Collisional energy transfer is seen to be very efficient in all of the systems examined, with large fractions of the impinging species losing enough of their incident collision energy to thermalize with the surface. To further elucidate the energy transfer processes at a molecular level, we have employed classical-trajectory simulations. These simulations allow us the ability to investigate aspects of the gas/SAM collision not currently observable with our experimental apparatus, such as state-to-state information. Simulations also give us the opportunity to view a "molecular picture" of the scattering events.

12.2. INTERMOLECULAR POTENTIAL-ENERGY SURFACES

Classical trajectory simulations require accurate intermolecular potential-energy surfaces for a quantitative description of dynamics. We carried out extensive electronic-structure studies of the potential-energy surfaces of the interactions of the Ne, Ar, Kr, Xe, N_2, and CO species with the CH_4 and CF_4 molecules to obtain high-quality ab initio data for use in building analytic PESs. A systematic approach for obtaining highly-accurate energy estimates using the focal-point approach and extrapolation techniques was developed. Analytic pair-wise Buckingham potentials were fit to ab initio data at the fp-CCSD(T)/CBS level. The resulting intermolecular potential-energy surfaces were subsequently used in classical trajectory simulations of gas/organic-surface collisions.

12.3. MASS EFFECTS ON ENERGY TRANSFER

We studied the dynamics of rare gases scattering from CH_3- and CF_3-SAM surfaces using both molecular-beam scattering and classical-trajectory simulations. Experiments indicate that while 60 kJ·mol^{-1} Ne transfers more energy to the hydrogenated surface than the fluorinated surface, 60 kJ·mol^{-1} Kr transfers equal amounts of energy to each surface. We learned that energy transfer to the surfaces increases with increasing mass of the impinging gas-phase species. Results from our extensive molecular-dynamics simulations indicated that mass is the most important factor in determining the outcome of the collision. Other effects, such as differences in the potential-energy surfaces play only a minor role in the dynamics. In order for SAMs to efficiently absorb energy from an impinging gas species, the SAM chains must move laterally so neighboring chains can dissipate the energy of the collision. Fluorination at the monolayer terminus introduces an inertial barrier to this motion, and limits energy transfer to the surface in Ne collisions. Kr, however, possesses enough momentum to overcome this inertial barrier and equally excite the absorbing modes in the CH_3- and CF_3-SAMs, and results in similar energy transfer for both SAMs.

12.4. ROVIBRATIONAL INFLUENCES ON ENERGY TRANSFER

Comparison of 60 kJ·mol^{-1} Ne and CD_4 scattering from various monolayers reveals that CD_4 leaves the surfaces with substantially less translational energy than Ne, despite their

equal masses. Ab initio calculations designed to estimate the maximal attractions between Ne and CD_4 with the SAM surfaces indicated an increase in the CD_4 attractive forces with the surface of approximately tenfold over Ne. However, at the high collision energies examined (E_{coll}=60 kJ·mol^{-1}), effects due to these dispersion interactions will be less important than at low incident translational energies. CD_4 has rovibrational degrees of freedom that can accept some fraction of the collision energy upon impact with the SAM surfaces and affect the overall energy transfer characteristics. To address the influence of rovibrational degrees of freedom on energy transfer dynamics, we chose to study the simple diatomic molecules N_2 and CO scattering from CH_3- and CF_3-SAMs. Results of N_2 and CO molecular-beam scattering experiments show similar collision energy transfer properties. Comparison with previous rare-gas scattering data indicate that polyatomic scattering cannot adequately be described by simple kinematic models of gas/surface scattering in which the gas species is approximated by a structureless particle. Since our experimental apparatus does not currently have the capability to probe the initial or final rovibrational state populations of the scattering species, simulations were used to examine the influence the addition of rovibrational degrees of freedom has on the energy transfer dynamics. Our calculated state-to-state energy-transfer properties suggest that the collisions are vibrationally adiabatic. However, translational energy transfer to and from rotational modes, while relatively weak, is readily apparent. The presence of rotational modes impacts the overall energy transfer dynamics as these modes provide another pathway (other than into the SAM surface) for collisional energy disposal.

12.5. STEREODYNAMICS OF GAS/ORGANIC-SURFACE COLLISIONS

We also investigated how collision with SAM surfaces influences the orientation and alignment of the rotational angular momentum of a scattered diatomic molecule. Analysis of the alignment of the final rotational angular momentum in collisions involving initially rotationally cold diatomic molecules indicates a slight preference for "cartwheel" rotational motions, as has been seen in studies of gas/metal and gas/liquid scattering. Additionally, a preference for "corkscrew" motion was also seen. In contrast, collisions of initially rotationally excited molecules slightly favor retention of "helicopter" motion of the recoiling species. Orientation studies reveal that, while cartwheel "topspin" motion is favored for collisions in which

intially cold diatomics become rotationally excited, no preferred handedness is seen when the molecules leave with helicopter motion. Analysis of trajectories involving molecules with specfic initial alignment/orientation and collision geometries shows a non-negligible effect of the initial rotational motion on the dynamics of energy transfer. The calculated trends in the stereodynamic properties for the two SAMs indicate that the hydrogenated surface is effectively more corrugated than the fluorinated surface.

12.6. REACTIONS AT THE GAS/ORGANIC-SURFACE INTERFACE

Armed with the knowledge that collisional energy transfer from gas-phase projectiles to SAM surfaces is extensive, and thermalization therefore has a large probability, the feasibility of a collisional-energy promoted, direct gas/organic-surface reaction was interrogated. Initial investigations into translational-energy-induced promotion of the azide-alkyne cycloaddition 'click' reaction showed no evidence for alkynic gases to form products upon collision with azide-terminated SAMs. Time-of-flight profiles were recorded to ascertain any change in the scattering dynamics as a result of surface reaction, and coincident RAIR spectra were used to monitor surface-bound products. Both techniques revealed that no reaction had proceeded under the probed conditions. XPS data taken before and after exposure to high energy alkynic beams confirmed that cycloaddition of the impinging gas-phase species had failed. Methylene stretching mode intensities in the RAIR spectra, combined with complementary evidence from molecular-dynamics simulations of N_3-SAMs, indicate that the azide tailgroups are located at the interface with an unfavorable orientation for the reaction to proceed. Future efforts with this system will include: 1) confirmation that the alkynic gases used will react with the N_3-SAM surface in solution and 2) scattering from surfaces in which we have introduced disorder into the azide monolayer via mixed monolayer approaches and/or surface heating.

12.7. PROSPECTUS FOR FUTURE ENDEAVORS

In addition to the proposed experiments for the click reaction, there exist many areas for future research to extend the efforts described in this dissertation. First, extension of the mass effects study (see Chapter 5) to include collisions of rare gases with chlorine- and

bromine-terminated monolayers should be completed. The experimentally observed trends seen over the Ne, Ar, and Kr series should continue in a logical, kinematically determined manner when these gases collide with Cl- and Br-SAMs. Kr (which showed no difference when scattering from the CH_3- and CF_3-SAMs at E_{coll}=60 kJ·mol^{-1}) should show non-equivalent scattering dynamics upon collision with these more massive surfaces. These scattering experiments can be paralleled with complementary classical-trajectory simulations based on accurate potentials of the type described in Chapter 4.

It will be interesting to investigate the behavior of a diatomic with a large dipole (e.g. HCl) scattering from polar (e.g. OH-SAM) and non-polar surfaces. Ab initio data for various approaches of HCl to methanol have been calculated in our lab, and some preliminary analytic potentials have been fit. It remains to be seen if the Buckingham potential employed to fit the ab initio data is general enough to capture the long-range coulombic interactions present in the HCl/methanol system. Previous experimental work in the Morris group examined both Ar and HCl scattering from SAMs. Simulations of the HCl/OH-SAM system will no doubt be invaluable to elucidate further the microscopic detail of energy transfer and mass accommodation in this system.

Finally, study of proven gas/organic-surface reactions, such as OH radical reacting with a hydrocarbon surface to produce H_2O, will extend our knowledge of chemical reaction dynamics at the gas/organic-surface interface.